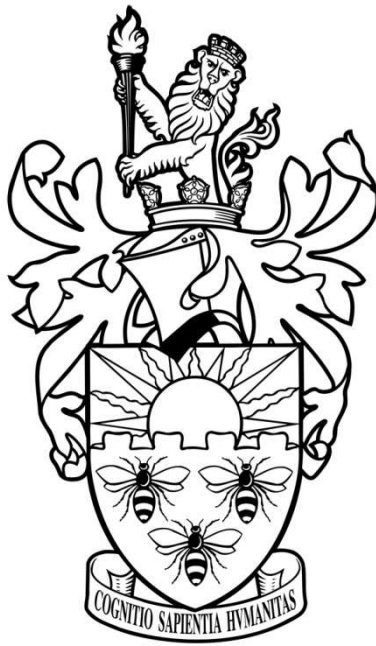


# **THERMAL FINITE ELEMENT ANALYSIS OF CERAMIC/METAL JOINING FOR FUSION USING X-RAY TOMOGRAPHY DATA**



A thesis submitted to the University of Manchester for the degree of  
PhD in the Faculty of Engineering and Physical Sciences

2013

Llion Marc Evans

School of Materials



# Contents

Contents .....	3
List of Figures .....	7
List of Tables.....	13
List of Abbreviations.....	15
Abstract .....	17
Lay abstract .....	19
Declaration .....	21
Copyright .....	21
Acknowledgements .....	23
The Author .....	25
CHAPTER ONE: Introduction .....	29
1.1 Outline .....	29
1.2 Programme of work.....	30
1.3 Collaborator contributions.....	35
1.3.1 Contributions to Chapter 3 .....	35
1.3.2 Contributions to Chapter 4 .....	35
1.3.3 Contributions to Chapter 5 .....	36
1.4 Background .....	36
1.4.1 Current status of world energy .....	37
1.4.2 The challenges facing delivery of fusion energy .....	38
1.4.3 Considerations for materials selection .....	42
CHAPTER TWO: Methods .....	47
2.1 Experimental collection of input material properties .....	49
2.2 Creating a digital geometry from 3D images .....	52
2.2.1 Image acquisition: X-ray Tomography .....	52
2.2.2 Segmentation and Meshing .....	58
2.3 Simulation: FEM .....	72
2.4 Development and use of parallel transient thermal analysis code.....	75
CHAPTER THREE: Thermal Characterisation of Ceramic/Metal Joining Techniques for Fusion Applications Using X-ray Tomography .....	81

Abstract.....	83
3.1 Introduction.....	84
3.2 Materials.....	86
3.3 Method .....	88
3.3.1 Thermal Analysis.....	88
3.3.2 X-ray tomography.....	90
3.3.3 Visualisation and analysis of CT data .....	91
3.4 Results & Discussion .....	92
3.4.1 Thermal Diffusivity .....	92
3.4.2 X-ray Tomography .....	98
3.4.3 Visualisation and analysis of CT data .....	99
3.5 Conclusions.....	108
Acknowledgements.....	109
References.....	109
CHAPTER FOUR: Thermal Finite Element Analysis on Massively Parallel Computing	
Platforms.....	113
Abstract.....	115
4.1 Introduction.....	116
4.2 Theory and Methodology.....	118
4.3 Results.....	125
4.3.1 Varying mesh density .....	126
4.3.2 Varying temporal resolution .....	128
4.3.3 Varying the iterative solver stopping criterion .....	129
4.3.4 Solution time profiling & scalability with varying number of cores.....	132
4.3.5 Image-based modelling case study .....	138
4.4 Discussion .....	139
4.5 Conclusions.....	142
Acknowledgements.....	143
References.....	143
CHAPTER FIVE: Transient Thermal Finite Element Analysis of CFC-Cu ITER Monoblock from X-ray Tomography Data .....	
Abstract.....	149
5.1 Introduction.....	150
5.2 Materials.....	153



5.3	Method.....	155
5.3.1	Thermal diffusivity.....	155
5.3.2	X-ray tomography .....	156
5.3.3	Finite element mesh generation .....	157
5.3.4	Finite Element Analysis .....	158
5.4	Results and discussion.....	166
5.4.1	Thermal Diffusivity.....	166
5.4.2	X-ray tomography images.....	169
5.4.3	Conversion of tomography data into finite element meshes.....	173
5.4.4	FEA .....	177
5.5	Conclusions .....	183
	Acknowledgements .....	184
	References .....	185
	CHAPTER SIX: Conclusions.....	187
6.1	Discussion .....	187
6.2	Further work .....	190
6.3	Research impact .....	192
	Bibliography.....	195
	Appendix .....	205
	A: Nikon Metrology 225/320 kV system at Manchester X-ray Imaging Facility .....	205
	B: Netzsch 457 MicroFlash®.....	207
	C: FORTRAN code for pre-processing of load distribution for LFA simulation.....	209
	D: FORTRAN code for transient thermal FEA in parallel .....	213
	E: FORTRAN code for post-processing of nodal temperatures .....	237
	F: xx12 input file details [68].....	239

Word Count: 45681



## List of Figures

Figure 1.1. Projection of world energy demand and supply [8].....	37
Figure 1.2. Global Fossil Carbon Emissions [16]. .....	38
Figure 1.3. Deuterium-Tritium (DT) fusion reaction [20]. .....	39
Figure 1.4. Fusion reaction cross-sections of light atoms; hydrogen (p), deuterium (D), tritium (T), helium (He) and boron (B) [23]. .....	40
Figure 1.5. Schematic representation of tokamak design [27]. .....	41
Figure 1.6. Schematic representation of a tokamak interior and its cross-section [32]. .....	42
Figure 1.7. Schematic drawing of various crystal lattice defects; a) Interstitial impurity atom, b) Edge dislocation, c) Self interstitial atom, d) Vacancy, e) Precipitate of impurity atoms, f) Vacancy type dislocation loop, g) Interstitial type dislocation loop, h) Substitutional impurity atom [34]. .....	43
Figure 1.8. Comparison of typical stress-strain curves for unirradiated and irradiated steel [35]. .....	44
Figure 1.9. Comparison of ideal stress-strain behaviour of monolithic and composite ceramics [36]. .....	45
Figure 1.10. Hydrocarbon build-up on graphite panels [47]. .....	46
Figure 2.1. Carbon fibre composite represented by (a) photograph (b) image-based model constructed from X-ray tomography data (c) unit cell and (d) analytical model. [48]. .....	48
Figure 2.2. Comparison of experiment and differing modelling approaches for a CFC composite, stress-strain curve for (a) a graphitised composite in perpendicular direction and (b) an ungraphitised composite in lamina direction [48]. .....	48
Figure 2.3. 3D image of Aluminium foam with hundreds of millions of elements made with tomography data [49]. .....	49
Figure 2.4. Typical temperature curve measured on rear face of sample after initial heat pulse. ....	51
Figure 2.5. Schematic representation of X-ray tomography image acquisition method [53]. .....	53
Figure 2.6. Example radiograph and tomography slices of CFC sample.....	55
Figure 2.7. Plot showing distribution of greyscale values rather than one value for a perfectly homogeneous material. ....	56
Figure 2.8. Schematic demonstrating of how contrast to noise ratio can effect resolving features in image from (a) actual sample geometry to (b) reconstructed image with	

spread sample boundaries due to image quality factors and (c) increased difficulty in resolving with lower resolution image. ....	56
Figure 2.9. Greyscale value profile across sample affected by beam hardening (a) before and (b) after applying a correction filter [58]. ....	57
Figure 2.10. Artefacts in reconstructed image of CFC sample due to (a) ring and (b) edge effects. ....	58
Figure 2.11. Tomography slices of carbon fibre preform in (a) x-z and (b) x-y planes. ....	59
Figure 2.12. Examples of tomography data visualisation techniques; (a) volume rendering with segmented porosity, (b) tomography greyscale slices, (c) volume rendering showing internal structure all of a 0/90 panox CFC and (d) X-ray absorption iso-surface of carbon fibre preform. ....	60
Figure 2.13. Surface rendering of 0/90 panox CFC (purple) segmented by greyscale thresholding, porosity segmented by boolean logic with remaining image volume then separated into internal porosity (red) and porosity connected to the external environment (green) by floodfill tools. ....	61
Figure 2.14. Tomography slice of CFC-Cu_GS sample, described in section 3.2, in x-z plane with annotations showing locations of greyscale profile lines used by Figure 2.15 and Table 2.1 data point locations. ....	62
Figure 2.15. Greyscale values along profile lines from the tomography slice in Figure 2.14; (a) showing profiles in x-direction through the Cu (yellow) and CFC (grey) materials separately and (b) in z-direction traversing both material layers. ....	62
Figure 2.16. Attempts at using automated segmentation by use of thresholding means only, with each range of greyscale values either failing to fully capture the desired material or, conversely, unintentionally including surrounding material. ....	64
Figure 2.17. Volume of three materials (surrounding air/porosity, CFC and Cu) contained within tomography image of CFC-Cu_GS sample, described in section 3.2, calculated from (a) measuring sample with micrometre callipers (b) greyscale data and (c) segmented data. ....	65
Figure 2.18. Tetrahedral and Hexahedral elements used in finite element analysis. ....	69
Figure 2.19. Example of curve described by an increasing number of nodes. ....	70
Figure 2.20. Comparison of structured and unstructured mesh of the same geometry [64]. ....	71
Figure 2.21. Surface of SiC <sub>f</sub> /SiC composite with a typical mesh density required by IBFEM to accurately describe misco-structures. ....	72
Figure 2.22. Using FEM to calculate the movement of nodes on an element from (a) initial state when (b) perturbed by strain of one node to (c) final equilibrium position defined by loading and material properties i.e. Young's modulus and Poisson's ratio in this instance. ....	73

Figure 2.23. Overview of program developed to solve transient thermal analysis in parallel, explaining functions of each section of the code. ....	78
Figure 3.1. Schematic of divertor monoblock.....	85
Figure 3.2. Samples used for thermal analysis; (a) CFC, (b) Cu, (c) CFC-Cu joined by; direct casting (DC), (d) one step brazing (OSB), (e) braze coated by galvanisation process (GG), (f) braze coated by sputtering process (GS). ....	88
Figure 3.3. Typical temperature curve measured on rear face of sample after initial heat pulse. ....	90
Figure 3.4. Thermal diffusivity measured by laser flash analysis.....	95
Figure 3.5. Specific heat capacity calculated by calibration of diffusivity against Pyroceram 9606. ....	95
Figure 3.6. Thermal conductivity calculated from diffusivity, density and spcific heat values.....	96
Figure 3.7. Difference, as a percentage, in sample thermal diffusivity compared to expected value as calculated from constituent material thicknesses.....	96
Figure 3.8. Difference, as a percentage, in sample specific heat capacity compared to expected value as calculated from constituent material thicknesses.....	97
Figure 3.9. Difference, as a percentage, in sample thermal conductivity compared to expected value as calculated from constituent material thicknesses.....	97
Figure 3.10. Cross sectional tomography slice showing (a) streaking artefacts from high absorption Cu masking internal CFC structures at interface, resolved by individually adjusting image brightness and contrast values for (b) Cu and (c) CFC. ....	99
Figure 3.11. Various artefacts that hinder automated segmentation of CT image caused by high absorption contrast ratio in an X-ray tomography slice from the midplane of a CFC-Cu divertor monoblock.....	99
Figure 3.12. 3D volumetric rendering of CT data, showing (a) CFC-Cu_GS, (b) same sample with porosity highlighted and (c) CFC removed to display porosity aligntment.....	100
Figure 3.13. CT data of CFC-Cu_DC sample represented by; (a), (b) 3D visualisation of Cu showing protruding interface features, (c) tomography slice in x-z plane showing Cu features (containing voids) entering porosity in CFC, (d), (e) and (f) tomography slices in x-y plane progressing through the interface from Cu into CFC. Cu, CFC and voids/porosity are respresented by light, medium and dark level greyscale pixels, respectively.....	105
Figure 3.14. CT data of CFC-Cu_OSB sample represented by; (a), (b) 3D visualisation of Cu showing protruding interface features and void layer between bulk Cu and braze, (c) tomography slice in x-z plane showing Cu features entering porosity in CFC, (d), (e) and (f) tomography slices in x-y plane progressing through the	

interface from Cu into CFC. Cu, CFC and voids/porosity are represented by light, medium and dark level greyscale pixels, respectively..... 105

Figure 3.15. CT data of CFC-Cu\_GG sample represented by; (a), (b) 3D visualisation of Cu showing protruding interface features, (c) tomography slice in x-z plane showing Cu veins of braze entering porosity in CFC, (d), (e) and (f) tomography slices in x-y plane progressing through the interface from Cu into CFC. Cu, CFC and voids/porosity are represented by light, medium and dark level greyscale pixels, respectively. .... 106

Figure 3.16. CT data of CFC-Cu\_GS sample represented by; (a), (b) 3D visualisation of Cu showing protruding interface features, (c) tomography slice in x-z plane showing Cu veins of braze entering porosity in CFC, (d), (e) and (f) tomography slices in x-y plane progressing through the interface from Cu into CFC. Cu, CFC and voids/porosity are represented by light, medium and dark level greyscale pixels, respectively. .... 106

Figure 3.17. Projection of void area (red) covering total sample area (black) in x-y plane for samples (a) DC, (b) OSB, (c) GG and (d) GS..... 107

Figure 3.18. Thermal conductivity of the four joined samples with points denoting experimental results and lines denoting predicted values based on contribution of constituent material thickness and percentage of sample area covered by voids.. 107

Figure 4.1. Analytical problem, a cuboid with unit initial temperature and zero surface temperature. .... 122

Figure 4.2. Cubic volume of analytical domain meshed with increasing mesh density using (a) 2 x 2 x 2 Cube, 40 tets, (b) 4 x 4 x 4 Cube, 320 tets and (c) 8 x 8 x 8 Cube, 2560 tets..... 123

Figure 4.3. Temperature of the central node versus time for varying mesh densities..... 127

Figure 4.4. Simulation of an analytical thermal conductivity problem of a copper cube, 1 °C initial temperature, has boundary conditions of 0 °C on all external surfaces for  $t > 0$  s. Figure shows visualisation of the results as a cross-section of the temperature distribution at  $t = 2.E-6$  s, calculated by ParaFEM..... 127

Figure 4.5. Temperature of the central node versus time for varying time-step sizes..... 129

Figure 4.6. Temperature of the central node with respect to time for varying iterative solver stopping criterion. .... 131

Figure 4.7. Error in calculating temperature of the central node with respect to time using optimal parameters..... 131

Figure 4.8. Scalability of absolute solution time for 50 time-steps and outputs of analytical problem (meshes 64x, 128x & 256x) with increasing numbers of cores. .... 133

Figure 4.9. Scalability of solution time (speed-up) for 50 time-steps and outputs of analytical problem (meshes 64x, 128x & 256x) with increasing numbers of cores. .... 133

Figure 4.10. Comparison of ParaFEM and commercial solver scalability. Absolute solution time for 50 time-steps and outputs of analytical problem (mesh 64x) with increasing numbers of cores.....	134
Figure 4.11. Computational cost profiling of each section required for the solver to initialise, complete and output one time step for a varying number of cores. ....	135
Figure 4.12. Computational cost profiling of a complete analysis of the analytical problem for varying number of cores.....	136
Figure 4.13. Computational cost profiling of a complete analysis of the analytical problem for optimal number of cores.....	136
Figure 4.14. Tomography slices of SiC <sub>f</sub> /SiC sample in top-down and cross-section views; (a) 100 %, (b) 25 % and (c) 5 % resolutions.....	138
Figure 4.15. 3D reconstruction from X-ray tomography data of SiC <sub>f</sub> /SiC composite sample, (a) 25% resolution (b) 5% resolution.....	139
Figure 4.16. Comparison of results from ParaFEM and a commercial solver using identical input parameters to solve the Carslaw & Jaeger analytical problem [104] described in Figure 4.1. ....	140
Figure 5.1. Schematic of section of ITER divertor [107]. ....	151
Figure 5.2. Samples used; (a) CFC, (b) Cu, (c) CFC-Cu disc and (d) CFC-Cu divertor monoblock.....	154
Figure 5.3. SEM image of CFC and brazing alloy interface.....	155
Figure 5.4. Laser energy for a given voltage for the NETZSCH LFA 457. ....	158
Figure 5.5. Typical energy pulse emitted from NETZSCH LFA 457 laser.....	159
Figure 5.6. Projecting flux over an area to nodal coordinates due to discretisation inherent in FEA. ....	160
Figure 5.7. Comparison of the area of (a) element faces and (b) the effective area seen by the laser in x-y plane. ....	160
Figure 5.8. Multivariate Gaussian distribution exhibited by laser beam. ....	161
Figure 5.9. MGD profile of 15 mm diameter spot size laser where energy reduces by 10 % between centre and $r = 5.0$ mm, i.e. $\sigma = 10.892$ .....	162
Figure 5.10. Schematic of applied loads in monoblock simulation. ....	166
Figure 5.11. Thermal diffusivity measured by laser flash analysis.....	168
Figure 5.12. Specific heat capacity calculated by calibration of diffusivity against Pyroceram 9606. ....	168
Figure 5.13. Thermal conductivity calculated from diffusivity, density and specific heat values.....	169
Figure 5.14. 3D reconstruction from X-ray tomography data for the CFC-Cu disc showing; (a) complete sample, (b) rough Cu surface at interface with CFC, (c) slice midway	

through CFC section, (d) contact area at CFC-Cu surface and (e) porosity within the CFC showing preferential alignment with direction of thermal transport..... 171

Figure 5.15. 3D reconstruction from X-ray tomography data for divertor monoblock showing; (a) complete sample, (b) rough Cu surface at interface with CFC, (c) slice through the midplane, (d) large area where CFC has delaminated from Cu during brazing process and (e) porosity within the CFC showing preferential alignment with direction of thermal transport. .... 171

Figure 5.16. Tomography slice from the midplane of the divertor monoblock showing internal porosity of CFC. Additionally a large void spanning the perimeter of one side of the Cu pipe can be seen, this was likely introduced during brazing due to orientation of sample. .... 172

Figure 5.17. X-ray tomography x-y planar slice midway through CFC layer of CFC-Cu disc showing effect of downsampling from (a) original resolution to (b) 30% and (c) 5% resolutions. .... 174

Figure 5.18. Cross section of temperature within CFC-Cu sample at  $t = 1.27 \times 10^{-2}$  s calculated by FEA, showing low thermal gradients in the x-y plane and low temperature rise. .... 177

Figure 5.19. Rear surface temperature of CFC-Cu disc during LFA experiment and simulation. .... 178

Figure 5.20. Time series analysis of the divertor monoblock tile created from an X-ray tomography image. .... 180

Figure 5.21. Temperature of nodes either side of Cu pipe, as shown in Figure 5.20, versus time for both orientations of the monoblock. .... 181

Figure 5.22. Temperature profile between the front and rear surfaces of the divertor monoblock with delamination not aligned with the heat source and sink. .... 181

Figure 5.23. Temperature profile between the front and rear surfaces of the divertor monoblock with delamination positioned between the Cu pipe and the thermal loads. .... 182

Figure 5.24. Example of localised “hot spots” caused by characteristic porosity located internally within the CFC section of the CFC-Cu divertor monoblock..... 182

Figure 6.1. Workflow overview of image-based modelling technique. .... 188

Figure A.1. Nikon Metrology 225/320 kV system. .... 205

Figure B.2. Netzsch 457 MicroFlash®. .... 207



## List of Tables

Table 2.1 Data from tomography slice of CFC-Cu_GS sample, see Figure 2.14, showing varying greyscale values at different locations within same material.....	63
Table 3.1 Sample dimensions. ....	88
Table 3.2 X-ray tomography parameters used. ....	91
Table 3.3 Reconstruction settings. ....	91
Table 3.4 Materials properties of CFC and Cu as specified by ITER MPDB. ....	98
Table 3.5 Comparison of Cu area calculated by diameter and measured by CT, also percentage of area in contact with CFC and void volume as percentage of total volume and void area in x-y plane as percentage of total planar area. ....	104
Table 4.1 Details of mesh densities used for simulation of analytical problem. ....	123
Table 4.2 Material properties used as input parameters.....	123
Table 4.3 Solution method parameters (iterative solver stopping criterion of 1.E-8). ....	126
Table 4.4 Solution method parameters (Mesh 32x, iterative solver stopping criterion of 1.E-8).....	128
Table 4.5 Solution method parameters (Mesh 256x, time-step size = 1.E-4, number of steps = 50, output frequency = 1).....	130
Table 4.6 Based on 5000 time steps, output every 20.....	137
Table 5.1 Sample dimensions. ....	154
Table 5.2 X-ray tomography parameters used. ....	156
Table 5.3 Reconstruction settings. ....	156
Table 5.4 Materials properties of CFC and Cu as specified by ITER MPDB. ....	169
Table 5.5 Segmentation and meshing output details for the CFC-Cu disc. ....	176
Table 5.6 Segmentation and meshing output details for the divertor monoblock sample. ....	176
Table 5.7 Material properties used for FEA.....	177
Table F.1 Input files required by program xx12 .....	239
Table F.2 Required variables for the .dat input file .....	240
Table F.3 Required variables for the xx12.d input file .....	241
Table F.4 Required variables for the xx12.fix input file.....	242
Table F.5 Required variables for the xx12.lids input file.....	243
Table F.6 Required variables for the xx12.mat input file .....	244
Table F.7 Required variables for the xx12.amp input file .....	245



## List of Abbreviations

CAD	Computer Aided Design
CCFE	Culham Centre for Fusion Energy
CVD	Chemical Vapour Deposition
CVI	Chemical Vapour Infiltration
DEMO	DEMONstration Power Plant
dpa	Displacements Per Atom
EPSRC	Engineering and Physical Sciences Research Council
FDTN	Fusion Doctoral Training Network
FE	Finite Element
GG	Gemco Galvenised
GS	Gemco Sputtered
HPC	High-Performance Computing
I/O	Input/Output
IAEA	International Atomic Energy Agency
IBFEM	Image-Based Finite Element Modelling
ICF	Inertial Confinement Fusion
JET	Joint European Torus
LHS	Left Hand Side
LIDAR	Light Detection and Ranging
MCF	Magnetic Confinement Fusion
MGD	Multivariate Gaussian Distribution
MPDB	Materials Property Database
MPI	Message Passing Interface
MRI	Magnetic Resonant Imaging
MTPS	Modified Transient Plane Source
OFHC	Oxygen Free High Conductivity
PFC	Plasma Facing Component
R&D	Research and Development
RF	Radio Frequency
RHS	Right Hand Side
RT	Room Temperature
SEM	Scanning Electron Microscope
SNR	Signal to Noise Ratio



## Abstract

The University of Manchester, 2013

Llion Marc Evans, PhD in the Faculty of Engineering and Physical Sciences

Thermal Finite Element Analysis of Ceramic/Metal Joining for Fusion Using X-ray Tomography Data

A key challenge facing the nuclear fusion community is how to design a reactor that will operate in environmental conditions not easily reproducible in the laboratory for materials testing. Finite element analysis (FEA), commonly used to predict components' performance, typically uses idealised geometries. An emerging technique shown to have improved accuracy is image-based finite element modelling (IBFEM). This involves converting a three-dimensional image (such as from X-ray tomography) into an FEA mesh. A main advantage of IBFEM is that models include micro-structural and non-idealised manufacturing features. The aim of this work was to investigate the thermal performance of a CFC-Cu divertor monoblock, a carbon fibre composite (CFC) tile joined through its centre to a CuCrZr pipe with a Cu interlayer. As a plasma facing component located where thermal flux in the reactor is at its highest, one of its primary functions is to extract heat by active cooling. Therefore, characterisation of its thermal performance is vital.

Investigation of the thermal performance of CFC-Cu joining methods by laser flash analysis and X-ray tomography showed a strong correlation between micro-structures at the material interface and a reduction in thermal conductivity. Therefore, this problem lent itself well to be investigated further by IBFEM. However, because these high resolution models require such large numbers of elements, commercial FEA software could not be used. This served as motivation to develop parallel software capable of performing the necessary transient thermal simulations. The resultant code was shown to scale well with increasing problem sizes and a simulation with 137 million elements was successfully completed using 4096 cores. In comparison with a low resolution IBFEM and traditional FEA simulations it was demonstrated to provide additional accuracy.

IBFEM was used to simulate a divertor monoblock mock-up, where it was found that a region of delamination existed on the CFC-Cu interface. Predictions showed that if this was aligned unfavourably it would increase thermal gradients across the component thus reducing lifespan. As this was a feature introduced in manufacturing it would not have been accounted for without IBFEM.

The technique developed in this work has broad engineering applications. It could be used similarly to accurately model components in conditions unfeasible to produce in the laboratory, to assist in research and development of component manufacturing or to verify commercial components against manufacturers' claims.



## Lay abstract

By harnessing the same process as that which powers the sun, fusion power promises to deliver an effectively limitless supply of energy without producing carbon emissions or long term nuclear waste. To achieve this, plasma is produced that is ten times hotter than the sun's core and is held in place by superconducting magnets. The edge of this plasma still reaches temperatures of up to 3000 °C and the challenge for engineers and materials scientists is to develop a vessel capable of containing this process.

Engineers often use computer models to predict how their design will perform under certain conditions. However, these models tend to be idealised and not include micro-scale features, such as defects introduced by the manufacturing process, which will cause unexpected behaviour of the component. An emerging technique shown to have improved accuracy converts three-dimensional images of manufactured components into computer models. These images can be collected by various methods, such as CT or MRI scanners similar to those found in hospitals. It was desired to use this image-based modelling to make design recommendations for components planned for a fusion reactor.

The difficulty with this method is that the models produced have very high resolutions requiring large amounts of computing power, currently available commercial software cannot be used to perform the simulations. This served as motivation to develop specialised software to be run on supercomputers. This enabled successful running of the models by dividing the calculations into manageable chunks to be solved using thousands of computer processors simultaneously. In applying this technique, small voids were found in the component being studied. If gone unnoticed these could have caused the component to fail, but this technique allowed recommendations to be made to reduce this risk.

Although developed for use with components for fusion, this technique has a broad application to most engineering fields. As well as being used for research and development, it is envisaged that a streamlined or automated deployment of the technique could be included in a manufacturing line to assist with quality assurance control.





## Declaration

No portion of the work referred to in the thesis has been submitted in support of an application for another degree or qualification of this or any other university or other institute of learning

## Copyright

- i. The author of this thesis (including any appendices and/or schedules to this thesis) owns certain copyright or related rights in it (the “Copyright”) and s/he has given The University of Manchester certain rights to use such Copyright, including for administrative purposes.
- ii. Copies of this thesis, either in full or in extracts and whether in hard or electronic copy, may be made **only** in accordance with the Copyright, Designs and Patents Act 1988 (as amended) and regulations issued under it or, where appropriate, in accordance with licensing agreements which the University has from time to time. This page must form part of any such copies made.
- iii. The ownership of certain Copyright, patents, designs, trademarks and other intellectual property (the “Intellectual Property”) and any reproductions of copyright works in the thesis, for example graphs and tables (“Reproductions”), which may be described in this thesis, may not be owned by the author and may be owned by third parties. Such Intellectual Property and Reproductions cannot and must not be made available for use without the prior written permission of the owner(s) of the relevant Intellectual Property and/or Reproductions.
- iv. Further information on the conditions under which disclosure, publication and commercialisation of this thesis, the Copyright and any Intellectual Property and/or Reproductions described in it may take place is available in the University IP Policy (see <http://documents.manchester.ac.uk/DocuInfo.aspx?DocID=487>), in any relevant Thesis restriction declarations deposited in the University Library, The University Library’s regulations and in The University’s policy on Presentation of Theses (see <http://www.manchester.ac.uk/library/aboutus/regulations>).



## Acknowledgements

I'd like to express my gratitude to Dr Lee Margetts to whom I am wholly indebted. The majority of the software development contained within this work was built upon the resultant code of his PhD thesis. Not only that, but for his continual support through long hours of debugging and redrafting. Dr Margetts went beyond the call of duty to ensure that the work remained focussed to reach its main objective and that I grew as a scientist.

For their supervision I would also like to thank; Prof Paul Mummery who was always in the know of who to contact when I was in need of something particular and his advice on academia, Prof Howard Wilson the Director of the Fusion DTN for his encouragement and enthusiasm for both the field of research and his students, and Prof Sergei Dudarev for being so welcoming during my time at Culham Centre for Fusion Energy.

I am also grateful to Dr Valentina Calasegno for not only supplying the materials used for the majority of this work, but for patience in explaining the aspects of material manufacture that was so unfamiliar to a physicist.

My appreciation also goes to staff at various facilities at the University of Manchester, who took the time to guide me through the wide range of techniques I needed to accomplish the work. In particular; Rob Bradley, Fabien Leonard, Tristan Lowe, Chris Martin (Manchester X-ray Imaging Facility), Louise Lever (Research Computing Services), Marc Schmidt, Andy Wallwork (Thermal Analysis).

Most importantly I'd like to thank my wife Rhiân, who was happy for us to relocate across the country so that I could follow my ambition, for her endless support and patience when I was working long hours and for listening to my 'lectures' when I needed to sound out my ideas. Diolch o galon, gallan i ddim wedi'i neud e hebddot ti.



## **The Author**

Llion Marc Evans graduated from the University of Wales, Aberystwyth in 2005 with a BSc (first class honours) in physics. His final year dissertation focussed on developing a laser based tomography system for scanning liquids. After spending some time practicing his Italian and working as a web-designer in Padova, Italy, he attended Imperial College, London, where he gained an MSc in Advanced Computational Fluid Dynamics in 2007. As a lifelong Formula 1 fan and with the view of pursuing a career in the industry, his joint research project with Ferrari investigated the effect of adding an external wheel fairing on the heat flow over the carbon-fibre brake discs by CFD simulations.

An increase in media attention on Fusion Energy led the author to change course from one type of stars to another. His ambition to be part of the global effort to harness the power of the sun on earth brought him to his PhD at the School of Materials at Manchester, which boasts a wealth of experience in the Nuclear Fission sector. As a member of the first student cohort on the Fusion Doctoral Training Network, Llion attended an intensive six month training scheme at York University giving him a broad grounding in Fusion Energy. His PhD married his previous two avenues of work by utilising tomography data to build thermal computational models for fusion applications. In 2013 he was awarded the prestigious Culham Centre for Fusion Energy Fellowship where he presently works, investigating concept designs for the first demonstrational fusion power plant.



“**A**t present it probably is fair to say that the state-of-the-art has advanced to the point where solution of any structural engineering problem can be contemplated, but there may be a wide variation in the quality of the result obtained. Depending on the validity of the assumptions made in reducing the physical problem to a numerical algorithm, the computer output may provide a detailed picture of the true physical behavior or it may not even remotely resemble it. A controlling influence on where the final result lies along this scale is the skill of the engineer who prepares the mathematical idealization; when dealing with complex and unusual structures, this phase of the analysis is an art and the program cannot be treated merely as a “black box”. Because of the significant possibility that the analysis may have totally overlooked or misjudged some important aspects of the mechanical behaviour, experimental verification should be incorporated into the analytical process whenever it steps beyond the borders of experience and established practice. [1]

”

Ray W. Clough

The finite element method after twenty-five years: A personal view (1980)





# CHAPTER ONE: Introduction

## 1.1 Outline

The ability to perfectly predict the behaviour of a given item in its environmental setting has long been the pursuit of computational modelling. Having total confidence in primary designs before a single component has rolled off the production line would remove the need for test mock-ups, thus slashing the time taken for R&D and its associated budgets. It would open up new possibilities by allowing designs to operate to the limit whilst simultaneously increasing safety as failures would no longer happen unexpectedly [2]. Any significant developments in this pursuit, therefore, have far reaching implications. It is unlikely that one breakthrough will deliver this ambitious goal, rather it will be achieved by an incremental progression as computational hardware and algorithms improve and new techniques are implemented. The aim of this work is to contribute to that global effort by developing new code that utilises cutting edge computing hardware to open new avenues of modelling. This is done in the setting of fusion energy, a field of research heavily dependent on modelling. Even though plasma physics, the vehicle to realising fusion, has progressed since the attempt to achieve fusion began, there are still no facilities in existence capable of producing neutrons with the same energy and flux produced by deuterium-tritium reactions. Therefore there are no testing facilities to refine designs or perform materials research. This is why modelling has played such an instrumental role in the design of the plasma experiment ITER, the world's biggest scientific collaboration, with over 48,000 ITER related papers including references to finite elements between 1991 [3] and present day [4].

Not surprisingly, it has been observed that the microstructures within manufactured components govern the behaviour of the materials used [5]. Because of the large difference in scale between these features and the sample, they are almost exclusively omitted when modelling. However, by identifying these structures through 3D imaging this work incorporates them to build upon simplified geometries traditionally used in modelling. The combination of this with the novel materials to be used in environments not previously experienced, provides the landscape within which this work will develop modelling techniques that will aim to provide improved accuracy over those currently in common use.

## **1.2 Programme of work**

This thesis is submitted under the University of Manchester's 'alternative format', which allows inclusion of standalone sections suitable for publication in a peer-reviewed journal. These pieces of work can be in unpublished or published form. These papers are preceded by introductory and methods chapters to place the research in context. They are followed by conclusions and suggested further work to build a narrative that will form one coherent body of work. Because the work fell into distinctive categories of materials characterisation, code development and computer simulations, it was well suited for submission under this alternative format.

As the papers are presented in pre-publication form, the numbering for pages, figures, tables, equations and references appear in continuation with the rest of the thesis. For ease of referencing, each of the journal papers (i.e. Chapters 3-5) has its own standalone bibliography in addition to the main one.

This work was developed as part of the Fusion Doctoral Training Network (FDTN), which is a collaboration of academic and government research institutions working together to provide a world-leading fusion energy postgraduate training programme for UK scientists and engineers leading to the award of PhD degrees. The institutions involved are the Universities of Durham, Liverpool, Manchester, Oxford and York, in collaboration with the Culham Centre for Fusion Energy (CCFE) and the Central Laser Facility, and with funding from the Engineering and Physical Sciences Research Council (EPSRC). As such, the initial six months was spent understanding the mission of the community in making fusion power a reality, the overall design of a working magnetic confinement fusion (MCF) reactor and more specifically the interaction between the plasma and fusion process with the materials that would contain them. There is a delicate balance between the selection of materials and plasma confinement, which in turn impacts plant efficiency. As part of this, time was spent studying the literature on the use of ceramics in fusion engineering and the important role of computer modelling in supporting predictions about their behaviour. It was important to understand these principles before developing a programme of work to best distinguish areas of research that would benefit from further work.

The following year was spent gaining experience in ceramic composites through their machining, imaging, thermal and mechanical characterisation of their highly anisotropic behaviour. Initial 3D imaging through X-ray tomography highlighted the difficulty in fully resolving microstructures because of the near identical X-ray absorption coefficients of both matrix and fibre phases of the material. It was therefore decided to concentrate efforts on the joining of ceramics to metals, an important procedure for power plant design that has proven difficult to accomplish well. The components which were most readily available that made use of a ceramic/metal join were part of the power plant cooling

system. This naturally led the research to focus on the thermal performance at these interfaces.

This research formed the basis of the first paper which investigated a series of joining techniques. It was found, through experimental examination, that samples produced to have similar macroscopic geometries had drastically varying thermal performance. Investigation of the microstructures at the interface by X-ray tomography was performed to determine mechanisms which might cause this.

Despite realising the importance of these microstructures on performance, traditionally these would not be included in any modelling of designed components. It was decided to attempt to build upon previous work performed by the imaging group at the University of Manchester, which converts high resolution three-dimensional tomography images into finite element models of composites with the aim of producing more accurate results.

Using current tomography equipment, a 10 mm diameter sample would have a resolution of approximately 5  $\mu\text{m}$  with the final image being 2000 x 2000 x 2000 pixels in size, or 8 billion voxels. If the whole domain was turned into a finite element mesh at full resolution it would require 40 billion elements, where traditional finite element analyses use around 50 thousand elements. It quickly became clear that the tools available at the time were not adequate to cope with the significant increase in data associated with the high-resolution required to faithfully capture the microstructures. In order to successfully run on commercial FE software using a high-end workstation, the image required downsampling to 5% of its original resolution. This produced a model with approximately 1 million elements, two orders of magnitude greater than used by engineers, but only retained the largest of features, which served as little more than proof of principle. The

following year was dedicated to developing software capable of achieving a simulation of the thermal experiment at a resolution deemed high enough to capture the features of interest.

In order to maximise potential of computing power, a parallel solution was sought. It was decided to join an on-going open source parallel FEM project (ParaFEM, spearheaded by Dr Lee Margetts, University of Manchester) as this would benefit from collaboration that would bring a wealth of experience, a strong pre-existing framework for the code and would maximise exposure of any output hoped to achieve through the existing user community.

The ParaFEM project is based on a widely-used academic FEM text book which thus served as a guide for development [6]. The textbook contains a series of programs developed to solve specific analytical problems, which form the foundation for more complex simulations like the one in question. The work started by adapting a program that solved a steady state pressure gradient in serial to one that solved a thermal gradient. This worked as a way for the author to familiarise himself with the code's structure. Once successfully validated against an analytical problem and a commercial solver a progression was made to perform the same simulation with a parallel code.

After this had been achieved the code was generalised to be able to solve any given geometry and variable boundary conditions. Then features were added, one at a time, with each step requiring debugging and thorough validation. The largest change was the addition of the transient state, which required a rethinking of how the input/output (I/O) was handled and careful ordering of solution steps. The product of this development formed the second paper with particular interest not in speed of solution but scalability

with increasing number of computing cores. Compared to the currently available commercial solvers, it opened up new areas of simulations. Computations that previously could not be run were now possible and became practical, with simulation time reducing from a theoretical 224 days to 1 hour and 54 minutes.

Effort was also given to streamlining the workflow by creating pre- and post-processing tools specific to the thermal analysis and inputting to development of tools by Louise Lever (University of Manchester) as part of the wider ParaFEM project.

The final six months, a culmination of the experience gained through previous work, was spent collecting more tomography data for a component designed for a fusion reactor that utilised one of the previously studied joining techniques. Data for the original thermal analysis sample and the new component were then converted to an FE model. The former was used as validation of the technique, whilst the latter gave insight to *in situ* performance that was not yet testable experimentally. This gave the opportunity to provide recommendations for improvements in future designs. This work is presented in the third and final paper.

It is not intended for this technique to replace CAD modelling, rather to contribute at a later stage in the R&D process. CAD modelling allows the quick profiling of a series of design specifications for optimisation purposes. This is used to narrow the number of candidate designs to a few that will be manufactured for testing, a process which is iterated until a final design is nominated. Image-based modelling will highlight discrepancies between CAD and real world performance due to features introduced in the manufacturing process. This can be used to either target issues introduced in manufacturing or suggest design changes that take account of these features.

### **1.3 Collaborator contributions**

The papers, in their presented form, are ready for submission to peer-reviewed journals. The work was undertaken with co-authors; as such the following section will detail the contribution of each author for each paper.

#### **1.3.1 Contributions to Chapter 3**

The joining technique development and its implementation were entirely performed by the authors Casalegno and Ferraris at Politecnico di Torino. Further sample preparation for thermal analysis was performed by the first author. Tomography imaging was also performed by the first author in consultation with Leonard and Lowe to mitigate artefacts caused by high absorption contrast. Visualisation and image analysis was performed by the first author. Thermal analysis was performed by the first author in consultation with Schmidt to ensure accurate results for multilayer and composite samples. The paper and figures were produced by the first author with editorial contributions from Margetts, Lee and Mummery.

#### **1.3.2 Contributions to Chapter 4**

The software for this paper was co-developed by the main author and Margetts, and was based on extensive parallel libraries previously developed by Margetts. Pre and post processing tools were co-developed by the first author, Margetts and Lever. The materials used for the case study were supplied by Windes (Idaho National Laboratory). Simulations were prepared and performed by the first author in consultation with Margetts. The paper and figures contained within were the work of the first author. Again, Margetts and Mummery provided editorial comments.

### **1.3.3 Contributions to Chapter 5**

As with Chapter 3, the materials were manufactured by Casalegno and Ferraris, with additional SEM work by Casalegno. Tomography imaging of the samples was performed by the first author in consultation with Lowe. Thermal analysis was performed by the first author in consultation with Schmidt. Developing the parameters and boundary conditions to accurately represent the experimental thermal analysis was the work of the first author in consultation with Schmidt and Lindemann (Netzsch), who developed the experimental apparatus. Analyses of the experimental and computational results were performed by the author in consultation with Wallwork for the thermal diffusivity and Lever for high-end visualisation. The conceptual ideas for the paper were the first author's with Margetts providing an advisory role throughout. Margetts and Mummery provided editorial comments.

## **1.4 Background**

This background section will provide a general introduction to fusion energy. By looking at the current energy climate, mix of energy sources and the issues related to them an argument is presented as to why fusion should be a high priority for governments worldwide. Then consideration is given to the challenges facing the fusion energy research community in realising this goal. Finally, relating this work to the field, the specific issue of materials for fusion applications is introduced. The requirements asked of the materials are discussed and candidate materials are presented. To avoid repetition, background specifics on the materials investigated in this work are reserved for the journal papers (i.e. Chapters 3-5).



### 1.4.1 Current status of world energy

It has been known for many years that the world is heading towards a global energy crisis. Modern technology-hungry lifestyles have a higher demand per capita for electricity and fuel [7]. As large nations like China and India are going through their own ‘industrial revolution’, predictions see the world’s energy consumption set to soar over the coming century, as shown in Figure 1.1.

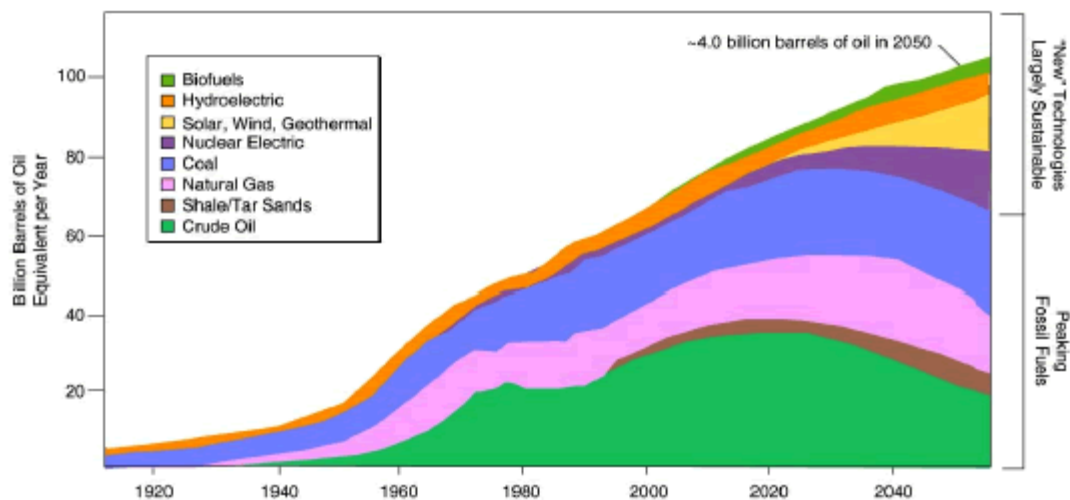


**Figure 1.1.** Projection of world energy demand and supply [8].

It is now the consensus that man has played some part in the earth’s global warming, most probably through CO<sub>2</sub> emissions due to burning fossil fuels [9] [10] [11]. It is not known if the effect already observed is reversible, but as energy consumption is set to rise, cutting carbon emissions is essential to prevent acceleration of global warming’s effects. Figure 1.2 shows the increase in carbon emissions over the past two centuries. There is currently research into carbon capturing technology to allow continued use of fossil fuels whilst mitigating carbon emissions [12]. But even if more sources of fossil fuels are discovered it would only defer the need to develop alternative ‘clean’ sources of energy to replace their finite supply [13] [14].

As fossil fuel reserves are depleted there will be more demand for less traditional fuels which have previously been considered too expensive. However, it is accepted that the current forecasts for energy demand will far outstrip what can feasibly be provided by energy sources such as renewables and biofuels. This would be true regardless of efforts to curb our energy uses or increase the efficiency of our appliances, gadgets etc. [15].

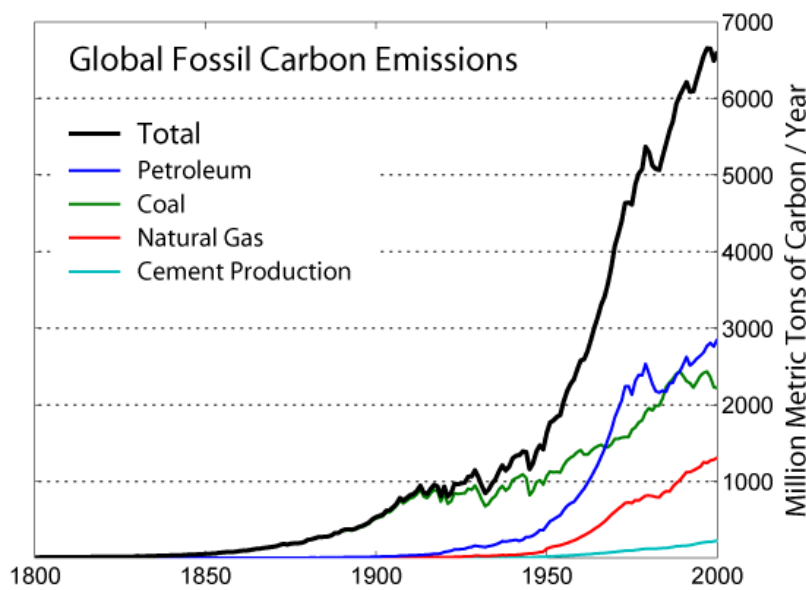


**Figure 1.2.** Global Fossil Carbon Emissions [16].

#### 1.4.2 The challenges facing delivery of fusion energy

Nuclear fission is regarded as one alternative energy source. But many nuclear research programmes were scaled back or abandoned in the wake of accidents in the 1970s and 80s (the biggest being Chernobyl [17]). Recently, due to the energy crisis becoming more apparent, there has been a recent resurgence in nuclear research. The United States, for example, are now commissioning the construction of the first new fission power plants to be built in 30 years [18]. Fission reactors remain a contentious political issue mainly due to potential of enrichment for weapons and the waste legacy left by a reactor. Therefore any country planning to develop a nuclear programme must comply with strict codes of

conduct set out by the International Atomic Energy Agency (IAEA). These plans are often met with negative reactions by the media and a proportion of the public [19].

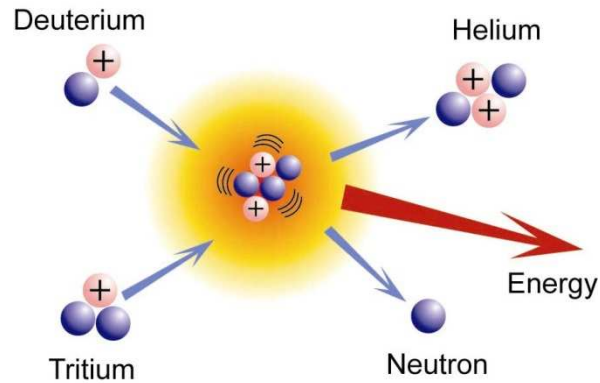


**Figure 1.3.** Deuterium-Tritium (DT) fusion reaction [20].

Since the early hydrogen bomb tests in the 1950s, fusion energy has been seen as a potential alternative to fission [21]. Fusion reactions require two nuclei to be fused together utilising very high temperatures or pressures to overcome the Coulomb barrier, resulting in the creation of new particles and emission of neutrons. This process is shown in Figure 1.3. The resultant mass loss from the system is released in the form of kinetic energy, which is carried by the reaction products [22]. The level of emitted energy released depends on particle selection. The likelihood of an interaction between particles is expressed as an atom's cross-section. As can be seen in Figure 1.4, deuterium-tritium reactions are most likely to bring commercial fusion energy due the higher probability of a reaction at lower, more achievable, energies.

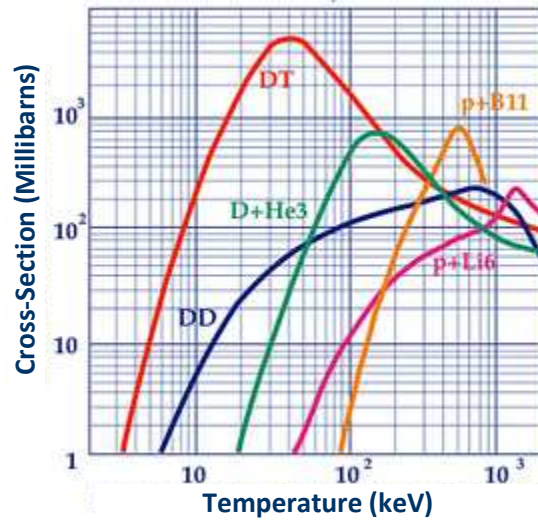


**Figure 1.4.** Fusion reaction cross-sections of light atoms; hydrogen (p), deuterium (D), tritium (T), helium (He) and boron (B) [23].

It was realised early on that confinement of plasma was the most likely avenue for successful results, but no real headway was made until the Russians developed the tokamak T-4 in 1968 [24] [25]. Early experiments used a linear confinement of the plasma, which suffered losses at either end. By bringing the two linear ends together, the toroidal shape of the tokamak overcomes this issue. The combination of a toroidal driving current through the plasma along with toroidal and poloidal magnetic fields further increased the confinement efficiency, thus greatly increasing the probability of the occurrence of fusion reactions [22]. A schematic representation of a tokamak can be seen in Figure 1.5. This brought the possibility of being able to harness the same great power that also drives the sun a big step closer. Today, more governmental money is invested in fusion research than all other energy research fields combined [26]. It is seen as a realistic and viable option for the future that could suffice the energy needs of the world whilst also answering many of the problems plaguing other forms of energy.

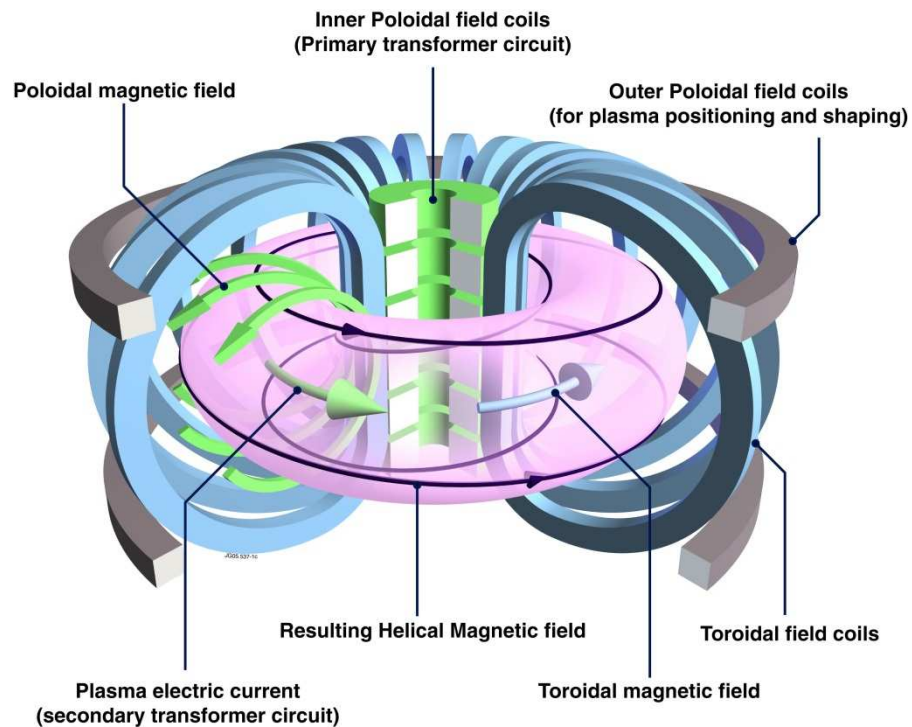


**Figure 1.5.** Schematic representation of tokamak design [27].

**Abundance of fuel** – the basic fusion reaction proposed for use in power plants depends solely on hydrogen. It uses two isotopes of hydrogen, deuterium and tritium. There is enough deuterium available in sea water to supply the world’s fusion power stations for the sun’s lifespan, however, tritium is rare due to its short half-life of approximately 12 years. A key obstacle in designing a fusion power plant is to have a self-sufficient tritium cycle by including a tritium breeding process [28].

**Clean energy** – The resulting particles from a DT fusion reaction are only hydrogen and neutrons, producing no active radionuclides. Therefore, if careful selection of the reactor’s structural materials is made, it would be possible to design a power plant with a very small amount of radioactive waste and zero carbon emissions [28].

**Safe energy** – Without drastically altering the design of a magnetic confinement fusion (MCF) tokamak, it would be very difficult to secretly use the process to develop weapons [29]. Inertial confinement fusion (ICF) depends on creating small

explosions at a high frequency. ICF technology is in relative infancy and currently no prospective designs for a power plant are available, but it is conceivable that the technology could be used for arms [30].

### 1.4.3 Considerations for materials selection

If fusion energy is to be accepted by the public it is essential that the amount of radioactive waste produced is kept to a minimum. Since the fusion reaction itself produces no waste, the only active products created are those when the neutrons interact with the structural materials of the reactor itself. But the demands on materials in a reactor are high. Depending on their position within the reactor and function they are expected to withstand; high thermal loads, plasma erosion, large forces from disruptions and a high neutron flux (causing a high number of displacements per atom (dpa)). The material is required to withstand this without interacting with the plasma, its current, the magnetic field and keeping activation levels low [31]. Therefore, careful selection of materials to meet these criteria is crucial to a successful power plant design. A schematic representation of the interior of a tokamak and its cross-section can be seen in Figure 1.6. This work will concentrate on plasma facing components, particularly the divertor.

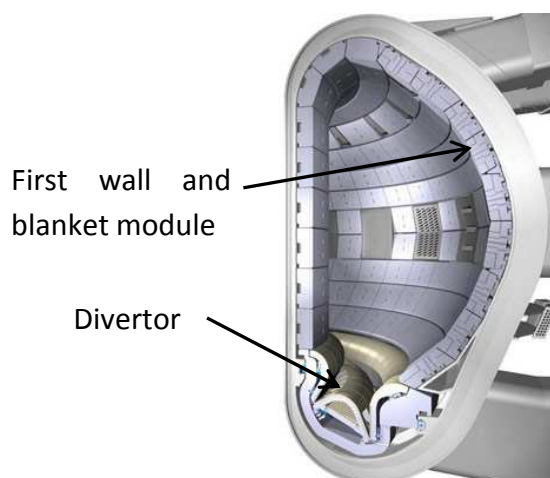


**Figure 1.6.** Schematic representation of a tokamak interior and its cross-section [32].

A large factor in considering material choice is its response to irradiation damage. Previously, there have been no examples where structural materials have been required to withstand such high neutron fluxes at high energy (14.7 MeV). As this is a requirement specific to fusion energy (the neutrons produced by existing fission reactions are at much lower energies and flux), work in this field is in its infancy.

Radiation damage is caused by collisions between radiated particles and the bulk material pp. 73-124 [33]. If the material is crystalline, these collisions will often cause permanent displacements of particles, which will produce vacancies and interstitial atoms within the crystal lattice. Figure 1.7 shows various lattice defects caused by collisions. With increasing damage from collisions, the interstitials or vacancies tend to group together to form dislocation loops. These loops diffuse through the crystal grain towards grain boundaries pp. 155-190 [33].

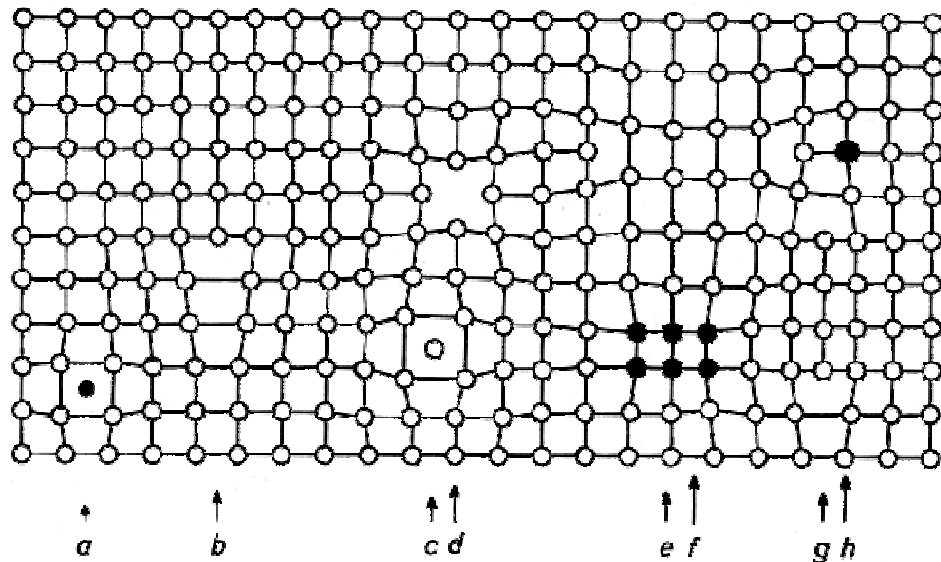


**Figure 1.7.** Schematic drawing of various crystal lattice defects; a) Interstitial impurity atom, b) Edge dislocation, c) Self interstitial atom, d) Vacancy, e) Precipitate of impurity atoms, f) Vacancy type dislocation loop, g) Interstitial type dislocation loop, h) Substitutional impurity atom [34].

The elasticity of a material is its ability to temporarily rearrange particles when stress is applied. The defects introduced by irradiation damage are obstacles to the movement of particles, working against this ability. Thus, irradiation-damaged material becomes hardened; the yield strength and ultimate tensile strength increase. However, the yield strength increases at a greater rate than the ultimate tensile strength, meaning that the plastic domain decreases and the material becomes more brittle (i.e. decreased ductility) pp. 581-642 [33]. A comparison of typical stress-strain curves for unirradiated and irradiated steel can be seen in Figure 1.8. Similarly, introduced defects act as obstacles to thermal and electrical conductivity, decreasing the material's conductivity.

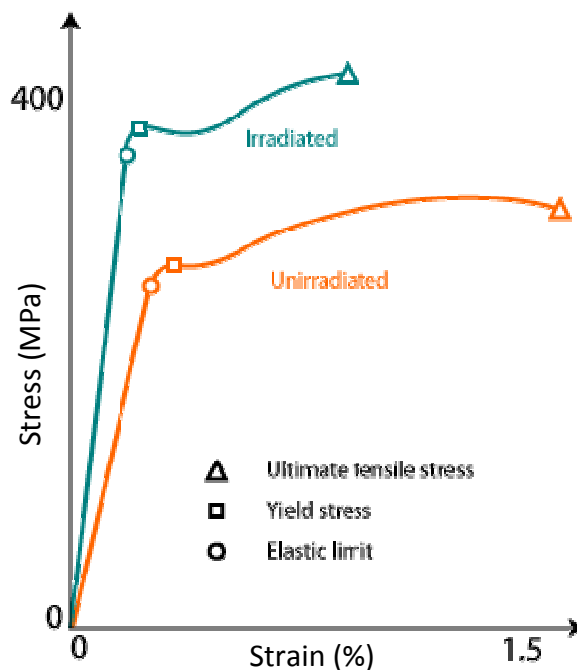


**Figure 1.8.** Comparison of typical stress-strain curves for unirradiated and irradiated steel [35].

The radiated particle can sometimes interact directly with the nucleus of lattice atoms in collisions which cause transmutations. This mechanism commonly produces hydrogen or helium atoms that quickly accumulate to form bubbles and become nucleation points for voids. The presence of these voids in the material cause it to swell pp. 343-432 [33]. Depending on the geometry of the irradiated sample, the swelling often causes a stress to



be developed within a component. Due to the decreased ductility and void formation, this usually leads to cracking pp. 643-710 [33] which can have a significant effect on the mechanical properties.

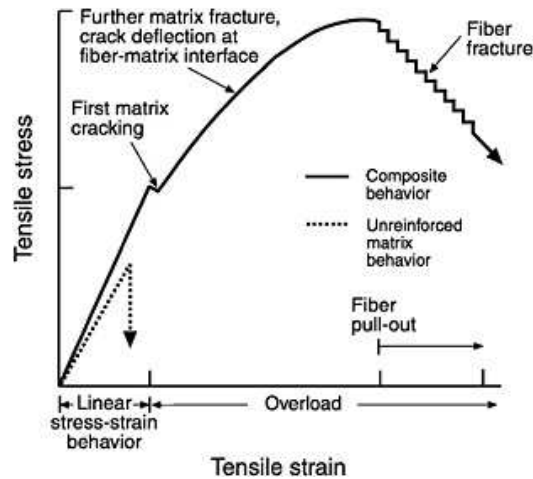


**Figure 1.9.** Comparison of ideal stress-strain behaviour of monolithic and composite ceramics [36].

Because of the extreme environment in fusion reactors, much interest has been shown in ceramics because of their improved performance at high temperatures compared to steels [37]. However, due to their brittle behaviour with ultimate tensile failure at relatively low strains, their use in monolithic form is limited. Despite this, when used as a ceramic composite (such as  $C_f/C$ ) they display mechanical behaviour analogous to metals (i.e. having a plastic deformation zone) that allows for damage tolerance, but can be used at higher temperatures. A comparison of monolithic (matrix) and composite ceramic behaviour can be seen in Figure 1.9. This change in behaviour occurs due to the reinforcing fibres redistributing stresses from a crack tip propagating through the matrix. Thus, the fibre reinforcement impedes the crack propagation. The slower the crack propagation, the more ‘ductile’ the ceramic composite is seen to behave [38] i.e. it is considered to be pseudo-ductile. In addition to this, higher operating temperatures, lower mass densities and electromagnetic insulating properties make ceramics an attractive choice for fusion.

Because low atomic numbers ( $Z$  values) aid the mitigation of plasma impurities, carbon is a strong candidate material for fusion reactors [39]. In addition to this it also possesses attractive structural and thermal properties. Until recently, tokamaks used graphite tiles for the 1<sup>st</sup> wall (shown in Figure 1.6), but this has been problematic. Due to the interaction with plasma, it suffers from erosion caused by sputtering [40] and a build-up of hydrocarbons on the surface [41] [42], as seen in Figure 1.10. This releases dust into the plasma which detrimentally effects its confinement [43]. Carbon also retains tritium, which is radioactive and is dangerous if inhaled or digested [44]. This is problematic because if the on-site tritium inventory exceeds acceptable levels, power-plant operation must be halted until cleaning procedures reduce these to be within the safety limits [45]. With no solution to these problems being found, the Joint European Torus (JET) has recently replaced its graphite panels with beryllium ones for testing [46]. However, as ITER will initially operate without tritium, carbon is still being used in composite form within some components, most notably the lower part of the divertor (see Figure 1.6). It is currently planned to replace these sections with tungsten later in ITER's life, and it is not known if carbon will be used in the first DEMO reactor. Work, such as the research presented in the following papers, will contribute towards the knowledge required to make informed decisions regarding choice of materials and their allowable uses.

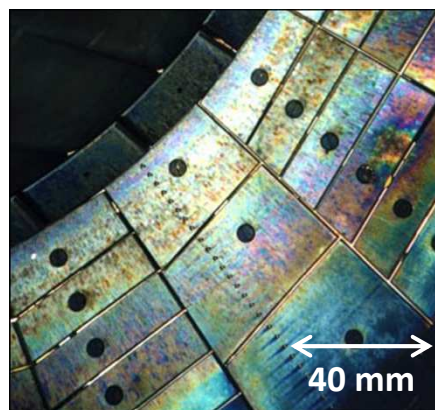


**Figure 1.10.** Hydrocarbon build-up on graphite panels [47].

## CHAPTER TWO: Methods

This project uses image-based finite element modelling (IBFEM). This entails using a designated scanning method to build a 3D geometric map of a sample. Traditionally, finite element modelling (FEM) uses idealised geometries created in computer aided design (CAD) packages.

The two main benefits seen by modelling real, rather than idealised, geometries are:

- Flaws in the manufacturing of the material, such as porosity, cracks or any other manufacturing defects are included directly in the model.
- Direct comparison to experimental results can be made as the modelled sample can also be subjected to laboratory tests.

This has been demonstrated in work by Ali *et al.* [48], which investigated mechanical performance of a carbon fibre composite (CFC) and compared results for stress-strain curves measured experimentally with ones calculated by IBFEM, unit cell analysis and analytically. Representative images of each analysis are shown in Figure 2.1 (a) - (d) respectively. Experimental data was collected using an Instron universal testing machine. Simulations were performed using commercial FEA software, with IBFEM constructed from X-ray tomography data, unit cell analysis is a representation of the smallest repeatable volume within the composite and the analytical model was a simplified 0 °/90 ° laminate. Comparison of results, shown in Figure 2.2, demonstrated that the IBFEM approach in this instance could give more accurate predictions than unit cell or analytical models.

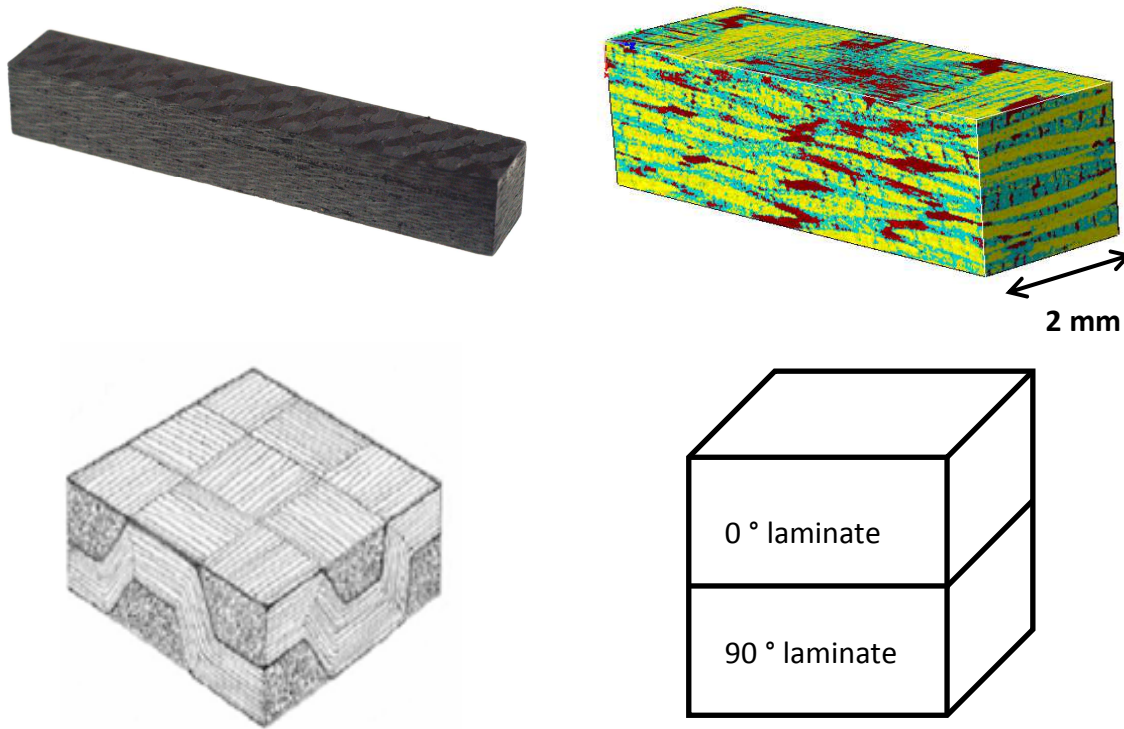


**Figure 2.1.** Carbon fibre composite represented by (a) photograph (b) image-based model constructed from X-ray tomography data (c) unit cell and (d) analytical model. [48].

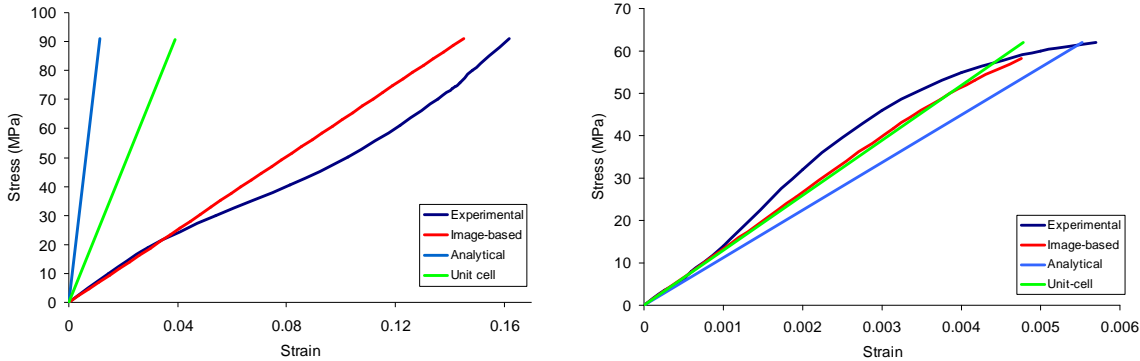


**Figure 2.2.** Comparison of experiment and differing modelling approaches for a CFC composite, stress-strain curve for (a) a graphitised composite in perpendicular direction and (b) an ungraphitised composite in lamina direction [48].

Another benefit of IBFEM is the ability to model very complex structures that would otherwise be too time-consuming to realistically reconstruct. Figure 2.3 is a scanned image of aluminium foam, an example of a structure too complex to produce on a traditional CAD program.

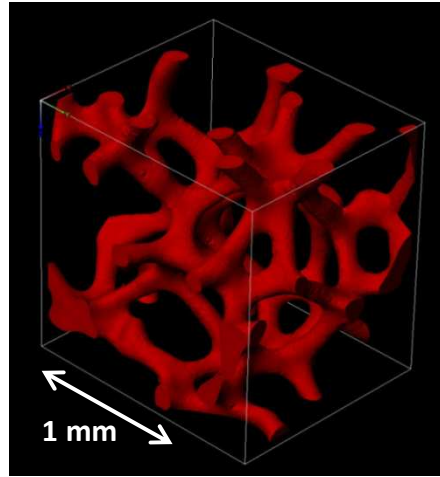


**Figure 2.3.** 3D image of Aluminium foam with hundreds of millions of elements made with tomography data [49].

This chapter will introduce the techniques used to implement image-based modelling. Each subsection will concentrate on an element of the workflow giving some background information, theory and reasoning for method selection. However, experiment specific parameters are reserved for presentation in the journal papers (i.e. Chapters 3-5).

## 2.1 Experimental collection of input material properties

Material behaviour is a complex combination of environmental conditions, loading regimes, previous material history, molecular structure and other similar key factors. However, component performance for a specific set of environmental conditions is largely dominated by the material it is composed of and its geometry. To create a computational model, in order to predict the behaviour of a material in some environment, the material must first be characterised. This is achieved by collecting experimental data for the individual materials to obtain characteristics such as thermal or mechanical behaviour, which are used as input data for the model.

As this work is concerned with thermal modelling of the materials, the material properties required to model this in transient state are thermal conductivity,  $K$ , specific heat capacity,  $c_p$ , and mass density,  $\rho$ .

As the samples are manufactured to a known geometry, the volume can be calculated, whereas mass is measured by the use of a balance which means density is easily calculated by combining the aforementioned properties.

Measuring the thermal properties requires an experimental setup which is rather more involved. A range of techniques exist including, but not exclusive to, modified transient plane source (MTPS), transient line source, laser flash analysis (LFA) and thermoreflectance. Each method has its advantages and disadvantages for a given set of requirements. Laser flash was the method of choice due to its suitability to measure small solid samples non-destructively (if kept within a temperature range suitable for the material), its wide temperature range to provide temperature dependent data and its ability to provide values for both thermal conductivity and specific heat in one set of measurements [50].

This experiment is performed by subjecting the front face of a disc-shaped sample of thickness  $L$  to a uniform heat pulse of energy  $Q$  using a laser. The instantaneous temperature rise on the rear face,  $T$ , is measured by an infra-red camera. If the maximum temperature increase of the rear face,  $T_{max}$ , is given by Equation (2.1), the normalised temperature increase on the rear face,  $V$ , can be represented by Equation (2.2).

$$T_{max} = \frac{Q}{\rho c_p L} \quad (2.1)$$

$$V = \frac{T}{T_{max}} \quad (2.2)$$

At any time,  $t$ ,  $Q$  can also be non-dimensionalised to  $\omega$  by Equation (2.3).

$$\omega = \pi^2 \kappa \frac{t}{L^2} \quad (2.3)$$

where  $\kappa$  is the thermal diffusivity. Parker *et al.* [51] show that, if no heat losses occur, the temperature distribution at any time,  $t$ , given by Carslaw and Jaeger [52] (Equation (2.4)), can be combined with Equations (2.2) and (2.3) to represent the normalised temperature increase on the rear face,  $V$ , as Equation (2.5).

$$T = \frac{Q}{\rho c_p L} \left[ 1 + 2 \sum_{n=1}^{\infty} (-1)^n \exp\left(\frac{-n^2 \pi^2}{L^2} \kappa t\right) \right] \quad (2.4)$$

$$V = 1 + 2 \sum_{n=1}^{\infty} (-1)^n \exp(-n^2 \omega) \quad (2.5)$$

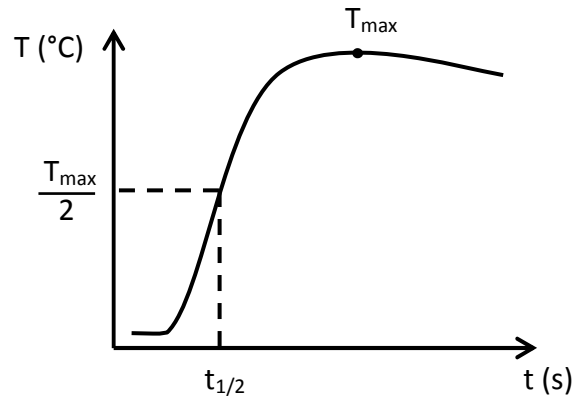


**Figure 2.4.** Typical temperature curve measured on rear face of sample after initial heat pulse.

Experimentally, the temperature on the rear face of the sample is measured and plotted against time, as in Figure 2.4. The rise-time can be measured from this. If the pulse length is assumed to be sufficiently small, Equation (2.5) becomes the Parker expression (Equation (2.6)) [51]. The half rise-time,  $t_{1/2}$ , along with sample thickness, can then be

used to calculate the thermal diffusivity. With the available apparatus, absolute temperature is not measured and the energy incident on the sample from the laser is unknown, therefore specific heat capacity is calculated by the comparison of results to those of a reference sample, measured in the same experiment. Thus, thermal conductivity can be calculated from the combination of thermal diffusivity, specific heat capacity and mass density (see Equation (2.7)). This information is enough to provide material property input parameters for the simulations planned in this work.

$$\kappa = \frac{0.1388 \cdot L^2}{t_{1/2}} \quad (2.6)$$

$$K = \kappa c_p \rho \quad (2.7)$$

## 2.2 Creating a digital geometry from 3D images

### 2.2.1 Image acquisition: X-ray Tomography

The first step in IBFEM is to reproduce a 3D map of the sample by a chosen method. Different methods are used depending on the type of sample. Popular examples are; X-ray tomography, magnetic resonant imaging, acoustic imaging (such as sonar) or LIDAR (Light Detection and Ranging, which uses lasers). These different methods are used in very different circumstances, such as study of upper atmospheric physics, deep sea navigation or medical imaging. The strength they have in common is their non-destructive testing qualities. The choice of method would depend on;

- the environment in which the scanning was made (e.g. if scanning under water, certain equipment might not be easily transportable)
- the type of sample being scanned (e.g. it would be undesirable to use X-rays to scan a live embryo)



Other factors must be considered, such as the desired resolution and the size of the sample.

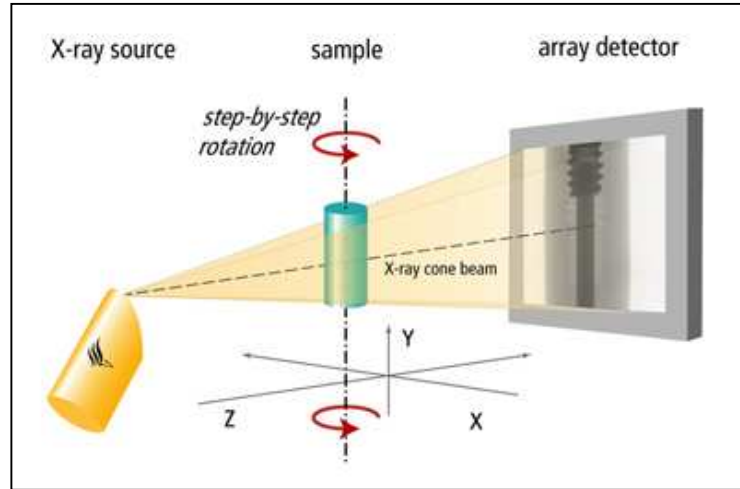


**Figure 2.5.** Schematic representation of X-ray tomography image acquisition method [53].

The current study requires high resolution imaging of relatively small samples, typically 1 to 3 cm in diameter. As the sample material is opaque, but insensitive to X-rays, it has been decided to use X-ray tomography. In medical circles this method is also known as computerised/computer aided tomography (CT/CAT scan). Work completed by Berre *et al.* [54] shows an experiment with a similar procedure to the one planned for this work and results demonstrating the potential of this method.

The principle behind CT is to place the sample between an X-ray source and a detector and take a 2D image (radiograph) which is a projection of the total X-ray attenuation along each path from the source to the detector. This is repeated, each time rotating the sample a small amount until a full rotation has been completed, as shown in Figure 2.5. It is sometimes preferable to rotate the source and detector around the sample, depending on its size and geometry. The set of radiographs is reconstructed to form a tomograph. A number of methods can be used to combine the individual 2D images and then reconstruct a 3D image [55]. Most commonly, fast Fourier transform techniques are used for 2D image combination and a back-projection algorithm to reconstruct the 3D image. The 3D

reconstruction is usually exported as a stack of images which represent 2D slices through the tomography data.

At the University of Manchester, the Manchester X-ray Imaging Facility has several imaging scanners and a reconstruction and visualisation computer suite. For this work the Nikon Metrology 225/320 kV system (using the 225 kV source) was used, the specifications of which are in Appendix A: Nikon Metrology 225/320 kV system at Manchester X-ray Imaging Facility and are taken from the School of Materials' website.

An example radiograph and tomography slices of a CFC sample can be seen in Figure 2.6. The CFC is developed using a preform of panox precursor fibres. Continuous unidirectional fibre layers (approximately 85%) are 'needle punched' together with a mat of fibres with random directionality (approximately 15%). This fabric is then laid up with a 0/90 orientation and needle punched further. The fibre preforms are then carbonised at 1700°C. Densification is carried out via a naphthalene route at 1400°C using a Lewis acid catalyst. These samples are in their pre-graphitisation stage. The fibre diameter is approximately 7µm.

In clockwise order, commencing at the upper left, Figure 2.6 shows an example radiograph, a cross-section where layers can be distinguished by change in porosity alignment, a felt layer (random fibre direction) made visible by random distribution of porosity and a layer of unidirectional fibres made visible by aligned porosity.

Tomography is now a well-established technique which is still constantly improving due to advances in computational power. A thorough treatment of the technique can be found in text books such as [55], [56] and [57] which are the basis of the following brief introduction to issues surrounding acquisition of X-ray tomography images.

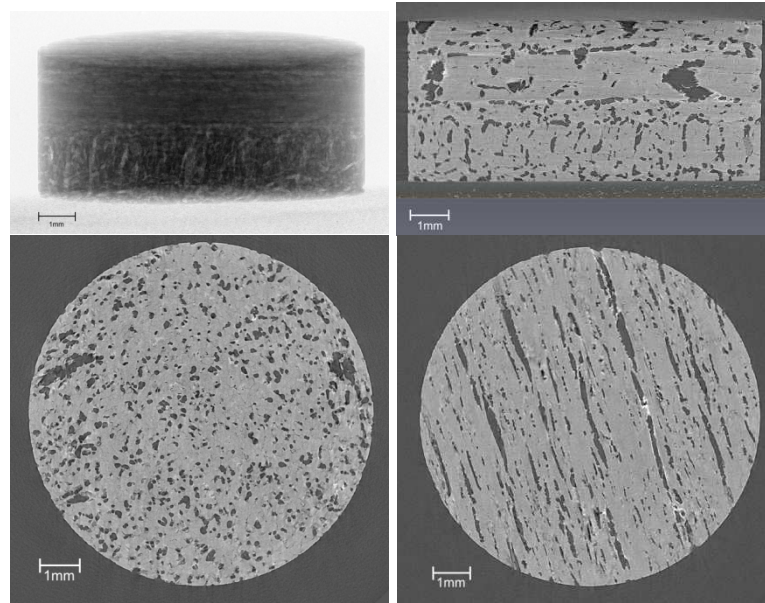


**Figure 2.6.** Example radiograph and tomography slices of CFC sample.

The quality of the final 3D image is a combination of several factors which fall into two categories: those affecting the individual 2D radiographs and those introduced when combining the radiographs to make a 3D tomograph. Of the former, there are two main influences on image quality: spatial resolution and signal noise. The spatial resolution depends on the detector resolution. However, a cone beam projection can be used to ‘magnify’ the image by varying the distance between X-ray source, sample and detector. Signal noise are fluctuations in the X-ray counts measured caused by transient variations in the X-ray photons emitted from the source or the number counted by the detector itself. Even for a perfectly homogeneous sample a distribution of attenuation data would be observed, rather than one value, as shown in Figure 2.7. This type of noise can be reduced by counting X-ray photons for a longer acquisition time, thus improving data statistics i.e. signal to noise ratio (SNR).

When producing a tomography image it is beneficial to maximise the signal contrast between the background and the various materials within the scanned sample to facilitate differentiation in analysis. To achieve this requires fine tuning of the X-ray energy used

(current and voltage) and use of filters to remove unwanted sections of the X-ray spectrum. This is a process which will depend on the material types and thickness of the sample. Figure 2.8 demonstrates how these factors can impact the ability to resolve the boundaries of samples in a reconstructed tomography image.

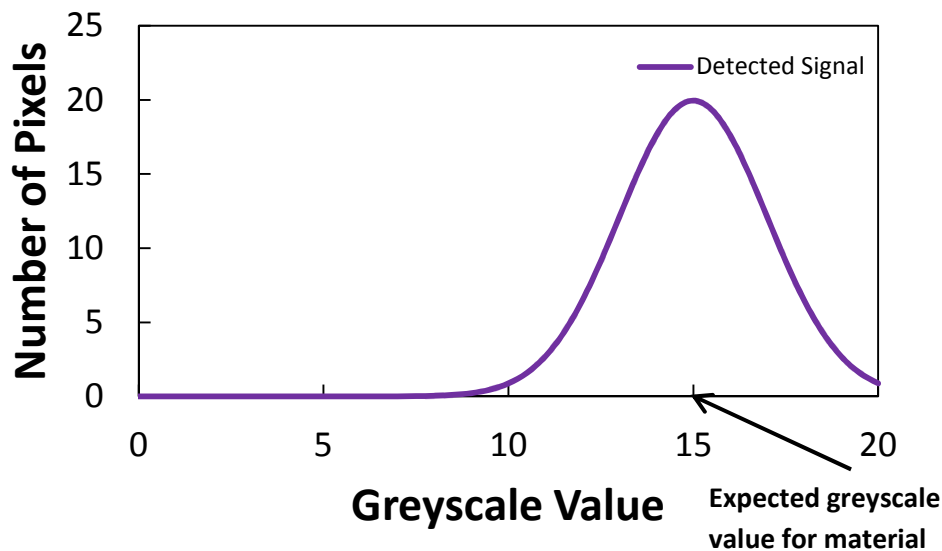


**Figure 2.7.** Plot showing distribution of greyscale values rather than one value for a perfectly homogeneous material.

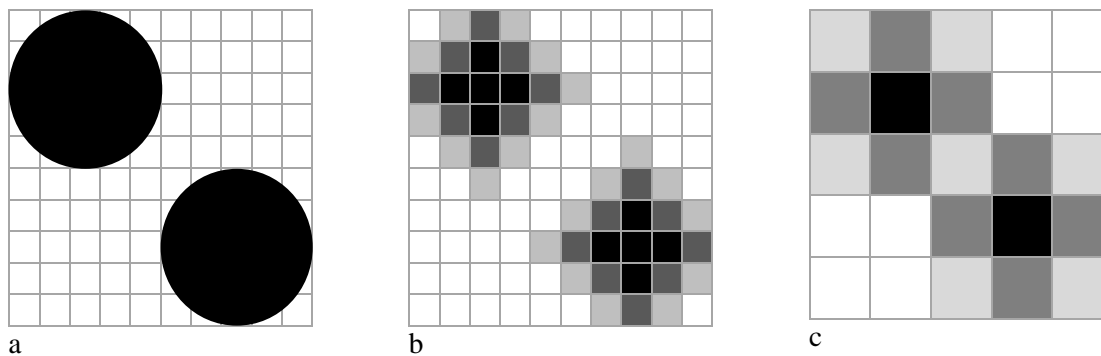


**Figure 2.8.** Schematic demonstrating of how contrast to noise ratio can effect resolving features in image from (a) actual sample geometry to (b) reconstructed image with spread sample boundaries due to image quality factors and (c) increased difficulty in resolving with lower resolution image.

The features introduced when combining radiographs into a tomograph are caused by mathematical phenomena of the projection algorithms. The main ones are known as; streaking artefacts, beam hardening artefacts, image doubling (ghosting) artefacts, ring artefacts and edge artefacts. Streaking, see Figure 3.11, is caused by insufficient data for

reconstruction due to low number of projections. Its effects are reduced by increasing this number (i.e. reducing the angular step size between each sample rotation). Beam hardening, also Figure 3.11, occurs when low energy X-rays are entirely attenuated by the sample, thus changing the mean energy of the spectrum. This causes boundaries to appear brighter (i.e. have a higher coefficient of attenuation). By using filtering algorithms during the reconstruction stage the effect these can be reduced, as shown in Figure 2.9.

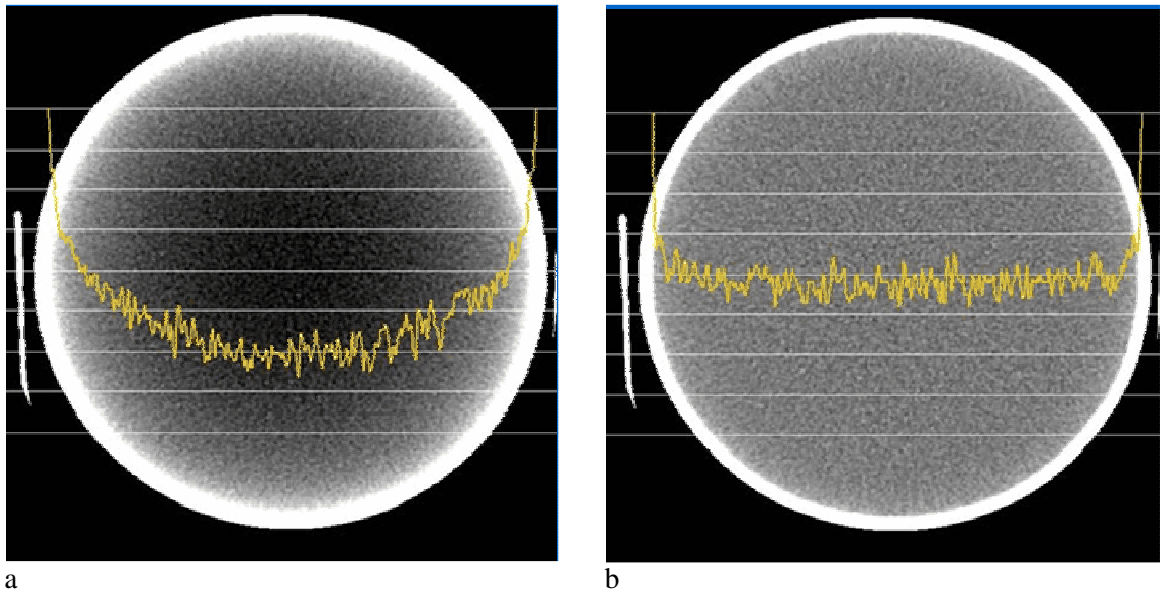


**Figure 2.9.** Greyscale value profile across sample affected by beam hardening (a) before and (b) after applying a correction filter [58].

Image doubling happens when the centre of rotation, required for reconstruction, is not calculated correctly. The centre of rotation can be difficult to calculate when the sample's central axis is at an angle. Ring artefacts, shown in Figure 2.10 (a), are caused by hardware issues, and thus are manifested as systematic artefacts spread across the whole sample rotation. Edge artefacts are observed where there are large gradients in the coefficient of attenuation i.e. at the edge of a sample or on the boundary between two materials, seen in Figure 2.10 (b). These artefacts can be difficult to mitigate during the scanning or reconstruction stages and therefore require attention during image post processing.

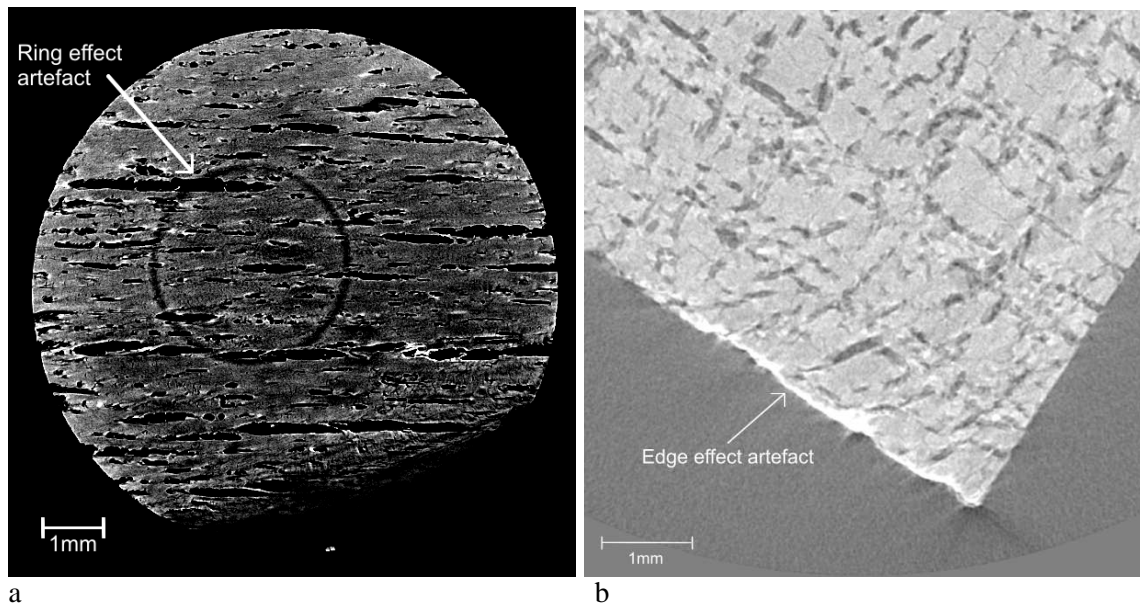


**Figure 2.10.** Artefacts in reconstructed image of CFC sample due to (a) ring and (b) edge effects.

These features ultimately all contribute towards the resolution of the image and dictate what micro-structures within your sample are observable, therefore can be included in IBFEM, and which ones are obscured by noise or artefacts. However, despite the aforementioned techniques to improve image quality, it is not always the best option to run a very ‘high-quality’ scan (i.e. large number of 2D images and long acquisition time). Data files can rapidly become very large (currently files of up to 320 Gb have been used), this causes the time required for reconstruction to increase and rendering images of this size for study would be impossible without a computer with a high specification graphics card.

### 2.2.2 Segmentation and Meshing

The majority of CT scanners come with their own bespoke image acquisition software and reconstruction algorithms. However, the output of all scanners will be of a similar format (i.e. a stack of 2D tomography slices). Each slice is a greyscale image, with each pixel’s greyscale value corresponding to an X-ray attenuation coefficient i.e. if an area of the sample is highly X-ray absorbent it will appear light on the image (high greyscale value),

as seen in Figure 2.11. This work made use of CT Pro (Nikon Metrology NV, Tring, Hertfordshire, UK) for tomograph reconstructions.

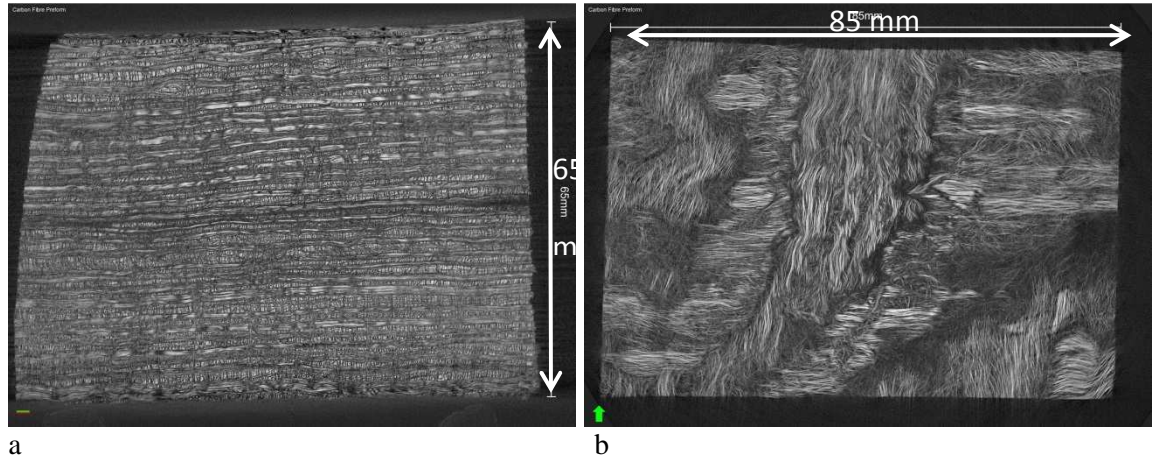


**Figure 2.11.** Tomography slices of carbon fibre preform in (a) x-z and (b) x-y planes.

Software can then be used to visualise the resulting image in 3D by combining the stack of 2D tomography slices, an example of which can be seen in Figure 2.12. The 3D volume is visualised as a 2D image with perspective which can be manipulated interactively, it is now also possible to display the images stereoscopically ('real' 3D) with the appropriate software and hardware.

Depending on the software, many different techniques may be used to aid visualisation of the scanned geometry. The software used in this work are Avizo (VSG, Mérignac Cedex, France) and Simpleware (Simpleware Ltd., Exeter, Devon, UK).

Little quantifiable data can be gained from visualisation alone, but it can be a powerful tool to view inside samples. Empirically, it can be beneficial to view the size and frequency of cracks, the quantity of porosity etc. thus, a better idea of the sample's structure is obtained. Visualisation is done by assigning a range of colours corresponding to the X-ray absorption levels to each voxel (3D pixel). Alternatively, certain ranges of greyscale can be



filtered completely. Other techniques are to create iso-surfaces or block volumes that include a range of greyscale values, this can be used to measure surface areas or volumes.

Creating block volumes is the technique that is best suited to create geometries for modelling purposes. This procedure involves dividing the volume into different sections (i.e. separating the different materials) and as such is called segmentation, as seen in Figure 2.13. Because of the author's personal preference of the tools available, this work uses the Simpleware software for the segmentation procedure.

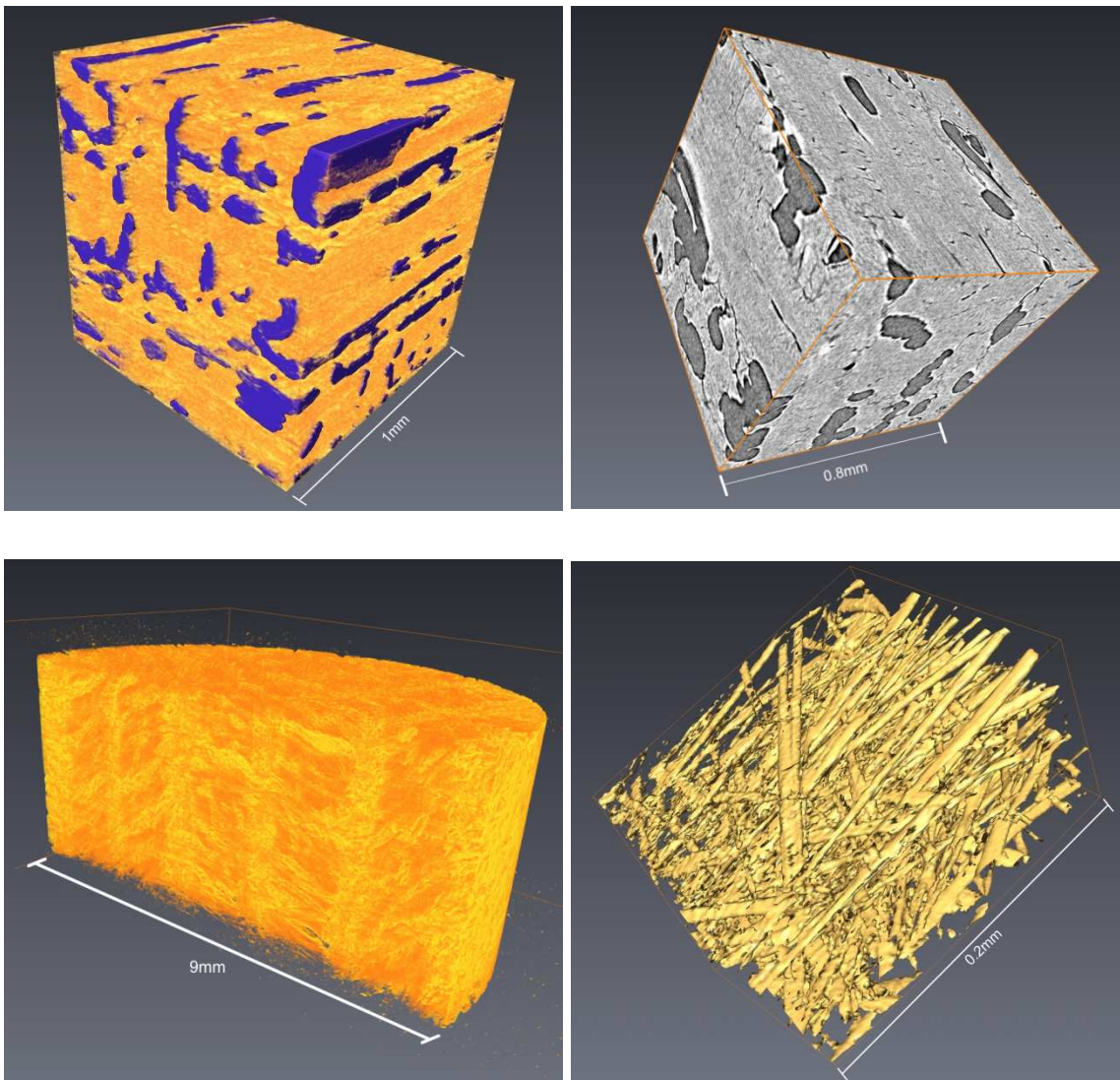


**Figure 2.12.** Examples of tomography data visualisation techniques; (a) volume rendering with segmented porosity, (b) tomography greyscale slices, (c) volume rendering showing internal structure of a 0/90 panox CFC and (d) X-ray absorption iso-surface of carbon fibre preform.



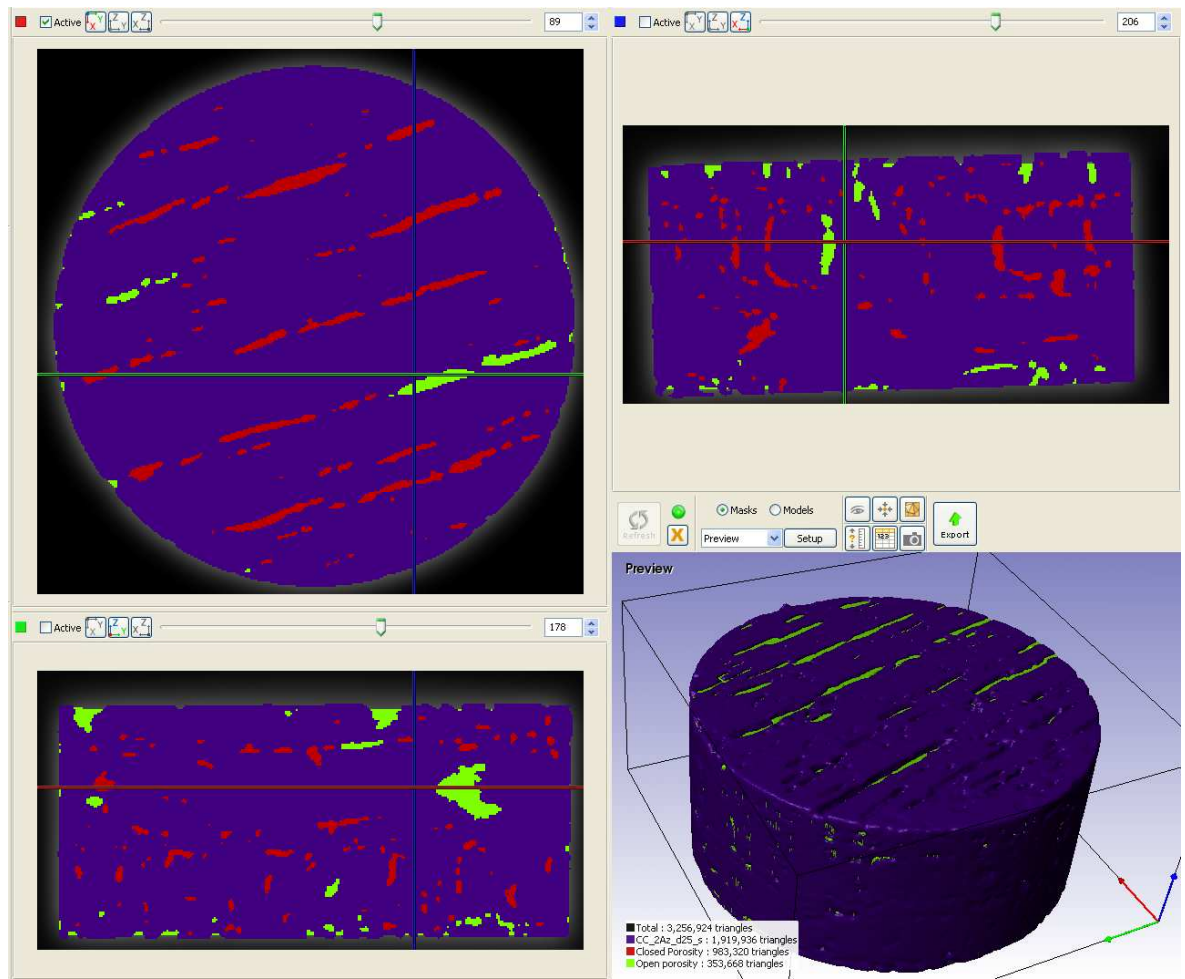


**Figure 2.13.** Surface rendering of 0/90 panox CFC (purple) segmented by greyscale thresholding, porosity segmented by boolean logic with remaining image volume then separated into internal porosity (red) and porosity connected to the external environment (green) by floodfill tools.

The aim of segmentation is to create an accurate digital representation of the sample geometry by defining the material boundaries within a tomography image to the maximum allowable accuracy. This accuracy is dependent on the image quality as mentioned in section 2.2.1.

The difficulty in accurate segmentation, introduced by these artefacts and noise, is that the material boundaries become broadened (i.e. ill-defined) and single materials aren't composed of a single greyscale value but rather a range of values. If the greyscale contrast at these boundaries isn't sufficient it can become very difficult to accurately distinguish the various materials, especially if using automated segmentation tools [59].

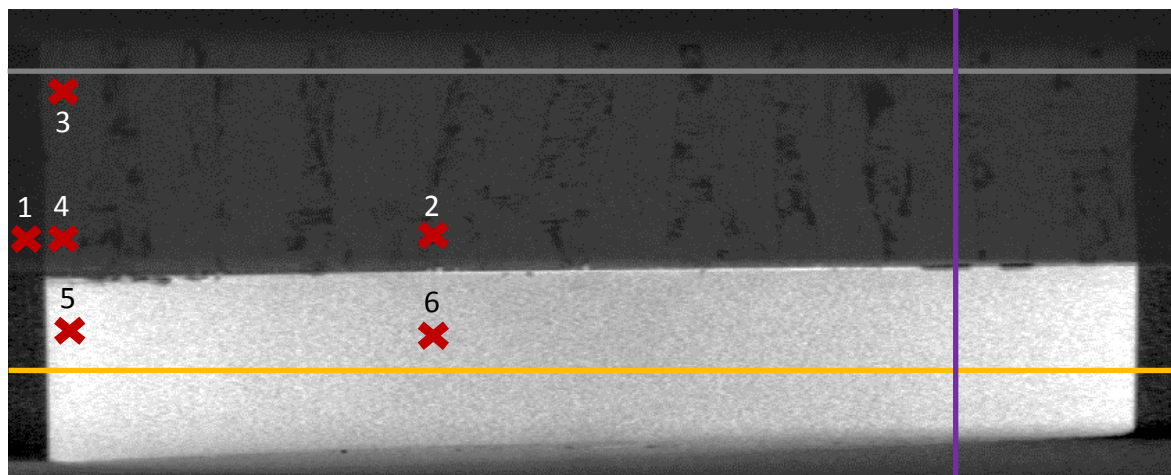
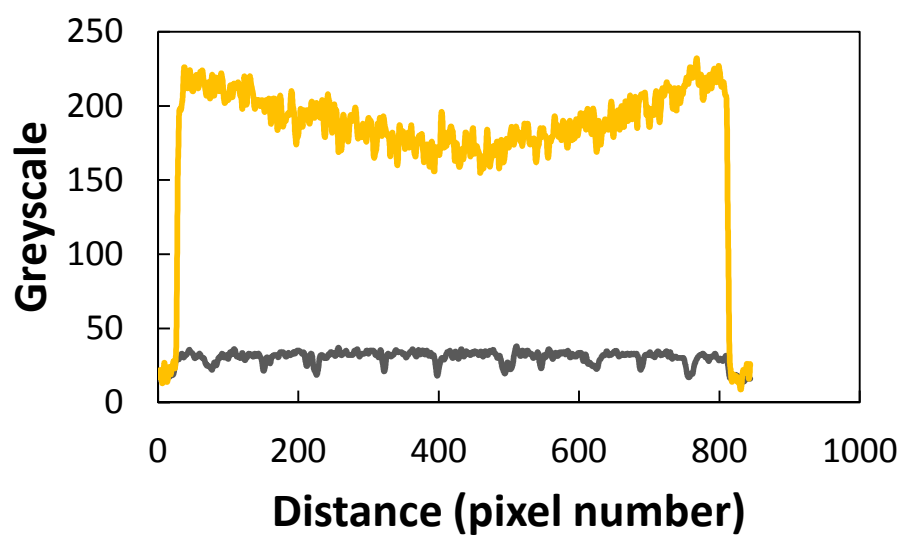
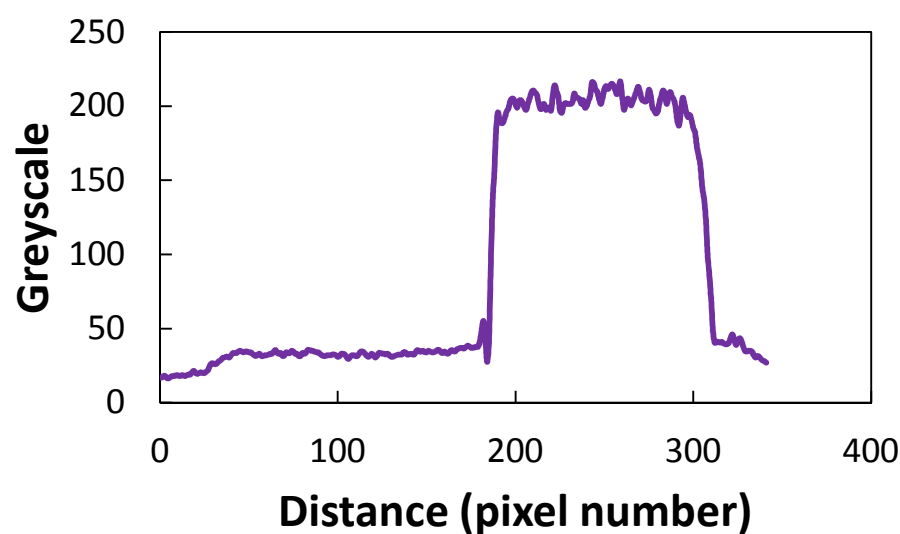


**Figure 2.14.** Tomography slice of CFC-Cu\_GS sample, described in section 3.2, in x-z plane with annotations showing locations of greyscale profile lines used by Figure 2.15 and Table 2.1 data point locations.



a



b

**Figure 2.15.** Greyscale values along profile lines from the tomography slice in Figure 2.14; (a) showing profiles in x-direction through the Cu (yellow) and CFC (grey) materials separately and (b) in z-direction traversing both material layers.

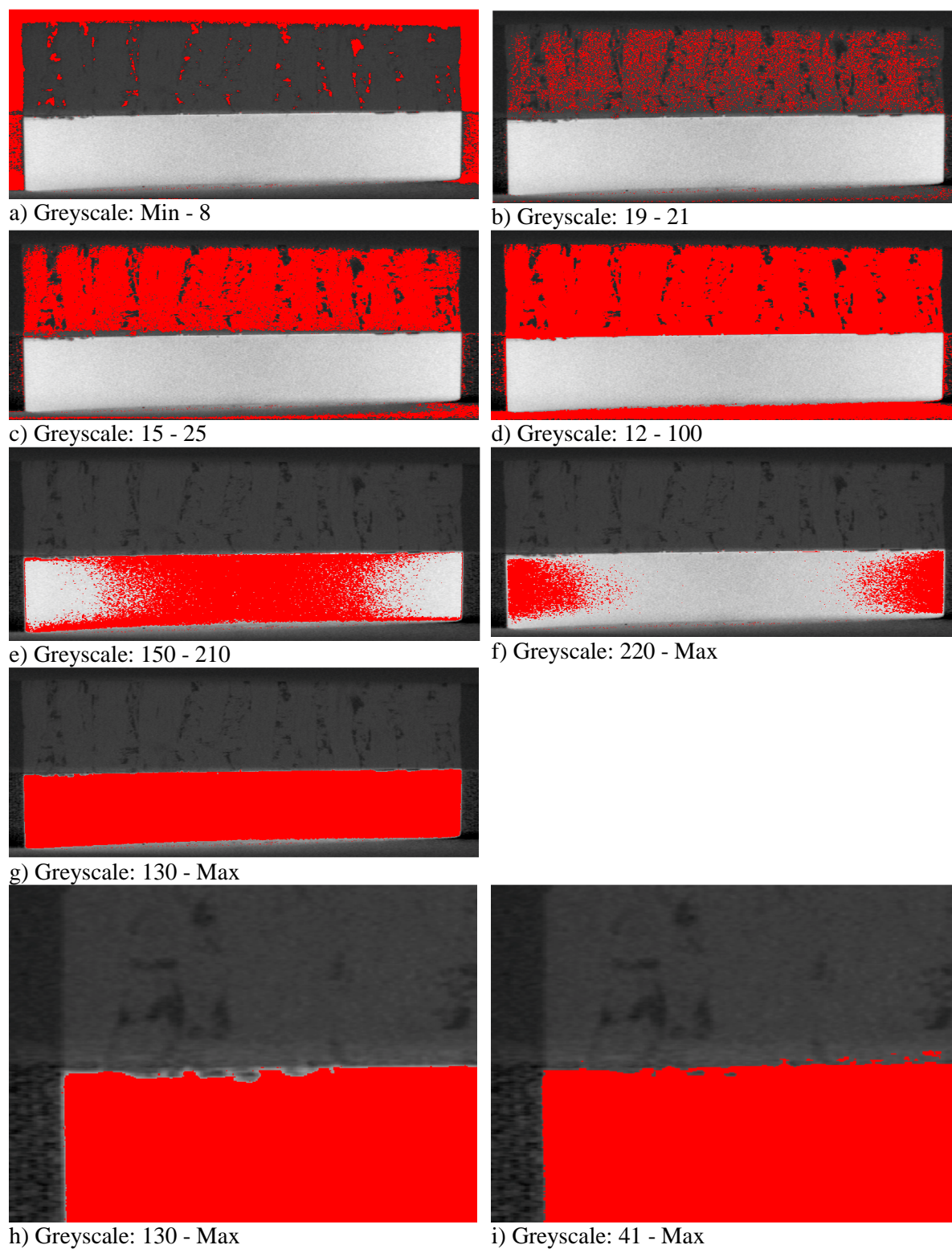
**Table 2.1**

Data from tomography slice of CFC-Cu\_GS sample, see Figure 2.14, showing varying greyscale values at different locations within same material.

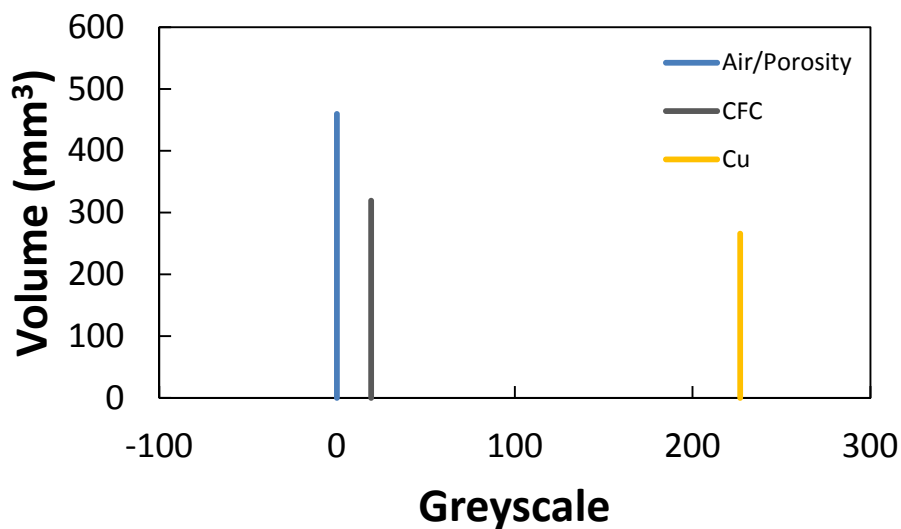
Point	Surrounding Material	Greyscale Value
1	External Air	2
2	Porosity	8
3	CFC	20
4	CFC	28
5	Cu	230
6	Cu	170

Figure 2.14 shows a tomography slice containing Cu, CFC and therefore porosity and the air surrounding the sample. By taking greyscale profiles across the image, shown in Figure 2.15, it can be seen that the contrast between CFC and air is low, making distinguishing features difficult. Additionally, beam hardening is present near the edges of the Cu layer. By comparing greyscale values from the same material at different locations, Table 2.1 enforces this observation that materials don't give a single greyscale value.

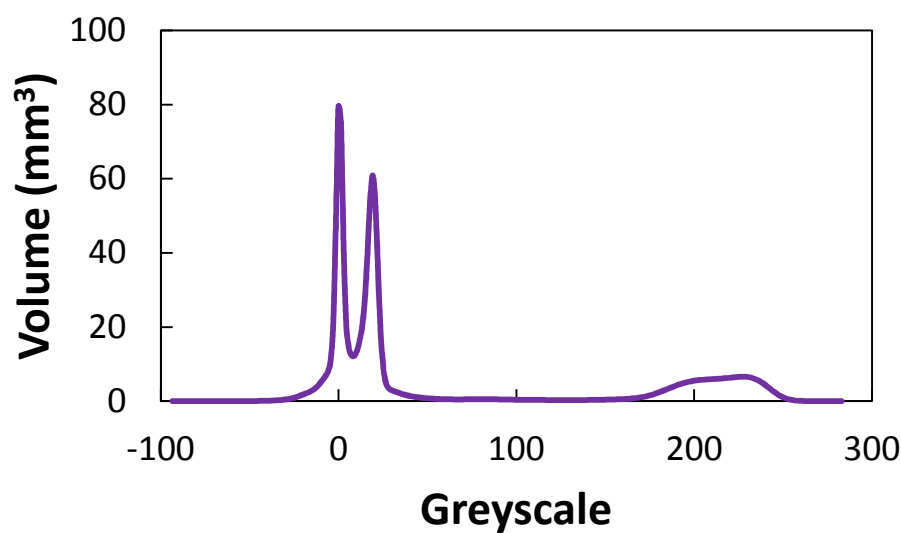
If automated segmentation by thresholding was attempted globally across the image it would, in actuality, result in boundaries which mixed differing materials. This is what's seen in Figure 2.16, where the greyscale values found in Table 2.1 were used as guides for thresholding. Images (a) – (d) demonstrate that finding a balance between air/porosity and CFC is difficult, especially around the lower portion of the frame where artefacts from the Cu cause the surrounding air to have increased greyscale values. Image (g) apparently shows the Cu as being well defined. Closer inspection, image (h), shows surface micro-structures which aren't included in the segmentation. Broadening the thresholding values captures these features but also includes regions of CFC. It can therefore be concluded that naïve thresholding on a global level does not suffice in accurately defining the material boundaries.



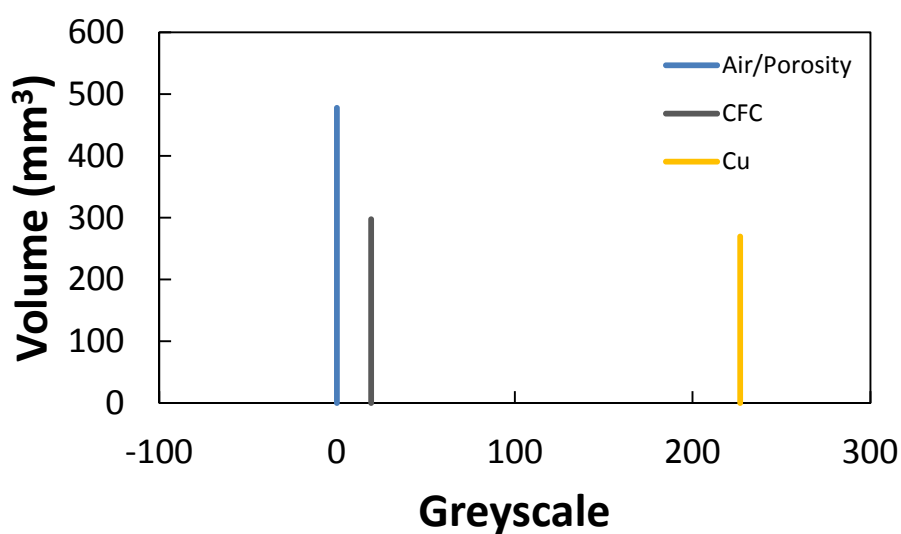
**Figure 2.16.** Attempts at using automated segmentation by use of thresholding means only, with each range of greyscale values either failing to fully capture the desired material or, conversely, unintentionally including surrounding material.



a



b



c

**Figure 2.17.** Volume of three materials (surrounding air/porosity, CFC and Cu) contained within tomography image of CFC-Cu\_GS sample, described in section 3.2, calculated from (a) measuring sample with micrometre callipers (b) greyscale data and (c) segmented data.

To produce geometry with increased accuracy, several techniques may be used to clean the data (such as smoothing, resampling etc.) and apply automated processes on smaller localised volumes. As previously mentioned, reconstruction algorithms can often create artefacts in the tomography slices. Often it is necessary to manually clean data using a paintbrush/eraser combination on individual 2D slices in regions of low contrast. The human eye is well equipped for this task as it can discern boundaries by considering a larger surrounding area and following micro-structures through the volume. Getting a final clean geometry usable for modelling can be a slow and arduous process involving much manual manipulation (sometimes taking days to clean, depending on the complexity of the sample). However, the usefulness of the human eye cannot be overestimated. Its value is increasingly being recognised with projects such as EyeWire aiming to exploit this via ‘crowdsourcing’, by providing ‘games’ where members of the public perform image segmentation in exchange for in-game rewards [60], [61].

Accuracy of medical CT is often verified by the use of a phantom, a sample of known geometry and material properties to which images can be calibrated, possible due to the nature of repetitively scanning similar samples (i.e. in-vivo tissue). Unfortunately it would be impractical to produce phantoms of specific geometries tuned to each individual sample in investigative research. But segmentation results can be verified against what is known about the sample. Returning to the example in Figure 2.14, this sample was fully segmented for the work in chapter 5. The sample dimensions were initially measured using micrometre callipers, the calculated volumes are shown in Figure 2.17 (a). In imaging it would be expected that as these materials would not be represented by a single greyscale value, these peaks would broaden. This is indeed what we see in Figure 2.17 (b), where the volumes have been calculated from the number of voxels at each greyscale level. It can be seen here that the broadening of the peaks causes an overlap of data for air/porosity and

CFC materials. Thus it can be expected that the contrast between them would be low and complexity of segmentation would increase (observed in Figure 2.16). Segmentation attempts to 're-binarise' this data, a successful effort would see segmented volumes matching those calculated initially. Although volumetric comparison is not a guarantee of accurate segmentation, it is a good indicator. Comparison of Figure 2.17 (a) and (c) demonstrates the apparent success of segmentation for this sample. The most sensitive features to changes are the ones with most complex geometries, the porosity in this sample. Manufacturer data states the volume of porosity in this CFC as 8 %. The segmentation returned a value of 7.5 % (see chapter 5) showing relative agreement with loss of porosity fraction most probably coming from pore sizes smaller than the spatial resolution of the detector.

As demonstrated, the tomography images acquired in this work (chapters 3 and 5) were very noisy due to the high contrast in the attenuation coefficients of CFC and Cu. To produce segmented images of the desired accuracy much localised thresholding combined with manual editing was required. To achieve this, the following steps were followed iteratively until the segmentation was of an adequate accuracy (using visual verification against the background image to decide when that stage had arrived).

- Import raw data.
- Crop excessive external volume.
- Segment sample as one whole volume, ignoring internal structures done by;
  - Threshold with range containing CFC and Cu.
  - Cavity fill to include porosity whilst excluding external air.
  - Due to thresholding overlap with some external air manual cleaning is required using paint/unpaint.
  - Ensure CFC, Cu and porosity are one continuous volume with flood fill and island removal.
  - Use Boolean logic to create internal and externals masks to be used as basis for rest of segmentation.
- Start sub-segmenting one material from ‘internal mask’ using the steps mentioned above on a more local basis. This is achieved using a combination of ‘temporary’ and ‘final’ masks in order that thresholding locally can be used as an initial step then refined until ‘clean’.
- Repeat for remaining materials.
- Smooth surfaces using recursive Gaussian filter to reduce discontinuities due to nature of voxelised data.
- Once completed, downsample data to required resolution (for targeted computational hardware).
- Re-clean data, as noise can be introduced by resampling algorithm.

Once confident that the segmented geometry is adequately accurate it is ready for meshing. This involves dividing the geometry into smaller elements, normally tetrahedral, hexahedral or a combination of both elements (see Figure 2.18). Each element is composed of nodes (4 and 8 nodes for tetrahedral and hexahedral elements, respectively) and connecting vertices.



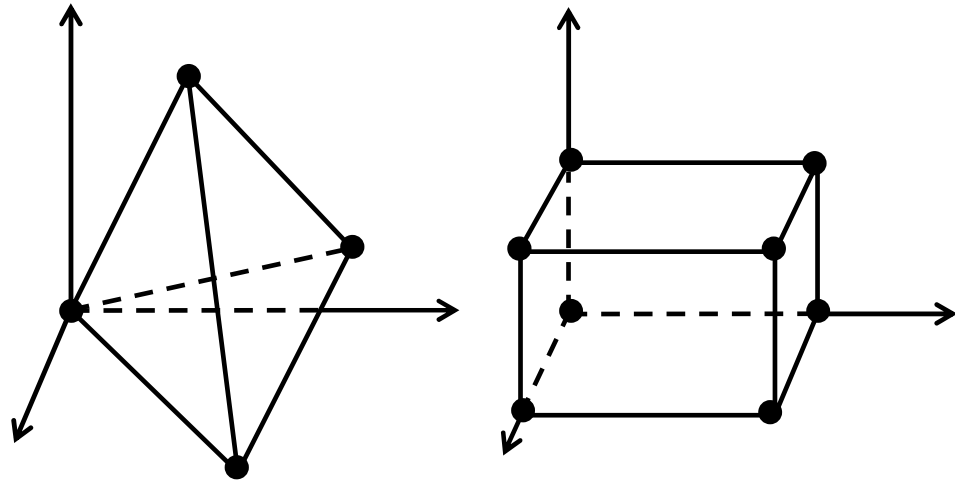


**Figure 2.18.** Tetrahedral and Hexahedral elements used in finite element analysis.

A thorough discussion can be found in Benzley *et al.* [62] on the benefits of the different element types. Preference often depends on the type of modelling conducted (such as finite element modelling or computational fluid dynamics) and whether the mesh will be adaptive or not. A discussion on the use of FEM to predict material behaviour can be found in Chapter 2.3.

Meshing procedure must follow good practice, as a ‘bad’ mesh will often result in erroneous output or, worst case, a non-converging solution.

As the number of elements increase (by making them smaller) the results will tend towards a more accurate solution, a schematic demonstrating this principle can be seen in Figure 2.19, but this will also increase computational expense and memory requirements. Therefore a compromise must be reached between system resources, number of elements and time afforded to computation.

The size of elements within a model can be varied. This is used to reduce the total number of elements required. Smaller elements are needed where a large property change gradient is expected (e.g. thermal) such as in the proximity of features like cracks or pores. Whilst

meshing, this can be achieved by associating an initial element size to surfaces or point locations and prescribing a growth condition. From these conditions, the meshing algorithms will calculate the ‘best’ structure for the mesh through an iterative process. In other words, small elements will be placed where defined by the user and the algorithm will ensure that no highly skewed elements will be created whilst growing the element size [63].

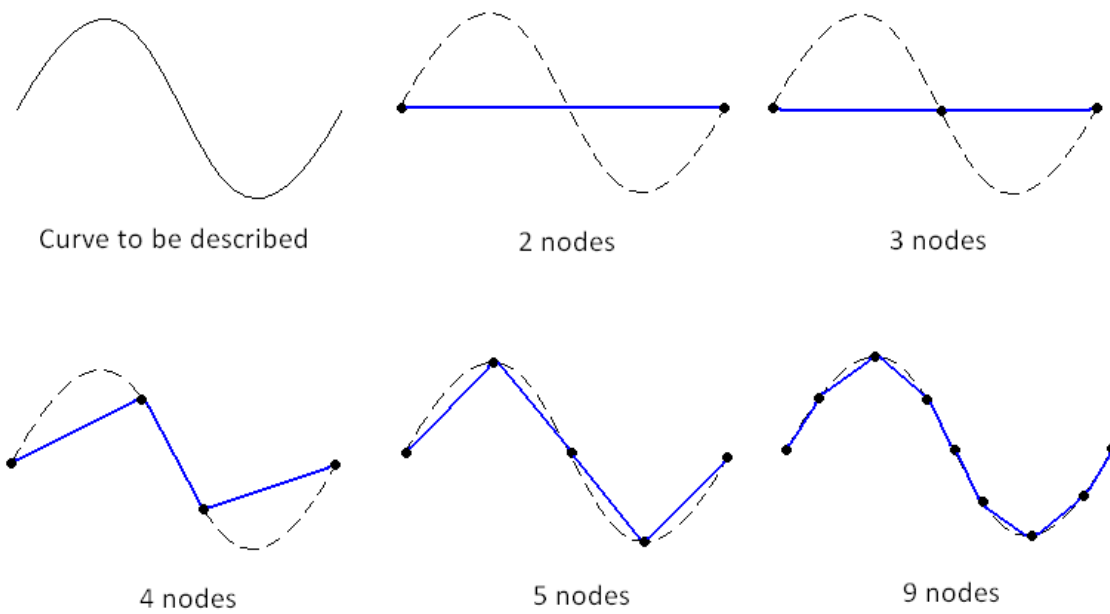


**Figure 2.19.** Example of curve described by an increasing number of nodes.

When meshing CAD geometries, which often consist of regular shapes (cylinders etc.), it is possible to use structured meshes. However, if the model geometry is irregular in shape (as would be expected in this work) unstructured meshes are more appropriate [62]. A comparison of structured and unstructured meshes used for the same geometry can be seen in Figure 2.20.

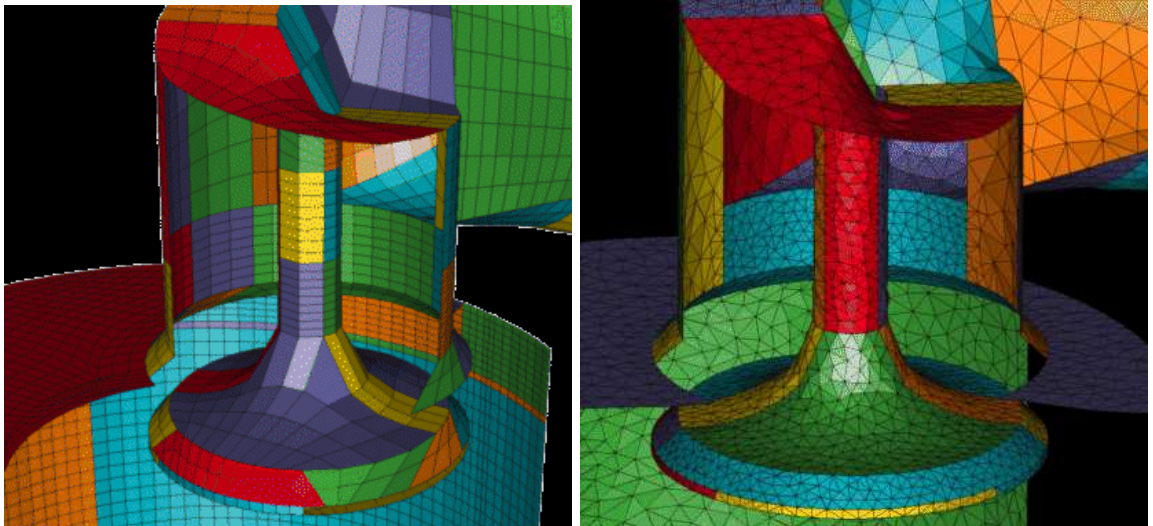


**Figure 2.20.** Comparison of structured and unstructured mesh of the same geometry [64].

After the software has completed meshing it is important to take note of the output statistics. The values of most interest are;

- total number of elements
- maximum growth ratio
- proportion of skewed elements
- ‘skewness’ of elements

The first property gives an idea of what computational power the model will require. The following three give an idea of the ‘quality’ of the model. The user is required to know what computer resources are available and what limits are acceptable for mesh quality. If these properties are within reasonable limits, the model is ready to be exported to a finite element solving package. This work used the Simpleware software to perform meshing due to its stability in preserving material volumes and creating a sufficiently low proportion of skewed elements in comparison to other software available. An example image of a SiC<sub>f</sub>/SiC composite mesh can be seen in Figure 2.21.

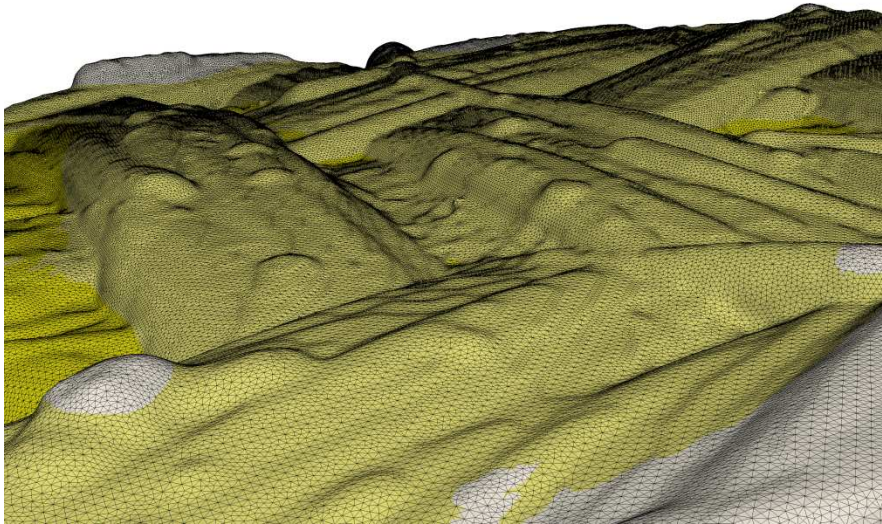


**Figure 2.21.** Surface of SiC<sub>f</sub>/SiC composite with a typical mesh density required by IBFEM to accurately describe misco-structures.

### 2.3 Simulation: FEM

With the 3D model mesh completed and input mechanical & thermal data obtained it is now possible to import the mesh into a finite element solver package which will be used to predict the material's behaviour.

FE models are a way of discretising a volume to then solve a boundary value problem, which is a set of partial differential equations. The method of doing this will depend on the discretisation of the geometry (i.e. which type of elements used; tetrahedron, hexahedron or a combination of these). Most methods use iterative integration such as Runge-Kutta, Euler or other such schemes to track the movement or change in property value of each node on an element. Each node on an element contains data relating to position and any other properties which are part of the model's solution. For example, in a compression test where the nodes will move these could be strain values, or in a thermal test that is tracking diffusivity, nodal temperature will be recorded. The more properties that are recorded, the more calculations it will take for the solution to complete. This will also mean that the size

of data output files will increase. A good introduction to FEM can be found in ‘The Finite Element Method, A practical course’ by Liu and Quek [65].

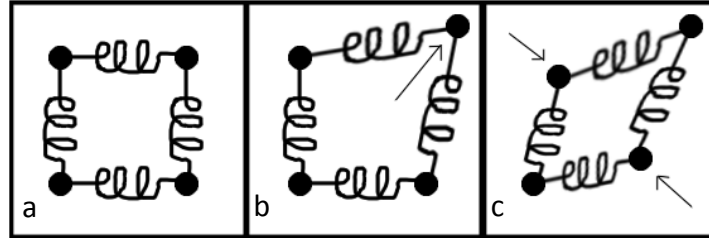


**Figure 2.22.** Using FEM to calculate the movement of nodes on an element from (a) initial state when (b) perturbed by strain of one node to (c) final equilibrium position defined by loading and material properties i.e. Young's modulus and Poisson's ratio in this instance.

Figure 2.22 demonstrates a very simple system of masses connected by springs. In the first image the system is at equilibrium. If one node of the element is displaced, FEM can be used to calculate the magnitude and direction of movement of the other nodes.

For problems of low to middling complexity, commercial packages such as ABAQUS or ANSYS are sufficient. However, as the complexity of a problem increases so does the computational power required for a solution. If a problem becomes complex, solving on a desktop computer with traditional solvers becomes impractical. If this is the case, codes designed for high performance computing (HPC) are required. For example, this work used the ParaFEM library of MPI subroutines, developed by Lee Margetts, to create a custom code for analysis. This allows the FEM code to be used in a parallel environment such as HECToR, the UK's high-end computing resource, funded by the UK Research Councils. Further discussion on the development, capabilities and implementation of the code can be found in section 2.4.

After importing the mesh, the model must be built by setting up the problem that is to be solved. This involves three main steps, which are; to assign material properties, environmental conditions, and computational parameters.

The first step is to define any material properties, such as thermal conductivity, density etc. These properties may be set to vary with direction e.g. higher thermal conductivity along, rather than across, the fibre direction. If a material within the model has been segmented to have different sections, each section may be given its own unique properties. Recent work has even set material property values to vary based on the greyscale levels from the tomography images [63].

Secondly, the solution method must be decided upon. This includes choosing;

- between steady and transient states
- which properties are to be solved (e.g. thermal or mechanical)
- which equations are suitable for use
- an acceptable level of accuracy

This, in turn, dictates what initial and boundary conditions must be chosen. These are chosen in a way that best represents the environmental conditions. Examples of these are;

- initial temperatures
- the number of degrees of freedom for each section of the model
- the location and magnitude of any mechanical or thermal forces applied

The setup methods of each FE package differ slightly. But all solvers require the steps above to be completed before a solution can be found.

## 2.4 Development and use of parallel transient thermal analysis code

Although not strictly a method, this section details the record of work undertaken to adapt a program from Smith and Griffiths [66] to solve transient thermal analyses and the addition of features required for this work to simulate the LFA experiment and in-service behaviour of a fusion reactor component.

Theory on heat transfer in FE is discussed in Chapter 4 to a detail sufficient for this work and will not be included in this section to avoid repetition. A more thorough treatment can be found in the excellent textbook ‘Fundamentals of the Finite Element Method for Heat and Fluid Flow’ by Lewis *et al.* [67].

In order for the author to familiarise himself with variable names, subroutine calls, coding convention etc. effort started with program ‘p75’ pp. 344-346 [6], which performs a general three-dimensional analysis of steady seepage in serial. Little change was required to adapt the code to solve a thermal problem as the equations involved have the same form. Therefore, input material properties were changed accordingly, along with formatting of output, to ensure a form more suitable to nodal temperatures and the ParaFEM convention.

In addition, a section of code was added to calculate the thermal fluxes,  $Q$ , in each element, see Equation (2.8), where  $\frac{dU}{dx}$  is the thermal gradient between two points. In Cartesian three-dimensional space this becomes Equation (2.9). FEA solves this as a system of equations stored in arrays which can be represented in its strong form as Equation (2.10), where  $N$  is the element shape function. These are calculated at the element integration points, or Gauss points, and are then projected to the nodal locations. The FORTRAN code is shown in Equation (2.11), where  $kay$  is the thermal conductivity matrix,  $MATMUL$  and  $derive$  are matrix multiplication and shape function derivative operators respectively.

$$Q = -K \frac{dU}{dx} \quad (2.8)$$

$$q = -\left(K_x \frac{\partial u}{\partial x} + K_y \frac{\partial u}{\partial y} + K_z \frac{\partial u}{\partial z}\right) \quad (2.9)$$

$$\{q\} = -[K] \left\{ \frac{\partial}{\partial x} [N]u \right\} \quad (2.10)$$

$$q = - \text{MATMUL}(\text{kay}, \text{MATMUL}(\text{derive}, u)) \quad (2.11)$$

The code was checked against an analytical solution (a cube with a thermal flux applied to a set of nodes on one surface) and with results from a commercial solver. Results are given in Chapter 4 where it was found to be accurate to whichever iterative tolerance criterion was specified.

The following step was to move fully into the ParaFEM framework and solve the same problem in parallel. This was achieved by adapting program 'p123' pp. 533-535 [6] which was originally written to solve a specific example problem for a given geometry. The first stage, conducted by Lee Margetts, was to generalise the solver to accept any given geometry. Further work was then made to allow user defined boundary conditions (fixed or loaded nodes). Finally the same changes applied to p75 were made, allowing output of nodal temperatures and the x, y, z components of heat flux, albeit in parallel. For validation, the same problem was solved as used to verify p75. When compared to p75, results were identical to all written decimal places.

The final phase, other than introducing additional features, was to move from steady state to transient state, achieved by adapting program 'p124' pp. 537-539 [6]. A comparison of the p124 and xx12 codes is shown in Appendix D. The first step was to apply the same



changes as those made to p75 and p123. Then, the two biggest changes involved in turning this into transient state were introducing time-dependent terms into the equation solved and adding a time-stepping loop.

$$[K]\{\Phi\} + [m_m]\left\{\frac{d\Phi}{dt}\right\} = \{Q\} \quad (2.12)$$

$$([m_m] + \theta\Delta t[K])\{\Phi\}_1 = ([m_m] - (1 - \theta)\Delta t[K])\{\Phi\}_0 + \theta\Delta t\{Q\}_1 + (1 - \theta)\Delta t\{Q\}_0 \quad (2.13)$$

In Equation (2.12) the second term on the LHS is the time-dependent one. This term reduces to zero for steady-state, hence was not previously required. Additionally, because this term is not present in steady-state, the mass matrix was never formed meaning density and specific heat were not required. All these items needed introducing at this stage. In practice, this requires solving simultaneous equations to advance the solution from one time-step to the next. By using a weighted average time-stepping scheme and elimination of terms, Equation (2.13) is formed, where the subscripts denote the initial and next step. Again, discussion on the choice of solution and time-stepping methods can be found in Chapter 4. The time-stepping loop was wrapped around the iterative solver, necessitating careful selection of the operations required for; initiation, each time-step and each iteration within a time-step.

Once the simple analytical problem could be solved and verified, the additional features required to simulate the LFA and in-service monoblock behaviour were introduced. Those features were the ability to allow; multiple material types, an initial non-zero global temperature, varying of loading conditions in time (e.g. to simulate the laser pulse). Each feature was added individually with validation at each stage. As a breakdown of the final code, an overview is given on Page 78 explaining the functions of each section.

- Declare libraries, variables and dynamic arrays used
- Read input data
- Allocate array sizes for global variables
- Divide problem between number of processors available and setup necessary inter-processor communications
- Allocate array sizes for processor local variables
- Create element stiffness and mass matrices
- Build the diagonal preconditioner
- Open output files
- Set fixed nodal temperatures
- Invert the preconditioner
- Read thermal fluxes (loads) to apply at nodes
- Start time-stepping
  - o Apply loads for current time-step
  - o (1<sup>st</sup> step only) Apply global initial temperatures and fixed temperatures
  - o (1<sup>st</sup> step only) Write first step values
  - o (2<sup>nd</sup> step onwards) Compute RHS of Equation (2.13)
  - o Start iterative process
    - Apply fixed temperatures at start of each iteration
    - Solve PCG equations (see 'Theory and Methodology', Chapter 4)
    - Check for convergence
    - Repeat or exit loop
  - o Write nodal temperatures
  - o Repeat for given number of time-steps
- Output solver performance
- Exit program

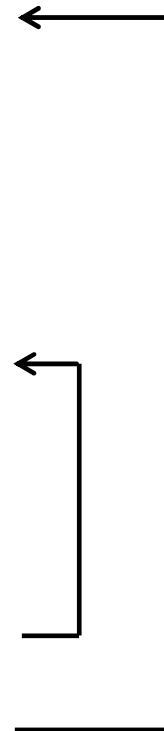


**Figure 2.23.** Overview of program developed to solve transient thermal analysis in parallel, explaining functions of each section of the code.

Due to the intended use of the code to solve extremely large and computationally expensive problems, it was necessary to use specialised hardware capable of maximising the potential of parallel software. The facilities used for this work were HECToR, the UK's national high-performance computing service, and Polaris, provided by the N8 consortium.

The program was written to expect a series of input files which would describe the problem to be solved and its solution parameters. These files included; material properties, geometric data, boundary conditions (loaded and fixed nodes) and a control data file (i.e. number and size of time-steps etc.). Full details of input files are in Appendix F, updated versions for the most recent code version are found on the ParaFEM project wiki [68].

Because a high resolution mesh includes such a large number of elements, the associated files become very large. For example, the problems solved in this work had geometry files of around 5 Gb. Depending on the amount of output data required these were even larger, a single output file being typically over 100 Gb for this project. With such large files it becomes unfeasible to open in a text editor for the purpose of setting boundary conditions or extract result data. Therefore, a complementary set of tools (short stand-alone open-source programs also available from the ParaFEM repository) were developed to undertake the tasks required to set up and analyse data for the simulations. These programs, co-developed with Margetts and Lever were;

- inp2pf – conversion of Simpleware output to ParaFEM input
- gaussianlds – creation of load input files to simulate laser profile of LFA
- ttrb2ttr – conversion of binary output to readable text file
- pf2ensi – conversion of ParaFEM output to visualisation software input
- ndttrget – extract temperature data for a specific node over all time

The aim of developing the main program and complementary tools was not to solve new underlying physical problems but rather, by efficient handling of computations and data management, to solve simple problems (i.e. thermal conductivity) for extremely large and geometrically complex meshes. This was to allow investigation of the effects of micro-structures on a ‘whole component’ scale without the need for multi-scale modelling approximations.

Once simulations and appropriate conversions had finished, a visualisation workstation could be used to display the results. The software used was ParaView, version 3.14.1 64-bit (Kitware Inc., Clifton Park, New York, USA) [69]. This, along with the developed post-processing tools, made it possible to collect and present both qualitative and quantitative results. Examples of its use and simulation specific settings can be found in the appropriate sections of Chapters 4 and 5.

# **CHAPTER THREE: Thermal Characterisation of Ceramic/Metal Joining Techniques for Fusion Applications Using X-ray Tomography**

A paper submitted to the peer reviewed journal: Journal of Nuclear Materials

Presented in submitted form.

Ll.M. Evans, L. Margetts, V. Casalegno, M. Ferraris, F. Leonard, T. Lowe, P.D. Lee,  
M. Schmidt, P.M. Mummery



# Thermal Characterisation of Ceramic/Metal Joining Techniques for Fusion Applications Using X-ray Tomography

Ll.M. Evans<sup>a,\*</sup>, L. Margetts<sup>b</sup>, V. Casalegno<sup>c</sup>, M. Ferraris<sup>c</sup>, F. Leonard<sup>a</sup>,  
T. Lowe<sup>a</sup>, P.D. Lee<sup>a</sup>, M. Schmidt<sup>d</sup>, P.M. Mummery<sup>d</sup>

<sup>a</sup>*School of Materials, University of Manchester, Grosvenor Street, Manchester M1 7HS, UK*

<sup>b</sup>*School of Earth, Atmospheric and Environmental Sciences, University of Manchester, Williamson Building, Manchester M13 9PL, UK*

<sup>c</sup>*Department of Applied Science and Technology, Politecnico di Torino, Corso Duca degli Abruzzi 24, I-10129 Torino, Italy*

<sup>d</sup>*School of Mechanical, Aerospace and Civil Engineering, University of Manchester (MACE), Manchester M13 9PL, UK*

---

## Abstract

An integral component in a fusion reactor cooling system makes use of carbon fibre composite (CFC) tiles joined to a CuCrZr cooling pipe with a Cu interlayer. A main requirement of the materials used, and therefore the interfaces that join them, is high thermal conductivity. This work investigates the thermal performance of four novel CFC-Cu joining techniques. Two involve direct casting and brazing of Cu onto a chromium modified CFC surface, the other two pre-coat a brazing alloy with chromium using galvanisation and sputtering processes. The chromium carbide layer at the interface has been shown to improve adhesion.

The thermal diffusivity across the interface of the joins was measured by means of laser flash analysis. Calibration of results with a reference sample gave values for specific heat capacity and thermal conductivity. X-ray tomography of the CFC-Cu interfaces was performed to investigate micro-structures that might influence the thermal behaviour.

It was found that, although test specimens had similar quantities of CFC and Cu, thermal conductivity varied by up to 72 %. Quantification of the X-ray tomography data showed that the dominant feature in reducing thermal conductivity was the lateral spread of voids at the interface. Correlations were made to estimate the extent of the effect.

The join that exhibited the highest conductivity was made by direct casting. With only a 26 % reduction in thermal conductivity, the sputter coated braze provides an alternative with lower manufacturing costs.

*Keywords: thermal conductivity, laser flash, X-ray tomography, CT, carbon fibre composites, CFC, copper, Cu, joining, direct casting, brazing, fusion, divertor*

---

---

\* Corresponding author. Tel.: +44 1235 466524;

E-mail address: [llion.evans@postgrad.manchester.ac.uk](mailto:llion.evans@postgrad.manchester.ac.uk) (Ll.M. Evans).

### 3.1 Introduction

ITER, the next step on the world's pathway to realising fusion energy, aims to demonstrate the feasibility of using fusion reactions to drive a power plant by successfully sustaining a controlled large scale plasma burn. As well as controlling the plasma, it must show that the construction materials will withstand the thermo-mechanical loading caused by the plasma and any disruptions experienced [70]. As such, the main role of the plasma facing components (PFC) is to protect the machine from this loading by absorbing the energy released whilst minimising plasma impurities and retaining structural integrity [71]. ITER's design specifications will achieve this by active water cooling of the PFCs through heat sinks made from copper chromium zirconium (CuCrZr), a precipitation hardened copper alloy. Thus, the ability to join the PFCs to the CuCrZr is essential [72].

The divertor, which is a target at the intersection of magnetic field lines carrying the plasma, is expected to experience the highest loads, around  $10 \text{ MW}\cdot\text{m}^{-2}$ , as the kinetic energy is dumped over this region [73]. Materials selected for this component will be required to have high thermal conductivity and high thermal shock and fatigue resistance without impacting plasma purity. The two materials under consideration that meet these requirements are carbon fibre composites (CFC) and tungsten [74]. ITER has been designed to have a two tier divertor, using both materials, with the CFC being replaced by tungsten at a later phase of ITER's lifecycle.

The CFC region of the divertor will consist of rows of monoblock tiles along the cooling system. This design was chosen because of its favourable thermal performance compared with other designs, such as flat or saddleblock tiles [71] [75]. The monoblock is a CFC cuboid with a cylindrical hole in the centre through which a CuCrZr coolant pipe runs, as shown in Figure 3.1. The region between the two is the interface that requires joining. A



large difference in the coefficient of thermal expansion of the two materials causes large internal stresses during operation, which can lead to failure. It has been suggested that a thin Cu interlayer might be used in order to mitigate these stresses through its superior ductility. However, CFC does not bond well with pure Cu [76] since the wetting angle of molten copper on carbon substrates is very high, approximately  $140^\circ$ .

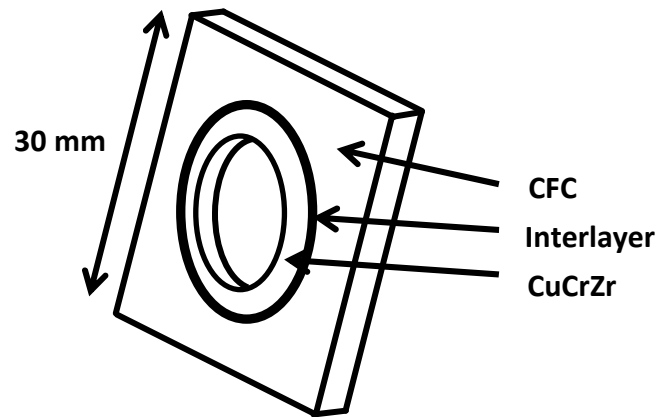


**Figure 3.1.** Schematic of divertor monoblock.

A wide range of techniques have been suggested to overcome this challenge [77] [78] [79] [80] [81] & [82]. This work investigates the thermal behaviour of four CFC-Cu joining methods, developed by Casalegno *et al.* [83] [76] [84], which involve introducing a thin layer of chromium carbide to improve adhesion. Thermal performance across the interfaces is investigated experimentally using laser flash analysis (LFA). The sample interfaces are then investigated by X-ray tomography. Particular interest is given to microstructural variations to identify mechanisms responsible for differences in thermal conductivity. The aim of this investigation is to determine which joining technique provides the greatest thermal conductivity across the CFC-Cu interface and which observable microstructures introduced in the joining process can impede thermal conductivity.

### 3.2 Materials

In order to create specimens suitable for thermal testing, tiles were manufactured in such a way as to represent the CFC-Cu interface present in the monoblock. Each tile consisted of a layer of CFC and Cu, with the interface created by one of the four differing methods of joining.

Two of these used a CFC where the interface surface is modified to form carbides by a solid state chemical reaction with chromium, which has been shown to improve wettability of Cu with CFC [85]. One sample (CFC-Cu\_DC) was joined by a direct casting of a Cu slurry to the modified CFC by placing both materials adjacently in a holder and being heated to 1100 °C for 20 minutes. The other (CFC-Cu\_OSB) was brazed using a commercial brazing alloy containing no active metals, where the tile is heated to 980 °C in an inert argon atmosphere and is kept at this maximum temperature for 15 minutes before being allowed to cool to room temperature. Adhesion between the two layers was facilitated by the use of a tungsten weight on the upper surface of the tile, exerting 1 kPa of pressure.

In a similar vein, the final two samples were brazed using the same brazing alloy and procedure but the chromium was pre-coated to the brazing foil rather than the CFC. This was achieved by a galvanic process (CFC-Cu\_GG) and RF magnetron sputtering (CFC-Cu\_GS). Coating the foil with chromium on a large scale would be technically less challenging than modifying the CFC surface of a monoblock and would therefore be a more cost-effective manufacturing process. The joining processes were performed at Politecnico di Torino according to the procedures detailed by Casalegno *et al.* [84].

The CFC used was Sepcarb NB31 (Snecma Propulsion Solid, France). The composite is composed of a 3D NOVOLTEX preform with needled ex-pitch (z-direction) and ex-PAN (x and y directions) fibres. Densification is performed by chemical vapour infiltration (CVI). The copper was an oxygen free high conductivity (OFHC) variety and the unmodified brazing foil was Gemco® (87.75 wt% Cu, 12 wt% Ge and 0.25 wt% Ni), both manufactured by Wesgo Metals, USA.

Further preparation, undertaken at The University of Manchester, was made to machine the tiles to appropriate dimensions for thermal analysis. This was achieved by using a lathe to produce cylindrical samples, except for the CFC-Cu\_DC sample which was cored out of the tile using the appropriate drill bit. A sample thickness suitable for analysis was achieved using an aluminium oxide cutting wheel on a Struers Accutom-5 cut-off machine at 3000 rpm using a medium force at a speed of 0.02 mm/s. Where required sample grinding using P800 SiC emery paper was performed to obtain parallel upper and lower surfaces. Finally, the samples were cleaned in acetone using an ultrasonic bath for 10 minutes. Photographic images of the samples can be seen in Figure 3.2. Details of the samples' final dimensions and properties can be found in Table 3.1. The cylindrical volumes were calculated using the samples' diameter and thickness, density was calculated using these values with their mass. As such, data for volume and density are bulk values inclusive of the porosity existing in the CFC.

In addition to these were samples for each of the constituent materials (i.e. CFC and Cu) to obtain their individual material properties.

**Table 3.1**  
Sample dimensions.

Sample	Diameter $\pm 0.02$ (mm)	Thickness $\pm 0.02$ (mm) Total	Thickness (%) Cu	CFC	Mass (g)	Volume (cm <sup>3</sup> )	Density (g·cm <sup>-3</sup> )
CFC	12.66	2.06			0.447	0.2593	1.72
Cu	10.10	2.06			1.421	0.1650	8.61
CFC-Cu_DC	10.08	5.36	48.7	51.3	2.191	0.4277	5.12
CFC-Cu_OSB	10.08	4.40	46.8	53.2	1.752	0.3511	4.99
CFC-Cu_GG	12.66	4.96	43.5	56.5	2.978	0.6244	4.77
CFC-Cu_GS	12.70	4.84	43.4	56.6	2.916	0.6131	4.76

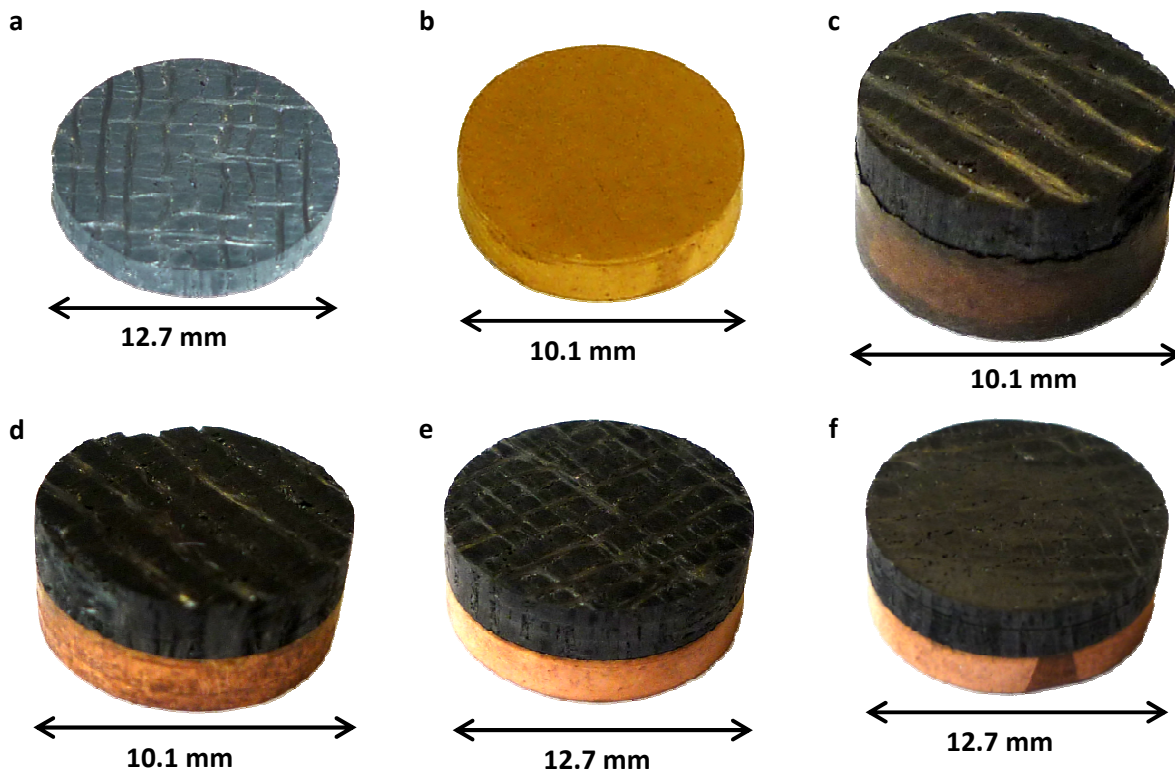


**Figure 3.2.** Samples used for thermal analysis; (a) CFC, (b) Cu, (c) CFC-Cu joined by; direct casting (DC), (d) one step brazing (OSB), (e) braze coated by galvanisation process (GG), (f) braze coated by sputtering process (GS).

### 3.3 Method

This section details the experimental setup used to perform thermal analysis and three dimensional imaging. Details are also provided for image post-processing techniques.

#### 3.3.1 Thermal Analysis

LFA was performed using a Netzsch 457 MicroFlash® system [50] at the School of MACE, University of Manchester, UK. This method measures thermal diffusivity,  $\kappa$ , by

subjecting the front face of a disc shaped sample to a short duration heat pulse, produced by a Nd:YAG laser, whilst measuring the temperature rise with respect to time on the rear face (see Figure 3.3). The half rise time,  $t_{1/2}$ , along with sample thickness,  $L$ , and correction factor,  $\omega$ , are used by the ‘Cowan + pulse correction’ method [86], a modified version of the Parker expression [51] to account for finite-pulse-time and heat losses (3.1), to determine the sample’s thermal diffusivity. Specific heat,  $c_p$ , is measured by calibrating diffusivity results against a Pyroceram 9606 reference sample. Thermal conductivity,  $K$ , can be calculated from its relation to these values and density,  $\rho$ , (3.2).

$$\kappa = \frac{(\omega \cdot L^2)}{(\pi^2 \cdot t_{1/2})} \quad (3.1)$$

$$K = \rho \cdot c_p \cdot \kappa \quad (3.2)$$

The measurements were conducted in an inert nitrogen atmosphere at temperatures ranging from 100 °C to 700 °C at intervals of approximately 100 °C. Because of the relatively high thermal conductivity of the samples the laser voltage was set to its minimum setting. An average value was obtained from 5 measurements at each temperature. The Proteus software package, version 5.2.1 (NETZSCH-Gerätebau GmbH, Wittelsbacherstraße, Selb, Germany), was used to control the measurements and analyse results. Additional parameters specified were to use a linear baseline, 100 % laser filter transmission, 3000 signal acquisition points and to auto optimize amplifier gain and measurement duration.

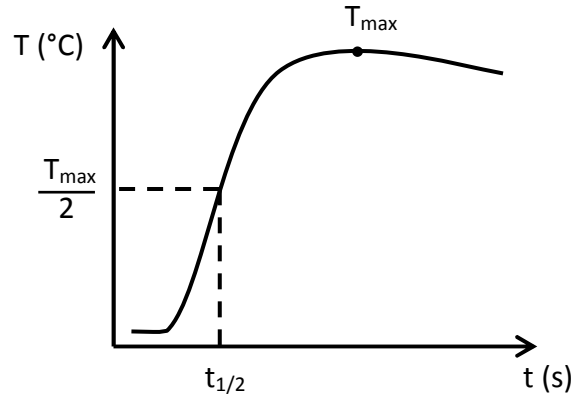


**Figure 3.3.** Typical temperature curve measured on rear face of sample after initial heat pulse.

To ensure maximum absorption of the laser energy and emission on the rear face, the samples were given a conductive graphite coating (Kontakt-Chemie Graphit 33). Multiple coatings are applied to both surfaces, allowing time to dry between applications. Due to the highly anisotropic behaviour of CFCs, it was ensured that fibres in both CFC and CFC-Cu samples were aligned identically to the expected setup of the divertor monoblock [87]. The CFC-Cu samples were tested in both orientations (i.e. laser incident on CFC then Cu), the variation in results was less than 3 % and can be considered negligible. Results reported here are with the laser incident on the Cu surface and temperature measured on the CFC surface.

### 3.3.2 X-ray tomography

X-ray tomography scans of the samples were produced using a Nikon Metrology 225/320 kV system (using the 225 kV source) at the Manchester X-ray Imaging Facility, University of Manchester, UK [88]. The samples were placed on a rotating stage between the X-ray source and detector. 2D radiographs are acquired whilst the sample is rotated through 360°. 3D reconstruction is performed from the radiographs, to be exported as an individual 3D image or a collection of 2D ‘slices’.

The sample specific settings for X-ray source voltage and current, radiograph acquisition time and information about filters used are presented in Table 3.2. The CT-Pro (Nikon Metrology NV, Tring, Hertfordshire, UK) software was used for tomographic reconstruction. Details for beam hardening and noise reduction settings are noted in Table 3.3. Resultant voxel sizes (3D pixel), which are dependent on distances between source, sample and detector, are also reported.

**Table 3.2**  
X-ray tomography parameters used.

Sample	Target	Voltage (kV)	Current ( $\mu$ A)	Filter (mm)	Acquisition Time (ms)	Number of Projections	Frames / Projection
CFC	Cu	120	200	N/A	500	2001	1
Cu	W	220	210	Sn, 1.0	700	3142	1
CFC-Cu_DC	W	210	135	Sn, 1.0	1415	2001	2
CFC-Cu_OSB	W	210	135	Sn, 1.0	1415	3142	2
CFC-Cu_GG	W	210	135	Sn, 1.0	1415	2001	2
CFC-Cu_GS	W	210	135	Sn, 1.0	1415	2001	2

**Table 3.3**  
Reconstruction settings.

Sample	Beam Hardening	Noise Reduction	Voxel Width (mm)
CFC	1	3	0.0100
Cu	2	2	0.0082
CFC-Cu_DC	2	4	0.0083
CFC-Cu_OSB	2	4	0.0083
CFC-Cu_GG	2	4	0.0097
CFC-Cu_GS	2	4	0.0097

### 3.3.3 Visualisation and analysis of CT data

Each two dimensional slice forming the complete volume is a greyscale image, with higher pixel values denoting a greater level of X-ray absorption. In order to visualise the sample in three dimensions the greyscale data must first be segmented, a process which assigns a material type to each voxel (3D pixel). Segmentation and visualisation were performed using a combination of the software packages Avizo, version 7 (VSG, Mérignac Cedex, France) and Simpleware, version 6 (Simpleware Ltd., Exeter, Devon, UK). This process also allows the collection of quantitative data about the sample, such as porosity fractions,

volumes or surface area of each material and can be used to measure lengths of internal features e.g. cracks.

### **3.4 Results & Discussion**

Results are firstly presented on the thermal behaviour of the samples, comparing the performance variations caused by the differing joining techniques. These are benchmarked against the results for the constituent materials and the material property values reported in the ITER materials property database (MPDB). The outcome of the scanning process is then discussed, making particular note of any features likely to affect overall image quality due to sample geometry or material composition. The CT data is then visualised for investigation of the CFC-Cu interface by both qualitative and quantitative methods. Finally conclusions are drawn based on these observations as to the cause of the thermal performance variations and which joining technique provides the best performance.

#### **3.4.1 Thermal Diffusivity**

The thermal properties of six samples (CFC, Cu and four joined variants) were measured experimentally. The results for diffusivity, specific heat and conductivity are shown in Figure 3.4, Figure 3.5 and Figure 3.6 respectively. It is difficult to directly compare the results of the joined samples with each other because each has a different ratio of CFC to Cu thickness. In order to compare results, the average values were calculated for each sample as expected based on the thickness fraction,  $R$ , of each constituent material, shown in Table 3.1. The difference,  $\partial$ , between experimental and expected average values for each thermal property are shown in Figure 3.7, Figure 3.8 & Figure 3.9, e.g. for thermal diffusivity;



$$\partial_{\kappa} = \frac{(\kappa_{avg} - \kappa_{exp})}{\kappa_{avg}}$$

(3.3)

$$\kappa_{avg} = \kappa_{CFC} \cdot R_{CFC} + \kappa_{Cu} \cdot R_{Cu}$$

(3.4)

Firstly it is pertinent to compare the individual results for CFC and Cu to the reference values provided in the ITER MPDB, shown for specific heat and thermal conductivity in Figure 3.5, Figure 3.6 & Table 3.4. The thermal diffusivity values shown in Figure 3.4 have been calculated from the aforementioned values. It can be seen that the thermal conductivities were slightly lower for CFC and higher for Cu, although these are still within acceptable limits. The experimental results show that Cu is relatively stable over the range of temperatures, with only thermal conductivity experiencing an appreciable drop of approximately 20 % of its initial value. The change in temperature has a greater effect on the performance of CFC, with thermal conductivity reducing by 45 % over the 600 °C range measured. In all of the joined samples it would therefore be expected to observe similar trends in thermal properties. This is indeed what can be seen although to differing degrees of magnitude.

Comparison of the differences, relative to averages based on material thickness fractions, grants further insight into the influence each bonding technique has on the thermal behaviour. It can be seen (Figure 3.9) that the differences in thermal conductivity for the four techniques are very distinct from each other. As the differences don't vary much across the temperature range, approximately 20 % for DC and 10 % for the others, their

tendency is to follow the conductivity of the average. That is, the effect of joining on thermal conductivity is relatively consistent across the temperatures investigated.

Interestingly, the samples' specific heat fell into two clear bands. The samples whose specific heat are higher, closer to CFC and change the least are the ones which have the modified CFC surface (DC and OSB). Whereas the samples joined by a modified braze (GG and GS) have lower values more similar to Cu. Even though the diffusivity of DC and GS samples are similar, it is this significant difference in specific heat which causes the DC sample to have an overall higher thermal conductivity.

The expectation is that the thermal conductivities of the joined samples would not be greater than the average values derived from constituent material thicknesses but would be between those. Other than DC performing a little better than the average at low temperatures, the first statement holds true, showing that the four joining techniques do reduce the conductivity. However for OSB and GG samples the conductivity is affected to such an extent that it is lower than that of only CFC.

The joining techniques' effectiveness of carrying thermal energy away is ranked, from low to high, as OSB, GG, GS and DC.

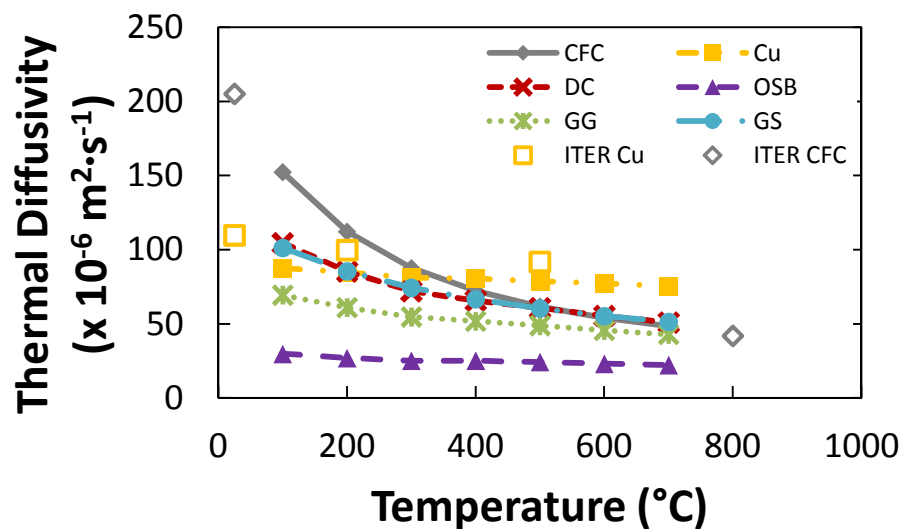


**Figure 3.4.** Thermal diffusivity measured by laser flash analysis.

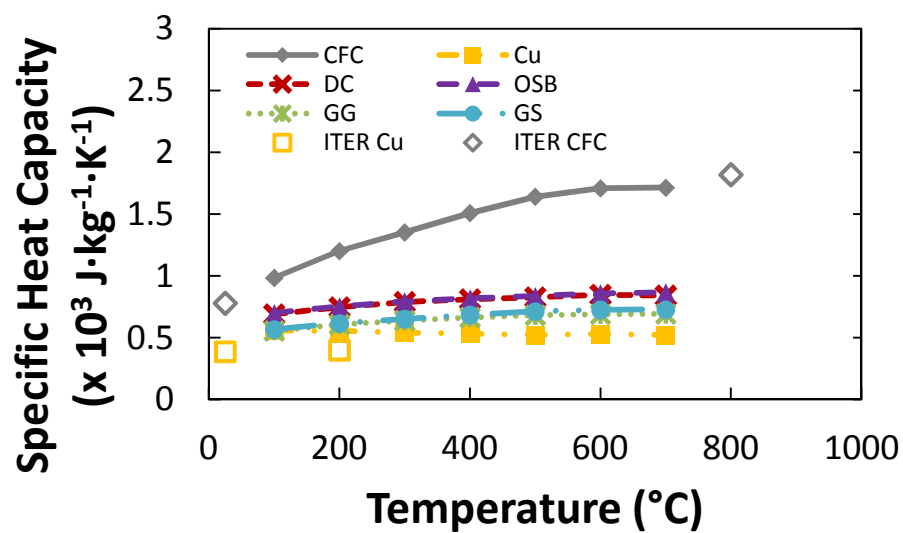


**Figure 3.5.** Specific heat capacity calculated by calibration of diffusivity against Pyroceram 9606.

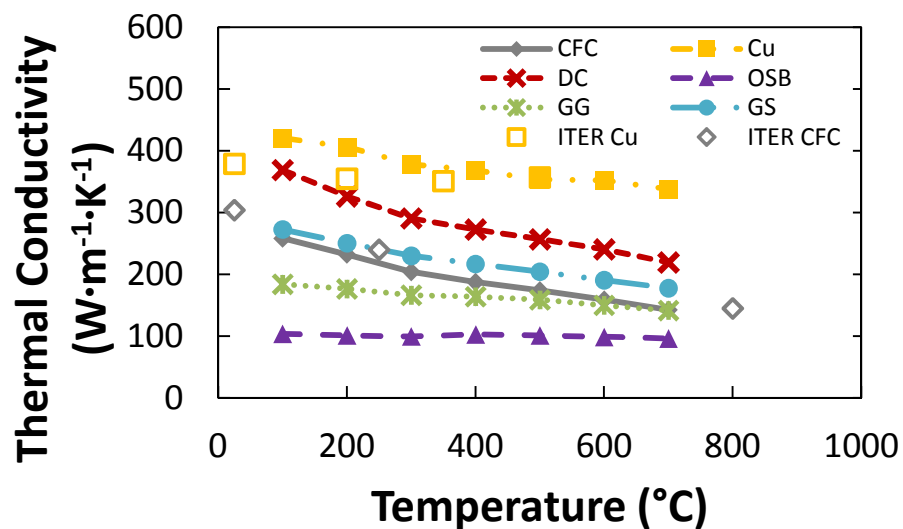


**Figure 3.6.** Thermal conductivity calculated from diffusivity, density and specific heat values.

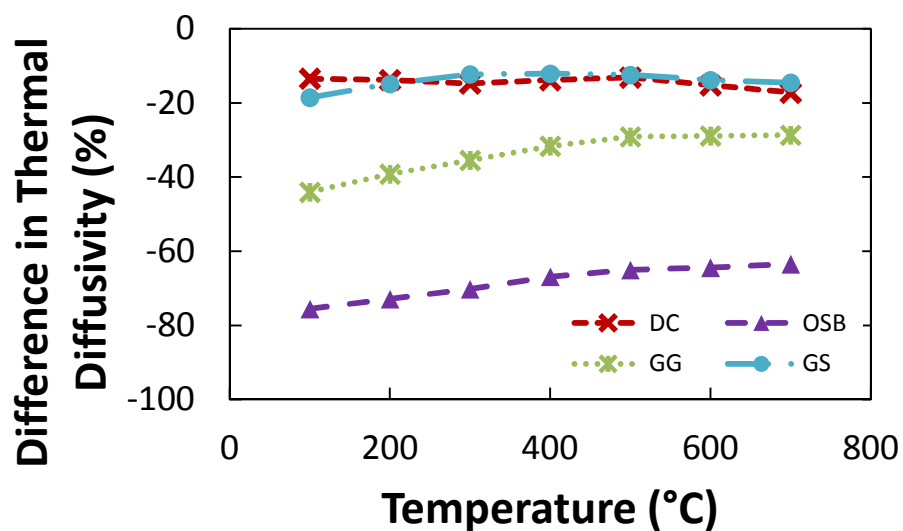


**Figure 3.7.** Difference, as a percentage, in sample thermal diffusivity compared to expected value as calculated from constituent material thicknesses.

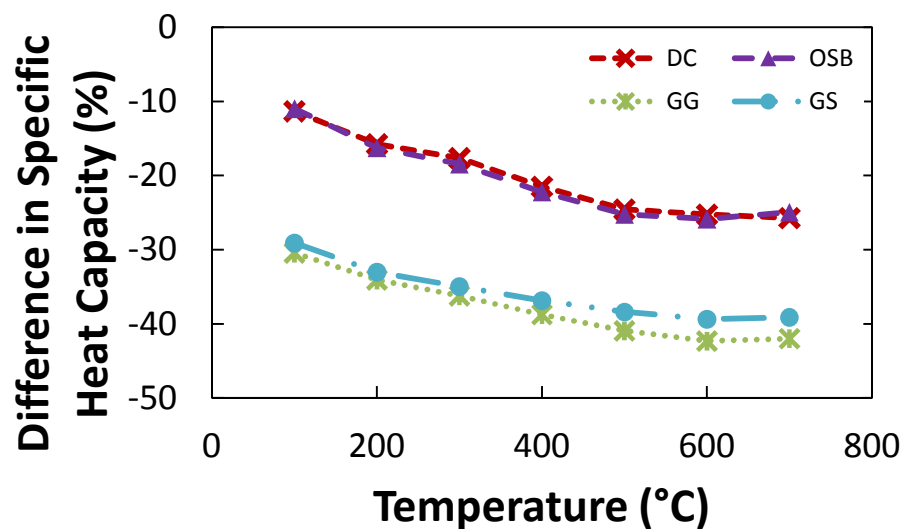


**Figure 3.8.** Difference, as a percentage, in sample specific heat capacity compared to expected value as calculated from constituent material thicknesses.

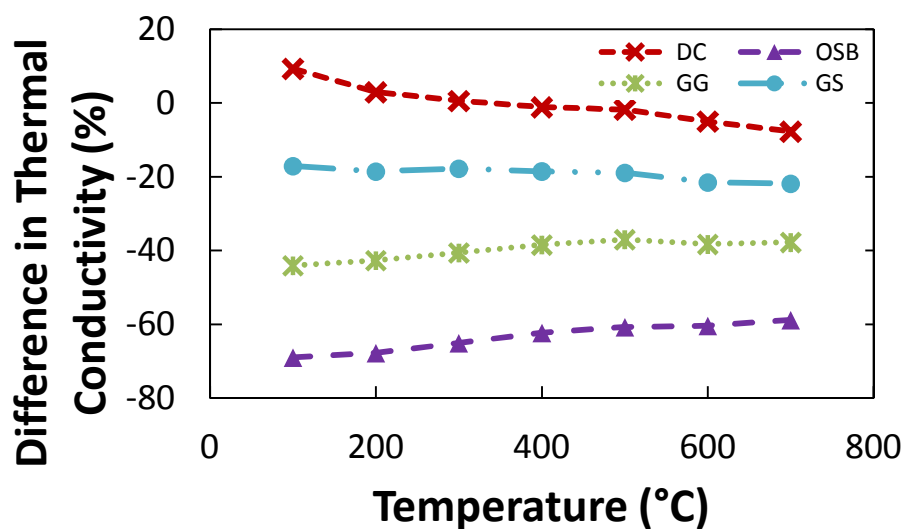


**Figure 3.9.** Difference, as a percentage, in sample thermal conductivity compared to expected value as calculated from constituent material thicknesses.

**Table 3.4**

Materials properties of CFC and Cu as specified by ITER MPDB.

Properties	Temperature (°C)		CFC (z direction)	Cu
	CFC	Cu		
Thermal conductivity ( $\text{W}\cdot\text{m}^{-1}\cdot\text{K}^{-1}$ )	RT <sup>+</sup>	RT	304	379
	250	200	240	355
	800	350	145	351
	1000	500	141	357
Specific Heat ( $\text{J}\cdot\text{g}^{-1}\cdot\text{K}^{-1}$ )	RT	RT	0.780	0.388
	800	200	1.820	0.400
	1000	500	2.000	0.437
CTE ( $10^{-6} \text{K}^{-1}$ )	800	200	0.4	17.0
	1000	500	0.5	18.6
Density ( $\text{g}\cdot\text{cm}^{-3}$ )	RT	RT	1.90	8.90
Porosity (%)	RT	RT	8	N/A

<sup>+</sup>Room Temperature

### 3.4.2 X-ray Tomography

Samples with high X-ray absorption contrasts, such as that between CFCs and Cu, are notoriously difficult to image well [89]. If there is too much X-ray penetration of a region it will appear ‘washed-out’ and be difficult to distinguish from the surrounding air. Conversely, if penetration is insufficient internal features are very difficult to resolve and large ‘streaking’ artefacts will be observed emanating from the edges of this region. In consideration of this, careful selection of filters and source energy was made (shown in Table 3.2) to mitigate these effects which are likely to be more pronounced at the interface where contrast is greatest. It can be seen in Figure 3.10 that these effects are not completely suppressed; in the combined image the interface is ill-defined with streaking artefacts from the Cu overlapping the CFC. With an appropriate balance of image contrast and brightness levels individual images can be produced that provide enough detail to distinguish between the various materials at the interface. Further artefacts that hinder the process of automated segmentation are displayed in Figure 3.11, these must typically be dealt with manually. In this instance, such artefacts were removed using paint/un-paint tools on a slice-by-slice basis by eye to discern material boundaries, using similar structures in the surrounding region for guidance.

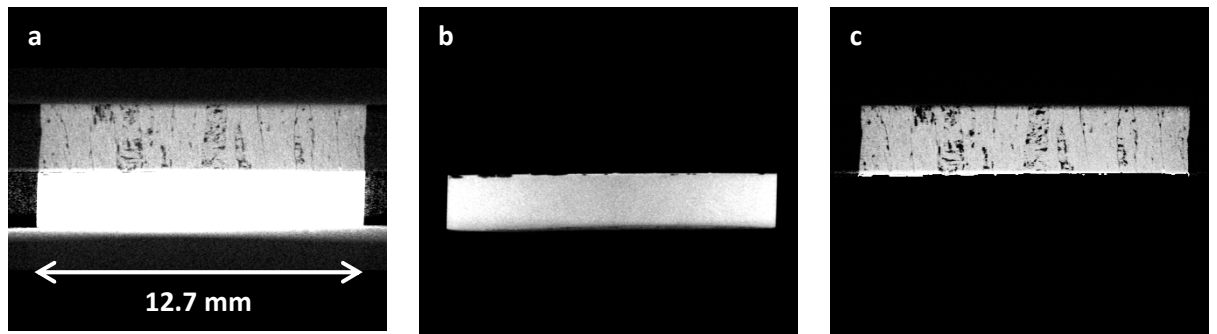


**Figure 3.10.** Cross sectional tomography slice showing (a) streaking artefacts from high absorption Cu masking internal CFC structures at interface, resolved by individually adjusting image brightness and contrast values for (b) Cu and (c) CFC.

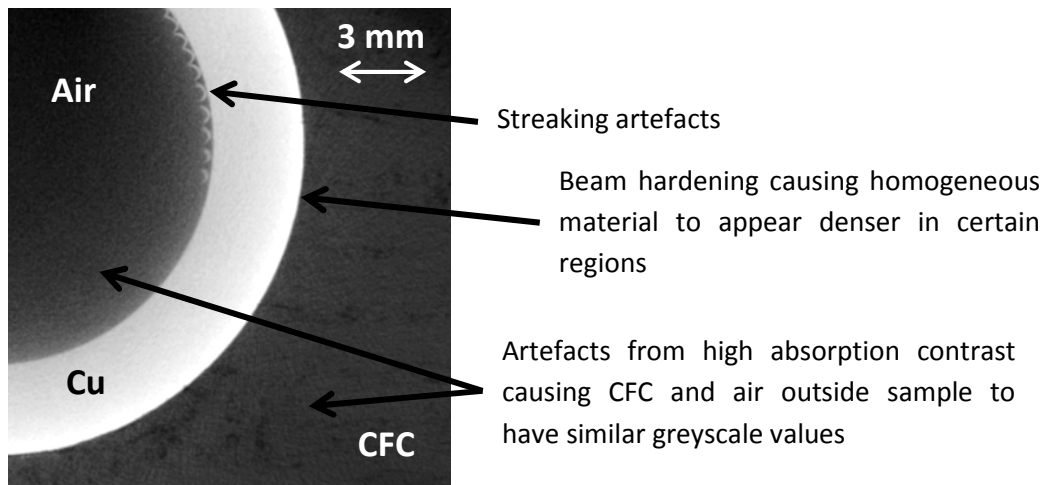


**Figure 3.11.** Various artefacts that hinder automated segmentation of CT image caused by high absorption contrast ratio in an X-ray tomography slice from the midplane of a CFC-Cu divertor monoblock.

### 3.4.3 Visualisation and analysis of CT data

The porosity contained within the CFC is a good example of where qualitative and quantitative observations can be complementary. Figure 3.12 (a) shows the full volume of the CFC-Cu\_GS sample. Having distinguished the CFC and Cu phases it is possible to determine the location of the porosity. By digitally removing the CFC it is then possible to see the alignment of the porosity with fibre direction, the thickness of the layers and additional features such as size, shape and distribution of closed or open porosity. By measuring the volume of the CFC and porosity it was possible to measure the volume fraction of the porosity to be 7.5 %. By comparison with the ITER MPDB, where porosity fraction is reported as 8 %, this can be seen to be in agreement. Across the range of samples, the porosity varied little as all samples used the same manufactured CFC.

Therefore, analysis of the CT data concentrates on the CFC-Cu interface, more specifically the differences in how the Cu/braze deforms to bond with the CFC, dependent on joining technique. Although the Cr layer will have some effect on the interface, its thickness is similar to that of the image resolution and therefore will not be discernible.

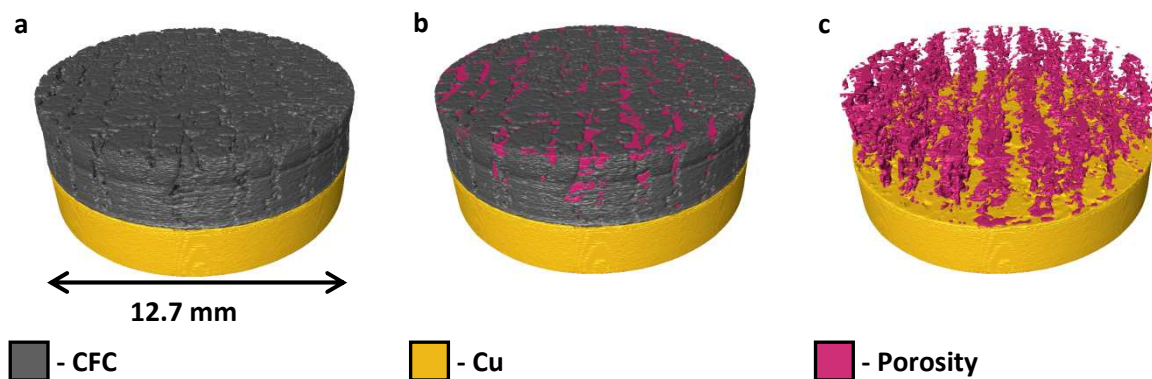


**Figure 3.12.** 3D volumetric rendering of CT data, showing (a) CFC-Cu\_GS, (b) same sample with porosity highlighted and (c) CFC removed to display porosity alignment.

Two notable features, seen in Figure 3.13, were apparent in the DC sample. Firstly, the perimeter of the CFC is surrounded by a thin layer of Cu. The Cu seems to be pulled from the main Cu layer over the CFC layer. This was most probably caused by the process of boring the sample out of a larger tile, the only sample not produced by using a lathe, and not a by-product of the joining technique. It is perceivable that this will have an effect on the conductivity across the sample, however the contact between the pulled Cu and the bulk CFC is poor therefore so will thermal conduction. Additionally, with the LFA technique the thermal flux from the laser is at its greatest along the central profile of the sample and lowest at the edge and, due to this accounting for a low percentage of the CFC-Cu contact area, it is expected that the effect will be limited. Secondly, of the four samples this one has the largest structures, in height and diameter, protruding from the Cu surface. These structures can be seen to fill pores in the CFC at the interface, however they are not solid Cu, but themselves contain large voids. The pores containing the Cu structures are larger than the characteristic porosity seen in these CFCs. As the CFC is previously well



characterised, it is unlikely that this specific sample had such large pores previous to the joining process. Therefore, it can be inferred that the direct casting process damages the CFC structure by enlarging some already existing porosity. In doing so, the molten Cu fills the newly formed large pores but leaves behind almost equally sized pores in the bulk Cu. In addition to these large protruding Cu structures, small veins of Cu can be seen entering the smaller pores on the CFC surface.

The most notable feature seen in the sample joined by the one step brazing technique is a large void formed as a layer between the bulk Cu and the braze, shown in Figure 3.14. This void spans the majority of the surface with the exception of a few ‘pillars’ which connect the upper and lower parts of the sample. On the CFC-Cu interface it can be seen that the braze is present across the greater part of the CFC surface, showing it has successfully bonded. Here it infiltrates the majority of the pores, to a lesser depth than sample DC but deeper than both GG and GS samples. Initially this suggests a superior bond but this is undermined by the large void which suggests substantial delamination between the braze and Cu.

Samples GG and GS, joined by the modified braze, shown in Figure 3.15 and Figure 3.16 respectively, show much fewer voids between the bulk Cu and CFC. Additionally, the veins of braze entering the porosity are fewer and less deep. Of the two, sample GS shows the fewest voids in addition to having the fewest and shortest veins protruding from the bulk Cu.

It therefore appears that as the quantity of Cu or braze which enters the CFC porosity increases, so does the volume of voids between the two layers. In the case of DC, this is probably due to the gas which was present in the porosity being forced out as bubbles

when the molten Cu is introduced but not able to completely escape. With brazed samples, small voids will inherently be present as part of the layup between layers before the joining process. In joining, it appears these are trapped between layers and locate to the regions where there is the most displacement of braze material i.e. where braze enters the pores. Alternatively, it is possible that as the braze melted and filled the pores, there was insufficient braze material to remain between the CFC and Cu. Due to the brazing process happening at a temperature below the melting point of Cu, the Cu would not then fill the region vacated by the braze thus leaving a void in its place.

Verification of the visual investigation can be made by comparison with the statistical measurements of the data, shown in Table 3.5. This is done by comparing the surface area of the Cu, calculated as the area of a circle using its diameter, with that measured from the CT data which accounts for surface roughness. To give an indication of joining success, the percentage of this area in contact with the CFC is measured. Quantification of the interlayer voids is also given as percentages of volume and area in the x-y plane with respect to that of the total volume and planar area of the sample.

Compared to the geometrically calculated surface, all samples have an increased Cu surface area at the interface i.e. none are perfectly smooth. This is due to the deformations introduced in the Cu/braze whilst joining to the CFC. The greatest changes seen are in the DC and GG samples.

It can be seen that both samples with a modified CFC surface (DC and OSB) have a high percentage of the Cu/braze in contact with the CFC, 96.7 % and 91.6 % respectively, with GG only having 56.3 % contact. Therefore, we observe that an increase in Cu surface area does not necessarily lead to a large CFC-Cu contact area. However, recalling the sample

thermal conductivities, it must be noted that neither does a high contact area imply higher thermal conductivity e.g. OSB has the second highest contact area ratio but the lowest conductivity by a considerable margin.

This can be attributed to the other major mechanism affecting conductivity across the interface, the existence of voids. A comparison of volume ratio shows that OSB does indeed have a significantly higher volume ratio of porosity. However, GS has the lowest ratio but not the highest conductivity. It is therefore appropriate to further investigate the voids by considering their shape and distribution.

The thermal pulse from the LFA travels in the z-direction, therefore features acting as thermal barriers will be most effective in impeding thermal transport by spanning the x-y plane. Figure 3.17 displays the area in that plane covered by the voids (this is given as a percentage of the total sample area in Table 3.5). By making the assumption that the voids were perfectly insulating, the lateral area of the voids was used to predict thermal conductivity of the joins, as shown in Equation (3.5)

$$K = K_{avg} \cdot (1 - A_{void})$$

(3.5)

where  $K_{avg}$  is the average thermal conductivity calculated from the constituent material thicknesses as defined in Equation (3.4) and  $A_{void}$  is the lateral area of the sample covered by voids as a fraction.

The predicted thermal conductivities are shown along with experimental results for comparison in Figure 3.18. The predictions are lower than experimental results because assuming voids are perfectly insulating has artificially increased the thermal resistance. But

even with this bold assumption it can be seen that this is a fair approximation of thermal conductivities across the interface. Therefore, when considering samples not easily tested by LFA, quantification of interface voids could provide rough estimates for conductivity. It can be seen that, of the micro-structural features considered, the lateral void area shows the best indication of which samples are expected to have the highest thermal conductivity.

Although the overall performance across the interface is a combination of the factors discussed, it is implied that the greatest influence on the thermal conductivity comes from the existence of voids between the bulk Cu and CFC and not the CFC-Cu contact area. Therefore to maximise conductivity it is more important to minimise the lateral spread of voids rather than minimise void volume.

Of the samples considered, it was shown that DC had the highest thermal conductivity and lowest lateral void area. This was the only sample not joined by brazing; consequently it is apparent that the brazing technique itself is the cause of the lateral spread in voids observed in the other samples. A possible explanation for this is that too little brazing material was used between the Cu and CFC, therefore leaving these voids when becoming molten and entering the CFC porosity. As a more cost effective alternative, GS shows promise in retaining an adequately comparable thermal conductivity whilst requiring a simpler manufacturing process.

**Table 3.5**

Comparison of Cu area calculated by diameter and measured by CT, also percentage of area in contact with CFC and void volume as percentage of total volume and void area in x-y plane as percentage of total planar area.

Sample	Cu Geometric Area (mm <sup>2</sup> )	Cu CT Area (mm <sup>2</sup> )	Ratio	CFC-Cu Contact Area (%)	Void Volume (% of Total Vol.)	Void Area in x-y (% of Total Area)
DC	79.80	101.66	1.27	96.7	0.48	10.3
OSB	79.80	87.38	1.09	91.6	2.83	77.2
GG	125.88	154.48	1.23	56.3	0.79	61.2
GS	126.68	132.18	1.04	80.4	0.34	26.7

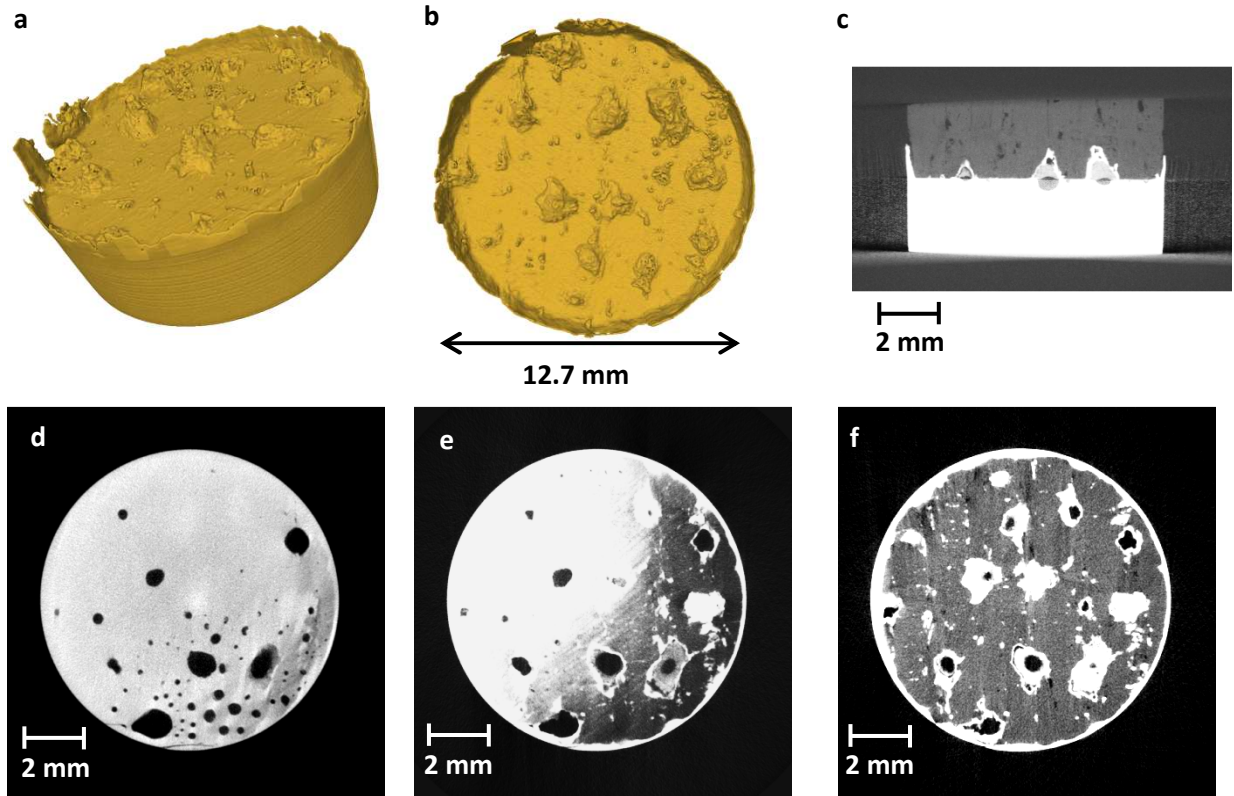


**Figure 3.13.** CT data of CFC-Cu\_DC sample represented by; (a), (b) 3D visualisation of Cu showing protruding interface features, (c) tomography slice in x-z plane showing Cu features (containing voids) entering porosity in CFC, (d), (e) and (f) tomography slices in x-y plane progressing through the interface from Cu into CFC. Cu, CFC and voids/porosity are represented by light, medium and dark level greyscale pixels, respectively.

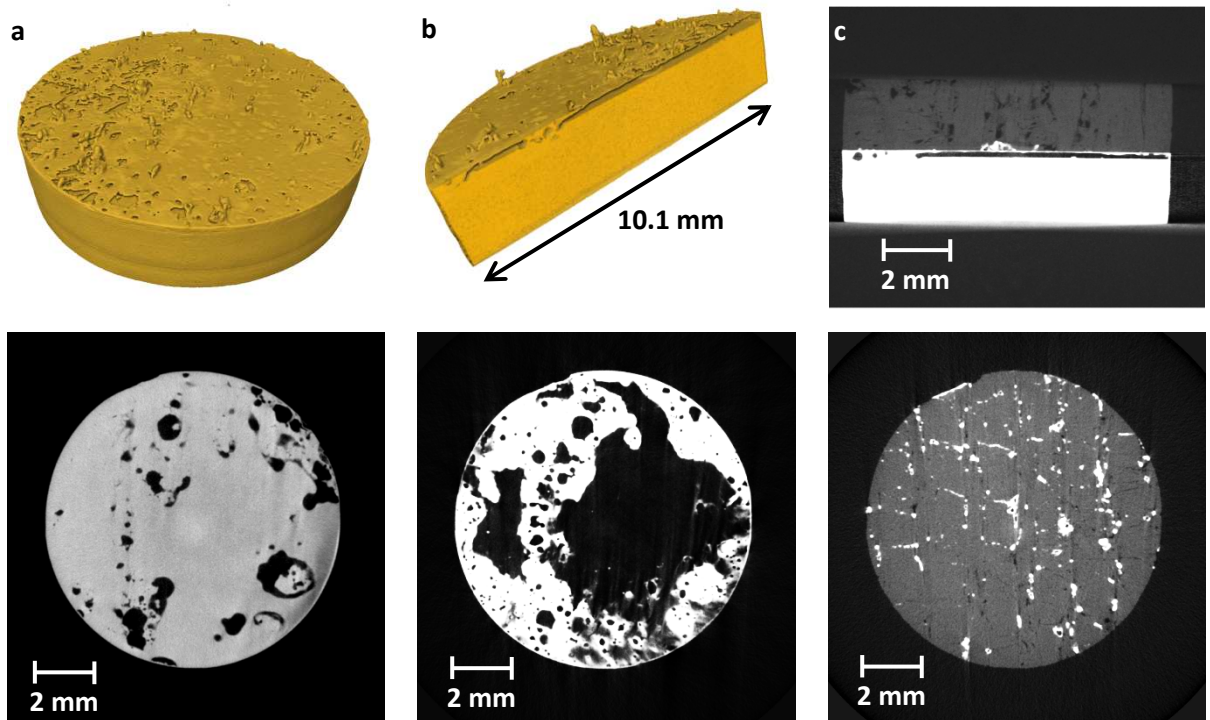


**Figure 3.14.** CT data of CFC-Cu\_OSB sample represented by; (a), (b) 3D visualisation of Cu showing protruding interface features and void layer between bulk Cu and braze, (c) tomography slice in x-z plane showing Cu features entering porosity in CFC, (d), (e) and (f) tomography slices in x-y plane progressing through the interface from Cu into CFC. Cu, CFC and voids/porosity are represented by light, medium and dark level greyscale pixels, respectively.

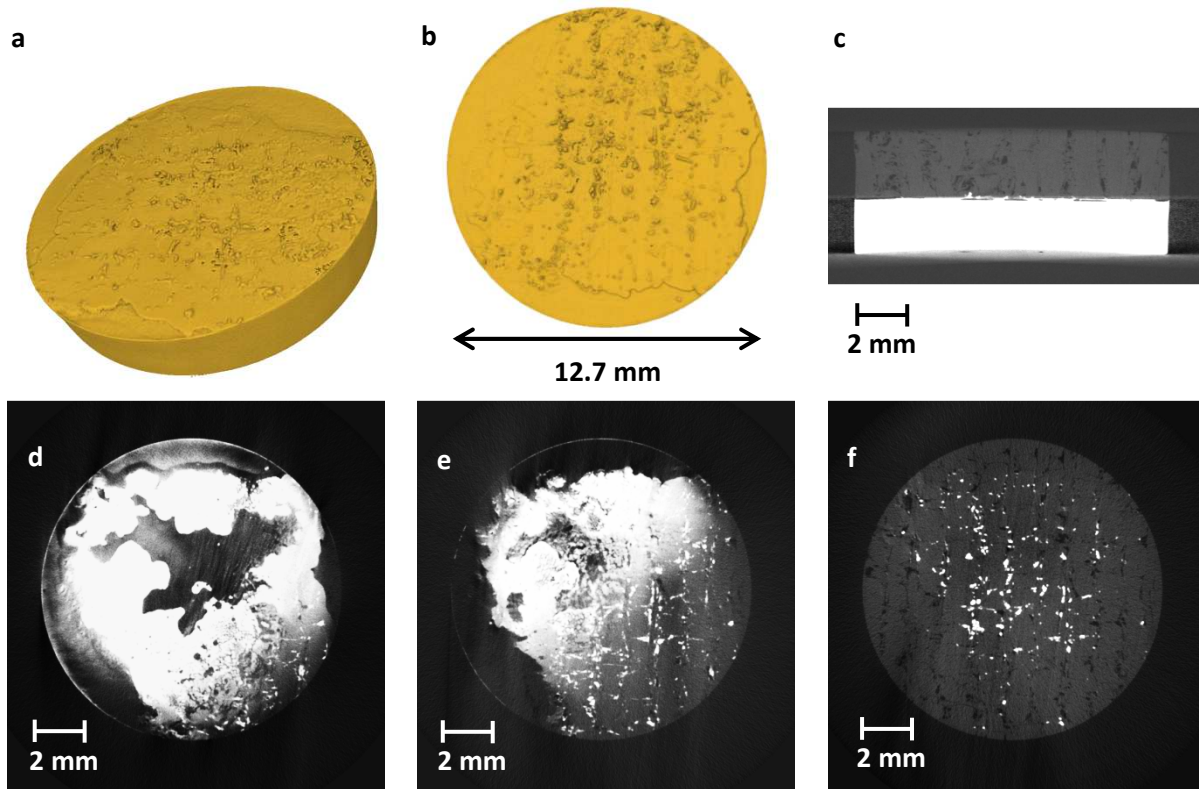


**Figure 3.15.** CT data of CFC-Cu\_GG sample represented by; (a), (b) 3D visualisation of Cu showing protruding interface features, (c) tomography slice in x-z plane showing Cu veins of braze entering porosity in CFC, (d), (e) and (f) tomography slices in x-y plane progressing through the interface from Cu into CFC. Cu, CFC and voids/porosity are represented by light, medium and dark level greyscale pixels, respectively.

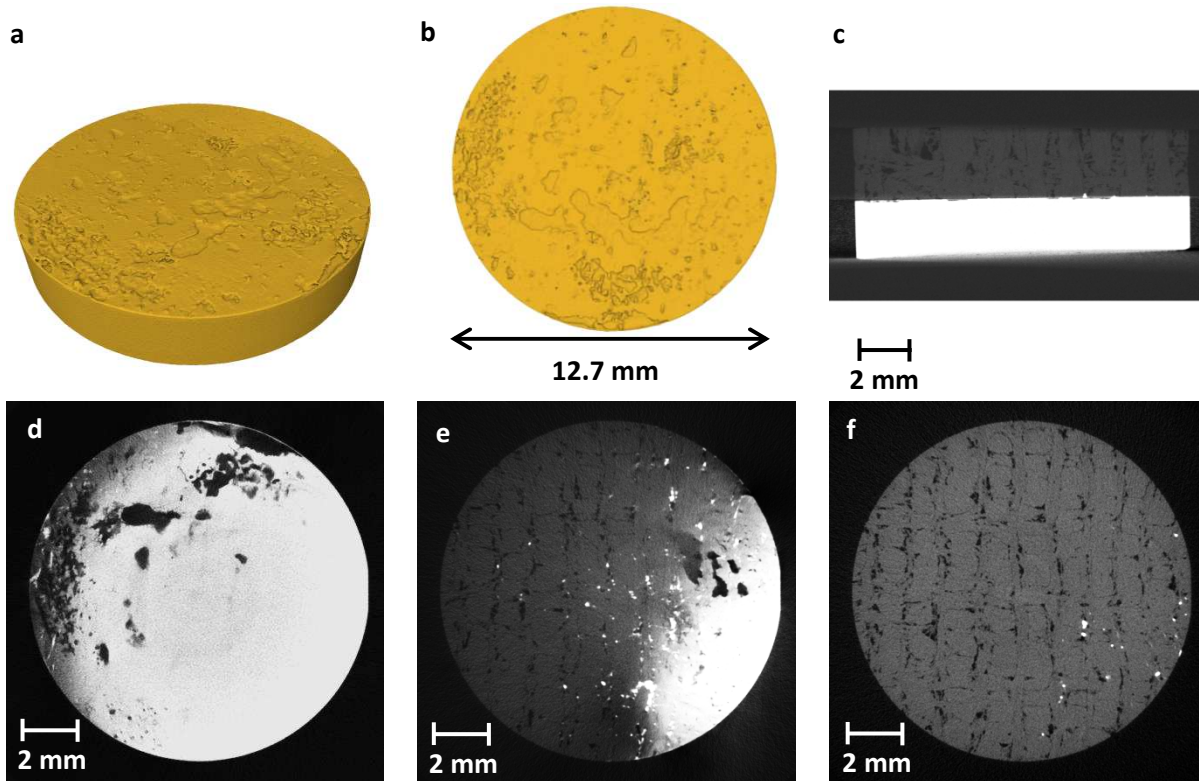


**Figure 3.16.** CT data of CFC-Cu\_GS sample represented by; (a), (b) 3D visualisation of Cu showing protruding interface features, (c) tomography slice in x-z plane showing Cu veins of braze entering porosity in CFC, (d), (e) and (f) tomography slices in x-y plane progressing through the interface from Cu into CFC. Cu, CFC and voids/porosity are represented by light, medium and dark level greyscale pixels, respectively.



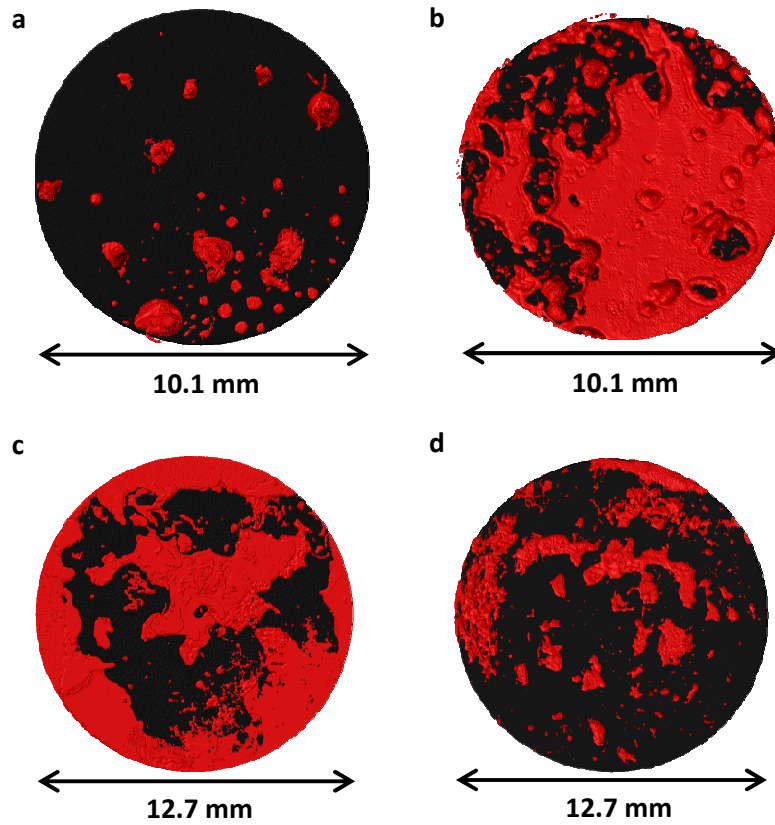


**Figure 3.17.** Projection of void area (red) covering total sample area (black) in x-y plane for samples (a) DC, (b) OSB, (c) GG and (d) GS.

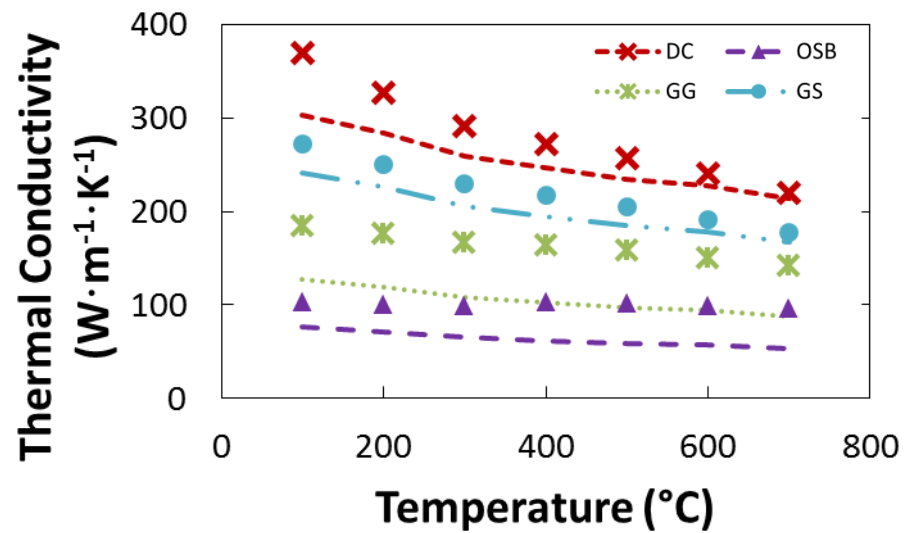


**Figure 3.18.** Thermal conductivity of the four joined samples with points denoting experimental results and lines denoting predicted values based on contribution of constituent material thickness and percentage of sample area covered by voids.

### 3.5 Conclusions

The thermal performances of four different ceramic/metal joining techniques were investigated by measuring the thermal diffusivity across a CFC-Cu interface. Two samples, joined by direct casting (DC) and a brazing process (OSB), had the CFC modified by applying a coating of chromium to improve its adhesion. The other two used the same brazing process but with the brazing foil pre-coated with chromium. The two methods used for chromium coating were galvanisation (GG) and sputtering (GS). The thermal diffusivities of the joined CFC-Cu samples as well as CFC and Cu only samples were measured by laser flash analysis from 100 °C to 700 °C. Their specific heat capacities were calculated by calibrating results with the reference sample Pyroceram 9606 and thermal conductivities calculated by the combination of these results with their measured densities. Even though samples of similar geometries were tested, each join exhibited a different thermal conductivity across the CFC-Cu interface.

Further investigation of the micro-structures at the CFC-Cu interface was performed by X-ray tomography. Through quantification of this data a clear link was made between the lateral spread of void area at the interface and thermal conductivity. Measurement of the lateral void area made it possible to estimate the samples' thermal conductivity. Recommendations were made to increase thermal conductivity at the CFC-Cu interface by ensuring the mitigation of lateral void spread during the joining process as this was the dominant process in reducing thermal performance.



## Acknowledgements

The support of the Engineering and Physical Sciences Research Council for the Fusion Doctoral Training Network (Grant EP/K504178/1) and Culham Centre for Fusion Energy (CCFE) is gratefully acknowledged. The authors would like to acknowledge the assistance provided the Manchester X-ray Imaging Facility for use of tomography equipment, which was funded in part by the EPSRC (grants EP/F007906/1, EP/F001452/1 and EP/I02249X/1). Additionally, the authors would like to thank the staff at the University of Manchester and David Yapp (CCFE) for guidance in preparing this work, also Dr. G.Pintsuk and Mr. T.Koppitz (Forshungszentrum Jülich, Germany) for manufacturing the GG sample.

## References

- [70] “ITER - the way to new energy,” [Online]. Available: <http://www.iter.org/proj/itermission>. [Accessed 25 July 2013].
- [71] R. Tivey, T. Ando, A. Antipenkov, V. Barabash, S. Chiochio, G. Federici, C. Ibbott, R. Jakeman, G. Janeschitz, R. Raffray, M. Akiba, I. Mazul, H. Pacher, M. Ulrickson and G. Vieider, “ITER divertor, design issues and research and development,” *Fusion Engineering and Design*, vol. 46, no. 2-4, pp. 207-220, 1999.
- [72] E. Rigal, P. Bucci and G. Le Marois, “Fabrication of monoblock high heat flux components for ITER divertor upper vertical target using hot isostatic pressing diffusion welding,” *Fusion Engineering and Design*, Vols. 49-50, pp. 317-322, 2000.
- [73] A. Kukushkin, H. Pacher, V. Kotov, G. Pacher and D. Reiter, “Finalizing the ITER divertor design: The key role of SOLPS modeling,” *Fusion Engineering and Design*, vol. 86, no. 12, pp. 2865-2873, 2011.
- [74] R. Pitts, A. Kukushkin, A. Loarte, A. Martin, M. Merola and C. Kessel, “Status and physics basis of the ITER divertor,” *Physica Scripta*, vol. T138, p. 014001, 2009.
- [75] M. Merola and G. Vieider, “On the use of flat tile armour in high heat flux components,” *Journal of Nuclear Materials*, vol. 258–263, no. Part 1, pp. 672-676, 1998.
- [76] V. Casalegno, M. Salvo, S. Murdaca and M. Ferraris, “One-step brazing process for CFC monoblock joints and mechanical testing,” *Journal of Nuclear Materials*, vol.

393, no. 2, pp. 300-305, 2009.

- [77] B. Schedler, T. Huber, T. Friedrich, E. Eidenberger, M. Kapp, C. Scheu, R. Pippan and H. Clemens, "Characteristics of an optimized active metal cast joint between copper and C/C," *Physica Scripta*, vol. T128, pp. 200-203, 2007.
- [78] P. Appendino, M. Ferraris, V. Casalegno, M. Salvo and M. Merola, "Proposal for a new technique to join CFC composites to copper," *Journal of Nuclear Materials*, vol. 348, pp. 102-107, 2006.
- [79] E. Visca, S. Libera, A. Mancini, G. Mazzone, A. Pizzuto and C. Testani, "Hot radial pressing: an alternative technique for the manufacturing of plasma-facing components," *Fusion Engineering and Design*, Vols. 75-79, pp. 485-489, 2005.
- [80] M. Bisio, V. Branca, M. Di Marco, A. Federici, M. Grattarola, C. Gualco, P. Guarnone, U. Luconi, M. Merola, C. Ozzano, G. Pasquale, P. Poggi, S. Rizzo and F. Varone, "Manufacturing and testing in reactor relevant conditions of brazed plasma facing components of the ITER divertor," *Fusion Engineering and Design*, Vols. 75-79, pp. 277-283, 2005.
- [81] M. Salvo, V. Casalegno, S. Rizzo, F. Smeacetto, F. Ferraris and M. Merola, "One-step brazing process to join CFC composites to copper and copper alloy," *Journal of Nuclear Materials*, vol. 374, pp. 69-74, 2008.
- [82] K. Ezato, M. Dairaku, M. Taniguchi, K. Sato, S. Suzuki, M. Akiba, C. Ibbott and R. Tivey, "Development of ITER divertor vertical target with annular flow concept - II: development of brazing technique for CFC/CuCrZr joint and heating test of large-scale mock-up," *Fusion Science and Technology*, vol. 46, no. 4, pp. 530-540, 2004.
- [83] P. Appendino, M. Ferraris, V. Casalegno, M. Salvo, M. Merola and M. Grattarola, "Direct joining of CFC to copper," *Journal of Nuclear Materials*, Vols. 329-333, no. Part B, pp. 1563-1566, 2004.
- [84] V. Casalegno, T. Koppitz, G. Pintsuk, M. Salvo, S. Rizzo, S. Perero and M. Ferraris, "Proposal for a new brazing alloy for joining CFC composites to copper," *Composites Part B: Engineering*, 2013.
- [85] O. Abdel Gawad, M. H. Abou Tabl, Z. Abdel Hamid and S. F. Mostafa, "Electroplating of chromium and Cr-carbide coating for carbon fiber," *Surface and Coatings Technology*, vol. 201, no. 3-4, pp. 1357-1362, 2006.
- [50] S. Min, J. Blumm and A. Lindemann, "A new laser flash system for measurement of the thermophysical properties," *Thermochimica Acta*, vol. 455, no. 1-2, pp. 46-49, 2007.
- [86] R. D. Cowan, "Pulse Method of Measuring Thermal Diffusivity at High Temperatures," *J. Appl. Phys.*, vol. 34, no. 4, pp. 926-927, 1963.

- [51] W. J. Parker, R. J. Jenkins, C. P. Butler and G. L. Abbott, "Flash Method of Determining Thermal Diffusivity, Heat Capacity, and Thermal Conductivity," *J. Appl. Phys.*, vol. 32, no. 9, pp. 1679-1684, 1961.
- [87] R. Taylor, J. Jortner and H. Groot, "Thermal diffusivity of fiber-reinforced composites using the laser flash technique," *Carbon*, vol. 23, no. 2, pp. 215-222, 1985.
- [88] "MXIF," [Online]. Available: <http://www.mxif.manchester.ac.uk/>. [Accessed 25 July 2013].
- [89] V. Casalegno, M. Salvo, M. Ferraris, F. Smeacetto, M. Merola and M. Bettuzzi, "Non-destructive characterization of carbon fiber composite/Cu joints for nuclear fusion applications," *Fusion Engineering and Design*, vol. 83, no. 5-6, pp. 792-712, 2008.



# **CHAPTER FOUR: Thermal Finite Element Analysis on Massively Parallel Computing Platforms**

A paper submitted to the peer reviewed journal: Finite Elements in Analysis and Design

Presented in submitted form.

L.I.M. Evans, L. Margetts, L.M. Lever, W.E. Windes, P.M. Mummery



# Thermal Finite Element Analysis on Massively Parallel Computing Platforms

L.I.M. Evans<sup>a</sup>, L. Margetts<sup>b,\*</sup>, L.M. Lever<sup>c</sup>, W.E. Windes<sup>d</sup>, P.M. Mummery<sup>e</sup>

<sup>a</sup>*School of Materials, University of Manchester, Grosvenor Street, Manchester M1 7HS, UK*

<sup>b</sup>*School of Earth, Atmospheric and Environmental Sciences, University of Manchester, Williamson Building, Manchester M13 9PL, UK*

<sup>c</sup>*IT Services for Research, University of Manchester, Devonshire House, Oxford Road, Manchester M13 9PL, UK*

<sup>d</sup>*Idaho National Laboratory, 2351 N. Boulevard, Idaho Falls, ID 83415, United States*

<sup>e</sup>*School of Mechanical, Aerospace and Civil Engineering, University of Manchester, Manchester M13 9PL, UK*

---

## Abstract

Achieving improved accuracy in performance predictions of engineering designs can provide increased safety and financial savings. This is especially true of the atomic energy sector who work within generous safety limits. Image-based finite element modelling (IBFEM) has demonstrated accuracy gains by converting three-dimensional images (e.g. X-ray tomography data) into finite element analysis (FEA) meshes. This produces a high resolution simulation capable of describing complex geometries and including material micro-structures or manufacturing defects.

Such high resolution models typically require highly unstructured tetrahedral meshes in the order of hundreds of millions of elements. Due to the discretised nature of FEA, simulations are well suited for solving in parallel, however current commercial software packages have been shown to scale unfavourably with increasing core numbers. This work addresses the difficulties associated with such simulations by developing highly scalable parallel FEA code. This particular work concentrated on developing code for transient thermal analysis. To achieve full transparency, the code is open-source and freely available to allow peer review and encourage further development. Reliability was demonstrated through a series of validation tests where comparison of results with an analytical solution and a well-known commercial solver showed a high level of accuracy.

Solution time profiling was performed showing increased scalability with increasing element numbers. An example simulation using a mesh of 135 million elements was shown to complete in 1 hour 54 minutes using 4096 cores. Due to computational requirements this simulation was not possible on the commercial solver using a high-end workstation but was predicted to take 224 days. To demonstrate the code's feasibility and potential, an IBFEM case study of a nuclear grade composite was presented, consisting of 125 million elements at a resolution of 23  $\mu\text{m}$  and completing in 21 hours using 4096 cores.

*Keywords: finite element analysis, FEA, FEM, image-based, 3D imaging, thermal analysis, parallel computing, open source*

---

\* Corresponding author. Tel.: +44 161 275 6319;  
E-mail address: [lee.margetts@manchester.ac.uk](mailto:lee.margetts@manchester.ac.uk) (L. Margetts).

## 4.1 Introduction

Engineering in industries such as the nuclear sector works within generous safety limits to account for variation in components that cause their performance to deviate from that which is expected. As such, increased accuracy in modelling of components could provide significant financial savings through extended life cycles or a greater window of operational limits (e.g. maximum temperatures).

Since the promotion of Finite Element Analysis (FEA) in the 1960s, notably through work by Clough [90] and Zienkiewicz & Cheung [91], it is now the de-facto engineering tool. Standard engineering practice using computer aided design (CAD) drawn models rarely require the use of extremely large domains/meshes. However, a technique emerging from biomechanics [92] [93], called image-based finite element modelling (IBFEM), is gaining notoriety in engineering disciplines further afield [54]. This consists of converting a three-dimensional image (such as obtained from X-ray tomography) into a finite element mesh. By including the microstructures within the model this provides increased accuracy when dealing with complex geometries, such as composite materials [48]. To retain the geometrical information, resultant models typically consist of highly unstructured tetrahedral meshes with a very large number of elements (in the order of hundreds of millions). In addition to the ability to model complex geometries this microstructurally faithful method allows capture of manufacturing defects and experimental investigation of the modelled sample [94].

It can be argued that the major development in personal computing over the past decade has been the mainstream introduction of multi-core processing units which has enabled the utilisation of parallel codes. These codes ensure processing units work on more than one problem simultaneously or divide one problem between cores in a manner that was



previously restricted to specialised high-performance computing (HPC) facilities. The current projection is that future systems will further incorporate an increasing number of cores, emulating their ‘bigger-brother’ supercomputers.

A caveat of performance improvement depending on multi-core computing, rather than improved clock speed, is that code must be purposefully developed to exploit this new architecture. With much of the commercially available software predating the common use of multi-core computing, serial code adapted to work in parallel can often be seen to suffer from poor scaling with increasing number of cores [95] [96]. To obtain a higher degree of scalability this work builds upon a ‘ground-up’ approach to FEA in parallel, which has been shown to provide significant gains when dealing with large domains solved over a large number of cores [97].

This work addresses the difficulties associated with FEA of extremely large transient thermal models by developing a highly scalable parallel FEA code capable of dealing with the requirements of high-resolution image-based models. To gain accepted accredited status within the nuclear industry, the code must be shown to be reliable through validation testing. In describing their own software, Électricité de France (EDF) note

*“Because of the nuclear industry quality requirements, the software has been validated by independent companies. This validation entails comparing analytical and experimental results, and benchmarking...”* [98]

Firstly, the formation of the code and solution methods are detailed along with a summary of validation tests to be performed. The validation is achieved by comparison of results to an analytical solution. Results are then presented that investigate the relation between the accuracy of results given by the code to mesh density, temporal resolution and iterative

stopping criterion. These results are used to choose optimal operational parameters. The simulation of the analytical problem is then used to perform scalability profiling, detailing the amount of speed up achieved by solving in parallel over an increasing number of cores. Also feasibility of solving very large meshes using a large number of cores by use of this code is shown. Finally, a case study utilising image-based data from a real nuclear grade composite sample shows the code's improved capabilities over currently available commercial code. In order to achieve full transparency, this work uses freely available open source code that comes under the BSD 3-clause license, allowing peer review as well as encouraging others to further build upon this developmental work.

## 4.2 Theory and Methodology

Transient thermal FE analysis code was created using a pre-existing portable library of subroutines for parallel FEA called ParaFEM [99] which is an extension of the software developed by Smith, Griffiths and Margetts [66]. The subroutines, based on those developed by Margetts [100], are written in modern FORTRAN and use MPI [101] [102] for message passing.

The parallel program developed by the authors, solves the Heat Equation, which can be expressed as a first order ordinary differential equation (4.1)

$$c_p \rho \frac{\partial v}{\partial t} = K \left( \frac{\partial^2 v}{\partial x^2} + \frac{\partial^2 v}{\partial y^2} + \frac{\partial^2 v}{\partial z^2} \right) + q \quad (4.1)$$

where  $c_p$ ,  $\rho$ ,  $v$ ,  $t$ ,  $K$  &  $q$  are specific heat capacity, mass density, temperature, time, thermal conductivity and thermal flux respectively. Due to the discretisation introduced by FEA, (4.1) must be solved for each of the nodes within an element, thus a set of partial

differential equations are formed. The clearest way this can be shown is using the simplest problem of a 1D rod of length  $L$  represented by two nodes, the system of equations is as shown in (4.2).

$$-\int_0^L \begin{Bmatrix} N_1 \\ N_2 \end{Bmatrix} K \frac{\partial^2}{\partial x^2} [N_1 \quad N_2] dx \begin{Bmatrix} v_1 \\ v_2 \end{Bmatrix} + \int_0^L \begin{Bmatrix} N_1 \\ N_2 \end{Bmatrix} c_p \rho [N_1 \quad N_2] \frac{\partial}{\partial t} \begin{Bmatrix} v_1 \\ v_2 \end{Bmatrix} = \int_0^L \begin{Bmatrix} N_1 \\ N_2 \end{Bmatrix} q dx \quad (4.2)$$

By moving to 3D the complexity increases, but (4.2) can be rewritten as a ‘propagation problem’ in matrix notation (4.3), where  $[K]$  &  $[m_m]$  are the element conductivity and mass matrices,  $\{\Phi\}$  &  $\{q\}$  are the temperature and thermal loads, respectively.

$$[K]\{\Phi\} + [m_m] \left\{ \frac{d\Phi}{dt} \right\} = \{q\} \quad (4.3)$$

Traditionally, FEA software will form a global system of simultaneous equations to be solved by Gaussian elimination (or similar method) which are memory intensive. In order to reduce storage requirements, the system of equations are solved iteratively using a mesh-free element by element version of the conjugate gradient method. In addition to the solution only requiring simple matrix-vector multiplications, a major benefit of this implicit technique is its computational implementation can be easily parallelised as no global matrix is ever formed. To further accelerate iterative convergence a preconditioning scheme is used, which is initialised by specifying the residual,  $\{R\}$ , and the preconditioner,  $\{P\}$ , as (4.4) and the diagonal terms of (4.5) respectively.

$$\{\mathbf{R}\}_0 = \{\mathbf{q}\} - [\mathbf{K}]\{\Phi\}_0 \quad (4.4)$$

$$[\mathbf{m}_m] + \theta \Delta t [\mathbf{K}] \quad (4.5)$$

The following steps are then iterated until the residual is smaller than the specified convergence limit or a maximum number of iterations,  $i$ , is reached.

$$\{\mathbf{Q}\}_i = [\mathbf{K}]\{\Phi\}_i$$

$$\alpha_k = \frac{\{\mathbf{R}\}_i^T \{\mathbf{R}\}_i}{\{\mathbf{P}\}_i^T \{\mathbf{Q}\}_i}$$

$$\{\Phi\}_{i+1} = \{\Phi\}_i + \alpha_i \{\mathbf{P}\}_i$$

$$\{\mathbf{R}\}_{i+1} = \{\mathbf{R}\}_i - \alpha_i \{\Phi\}_i$$

$$\beta_i = \frac{\{\mathbf{R}\}_{i+1}^T \{\mathbf{R}\}_{i+1}}{\{\mathbf{R}\}_i^T \{\mathbf{R}\}_i}$$

$$\{\mathbf{P}\}_{i+1} = \{\mathbf{R}\}_{i+1} + \beta_i \{\mathbf{R}\}_i \quad (4.6)$$

where  $\{\mathbf{Q}\}$ ,  $\{\mathbf{P}\}$  and  $\{\mathbf{R}\}$  are vectors of equal length to the number of equations to be solved,  $\alpha$  and  $\beta$  are scalars.

Time stepping is achieved by linear interpolation using the ‘theta’ method. (4.3) at time-steps  $n$  and  $n+1$  can be connected using a weighted average of gradients (4.7). This system

is unconditionally stable for  $\theta \geq 0.5$ . This work uses the ‘Crank-Nicolson’ method where  $\theta = 0.5$ .

$$\begin{aligned}
 [K]\{\Phi\}_n + [m_m]\left\{\frac{d\Phi}{dt}\right\}_n &= \{q\}_n \\
 [K]\{\Phi\}_{n+1} + [m_m]\left\{\frac{d\Phi}{dt}\right\}_{n+1} &= \{q\}_{n+1} \\
 \{\Phi\}_{n+1} &= \{\Phi\}_n + \Delta t \left( (1 - \theta) \left\{\frac{d\Phi}{dt}\right\}_n + \theta \left\{\frac{d\Phi}{dt}\right\}_{n+1} \right)
 \end{aligned}
 \tag{4.7}$$

As previously mentioned, because no global assembly is ever formed the mesh can be freely divided into subdomains to be solved in parallel across the processors. This is analogous to having a collection of smaller FE models on each processor, with connecting regions providing boundary conditions for each other. Inter-processor communication, the barrier to scalability in parallel programs, is minimised by only being required for this boundary information. Further minimisation of inter-processor communication can be achieved by optimisation of boundary areas by careful selection of subdomain divisions [97] [103]. However, this work only uses a naïve division of total number of elements by number of processors, distributed by sequential element numbering order.

Validation of the parallel program developed by the authors was performed by constructing a problem whose results could be compared directly with an analytical solution. The problem chosen was a three-dimensional cuboid (confined by the domain  $-a < x < a$ ,  $-b < y < b$ ,  $-c < z < c$ ) with unit initial temperature and zero surface temperature, as shown in Figure 4.1. See Carslaw & Jaeger [104] for further details.

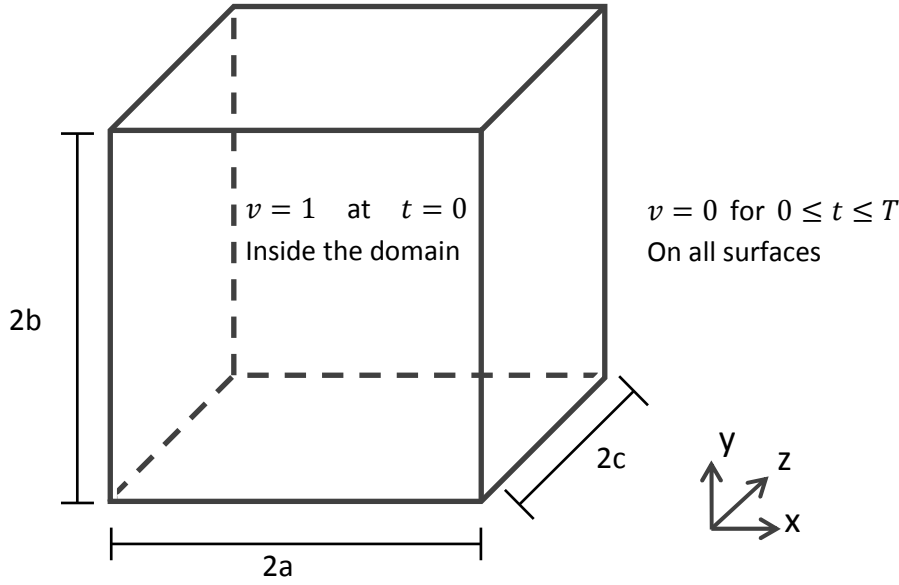


**Figure 4.1.** Analytical problem, a cuboid with unit initial temperature and zero surface temperature.

The analytical solution for the temperature,  $v$ , can be described by the triple Fourier series [104];

$$v = \psi(x, a)\psi(y, b)\psi(z, c)$$

$$v = \frac{64}{\pi^3} \sum_{l=0}^{\infty} \sum_{m=0}^{\infty} \sum_{n=0}^{\infty} \frac{(-1)^{l+m+n}}{(2l+1)(2m+1)(2n+1)} \cos \frac{(2l+1)\pi x}{2a} \cos \frac{(2m+1)\pi y}{2b} \cos \frac{(2n+1)\pi z}{2c} e^{-\alpha_{l,m,n}t} \quad (4.8)$$

where  $\alpha_{l,m,n} = \frac{\kappa\pi^2}{4} \left[ \frac{(2l+1)^2}{a^2} + \frac{(2m+1)^2}{b^2} + \frac{(2n+1)^2}{c^2} \right]$ , and the thermal diffusivity,  $\kappa$ , is defined by its relation to thermal conductivity, density, and specific heat capacity,  $\kappa = K/\rho c_p$ .

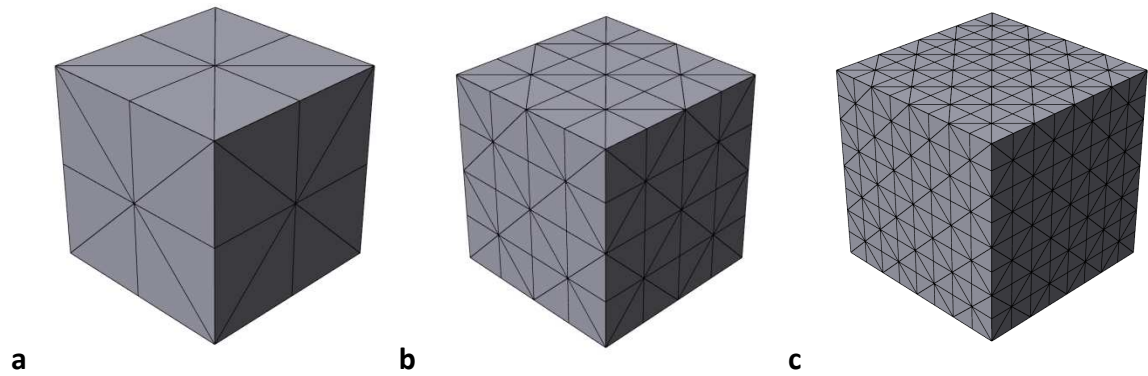
To represent the analytical problem in a FE form, a cuboid with dimensions  $a = b = c = 2$  was constructed. The main expected use of this program is image-based modelling which typically requires an unstructured mesh with large number of elements, therefore to best represent this use tetrahedral elements were chosen. The smallest number of tetrahedral elements a single cube can be divided into is five. In order to have a node at the centre of the cube it was firstly divided into eight smaller cubes then meshed with tetrahedral

elements i.e. 1 cube / 8 smaller cubes ( $2 \times 2 \times 2$ , 5 tetrahedra each) = 40 tetrahedra in total. This was the basis of the larger meshes, with each increase doubling the mesh density as shown in Figure 4.2. As a measure of a mesh's spatial resolution, it is convenient to report the average volume of one element as a percentage of the whole domain. This is recorded in Table 4.1 along with the element count for each mesh.

**Table 4.1**

Details of mesh densities used for simulation of analytical problem.

Mesh	4x	8x	16x	32x	64x	128x	256x
Element Count	320	2,560	20,480	163,840	1,310,720	10,485,760	83,886,080
Volume (%)	3.13E-1	3.91E-2	4.88E-3	6.10E-4	7.63E-5	9.54E-6	1.19E-6

**Figure 4.2.** Cubic volume of analytical domain meshed with increasing mesh density using (a)  $2 \times 2 \times 2$  Cube, 40 tets, (b)  $4 \times 4 \times 4$  Cube, 320 tets and (c)  $8 \times 8 \times 8$  Cube, 2560 tets.

The boundary conditions were such that the whole domain was given unit initial temperature and surfaces were fixed to zero for all subsequent time steps, with values being specified at the nodal locations. Material properties for oxygen free high conductivity copper (OHFC), as shown in Table 4.2, were used. Thermal conductivity and specific heat capacity values were obtained experimentally through laser flash analysis, density was calculated with the sample's volume and mass.

**Table 4.2**

Material properties used as input parameters.

Thermal Conductivity ( $\text{W}\cdot\text{m}^{-1}\text{K}^{-1}$ )	Density ( $\text{g}\cdot\text{cm}^{-3}$ )	Specific Heat Capacity ( $\text{J}\cdot\text{g}^{-1}\text{K}^{-1}$ )
408.16	8.6098	0.558

In order to save on computational expense, it is desirable to use solution parameters that provide an acceptable numerical accuracy whilst reducing the number of calculations. This is achieved by reducing the number of elements, number of time-steps and number of iterations required to converge. However, depending on the ‘sensitivity’ of the solution scheme, doing so can impact numerical accuracy. A series of validation runs were performed to investigate the effect on accuracy and solution time by varying the mesh density, time-step size, iterative solver stopping criterion and number of compute cores used. The parameters used for each set of validations tests can be found accompanying the relevant group of results. All simulations were conducted using program ‘xx12’ from revision 1445 of ParaFEM, accessible on the project hosting page [105]. These were performed on HECToR phase 3, the UK’s high-end computing resource. Each compute node consists of two 2.3 GHz 16-core AMD Interlagos chips and 32 Gb of RAM.

Additionally, the same analytical problem was constructed in a well-known commercial FEA software package for comparison. These simulations were performed using a powerful desktop based workstation comprising two 3.10 GHz 16 core Inter Xeon CPU E5-2687W processors with 192 Gb of available RAM.

The image-based model case study used a 2D woven Hi-Nicalon™ SiC fibre-reinforced SiC matrix composite fabricated by chemical vapour deposition (CVD) at Hypertherm High-Temperature Composites, Inc. To prepare the sample for laser flash analysis it was cut into a disc with diameter and thickness of 10.05 mm and 3.80 mm respectively, having a mass of 0.768 g. Its bulk density, i.e. including porosity, was  $2.548 \text{ g}\cdot\text{cm}^{-3}$ . Specific heat capacity and thermal conductivity were  $750 \text{ J}\cdot\text{kg}^{-1}\cdot\text{K}^{-1}$  and  $15.288 \text{ W}\cdot\text{m}^{-1}\cdot\text{K}^{-1}$  respectively.



An X-ray tomography scan of the sample was made with a Nikon Metrology 225/320 kV system (using the 225 kV source) at the Manchester X-ray Imaging Facility, University of Manchester, UK. The X-ray source voltage and current were set at 75 kV and 65  $\mu$ A, respectively. Each radiograph had an acquisition time of 4000 ms and the full tomography scan comprised a total of 3142 projections. The CT-Pro software (Nikon Metrology NV, Tring, Hertfordshire, UK) was used for tomography reconstruction using the level 3 and 2 setting for beam hardening correction and noise reduction respectively. The tomography data was segmented and meshed into tetrahedral elements using the Simpleware suite of programmes (Simpleware Ltd., Exeter, Devon, UK).

The model's boundary conditions were specified to simulate a laser flash analysis, which irradiates one surface of the sample with a thermal flux from the laser and measures the temperature change over time on the opposing surface. By measuring the half rise time it is possible to calculate the sample's thermal diffusivity. This was done by applying ramp loading to the nodes on the upper surface of the sample for a pulse duration of 0.64 ms. The simulation was performed over a time domain sufficiently large to allow the heat pulse to propagate through the sample.

### **4.3 Results**

Results are presented firstly on the validation of the code which performs transient thermal finite element analysis in parallel. These results are used to choose optimal operational parameters that achieve a balance between computational cost and solution accuracy. Then solution time profiling is reported, giving evidence of the code's scalability with increasing number of cores and the feasibility of using this code to solve extremely large problems, such as those associated with IBFEM. Finally an IBFEM case study is presented by using the code to analyse a real composite sample imaged by means of X-ray tomography.

### 4.3.1 Varying mesh density

In order to investigate the effect of mesh density on accuracy, the simulation of the analytical solution was performed on a range of meshes, detailed in Table 4.3, whilst keeping a high temporal resolution to minimise impact on results.

As expected for the inherently stable ‘Crank-Nicolson’ method, the FEA results oscillate around the analytical solution, seen in Figure 4.3 most prominently at  $t < 0.01$ . Where change in the analytical solution is greatest, the oscillation amplitude of the FEA results is at its largest but dampens quickly in regions of low change in analytical solution, seen here at  $t > 0.02$ . This effect is most clearly visible for the lower resolution models (4x & 8x) but rapidly diminishes as mesh density increases. Figure 4.4 shows a cross-sectional visualisation of the temperature distribution at  $t = 2.E-6$  s as calculated by ParaFEM. The 3D visualisation was created using ParaView, version 3.14.1 64-bit (Kitware Inc., Clifton Park, New York, USA) [69].

**Table 4.3**  
Solution method parameters (iterative solver stopping criterion of 1.E-8).

Mesh	Time-step size (s)	Number of steps	Total time (s)	Output frequency
4x	5.E-8	1000000	0.05	1000
8x	5.E-8	1000000	0.05	1000
16x	1.E-7	500000	0.05	100
32x	1.E-7	500000	0.05	2000
64x	5.E-6	10000	0.05	50

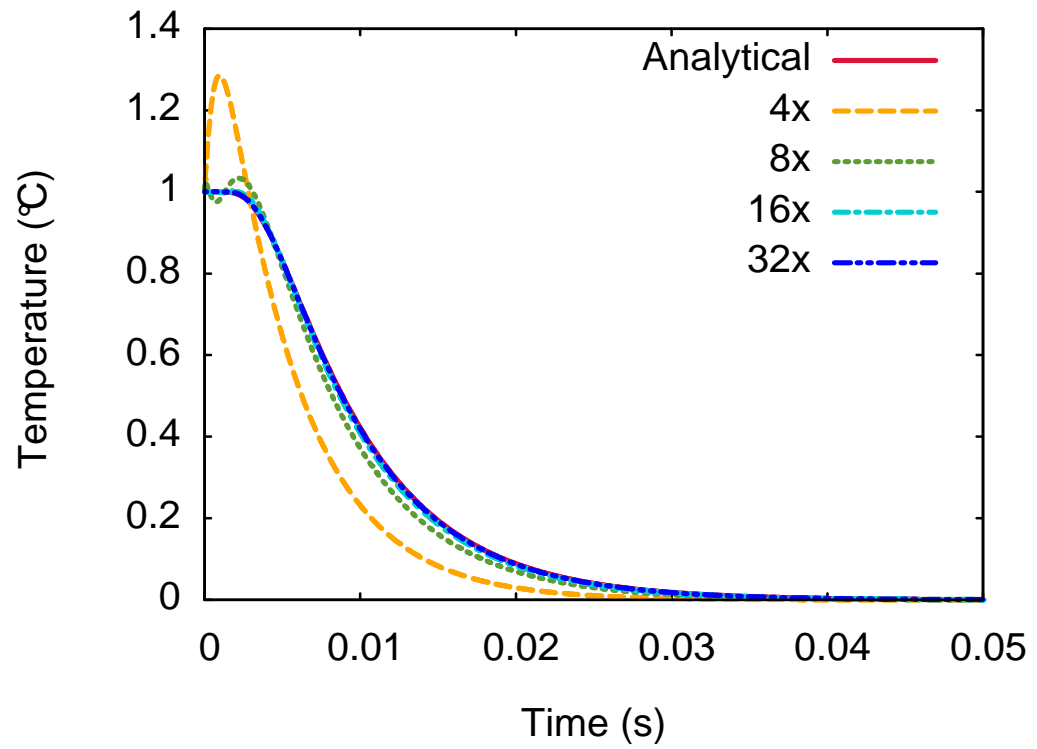


**Figure 4.3.** Temperature of the central node versus time for varying mesh densities.

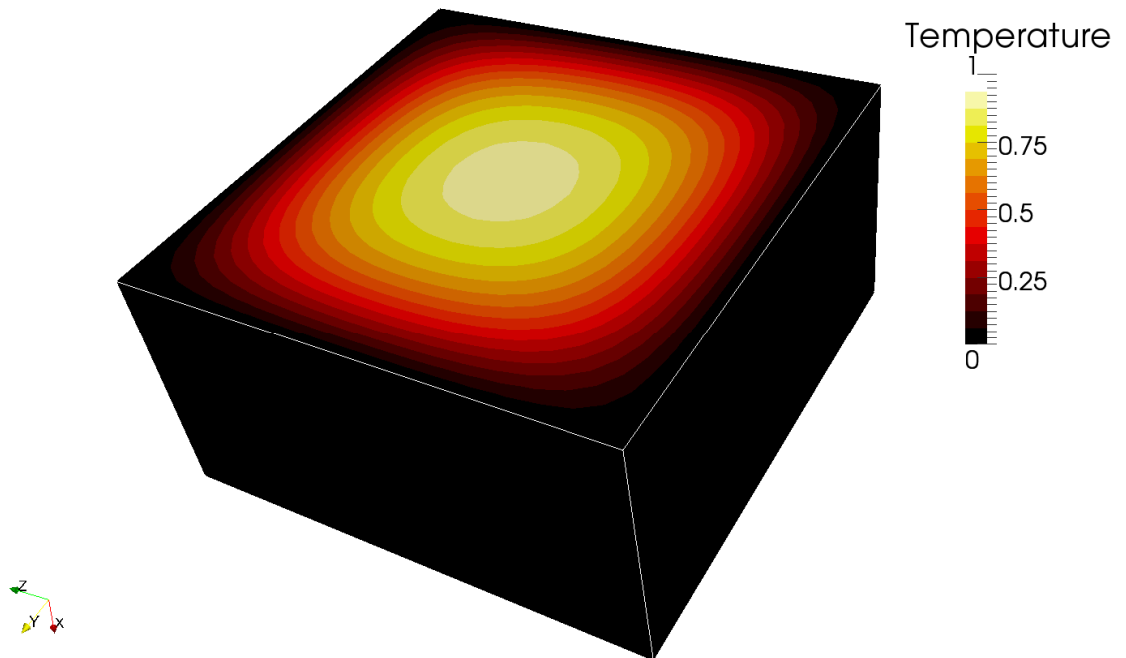


**Figure 4.4.** Simulation of an analytical thermal conductivity problem of a copper cube, 1 °C initial temperature, has boundary conditions of 0 °C on all external surfaces for  $t > 0$  s. Figure shows visualisation of the results as a cross-section of the temperature distribution at  $t = 2.E-6$  s, calculated by ParaFEM.

### 4.3.2 Varying temporal resolution

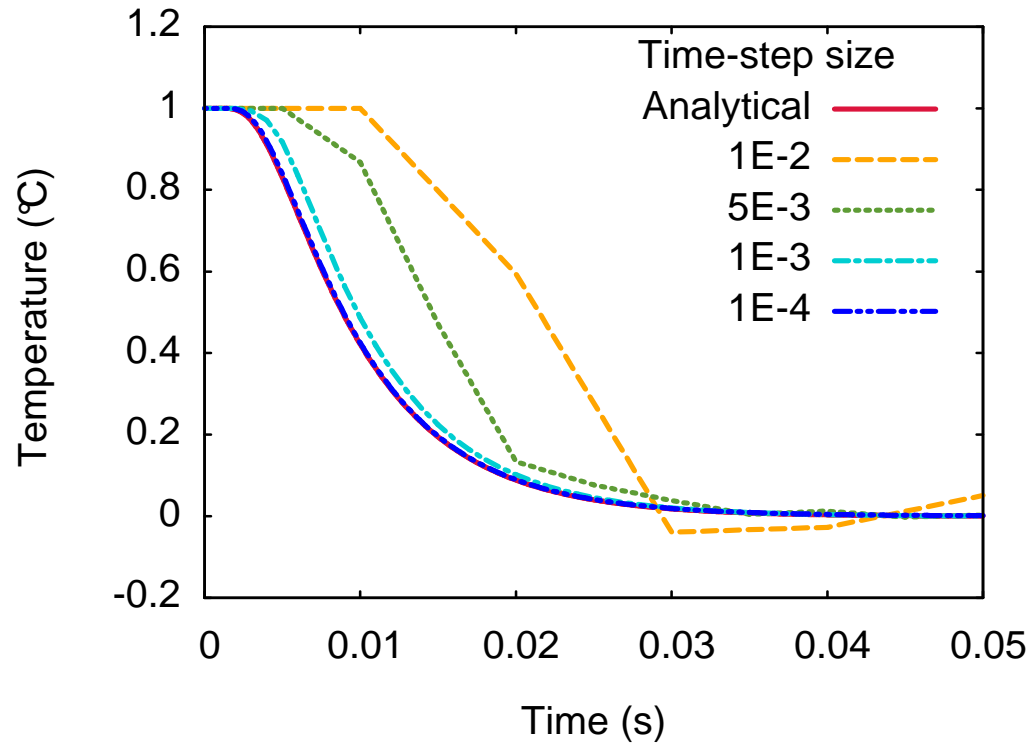
To remain microstructurally faithful to sample image data, the level of downsampling permissible is largely dictated by the smallest feature to be captured. Therefore, computational savings by reducing spatial resolution are limited. However, further savings can be made by increasing the time-step size, thus reducing the total number of steps required to complete the same time domain. In order to examine the effect of reducing temporal resolution the simulation of the analytical problem was performed on the 32x mesh with a sufficiently high iterative solver stopping criterion to minimize impact on results. In addition to accuracy of results, the change in time taken to complete the solution due to changing number of steps was recorded. These results are shown relative to the fastest solution i.e. the lowest temporal resolution, see Table 4.4.

Figure 4.5 shows an oscillation of FEA results around the analytical solution with a large error for low temporal resolution, similar to the effect of reducing spatial resolution. For this model this error becomes negligible for time-steps of less than 1.E-4. In decreasing the time-step size a larger number of time-steps are required to solve over same total time domain, therefore a larger number of calculations and in turn a greater solution time. It was found that decreasing the time-step size by an order of magnitude increased the solution time by approximately an equivalent amount, see Table 4.4.

**Table 4.4**

Solution method parameters (Mesh 32x, iterative solver stopping criterion of 1.E-8).

Time-step size (s)	Number of steps	Total time (s)	Output frequency	Relative solution time
1.E-2	5	0.05	1	1
5.E-3	10	0.05	1	1.6
1.E-3	50	0.05	1	4.8
1.E-4	500	0.05	2	12.0
<b>1.E-5</b>	<b>5000</b>	<b>0.05</b>	<b>20</b>	<b>80.7</b>
1.E-6	50000	0.05	200	854.8
1.E-7	500000	0.05	2000	10447.9



**Figure 4.5.** Temperature of the central node versus time for varying time-step sizes.

### 4.3.3 Varying the iterative solver stopping criterion

As a continued effort to find the optimal parameters that would obtain an accurate solution whilst minimising computational expense, the effect of varying the iterative solver stopping criterion was investigated by simulating the analytical solution whilst reducing the stopping criterion level. In addition to accuracy, the relative solution times compared to the fastest solution were recorded. Because the number of iterations required to converge decides the number of calculations, they were also noted.

Whilst using the optimum time-step of 1.E-5 s, as found in section 4.3.2, no discernible differences in results were observed by varying the stopping criterion. It was therefore decided to purposefully use the sub-optimal time-step value of 1.E-4 s to exaggerate the effect of changing stopping criterion levels. In doing so, even at the much higher 256x

mesh density, the solution did not converge with analytical values, emphasising the importance of selecting an appropriate time-step.

As shown in Figure 4.6, in reducing the stopping criterion, no significant improvement in accuracy could be detected below 1.E-4. However the number of iterations required continued to increase logarithmically thus impacting solution time, as shown in Table 4.5.

**Table 4.5**

Solution method parameters (Mesh 256x, time-step size = 1.E-4, number of steps = 50, output frequency = 1).

Stopping criterion	Number of iterations	Relative solution time
1.E-02	891	1
1.E-03	1417	1.5
1.E-04	1951	2.0
<b>1.E-05</b>	<b>2518</b>	<b>2.6</b>
1.E-06	3131	3.2
1.E-07	3790	3.8
1.E-08	4498	4.6

Combined observations made from the aforementioned validation tests were used to select the optimal solution parameters that would yield adequate accuracy whilst minimising solution time, thus providing a fair representation of a ‘real’ simulation. The time-step size and stopping criterion used were both 1.E-5. By measuring the difference between computed and analytical results, the error is calculated by taking this difference as a percentage of the analytical solution. Figure 4.7 shows the error for the 256x mesh is of the acceptable order 0.1%. All computations in the following section used those values for time-step size and stopping criterion.

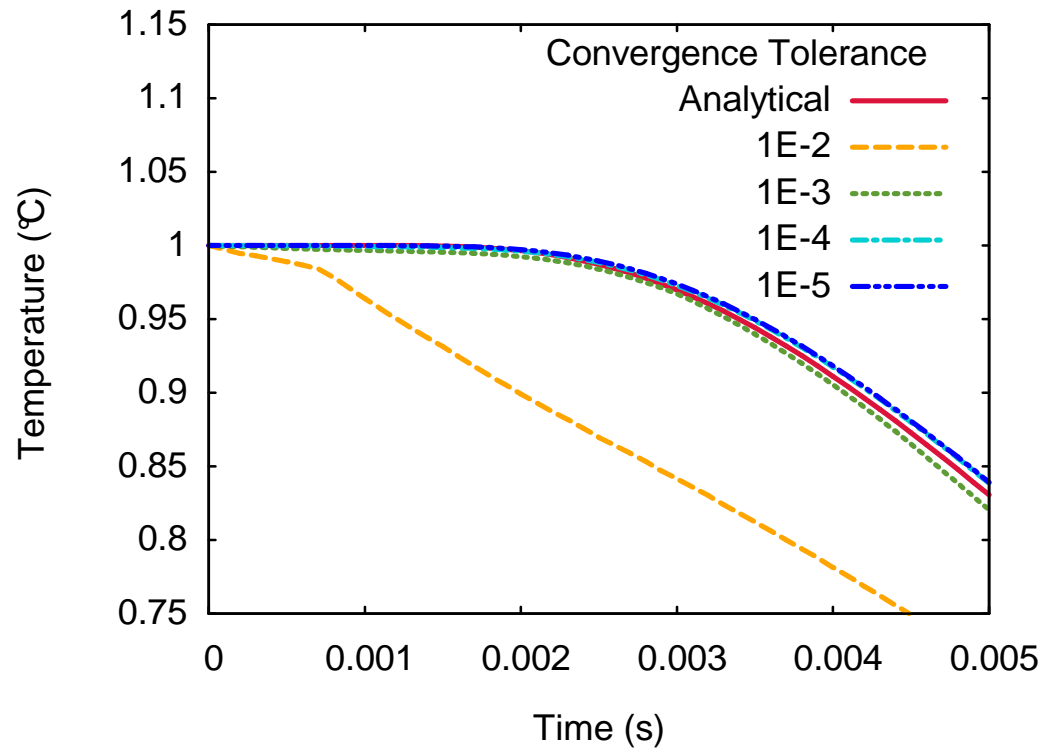


**Figure 4.6.** Temperature of the central node with respect to time for varying iterative solver stopping criterion.

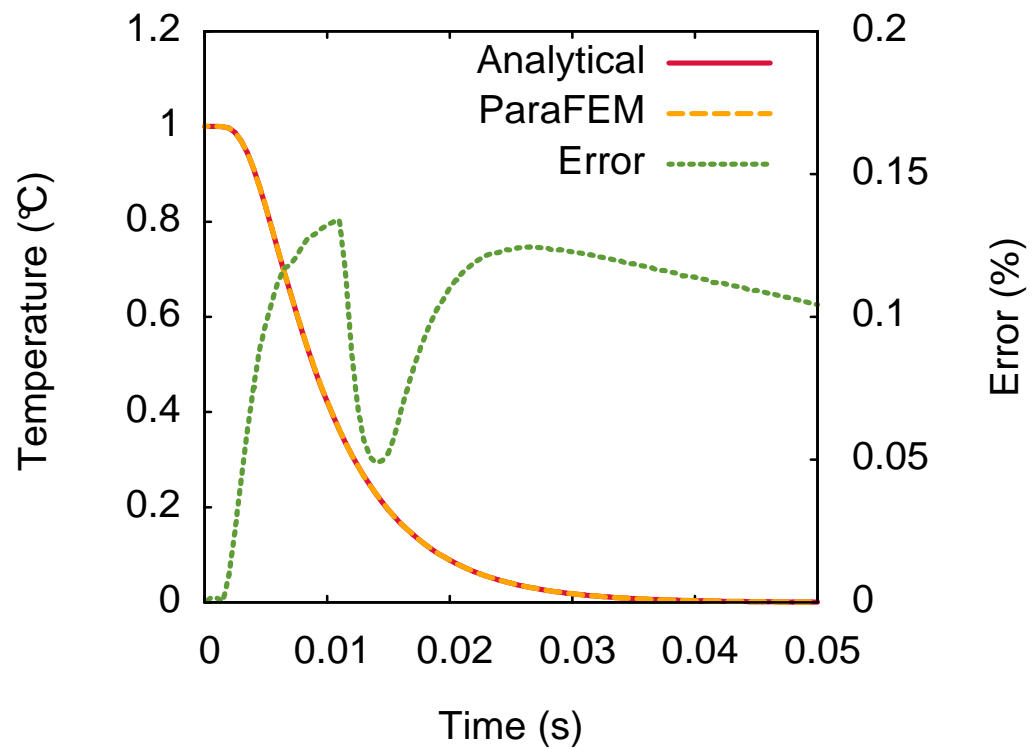


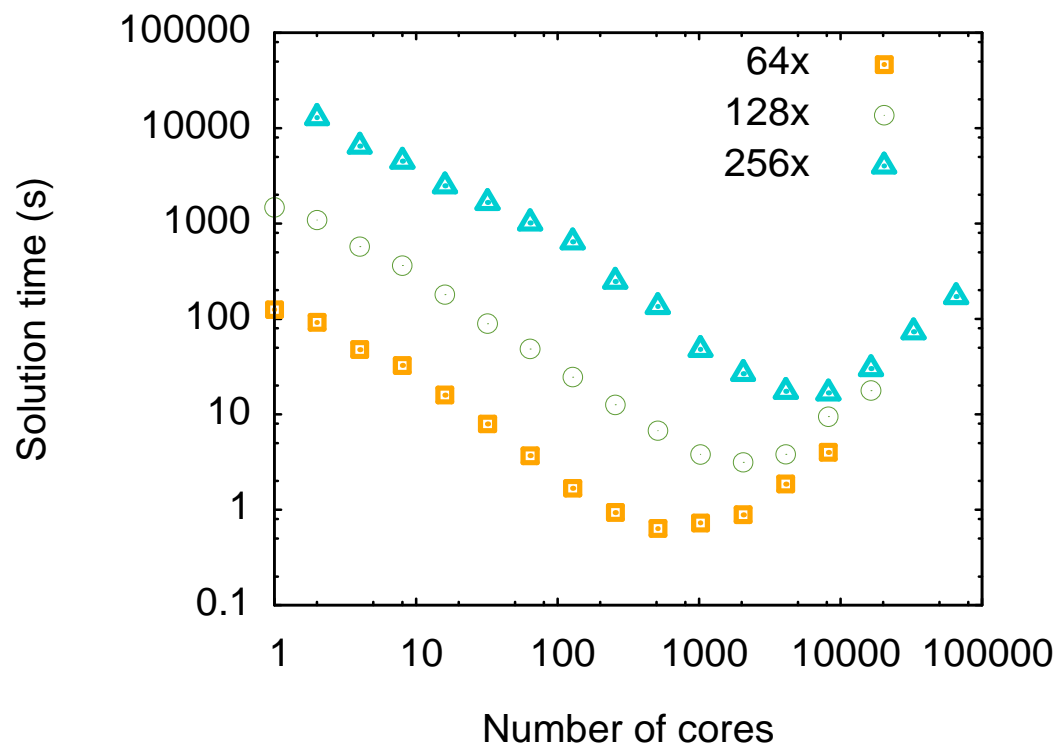
**Figure 4.7.** Error in calculating temperature of the central node with respect to time using optimal parameters.

#### **4.3.4 Solution time profiling & scalability with varying number of cores**

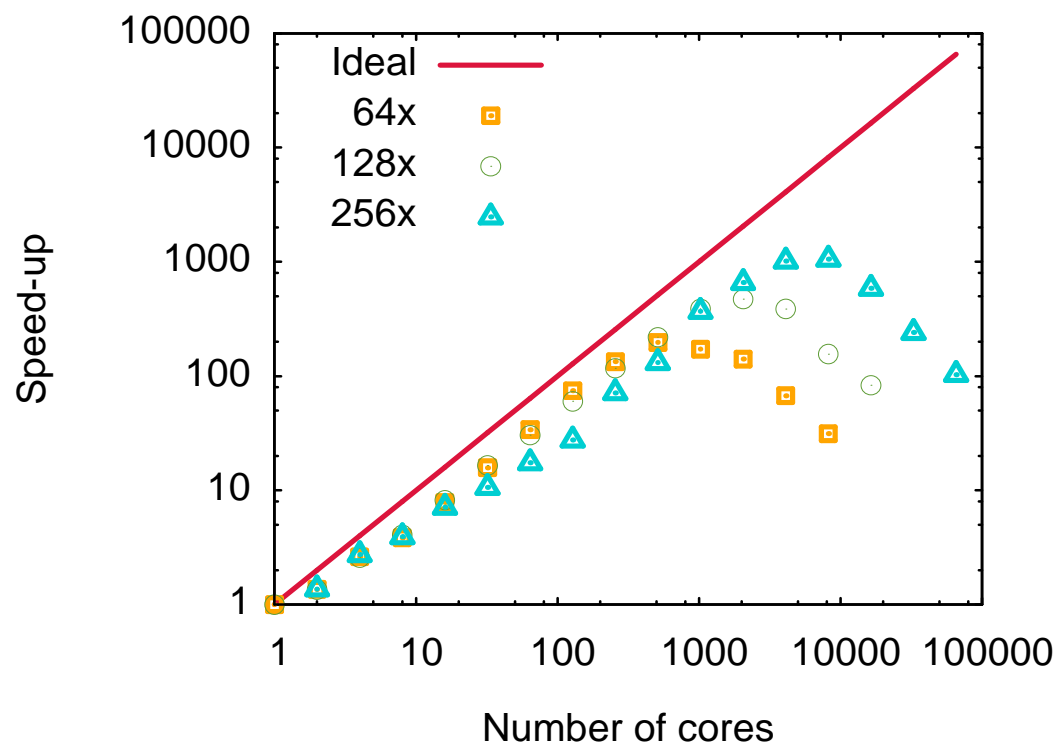
In order to profile the FEA program timing, aforementioned parameters were used to simulate the first 50 time-steps of the analytical solution, outputting results at each time step. This was performed with meshes 64x, 128x and 256x on a varying number of cores (1, 2, 4, 8, 16, 32, 64, 128, 256, 512, 1024, 2048, 4096, 8192, 16348, 32768, 65536) to investigate scaling performance.

Figure 4.8 shows the absolute solution times (excluding setup and output times) with increasing core numbers, whereas Figure 4.9 shows the speed-up gained by additional cores relative to running in serial. Ideally, when doubling the number of cores a speed-up of two should be observed. This curve is included for comparison with results. It can be seen in Figure 4.8 that solution times initially decrease by increasing cores until a critical value, after which they increase. Figure 4.9 reinforces this, by comparison to the ideal curve it can be seen that the code initially scales favourably. Additionally, it shows that as the number of elements in the mesh increase the critical point where solution times lose scalability also increases.





**Figure 4.8.** Scalability of absolute solution time for 50 time-steps and outputs of analytical problem (meshes 64x, 128x & 256x) with increasing numbers of cores.



**Figure 4.9.** Scalability of solution time (speed-up) for 50 time-steps and outputs of analytical problem (meshes 64x, 128x & 256x) with increasing numbers of cores.

Figure 4.10 compares total run times (including initialisation and output) of mesh 64x, containing 1.3 M elements, with an identical simulation performed in a commercial solver. It can be seen that the commercial solver offers no improvement in run time by using more than 8 cores. For the commercial solver, this was found to be the case regardless of mesh size. Additionally, using optimum settings ParaFEM completes in a total time two orders of magnitude faster than the commercial solver.

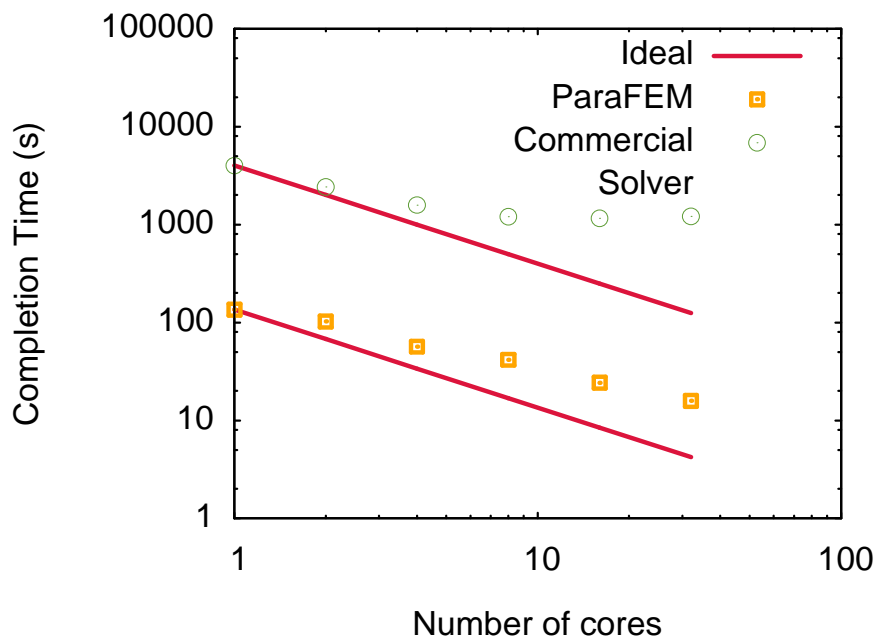


**Figure 4.10.** Comparison of ParaFEM and commercial solver scalability. Absolute solution time for 50 time-steps and outputs of analytical problem (mesh 64x) with increasing numbers of cores.

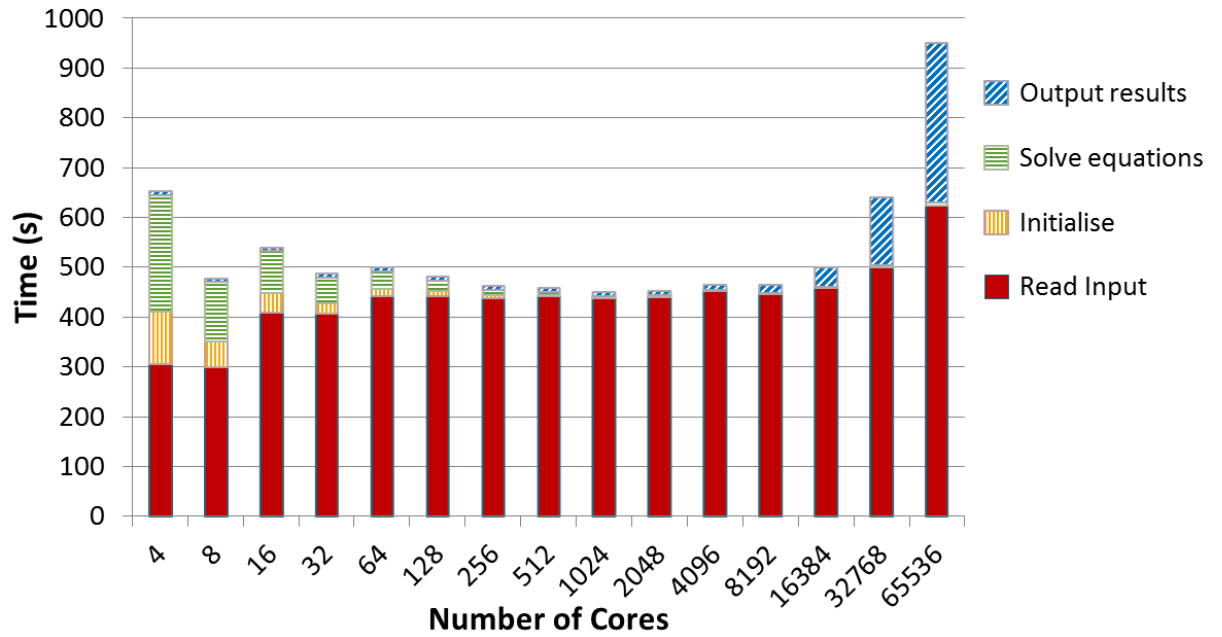


**Figure 4.11.** Computational cost profiling of each section required for the solver to initialise, complete and output one time step for a varying number of cores.

For the 300x mesh a timing breakdown of each section of the program was obtained, shown in Figure 4.11. This shows the correlation between decreasing solution time and increasing output time with increasing number of cores. It can also be seen that setup time (read and initialise) varies little with number of cores.

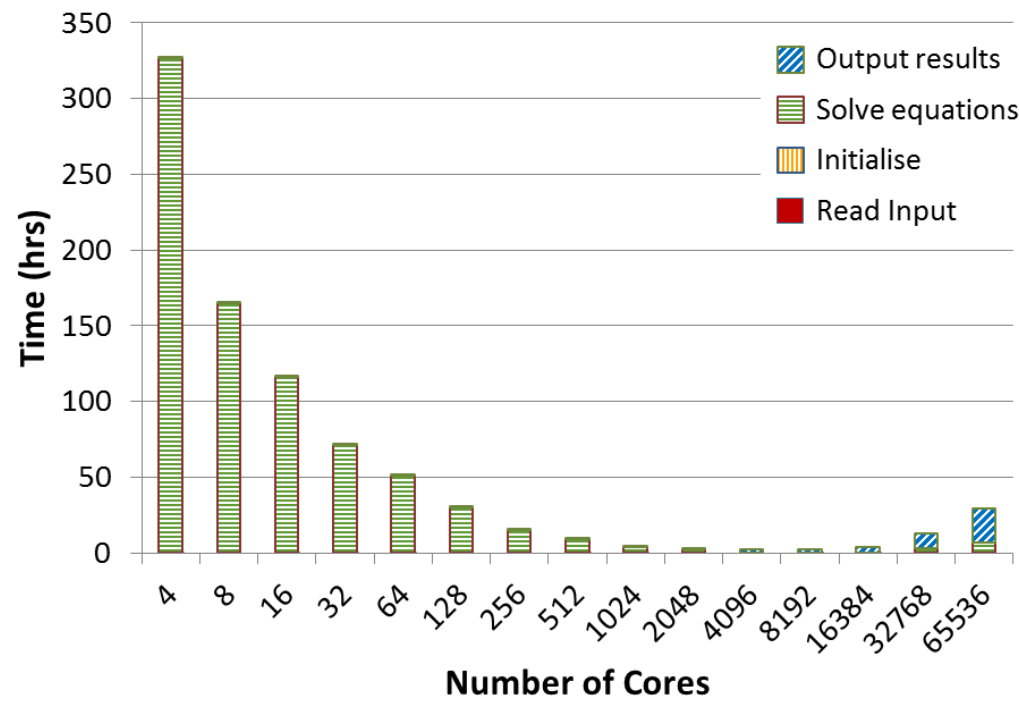


Figure 4.12. Computational cost profiling of a complete analysis of the analytical problem for varying number of cores.

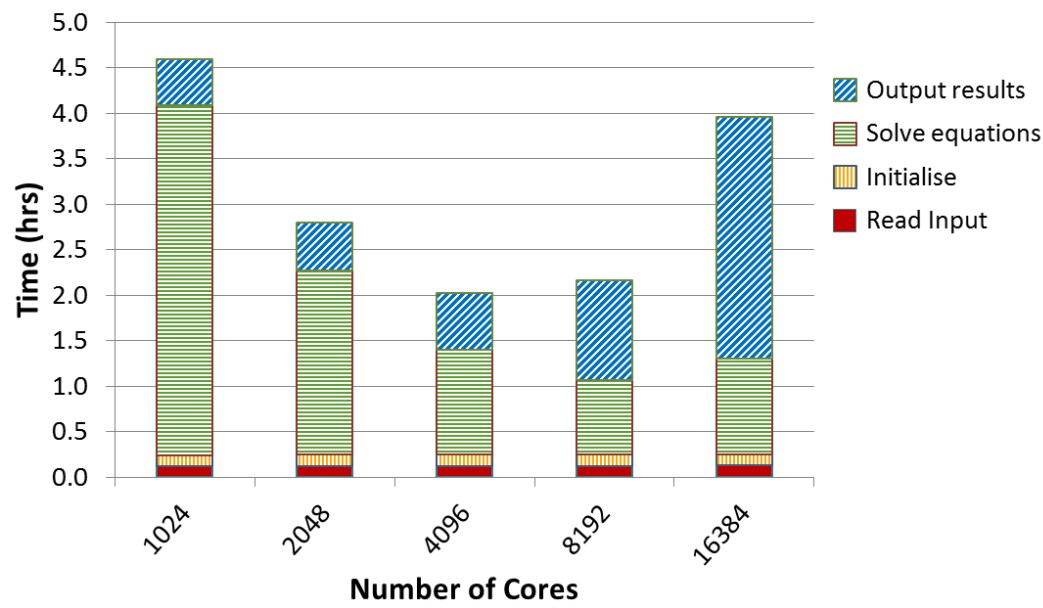


Figure 4.13. Computational cost profiling of a complete analysis of the analytical problem for optimal number of cores.

By taking the setup, solution and output times per from Figure 4.11 estimates were calculated for a complete ‘real’ simulation. This was based on the parameters implemented to produce Figure 4.7 i.e. a time-step size of 1.E-5 s would require 5000 time steps to solve

0.05 s and an output frequency of 20 steps would provide sufficient data. These calculated results are shown in Figure 4.12, which clearly demonstrates the benefit of utilising solution methods capable of exploiting a parallel computing environment. For such a large mesh (135 M elements) it was not possible to solve in serial, however the use of optimal settings offered a reduction from over 325 hrs on four cores to 2 hrs on 4096 cores. Figure 4.13 provides additional insight by concentrating on the number of cores providing best performance, more clearly showing the distribution of where time is spent in the program.

**Table 4.6**

Based on 5000 time steps, output every 20.

Mesh	Number of Elements	Commercial Solver		ParaFEM	
		Cores	Solution time	Cores	Solution time
32x	163,840	8	3 hrs	128	21 secs
64x	1,310,720	8	1 day 6 hrs	512	1 min 45 secs
128x	10,485,760	8	12 days 20 hrs	2048	12 mins
256x	83,886,080	Estimate	132 days	4096	1 hr
<b>300x</b>	<b>135,000,000</b>	<b>Estimate</b>	<b>224 days</b>	<b>4096</b>	<b>1 hrs 54 mins</b>

When comparing completion times with that of the commercial solver, the advantages become even more pronounced. Using the commercial solver it was not possible to run any meshes with an element count greater than approximately 20 M elements, ParaFEM was used on 135 M elements. Using the observed trends for commercial solver solution time with meshes 32x, 64x & 128x, projections were made for completion times with meshes 256x and 300x, shown in Table 4.6. By comparison with ParaFEM, not only are completion times vastly improved, but ParaFEM's capability of solving extremely large problems allow new avenues of research to be pursued, such as IBFEM at microstructurally faithful resolutions.

#### 4.3.5 Image-based modelling case study

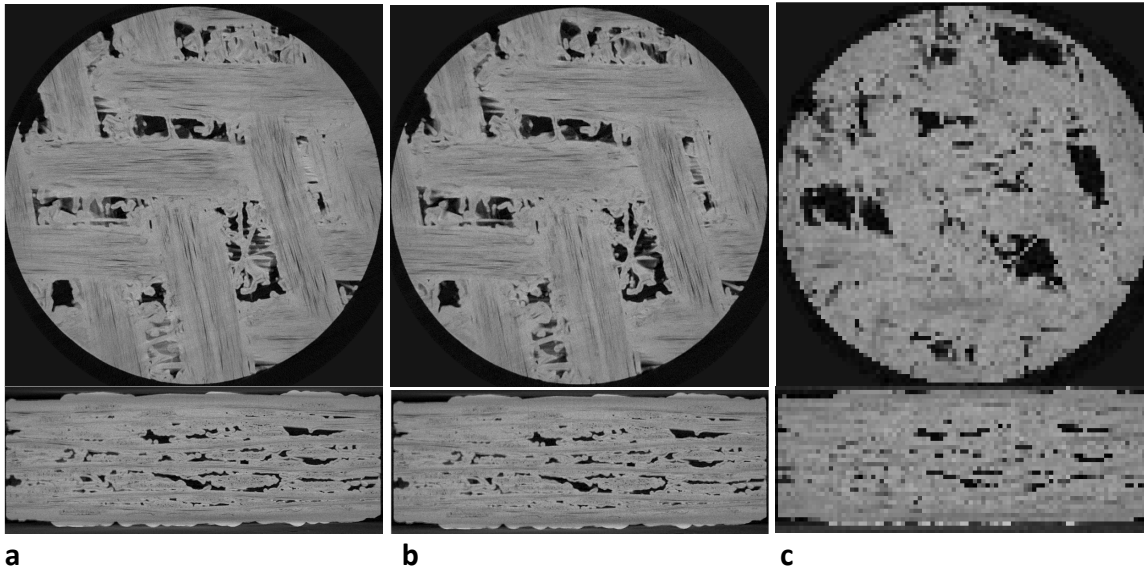


**Figure 4.14.** Tomography slices of SiC<sub>p</sub>/SiC sample in top-down and cross-section views; (a) 100 %, (b) 25 % and (c) 5 % resolutions.

In order to perform the IBFEM simulation of a laboratory laser flash analysis using the commercial solver within a reasonable timeframe, it was required to downsample the data to 5% of its original resolution (approximately 1 M elements). As shown in Figure 4.14, this is a clearly inadequate resolution which only retains the largest microstructural features. Through visual investigation it was decided that for this sample a resolution of 25% would provide enough detail to sufficiently capture the majority of the complex microstructures. This resulted in a mesh of 125 M elements, seen in Figure 4.15, which could be solved using ParaFEM's efficient management of distributing computational load in a highly parallel environment.

The commercial solver took 12 hrs to complete the 5 % model with adaptive time stepping using 8 cores. ParaFEM used 12,000 time steps with a time size and iterative stopping criterion of  $1.6 \times 10^{-5}$  s and  $1 \times 10^{-5}$  respectively, the 25 % model completed in 21 hrs using 4096 cores.

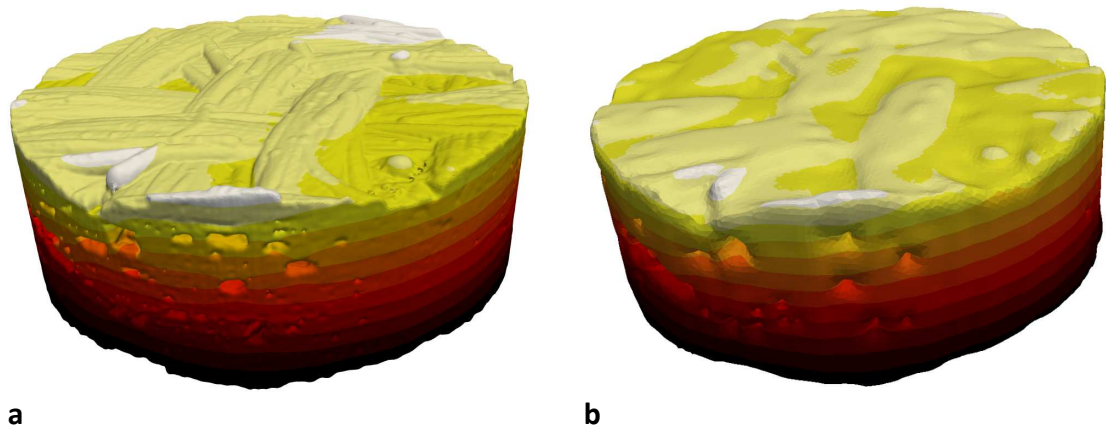


**Figure 4.15.** 3D reconstruction from X-ray tomography data of SiC<sub>p</sub>/SiC composite sample, (a) 25% resolution (b) 5% resolution.

#### 4.4 Discussion

In validating the code against an analytical solution, several observations regarding its operation came to light. Firstly, the test on spatial resolution clearly shows that results follow the analytical solution more closely as mesh density increases. It was decided that the 32x mesh provided adequate accuracy, although containing a relatively high number of elements (160k) when compared to traditional CAD modelling. Figure 4.16 compares the results between ParaFEM and the commercial solver using the exact same 32x mesh and input parameters. Even at this apparent ‘high’ resolution for an idealised simulation, it can be seen that the commercial solver includes a non-negligible error in its result not observed in ParaFEM’s results. Therefore it can be concluded that ParaFEM can offer sufficiently accurate results acceptable for use by industry if an appropriate selection of parameters is made.

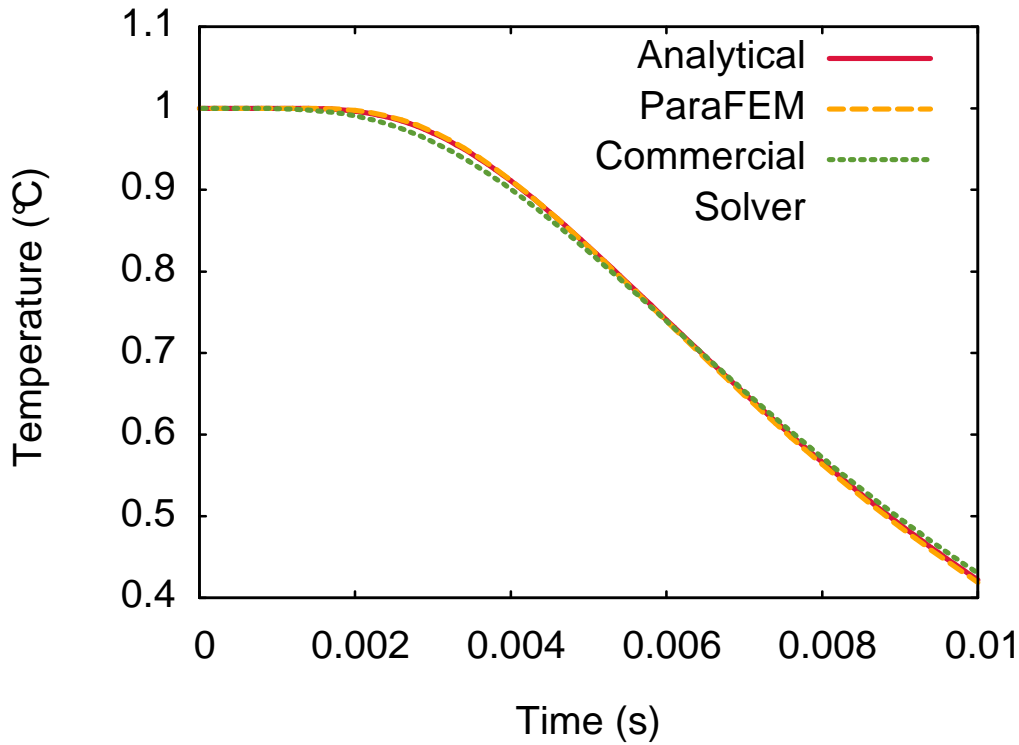


**Figure 4.16.** Comparison of results from ParaFEM and a commercial solver using identical input parameters to solve the Carslaw & Jaeger analytical problem [104] described in Figure 4.1.

Secondly, it was shown that setting the values for temporal resolution too low or iterative stopping criterion too high reduces accuracy but increases computational savings. Optimal values were found in this instance, but these would be problem specific and would change dependent on mesh density and material properties. The prescribed material properties relate to its thermal diffusivity, which can be seen as a kind of thermal ‘inertia’. This specifies how quickly heat can travel through the medium; therefore to accurately characterise a material with higher thermal diffusivity would require increasing temporal resolution. Adaptive time-stepping schemes can be used to provide computational savings [106], and it would be feasible to employ a similar method to control the stopping criterion, however the solver is naïve and these aren’t implemented here. Nevertheless, implementing smarter algorithms would be to the detriment of scalability due to increased inter-core communications. Although this could provide a more efficient technique for



solving smaller models, it would be restrictive at running very large models. This is the problem which affects current commercial solvers, and needs to be avoided to successfully maximise the potential of IBFEM.

After validation of the code accuracy, the solution time and scalability were profiled. It was shown that although initial scaling was favourable, a critical point was reached after which solution time increased. This can be attributed to the previously mentioned subdomain divisions; as the number of mesh elements per core decreases the computational effort per core also decreases but the number of inter-core communications increase. The scaling curves in Figure 4.9 demonstrate that for problems of increasing size the scalability will improve. An additional observation is that, at low numbers of cores, divergence from the ‘ideal’ scaling can be seen as discontinuous steps. It is probable that this is related to the processor architecture and the use of under populated nodes, where multiple processors use fewer cores than the maximum available. As each node has 32 Gb of RAM, in order to fit large problems in memory this can be implemented to exploit additional RAM resources but increases inter-core communication time.

The profiling of a complete simulation, shown in Figure 4.12 & Figure 4.13, show that for low numbers of cores the majority of the program time is spent in solving the equations, which is why this section of the code was prioritised for parallelisation. The additional insight provided by Figure 4.13 shows that future optimisation effort could be concentrated on parallelising output of results, currently in serial. Initially only a small proportion of the program time, as the solution time reduces its effect becomes more prominent amounting to 54% of the total time on 8192 cores.

As previously mentioned, the main aim of the program was not to achieve the greatest efficiency possible but to enable the running of very large meshes which would otherwise not be useable. This was to be performed within a reasonable timeframe in a verifiable open source framework, the purpose of this being to allow the use of IBFEM. Table 4.6 shows that the commercial solver was capable of solving meshes no larger than tens of millions of elements within a timeframe of a few weeks. The new ParaFEM code can solve problems containing hundreds of millions of elements in a few hours.

Reinforcing this statement, with ParaFEM it was possible to use the IBFEM case study of a real sample to perform a simulation of a laboratory experiment at a sufficiently high resolution that captured the majority of microstructural features. To complete in a similar time frame, the commercial solver required the data to be downsampled to a level of 5 %, and could not perform simulations with resolutions higher than approximately 12.5 %. The IBFEM model was not at the limit of what ParaFEM could achieve; modelling the analytical problem with a mesh of over a billion elements was also successfully performed.

#### **4.5 Conclusions**

An open source transient thermal FE analysis code was created using a pre-existing portable library of subroutines for parallel FEA called ParaFEM. Validation was performed and it was shown to provide accurate results when simulating the analytical problem of a three-dimensional cuboid with unit initial temperature and zero surface temperature. Solution time profiling showed that the program benefited from high scalability which increased with problem size, thus enabling solving problems many orders of magnitude greater than traditionally handled by commercial solvers in a reasonable time-frame. This was tested with meshes containing up to 135 million tetrahedral elements on 4096 cores, which would complete a simulation of an analytical problem in 1 hrs 54 mins. An

image-based modelling case study was presented as a potential use for the code. Further optimisation avenues identified were to parallelise outputting of results.

### Acknowledgements

The support of the Engineering and Physical Sciences Research Council for the Fusion Doctoral Training Network (Grant EP/K504178/1) and Culham Centre for Fusion Energy (CCFE) is gratefully acknowledged. This work made use of the facilities of HECToR (Project e254), the UK's national high-performance computing service, which is provided by UoE HPCx Ltd at the University of Edinburgh, Cray Inc and NAG Ltd, and funded by the Office of Science and Technology through EPSRC's High End Computing Programme. This work also made use of the facilities of N8 HPC provided and funded by the N8 consortium and EPSRC (Grant No.EP/K000225/1). The Centre is co-ordinated by the Universities of Leeds and Manchester. Additionally, the authors would like to thank Idaho National Labs for providing the sample material, the Manchester X ray Imaging Facility for use of tomography equipment, which was funded in part by the EPSRC (grants EP/F007906/1, EP/F001452/1 and EP/I02249X/1) and the staff at the University of Manchester for guidance in preparing this work.

### References

- [90] R. W. Clough, "The Finite Element Analysis in Plane Stress Analysis," in *Proc 2nd ASCE Conf. on Electronic Computation*, Pittsburgh, PA, 1960.
- [91] O. C. Zienkiewicz and K. Cheung, "Finite elements in the solution of field problems," *Engineer*, vol. 200, pp. 507-510, 1965.
- [92] H. J. Kim, I. E. Vignon-Clementel, C. A. Figueroa, K. E. Jansen and C. A. Taylor, "Developing computational methods for three-dimensional finite element simulations of coronary blood flow," *Finite Elements in Analysis and Design*, vol. 46, pp. 514-525, 2010.
- [93] R. Hambli, "Numerical procedure for multiscale bone adaptation prediction based on neural networks and finite element simulation," *Finite Elements in Analysis and*

*Design*, vol. 47, pp. 835-842, 2011.

- [54] C. Berre, S. Fok, B. Marsden, L. Babout, A. Hodgkins, T. Marrow and P. Mummery, "Numerical modelling of the effects of porosity changes on the mechanical properties of nuclear graphite," *Journal of Nuclear Materials*, vol. 352, no. 1-3, pp. 1-5, 2006.
- [48] J. Ali, C. Berre and P. M. Mummery, "Image based modelling of stress-strain behaviour in carbon/carbon composites," *Energy Materials: Materials Science and Engineering for Energy Systems*, vol. 1, no. 3, pp. 179-186, 2006.
- [94] P. Young, T. Beresford-West, S. Coward, B. Notarberardino, B. Walker and A. Abdul-Aziz, "An efficient approach to converting three-dimensional image data into highly accurate computational models," *Philosophical Transactions of The Royal Society A*, vol. 366, no. 1878, pp. 3155-3173, 2008.
- [95] S. Shaw and M. Dunbar, "Abaqus FEA Software on Multi-Core HP Servers," Hewlett-Packard Development Company, Richardson, TX, USA, 2007.
- [96] J. H. Kim, C. S. Lee and S. J. Kim, "Development of a high-performance domain-wise parallel direct solver for large-scale structural analysis," in *Proceedings of the Seventh International Conference on High Performance Computing and Grid*, Asia Pacific Region, 2004.
- [97] O. Goury, "Analysis and Optimisation of a parallel finite element code," MSc Dissertation, The University of Edinburgh, UK, 2010.
- [98] "Code\_aster - Software - EDF R&D," [Online]. Available: <http://research.edf.com/research-and-the-scientific-community/software/code-aster-44332.html>. [Accessed 15 July 2013].
- [99] "ParaFEM," [Online]. Available: <http://www.parafem.org.uk>. [Accessed 15 July 2013].
- [66] I. M. Smith, D. V. Griffiths and L. Margetts, *Programming the Finite Element Method* 5th Ed., Chichester: Wiley, 2013.
- [100] L. Margetts, *Parallel Finite Element Analysis*, PhD Thesis, University of Manchester, UK, 2002.
- [101] W. Gropp, E. Lusk and A. Skjellum, *Using MPI*, 2nd Edition: Portable Parallel Programming with the Message Passing Interface, Cambridge, MA, USA: MIT Press Scientific And Engineering Computation Series, 1999.
- [102] M. Snir, S. Otto, S. Huss-Lederman, D. Walker and J. Dongarra, *MPI: The Complete Reference*, Cambridge, MA, USA: MIT Press, 1995.
- [103] P. Kerfriden, O. Goury, T. Rabczuk and S. P. A. Bordas, "A partitioned model order reduction approach to rationalise computational expenses in nonlinear fracture

- mechanics,” *Computer Methods in Applied Mechanics and Engineering*, vol. 256, no. 1, pp. 169-188, 2013.
- [104] H. S. Carslaw and J. C. Jaeger, “VI. The flow of heat in a rectangular parallelepiped,” in *Conduction of Heat in Solids*, Oxford, Clarendon Press, 1959, pp. 184-185.
- [105] “xx12.f90 - parafem,” [Online]. Available:  
<http://code.google.com/p/parafem/source/browse/trunk/parafem/src/programs/dev/xx12/xx12.f90?r=1445>. [Accessed 15 July 2013].
- [69] “ParaView - Open Source Scientific Visualization,” [Online]. Available:  
<http://www.paraview.org/>. [Accessed 15 July 2013].
- [106] G. Söderlind and L. Wang, “Adaptive Time-Stepping and Computational Stability,” *Journal of Computational Methods in Sciences and Engineering*, vol. 2, no. 3, pp. 1-3, 2003.



# **CHAPTER FIVE: Transient Thermal Finite Element Analysis of CFC-Cu ITER Monoblock from X-ray Tomography Data**

A paper submitted to the peer reviewed journal: Journal of Nuclear Materials

Presented in submitted form.

Ll.M. Evans, L. Margetts, V. Casalegno, M. Ferraris, L.M. Lever, J. Bushell, T. Lowe,  
A. Wallwork, P. Young, A. Lindemann, M. Schmidt, P.M. Mummery





# Transient Thermal Finite Element Analysis of CFC-Cu ITER Monoblock Using X-ray Tomography Data

Ll.M. Evans<sup>a,\*</sup>, L. Margetts<sup>b</sup>, V. Casalegno<sup>c</sup>, M. Ferraris<sup>c</sup>, L. Lever<sup>d</sup>,  
J. Bushell<sup>a</sup>, T. Lowe<sup>a</sup>, A. Wallwork<sup>a</sup>, P. Young<sup>e</sup>, A. Lindemann<sup>f</sup>, M. Schmidt<sup>g</sup>,  
P.M. Mummery<sup>g</sup>

<sup>a</sup>*School of Materials, University of Manchester, Grosvenor Street, Manchester M1 7HS, UK*

<sup>b</sup>*School of Earth, Atmospheric and Environmental Sciences, University of Manchester, Williamson Building, Manchester M13 9PL, UK*

<sup>c</sup>*Department of Applied Science and Technology, Politecnico di Torino, Corso Duca degli Abruzzi 24, I-10129 Torino, Italy*

<sup>d</sup>*IT Services for Research, University of Manchester, Devonshire House, Oxford Road, Manchester M13 9PL, UK*

<sup>e</sup>*Simpleware Ltd., Bradninch Hall, Castle Street, Exeter, EX4 3PL, UK*

<sup>f</sup>*NETZSCH-Gerätebau GmbH · Wittelsbacherstraße 42 · D-95100 Selb/Bayern, Germany*

<sup>g</sup>*School of Mechanical, Aerospace and Civil Engineering, University of Manchester, Manchester M13 9PL, UK*

---

## Abstract

The divertor in a fusion reactor is a key component designed to extract heat. Its location at the intersection of magnetic field lines means it is the component that will be subjected to the largest amount of thermal flux from the plasma. Therefore, characterisation of its thermal performance is imperative. This work investigates the CFC-Cu monoblock, a divertor component, which consists of a carbon fibre composite (CFC) tile joined through its centre to a CuCrZr pipe with a Cu interlayer for active cooling. Predictions about the monoblock's in-service performance were made using finite element analysis (FEA).

A high-accuracy simulation was created using an emerging technique, image-based finite element modelling (IBFEM). By converting X-ray tomography data of a real specimen into an FEA mesh, it included non-idealised features introduced in manufacturing. To validate the IBFEM technique a case study was performed where the thermal analysis by laser flash of a CFC-Cu disc was simulated such that computational and experimental results could be compared directly. Results from the case study showed that a high resolution IBFEM simulation (102 million elements of 32  $\mu\text{m}$  width) provided increased accuracy over low resolution IBFEM (0.6 million elements of 194  $\mu\text{m}$  width) and idealised computer aided design (CAD) simulations. Using the IBFEM technique to analyse a monoblock mock-up, it was possible to detect and quantify the effects of delamination regions at the CFC-Cu interface likely to impact both component performance and expected lifetime. These features would not have been accounted for in idealised CAD simulations.

*Keywords: thermal analysis, laser flash, fusion, tokamak, divertor, ITER, finite element analysis, FEA, CT, X-ray tomography, carbon fibre composites, CFC, high performance computing, HPC, parallel computation, supercomputer, open source*

---

\* Corresponding author. Tel.: +44 1235 466524;

E-mail address: [llion.evans@postgrad.manchester.ac.uk](mailto:llion.evans@postgrad.manchester.ac.uk) (Ll.M. Evans).

## 5.1 Introduction

ITER, currently under construction, will be the world's largest nuclear fusion reactor. Its aim is to demonstrate the ability to produce an output power ten times that required to initiate fusion. Once operational, the plasma in which the reactions happen will subject the plasma facing components (PFCs) to  $10 \text{ MW}\cdot\text{m}^{-2}$  of thermal flux during steady-state operation. This value could be surpassed if plasma disruptions which release large amounts of energy over short time periods are not mitigated [73]. Therefore selection of materials for the PFCs is largely governed by their ability to withstand such a hostile environment whilst absorbing neutronic heating, minimising plasma impurities and protecting components shielded by the PFCs. Initially ITER will operate as a plasma experiment without the use of tritium, one of the fuels required for fusion reactions. Current designs for this operational phase will use beryllium for the first wall, with tungsten and carbon fibre composites (CFCs) for the divertor. These materials have been selected due to their favourable properties [74].

It is proposed that the lower part of the divertor will consist of a series of flat CFC tiles aligned in rows (see Figure 5.1) with one side being plasma facing [75]. In order to remain within operational temperature limits the components must be actively cooled. This is achieved by connecting the tiles through their centres to a copper pipe carrying coolant. As the function of this heat sink is to transfer thermal energy away from the CFC, it is imperative that the method of joining the CFC to the copper pipe must provide a bond that retains both structural integrity and a high thermal conductivity under large thermal loads. As this region will contribute to, and possibly dominate, performance of the component, it is of utmost importance that the thermal behaviour at the CFC-Cu interface is well characterised.

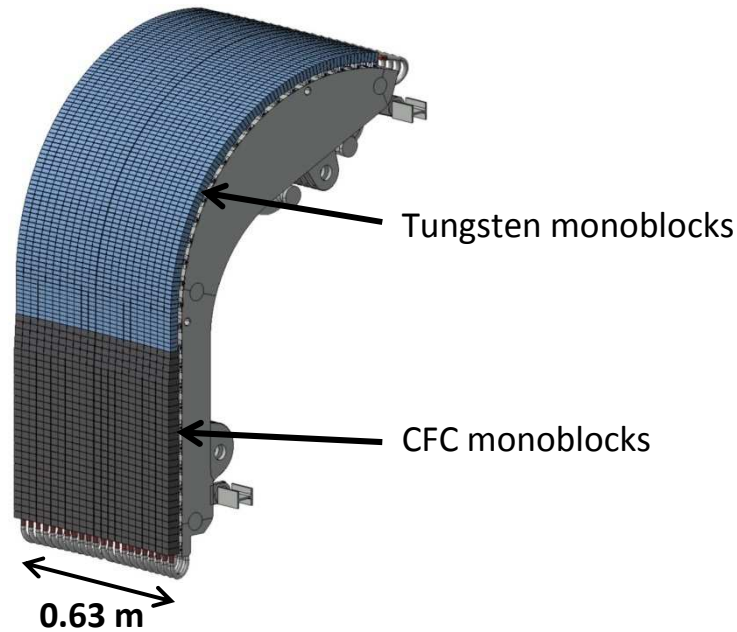


**Figure 5.1.** Schematic of section of ITER divertor [107].

Previous work has been carried out in order to characterise the thermal behaviour of a series of joining techniques for CFC-Cu samples [108]. The thermal performance across the interface has been investigated by measuring thermal diffusivity experimentally through laser flash analysis (LFA). Imaging by X-ray tomography provided high resolution images of the materials' microstructures at the interface, providing insight as to how they might affect thermal behaviour. The most promising joining technique was the one developed at Politecnico di Torino [84]. The technique involves a low cost process that requires no applied pressure and can be performed at relatively low temperatures (i.e. lower than required for Cu casting [109] or CFC modification [78]). The method uses a commercial braze (Gemco) which is modified by applying a layer of chromium. In joining, the braze is applied with the chromium face in contact with the CFC. When the component is heated the chromium reacts with the carbon to form chromium carbides. This leads to a better join between the CFC and the braze due to the improved wetting angle on chromium carbides, which would otherwise be poor.

In this paper, we explore the capabilities of a divertor monoblock mock-up manufactured using the Politecnico di Torino technique under reactor conditions. As this is difficult to carry out in the laboratory, we use Finite Element Analysis (FEA) to make our predictions.

FEA is usually performed by first creating a digital representation of the component using a computer aided design (CAD) package. This is typically a geometrically-ideal version of the component that does not include manufacturing flaws such as micro-cracking or porosity. In this paper we show that these imperfections play an important role in heat transfer. Creating the detailed models required is intractable using the CAD approach, so we use an emerging technique called Image-based Finite Element Modelling (IBFEM). IBFEM converts a three-dimensional image of a ‘real’ manufactured sample, including defects, into a digital geometry to be meshed for FEA. It has been shown that the IBFEM approach can give more accurate predictions than unit cell or analytical models [48]. Another benefit is that direct comparison to experimental results can be made, as we can digitise for simulation the sample that has been subjected to laboratory tests [94].

This paper presents two case studies. The objective of the first case study is to verify and validate the technique. It involves comparing experimental and simulated results carried out on a simple “disc” shaped sample of CFC bonded to Cu subjected to Laser Flash Analysis (LFA). There are three simulations: (i) a CAD based model, (ii) a low and (iii) a high resolution model generated from an X-ray Tomography scan. The CAD and low-resolution simulations can be carried out on a typical high end workstation, whilst the high resolution simulation requires access to supercomputing facilities. This exercise showed that the high resolution model provided the closest match to the experimental results. Therefore, the second case study uses high resolution IBFEM only to predict the behaviour of a CFC-Cu divertor monoblock mock-up under reactor conditions.

## 5.2 Materials

The CFC used was Sepcarb NB31 (Snecma Propulsion Solid, France). This is manufactured using a 3D NOVOLTEX preform needled in the z-direction with ex-pitch fibres and in x and y directions with ex-PAN fibres. Chemical vapour infiltration (CVI) is used for densification. The copper used was oxygen free high conductivity (OFHC) copper (Wesgo Metals, USA). The materials were joined by a brazing process using a Gemco® foil, 87.75 wt% Cu, 12 wt% Ge and 0.25 wt% Ni, (Wesgo Metals, USA). The foil was pre-coated with a 3  $\mu\text{m}$  layer of chromium using radio frequency magnetron sputtering. The divertor monoblock was produced by drilling a hole in a CFC tile, inserting the Gemco foil and finally the copper pipe before brazing. Joining was performed at Politecnico di Torino as detailed by Casalegno et al [84].

In order to carry out the CFC-Cu disc case study (the LFA experiment), further sample preparation was required. This was undertaken at The University of Manchester. The joined and individual samples, originally tile shaped, were machined using a lathe to produce cylindrical samples. A Struers Accutom-5 cut-off machine was used to obtain the thickness required for thermal analysis. The wheel was made of aluminium oxide and was set to rotate at 3000 rpm with a medium force and movement of  $0.02 \text{ mm}\cdot\text{s}^{-1}$ . To clean the samples they were placed in an ultrasonic bath of acetone for 10 minutes.

Figure 5.2 shows the samples in their prepared state. Table 5.1 details the resultant dimensions and properties. The samples' thickness and diameter were used to calculate the cylindrical volume, combined with mass this was in turn used to obtain density. Because these values included the porosity present within the CFC, reported values are for the bulk properties. Values for the constituent materials in the CFC-Cu disc were calculated from their respective thickness fractions. In this instance, the density values for CFC and Cu

layers were obtained from an average of four CFC samples and the pure Cu sample respectively.

Scanning electron microscope (SEM) investigation of the CFC and brazing alloy interface (seen in Figure 5.3) shows the formation of chromium carbide between the two layers. There is also infiltration of the carbide into open porosity on the surface.

**Table 5.1**  
Sample dimensions.

Sample	Diameter (mm)	Thickness (mm)	Mass (g)	Volume (cm <sup>3</sup> )	Density (g·cm <sup>-3</sup> )
CFC	12.66	2.06	0.447	0.2593	1.72
Cu	10.10	2.06	1.421	0.1650	8.61
CFC-Cu	12.70	4.84	2.916	0.6131	4.76
CFC (CFC-Cu)	12.70	2.74	0.631	0.3477	1.81
Cu (CFC-Cu)	12.70	2.10	2.285	0.2654	8.61

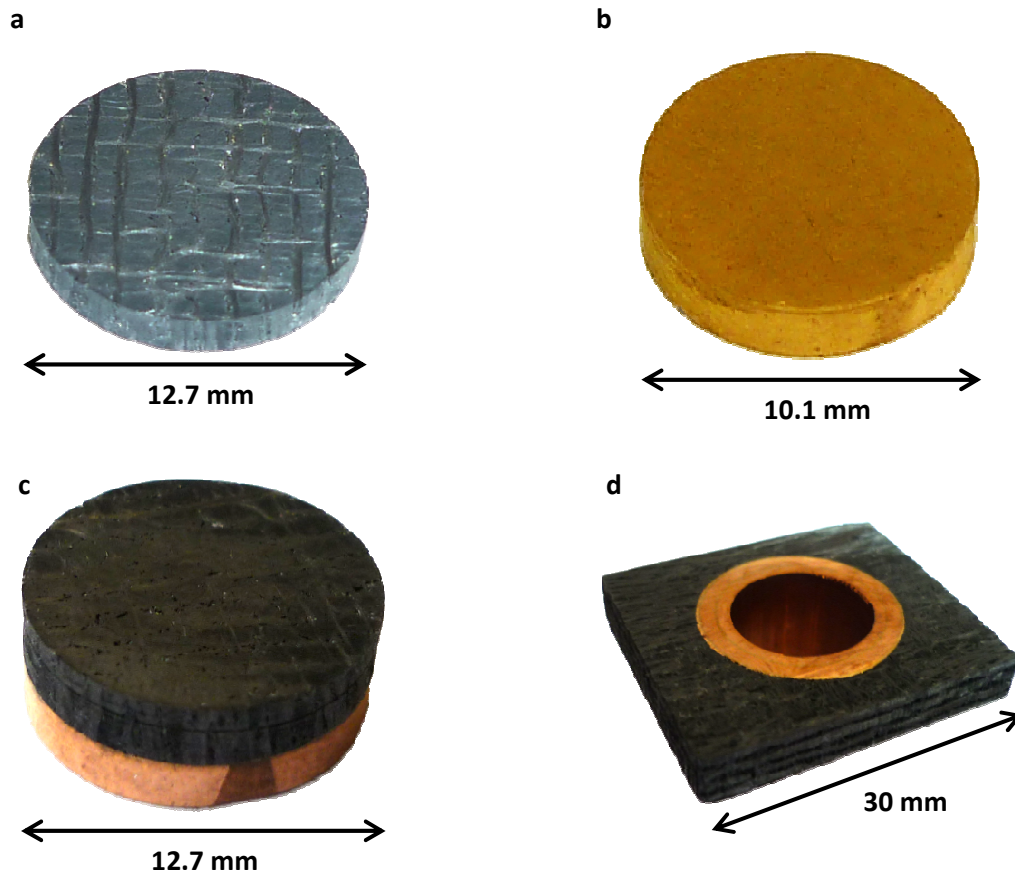


**Figure 5.2.** Samples used; (a) CFC, (b) Cu, (c) CFC-Cu disc and (d) CFC-Cu divertor monoblock.

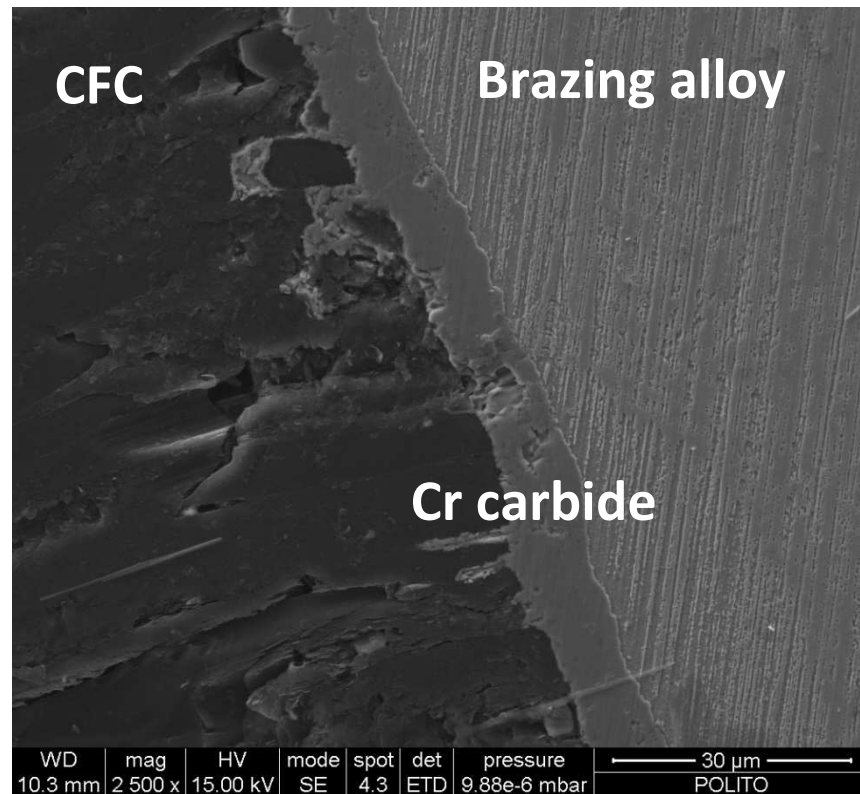


**Figure 5.3.** SEM image of CFC and brazing alloy interface.

### 5.3 Method

This section details the (i) experimental determination of thermal properties using LFA, (ii) three-dimensional imaging using X-ray computed tomography, (iii) finite element mesh generation, (iv) definition of simulation boundary conditions, (v) equation solution and finally (vi) results analysis.

#### 5.3.1 Thermal diffusivity

The Netzsch 457 MicroFlash® system [50] was used to perform LFA. This system is used to irradiate the surface of a disc shaped sample of known thickness with a short laser pulse. The time the heat pulse takes to travel through the sample is measured by an infra-red camera directed at the rear face. This is used to calculate thermal diffusivity. Specific heat and thermal conductivity can be calculated by comparing results with a calibration sample.

To ensure stability of the sample and maximum absorption of energy from the pulse, measurements were performed in an inert atmosphere after the sample had been coated with graphite. Results were collected at intervals of 100 °C, ranging from 100 °C to 700 °C. The average of 5 measurements at each interval was recorded.

### 5.3.2 X-ray tomography

The Nikon Metrology 225/320 kV system (using the 225 kV source) at the Manchester X-ray Imaging Facility [88], University of Manchester, UK, was used to create X-ray tomography scans of the CFC-Cu disc and the divertor monoblock. Imaging and reconstruction settings are shown in Table 5.2 and Table 5.3 respectively. In imaging, lower energy X-rays emitted are attenuated by the first few millimetres of samples making their edges appear denser (i.e. high greyscale values). Beam hardening corrections mitigate these effects. Noise reduction filters can be used by smoothing data. The values recorded in Table 5.3 are software pre-set levels where the maximum is 6 and 1 yields the lowest level of correction. Voxel widths of 9.7  $\mu\text{m}$  and 21.8  $\mu\text{m}$  were achieved for the CFC-Cu disc and divertor monoblock respectively. However, due to signal noise, not all features at these scales were resolvable e.g. the 10  $\mu\text{m}$  layer of chromium on the braze.

**Table 5.2**  
X-ray tomography parameters used.

Sample	Target	Voltage (kV)	Current ( $\mu\text{A}$ )	Filter (mm)	Acquisition Time (ms)	Number of Projections	Frames / Projection
CFC	Cu	120	200	N/A	500	2001	1
Cu	W	220	210	Sn, 1.0	700	3142	1
CFC-Cu	W	210	135	Sn, 1.0	1415	2001	2
Monoblock	W	200	190	Ag, 1.0	1415	2001	2

**Table 5.3**  
Reconstruction settings.

Sample	Beam Hardening	Noise Reduction	Voxel Width (mm)
CFC	1	3	0.0100
Cu	2	2	0.0082
CFC-Cu	2	4	0.0097
Monoblock	1	2	0.0218



### 5.3.3 Finite element mesh generation

The CFC-Cu disc and divertor monoblock scans were imported into the Simpleware [110] suite of programmes, version 6 (Simpleware Ltd., Exeter, Devon, UK) to convert the 3D images into FE meshes. Image segmentation was performed using a range of techniques including the thresholding, Boolean operators, flood-fill, cavity fill, island removal, manual paint tools and a recursive Gaussian smoothing filter. Linear 4-node tetrahedral elements were selected for meshing.

A low resolution and high resolution mesh was created for the CFC-Cu disc case study. The low resolution mesh captured the main features, such as surface roughness and large pores. The resolution of the higher fidelity model was carefully chosen, striking a balance between capturing fine details of the micro-structure and producing a model that could be easily handed on the various computer platforms available. Creating a finite element model at the same resolution as the original tomography scan is technically challenging and probably offers little benefit over the high resolution model selected.

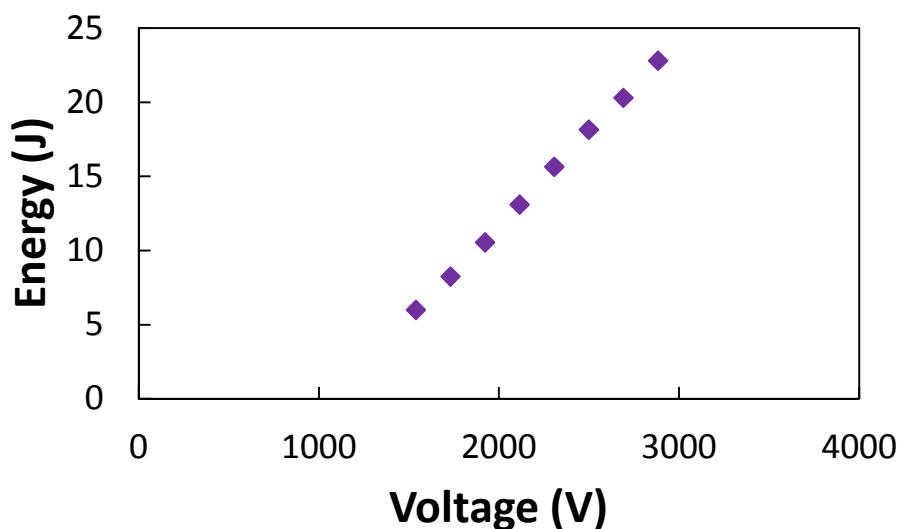
A Computer Aided Design (CAD) version of the CFC-Cu disc was created and meshed in Abaqus, version 6.12 (Simula, Providence, RI, USA). This model comprised a cylinder with three layers of varying thickness representing the CFC, Gemco and Cu. Porosity was not included. The CAD based mesh had approximately 50,000 tetrahedral elements (consistent with typical engineering practice). As the results presented later show, the high resolution model gives the closest match to the LFA experiment carried out on the CFC-Cu disc. Therefore, only a high resolution model was created for the divertor monoblock case study.

### 5.3.4 Finite Element Analysis

#### 5.3.4.1 Boundary conditions for CFC-Cu disc

In order to recreate the LFA experiment *insilico*, a thermal load matching the laser's must be applied to one surface of the finite element model whilst the temperature values on the opposite side are recorded with respect to time. In order to determine the magnitude and distribution of the load we must consider the laser's operation.

Experimental measurements showed that, at the operating voltage 1538 V, the laser delivered 6 J over the duration of the laser pulse (see Figure 5.4). The measurements were made without the optics in place. The LFA 457 has 3 focusing lenses, which cause an attenuation of approximately 0.5 % per surface (i.e. 6 lens surfaces). Thus, the resultant energy incident from a single pulse on the sample over a 15 mm diameter spot size is 5.8 J.



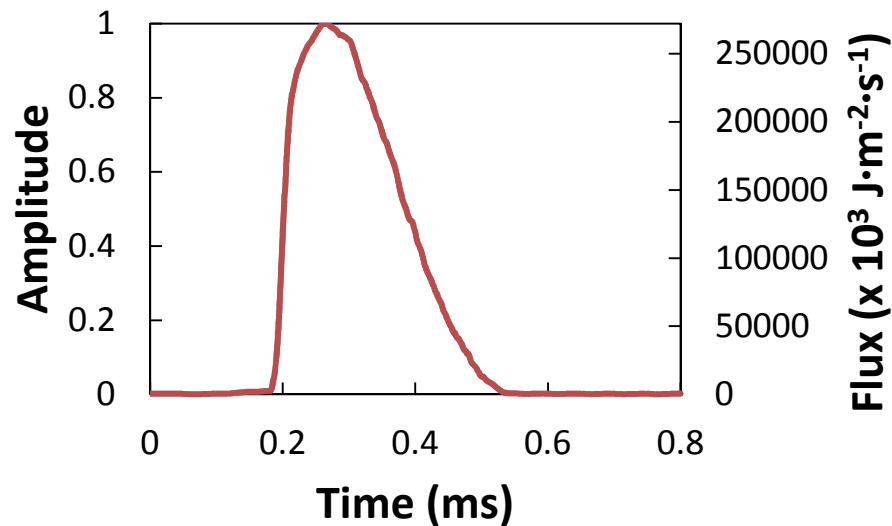
**Figure 5.4.** Laser energy for a given voltage for the NETZSCH LFA 457.

Figure 5.5 shows the energy amplitude of a typical laser shot for a given applied voltage. As no calibration data was available to link applied voltage to laser energy output, the energy amplitude is therefore normalised between minimum and maximum values. The

total energy output of the laser (calculated above to be 5.8 J) is the area under the curve in Figure 5.5. Thermal flux, the rate of energy transfer per unit of area, has the units  $\text{mJ}\cdot\text{mm}^{-2}\cdot\text{s}^{-1}$ . By knowing the total energy emitted over a certain area, it is possible to calculate the flux;

$$\text{i.e. peak flux} = \text{total energy (mJ)} / (\text{spot area (mm}^2) * \text{area under curve (s)})$$

This can be used with the non-dimensionalised amplitude curve to produce a flux profile with respect to time i.e. the curve in Figure 5.5 using the secondary axis values.



**Figure 5.5.** Typical energy pulse emitted from NETZSCH LFA 457 laser.

Flux is a quantity which applies to an area, but due to the discretisation in finite element analysis it must be applied at nodal points. Thus the equivalent flux value for an area must be projected to the nodes defining that area. Assuming the discretised area is sufficiently small the flux value over that area can be considered uniform. For first order finite elements, the projected flux value at the node is calculated by dividing the total flux equally between each of the nodes, as shown in Figure 5.6 [66]

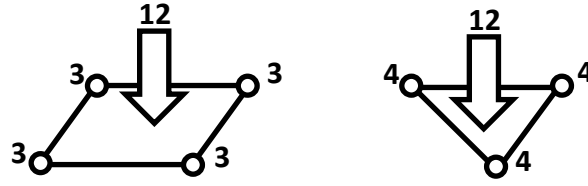


**Figure 5.6.** Projecting flux over an area to nodal coordinates due to discretisation inherent in FEA.

An additional consideration for the LFA scenario is that the surface onto which the laser is incident is not completely flat. Element faces describing this surface will be oriented at different angles in three-dimensional space. The laser path is considered to travel purely in the z-direction and will not arrive normal to the element face. Therefore it is important to calculate the effective elemental area in the x-y plane, as this is the area ‘seen’ by the laser. A simple example of a surface consisting of 4 triangular elements is shown in Figure 5.7. Even in such a simple case, the three dimensional area is 30% greater than the effective 2D area in the x-y plane.

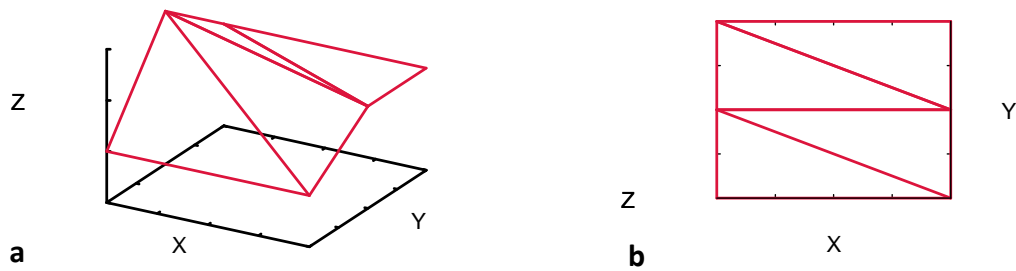


**Figure 5.7.** Comparison of the area of (a) element faces and (b) the effective area seen by the laser in x-y plane.

The 3D area is calculated by taking the cross product of any two of the three vectors defining the triangle, where A, B & C are the nodes.

$$area = \left| \frac{\overrightarrow{AB} \times \overrightarrow{AC}}{2} \right|$$

(5.1)

In 2D this simplifies to

$$A_{el} = \left| \frac{A_x(B_y - C_y) + B_x(C_y - A_y) + C_x(A_y - B_y)}{2} \right|$$

(5.2)

Therefore, the nodal contribution from a tetrahedral element as a fraction of the whole domain would be  $\frac{1}{3} \frac{A_{el}}{A_{tot}}$  where  $A_{el}$  is the area of the element face and  $A_{tot}$  is the area of the surface being thermally loaded.

These values assume a uniform distribution of flux over the whole sample surface area.

Lasers typically exhibit a Gaussian distribution of their beams, as shown in Figure 5.8.

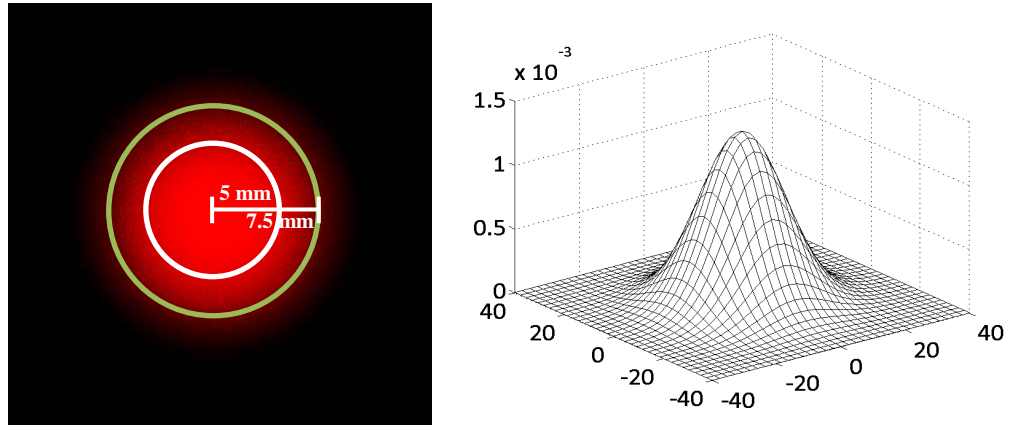


**Figure 5.8.** Multivariate Gaussian distribution exhibited by laser beam.

In 2D this is known as the multivariate Gaussian distribution (MGD) (5.3).

$$f(x, y) = \frac{1}{2\pi\sigma_x\sigma_y\sqrt{1-\rho^2}} \exp \left( -\frac{1}{2(1-\rho^2)} \left[ \frac{(x-\mu_x)^2}{\sigma_x^2} + \frac{(y-\mu_y)^2}{\sigma_y^2} - \frac{2\rho(x-\mu_x)(y-\mu_y)}{\sigma_x\sigma_y} \right] \right)$$

(5.3)

where  $\sigma_x$ ,  $\sigma_y$  are the standard deviation in x and y directions,  $\rho$  is the correlation between x & y and  $\mu_x$  &  $\mu_y$  are the mean values. For the case of the laser beam  $\sigma_x = \sigma_y$  and  $\rho$ ,  $\mu_x$  &  $\mu_y$  are zero. Therefore (5.3) simplifies to (5.4) and in polar coordinates (5.5).

$$f(x, y) = \frac{1}{2\pi\sigma^2} \exp\left(-\frac{x^2 + y^2}{2\sigma^2}\right)$$

(5.4)

$$f(r) = \frac{1}{2\pi\sigma^2} \exp\left(-\frac{r^2}{2\sigma^2}\right)$$

(5.5)

As the CFC-Cu disc is smaller than the laser spot size, calculating the total energy delivered must take into consideration the non-uniform distribution. Additionally the applied nodal loads must reflect this spatial variation in distribution.

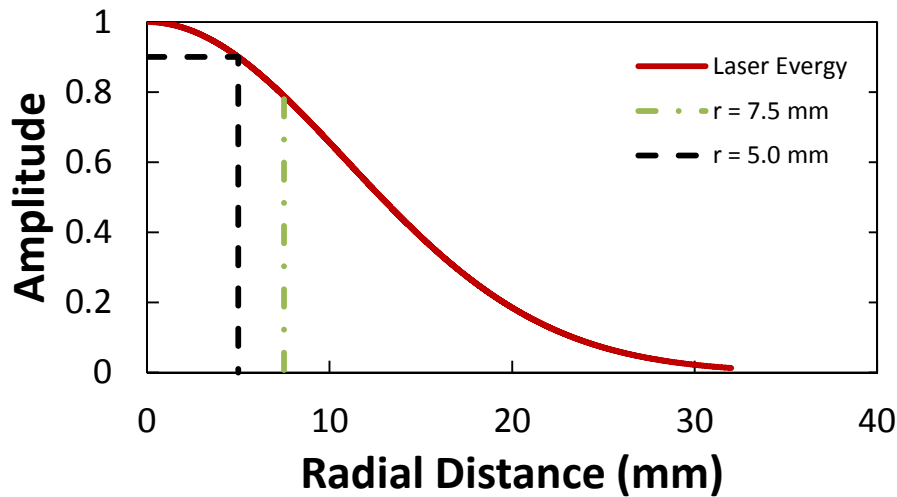


**Figure 5.9.** MGD profile of 15 mm diameter spot size laser where energy reduces by 10 % between centre and  $r = 5.0$  mm, i.e.  $\sigma = 10.892$ .

According to the LFA 457 manufacturers, it can be expected that the laser power reduces by 10 % of the peak value 5 mm from the centre. This is observed when the standard deviation is 10.892 (see Figure 5.9). In order to use the profile in Figure 5.9 to calculate the thermal loads to be applied, the peak energy needs to be determined, i.e. where  $r = 0$  mm. To do this it must be ensured that the volume under the 2D MGD (between -7.5 and 7.5 in  $x$  and  $y$ ) is equal to the volume under the uniform distribution over the same area. That is, within a given time-step, the energy delivered is equal to the uniform distribution calculation. This volume can also be seen as ‘power’ which has the units  $\text{mJ}\cdot\text{s}^{-1}$ .

To calculate the volume under the MGD we must integrate the equation describing the curve over the whole region,  $R$ , using polar coordinates as shown in equation (5.6).

$$V = \iint_R f(x, y) dA = \iint_R f(r) r dr d\theta$$

$$\iint_R f(r) r dr d\theta = 1 - \exp - \frac{1}{2} \left( \frac{r}{\sigma} \right)^2$$
(5.6)

When calculated to infinity, the volume under the MGD is unity. However, for this purpose it is necessary for the distribution delivered over the 15 mm diameter spot size to be unity. Therefore, a normalising factor,  $F_n$ , is required. This is given as the ratio of the volumes of the two distributions where ‘ $r$ ’ is infinity and 7.5, i.e.;

$$V_\infty = 1, V_{7.5} = 0.211$$

$$F_n = \frac{V_\infty}{V_{7.5}} = 4.738$$

$$V_{7.5}F_n = 1 \quad (5.7)$$

Thus, the flux at any point can be described as a function of its distance from the origin

$$\Phi(r, t) = F_n f(r) P_t \quad (5.8)$$

where  $P_t$  is the power for a given time step, calculated by multiplying the flux for a given time step,  $\Phi_t$ , (as found above, see Figure 5.5) by the spot size area ( $P_t = \Phi_t * \pi R^2$ ).

Combining the above for a triangular face on a tetrahedral element, the flux for a particular node at any given time step is;

$$\Phi(r, t) = \frac{1}{3} \frac{A_{el}}{A_{tot}} \frac{F_n}{2\pi\sigma^2} \exp\left(-\frac{r^2}{2\sigma^2}\right) P_t \quad (5.9)$$

The MGD is a function of the distance of the node from the central point of the sample. The radial distance,  $r$ , is defined as (5.10) where the  $nd$  and  $c$  subscripts denote the nodal and central x-y coordinates.

$$r = \sqrt{(x_{nd} - x_c)^2 + (y_{nd} - y_c)^2} \quad (5.10)$$

As this calculation must be repeated over all elements on the surface where the laser is incident, it is probable that a single node will receive a contribution from several adjacent elements. In this case, the values are summed to give a total nodal flux.



#### 5.3.4.2 Case Study 1: CFC-Cu disc

Once the method for determining the boundary conditions had been determined, verification and validation of the IBFEM technique could be performed by comparing experimental and simulated results of the LFA for the CFC-Cu disc sample. The CAD-based model, together with the low resolution IBFEM and high resolution IBFEM models were analysed using ParaFEM, an open source parallel finite element platform developed by the authors [99] [111] [112] [66] [105].

To ensure an accurate non-oscillatory (stable) solution a time step of  $2 \times 10^{-6}$  s was used together with an iterative solver stopping criterion of  $1 \times 10^{-6}$ .

The Laser Flash experiment was simulated at a furnace temperature of 200 °C, using the material properties measured by LFA for CFC and Cu. Properties for Gemco were obtained from the manufacturer [113] and standard values for air [114] were used for the porosity, shown in Table 5.7.

#### 5.3.4.3 Case Study 2: Divertor monoblock

In the second case study, the performance of the divertor monoblock was investigated under reactor conditions. Several design scenarios exist for ITER each with their own set of in-service parameters. Here, the transient response of the divertor monoblock going from initial state to steady-state operation was modelled.

A thermal flux of  $10 \text{ MW} \cdot \text{m}^{-2}$  was applied to one outer CFC surface of the divertor monoblock with a matching negative load (representing the liquid cooling process) on the inner surface of the Cu pipe (see Figure 5.10). The CFC surface was selected such that fibre orientation matched that of the CFC-Cu disc modelled in the first case study. Initial temperature was set to 200 °C throughout the domain, which is within the expected

operational window. This was done to match the CFC-Cu disc analysis so that the same material properties could be used. The simulation was run until steady-state operation was achieved. A time step of  $5 \times 10^{-4}$  s and an iterative solver stopping criterion of  $1 \times 10^{-6}$  were used.

The results of both case studies were post-processed using ParaView, version 3.14.1 64-bit (Kitware Inc., Clifton Park, New York, USA) [69].

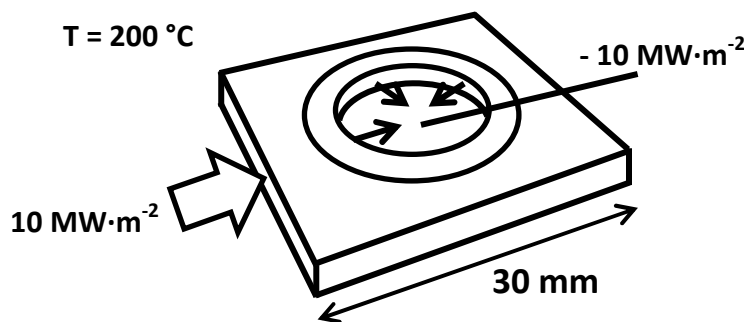


**Figure 5.10.** Schematic of applied loads in monoblock simulation.

## 5.4 Results and discussion

This section presents (i) the thermal diffusivity values determined experimentally for the constituent materials and the CFC-Cu disc; (ii) micro-structural observations regarding the CFC-Cu interface in both the CFC-Cu disc and the divertor monoblock; (iii) quantitative and qualitative analysis of the image-based meshing technique and (iv) results of the finite element analyses for the CFC-Cu disc and the divertor monoblock.

### 5.4.1 Thermal Diffusivity

Figure 5.11 shows the thermal diffusivity results measured experimentally by LFA. Figure 5.12 and Figure 5.13 chart the specific heat and thermal conductivity values calculated by calibration with the reference sample. The figures present results for the constituent materials, the projected values for the CFC-Cu disc based on the contributions by thickness of each material and finally the actual values measured for the CFC-Cu disc. The results

for the constituent materials are comparable to those found in the ITER materials properties database (MPDB), shown in Table 5.4.

Comparing the projected and actual thermal conductivity for the CFC-Cu disc, it can be seen that the measured conductivity is considerably lower than expected. The CFC appears to restrict heat flow, with the conductivity of the combined sample being only slightly higher than that of CFC. This is despite 43% of the sample's thickness consisting of the more highly conducting Cu. Interestingly, over the temperature range of 600 °C the conductivities of the CFC and Cu decrease by 45% and 20%, respectively. Thus, the average change would be a decrease of 34%, which is very close to the actual decrease of 35%.

The ITER MPDB specifies that the thermal conductivity must be greater than  $300 \text{ W}\cdot\text{m}^{-1}\cdot\text{K}^{-1}$  at room temperature and only decreasing to  $150 \text{ W}\cdot\text{m}^{-1}\cdot\text{K}^{-1}$  at 1000 °C. This is partly because it has been shown that plasma erosion decreases in CFCs with higher thermal conductivity [115], which ensures increased longevity for component life cycles. This component does not quite meet the specified criterion,  $273 \text{ W}\cdot\text{m}^{-1}\cdot\text{K}^{-1}$  at 100 °C (projected to be  $288 \text{ W}\cdot\text{m}^{-1}\cdot\text{K}^{-1}$  at room temperature) and  $178 \text{ W}\cdot\text{m}^{-1}\cdot\text{K}^{-1}$  at 700 °C (projected to be  $162 \text{ W}\cdot\text{m}^{-1}\cdot\text{K}^{-1}$  at 100 °C), but is relatively close.

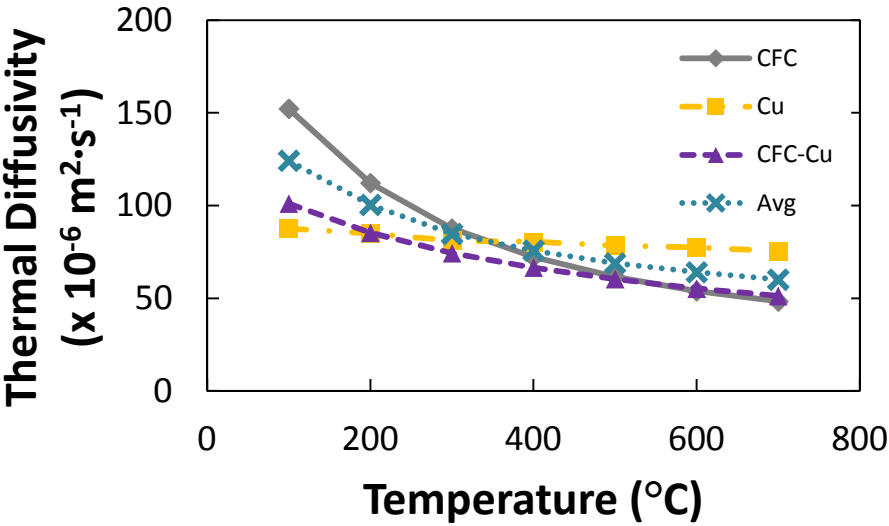


Figure 5.11. Thermal diffusivity measured by laser flash analysis.

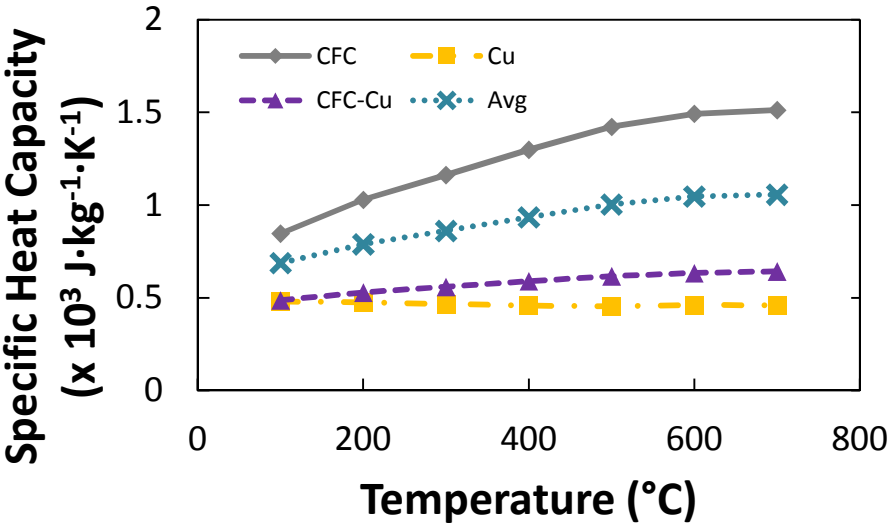
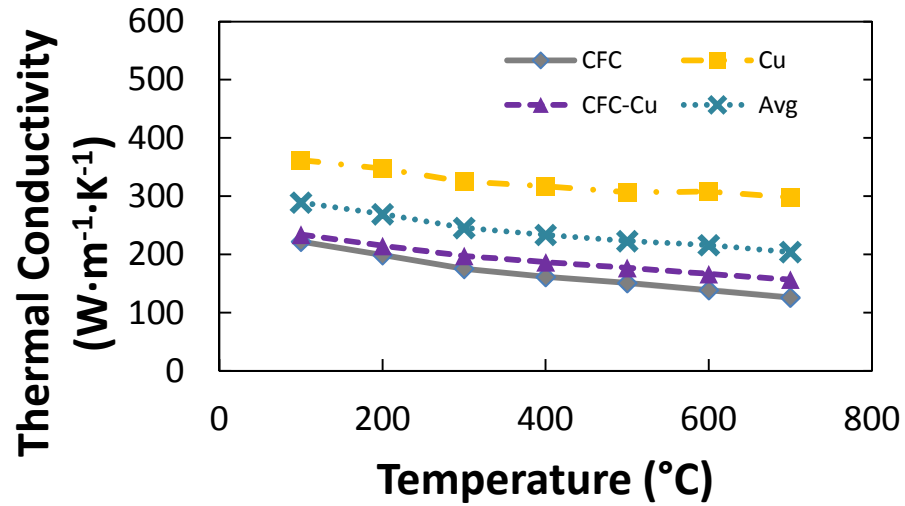


Figure 5.12. Specific heat capacity calculated by calibration of diffusivity against Pyroceram 9606.



**Figure 5.13.** Thermal conductivity calculated from diffusivity, density and specific heat values.

**Table 5.4**

Materials properties of CFC and Cu as specified by ITER MPDB.

Properties	Temperature (°C)		CFC (z direction)	Cu
	CFC	Cu		
Thermal conductivity (W·m <sup>-1</sup> ·K <sup>-1</sup> )	RT <sup>+</sup>	RT	304	379
	250	200	240	355
	800	350	145	351
	1000	500	141	357
Specific Heat (J·g <sup>-1</sup> ·K <sup>-1</sup> )	RT	RT	0.780	0.388
	800	200	1.820	0.400
	1000	500	2.000	0.437
CTE (10 <sup>-6</sup> K <sup>-1</sup> )	800	200	0.4	17.0
	1000	500	0.5	18.6
Density (g·cm <sup>-3</sup> )	RT	RT	1.90	8.90
Porosity (%)	RT	RT	8	N/A

<sup>+</sup>Room Temperature

#### 5.4.2 X-ray tomography images

Figure 5.14 shows that the Cu at the interface of the CFC-Cu disc is rough. In certain regions small veins of Cu rise from the surface. This shows that the brazing material does not remain in its initial position but contorts to the shape of the CFC and even fills open porosity. This greatly increases the interface surface area from 126.7 mm<sup>2</sup> if smooth, calculated geometrically, to 132.2 mm<sup>2</sup>, measured from the X-ray tomography image. It is expected that this enhances both bond strength and thermal transport across the interface.

The majority of the Cu at the surface (80.4 %) is in contact with the CFC, therefore it can be assumed that the bonding will be successful in maximising thermal conductivity.

In contrast, the X-ray scan for the divertor monoblock shows delamination on one side of the pipe (see Figure 5.15 and Figure 5.16). It appears that this area is linked with the orientation of the sample during the brazing process i.e. the divertor monoblock was on its side during joining and the upper surface is where the pipe has pulled away most probably due to a combination of the effects of gravity and a mismatch in thermal expansion coefficient between the CFC and Cu. It is expected that this region will act as a substantial thermal barrier during operation.

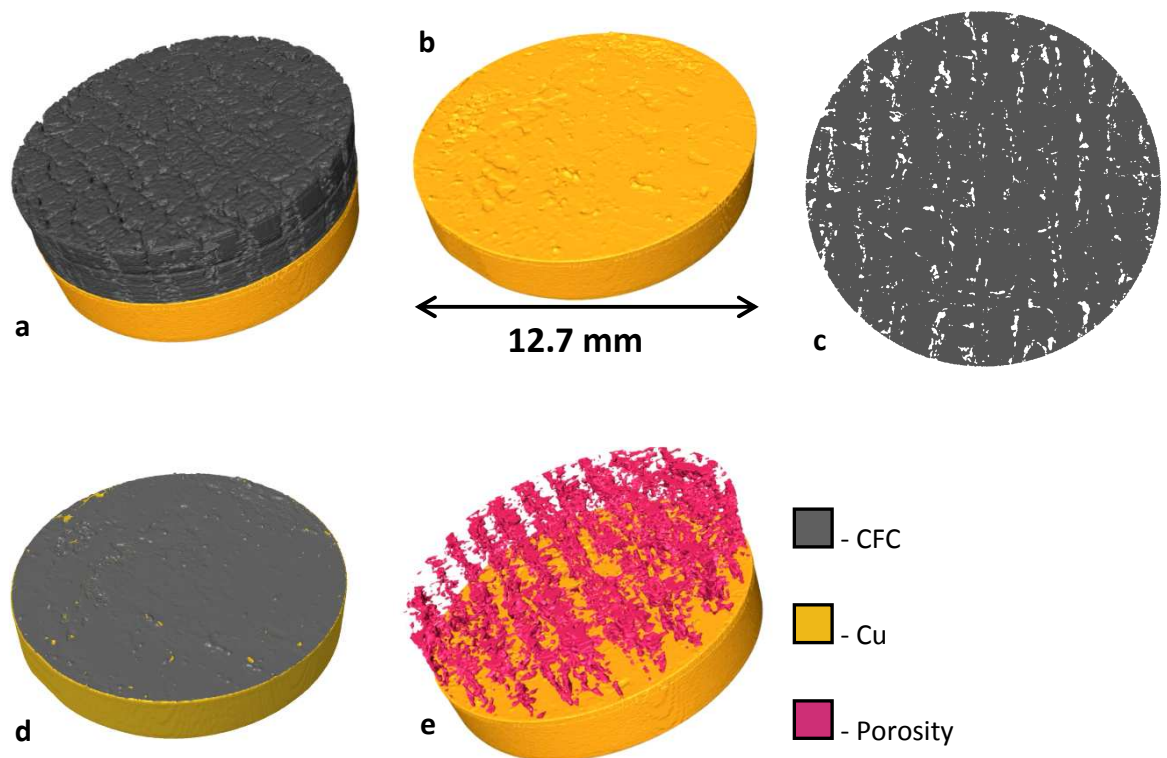


**Figure 5.14.** 3D reconstruction from X-ray tomography data for the CFC-Cu disc showing; (a) complete sample, (b) rough Cu surface at interface with CFC, (c) slice midway through CFC section, (d) contact area at CFC-Cu surface and (e) porosity within the CFC showing preferential alignment with direction of thermal transport.

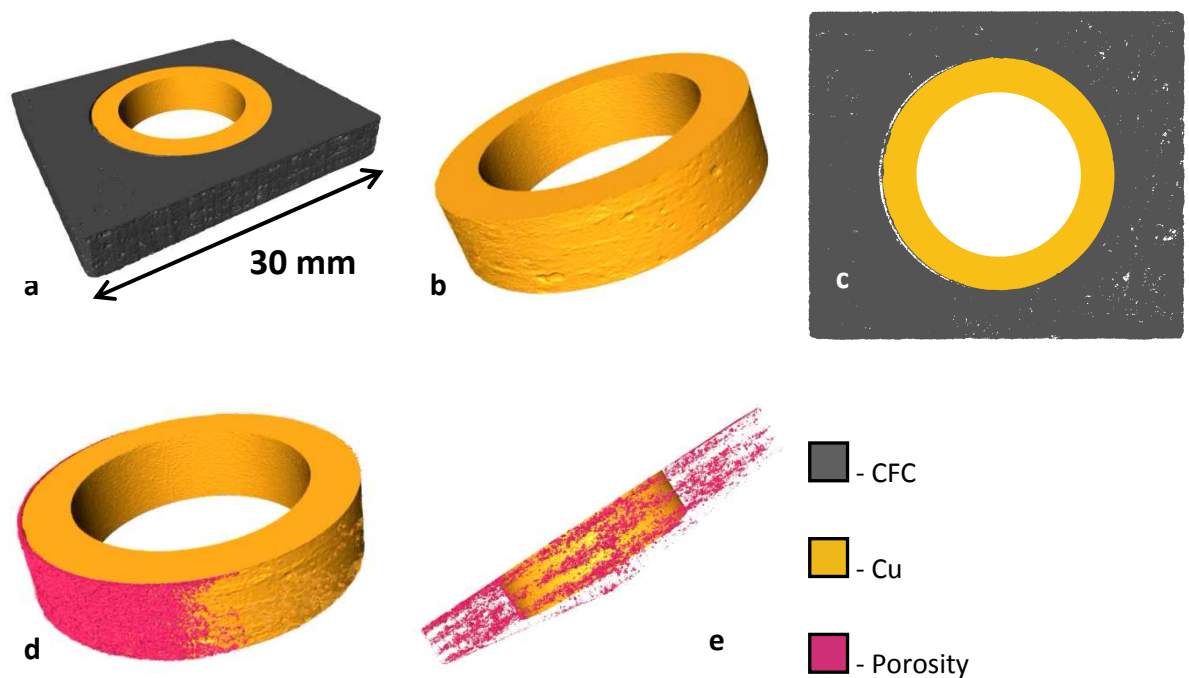


**Figure 5.15.** 3D reconstruction from X-ray tomography data for divertor monoblock showing; (a) complete sample, (b) rough Cu surface at interface with CFC, (c) slice through the midplane, (d) large area where CFC has delaminated from Cu during brazing process and (e) porosity within the CFC showing preferential alignment with direction of thermal transport.

Pores within CFCs are an unavoidable issue. They affect thermal conductivity by behaving as thermal barriers. The greatest concentration of porosity is typically found aligned between fibre layers. Thus, through composite layup design, it is possible to arrange these layers to give directionally preferential performance. It can be seen that the porosity in the divertor monoblock is aligned to promote thermal transport radially away from the pipe.

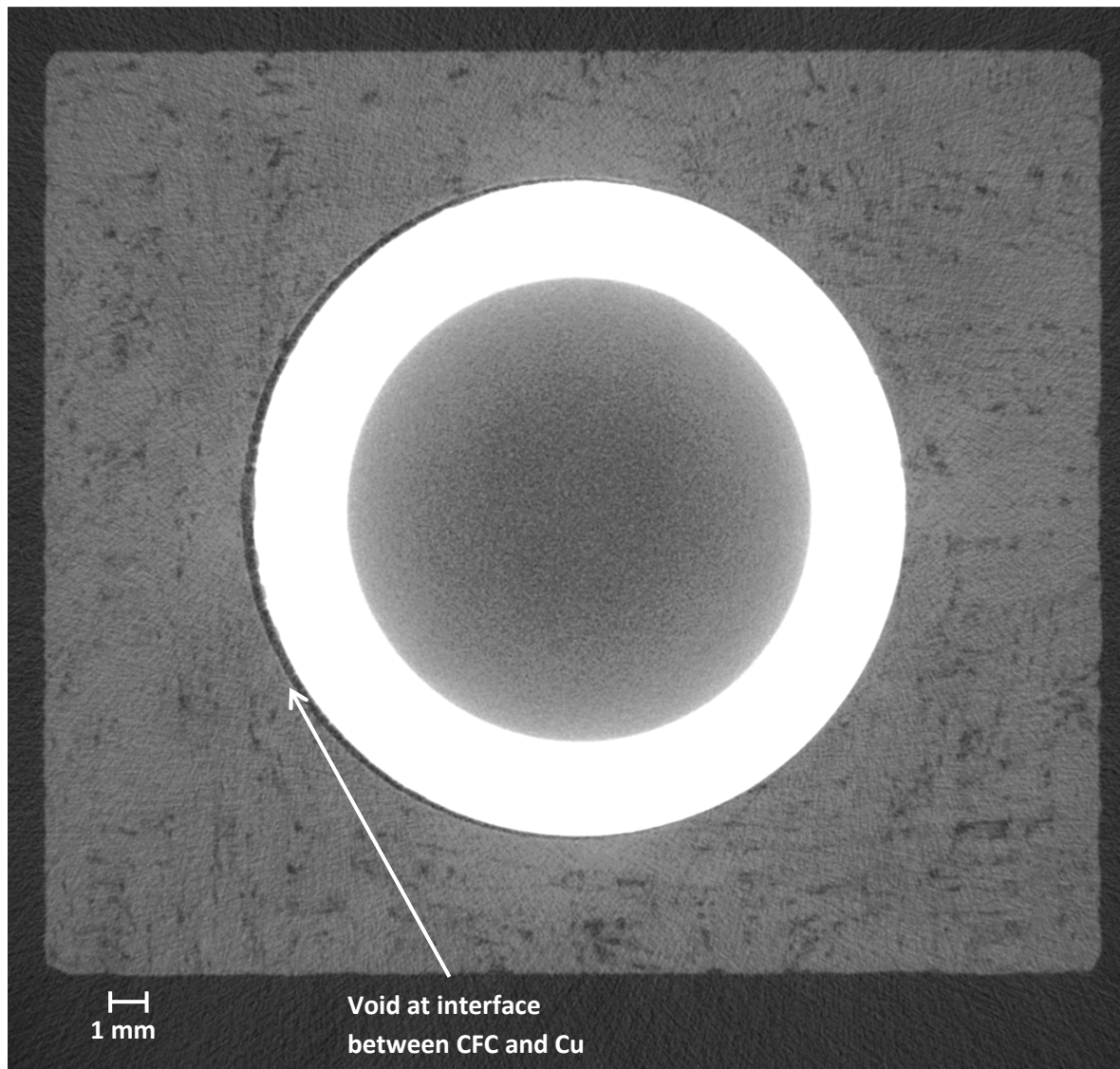


**Figure 5.16.** Tomography slice from the midplane of the divertor monoblock showing internal porosity of CFC. Additionally a large void spanning the perimeter of one side of the Cu pipe can be seen, this was likely introduced during brazing due to orientation of sample.



### 5.4.3 Conversion of tomography data into finite element meshes

Composite materials typically display highly anisotropic behaviour due to the alignment of fibres within the matrix and thus the induced porosity. Traditionally, directional material properties are prescribed to account for this behaviour when modelling composites. IBFEM does not require this as it aims capture the micro-structures causing anisotropic behaviour. To maximise its potential each phase must be segmented i.e. fibres, matrix and porosity. In this work, due to the near identical X-ray absorption of carbon fibres and matrix, differentiation of these phases was not possible. Therefore, only partial anisotropy is achieved by treating the CFC as amorphous carbon with aligned porosity. However, effects of anisotropy should be minimised because LFA is treated as a one-directional problem. Additionally, the monoblock analysis has thermal gradients largely in one direction and was aligned in consideration of this.

The automatic segmentation tool used by Simpleware [110] can segment images into different phases according to the voxel greyscale values. It was possible to segment the majority of the images automatically. Because of noise at the CFC-Cu interface and ring artefacts in the CFC, additional attention was required. Segmentation was carried out manually using paint/un-paint tools on a slice by slice basis. Before meshing, the images were downsampled, reducing computational cost whilst retaining micro-structural detail (see Figure 5.17).

Considering the CFC-Cu disc, at 30 % resolution, there is little difference in visible detail when compared with the full resolution achieved in the scan (100 %). A lower resolution (5%), suitable for analysis using a workstation, loses many features. Details characterising the models are given in Table 5.5 and Table 5.6 for the CFC-Cu disc and divertor monoblock respectively.

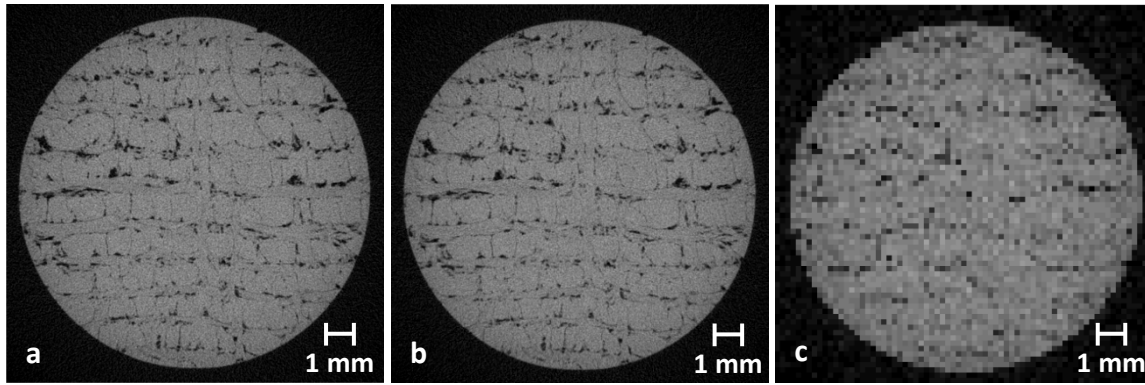


**Figure 5.17.** X-ray tomography x-y planar slice midway through CFC layer of CFC-Cu disc showing effect of downsampling from (a) original resolution to (b) 30% and (c) 5% resolutions.

As the image comprises voxels (cuboids), smoothing is applied in meshing to better describe the curved nature of the geometry. This can cause quantities derived from the mesh geometry to differ from those derived from the original image. Changes in volume and surface area for all meshes are recorded in Table 5.5 and Table 5.6 as a percentage of the original resolution. The total volumetric changes can be considered negligible.

When considering volumetric changes within the constituent materials there are two notable changes. Firstly, in the low resolution mesh, the Gemco layer is greatly increased by over 400 % in the CFC-Cu disc. The reason for this is that when downsampled, the layer becomes smaller than one voxel width. To retain the feature, it had to be artificially dilated (using the software) to the thickness of the new voxel width, resulting in the increase in volume. It is expected that this will affect the simulated conductivity at the interface because the conductivity of Gemco is lower than both CFC and Cu (see Table 5.7). Secondly, there is a decrease in porosity at each downsampling level, 28 % then 90 % for the CFC-Cu disc and 81 % for the divertor monoblock. This is because some of the pores are smaller than the new voxel widths. This should cause the simulated sample to have an artificially increased conductivity due to the loss of thermal barriers in the form of porosity (confirmed later in Figure 5.19).

The surface area of the models decreases with increasing levels of downsampling. This can be attributed to a reduction in surface detail as the image resolution decreases. The greatest variation can be seen in the CFC and porosity.

A few additional observations can be drawn from the segmented image statistical data. When comparing the total volume of the CFC-Cu disc with that calculated geometrically (see Table 5.1), the values agree to within 3 %. The porosity fraction of the CFC-Cu disc is 7.5 %, which closely agrees with the literature value of 8 %. However, this reduces to 1.2 % for the divertor monoblock because of the lower initial image resolution. Overall, the high resolution meshes were acceptable.

For the CFC-Cu disc, meshes with 0.6 million and 102 million elements were produced for the low and high resolution models, respectively. For the divertor monoblock, the high resolution mesh comprised 137 million elements. These numbers were within the target range for use on a laboratory workstation (low resolution) and modern supercomputer (high resolution).

**Table 5.5**

Segmentation and meshing output details for the CFC-Cu disc.

Name	Number of Voxels	Segmented Volume (mm <sup>3</sup> )	Surface area (mm <sup>2</sup> )	Number of Elements	Number of Nodes	Meshed Volume (%)
CFC-Cu (Original resolution, 0.0097 mm voxel width)						
Cu	289 M	264	478			
CFC	326 M	298	2600			
Porosity	26 M	24	1910			
Gemco	6.3 M	5.78	357			
Total	642 M	592	4988			
CFC-Cu (30% resolution, 0.0323 mm voxel width)						
Cu	7.8 M	-0.38%	-5.65%	40 M	8.2 M	-0.16%
CFC	8.8 M	-0.34%	-17.69%	53 M	11 M	1.40%
Porosity	0.70 M	-0.83%	-18.85%	7.1 M	2.2 M	-27.68%
Gemco	0.17 M	-1.38%	-10.64%	1.8 M	0.47 M	-5.23%
Total	17 M	-0.39%	-10.59%	102 M	22 M	-0.54%
CFC-Cu (5% resolution, 0.1940 mm voxel width)						
Cu	35 k	-3.79%	-12.97%	206 k	46 k	-4.85%
CFC	38 k	-6.38%	-63.00%	307 k	63 k	-2.79%
Porosity	3 k	-1.25%	-69.79%	29 k	17 k	-90.45%
Gemco	4 k	496.89%	-13.17%	46 k	12 k	460.52%
Total	81 k	-0.10%	-54.59%	587 k	137 k	-2.74%

**Table 5.6**

Segmentation and meshing output details for the divertor monoblock sample.

Name	Number of Voxels	Segmented Volume (mm <sup>3</sup> )	Surface area (mm <sup>2</sup> )	Number of Elements	Number of Nodes	Meshed Volume (%)
Monoblock (Original resolution, 0.0218 mm voxel width)						
Cu	42 M	434	723			
CFC	163 M	1690	3380			
Porosity	2.0 M	20.4	1560			
Gemco	1.2 M	12	592			
Total	208 M	2156.4	6255			
Monoblock (50% resolution, 0.0436 mm voxel width)						
Cu	5.2 M	0.23%	-1.38%	27 M	5.5 M	-0.95%
CFC	20 M	0.00%	-10.95%	106 M	22 M	-0.83%
Porosity	0.24 M	-2.45%	-23.08%	2.5 M	0.86 M	-37.31%
Gemco	0.14 M	0.00%	-0.84%	1.7 M	0.45 M	-1.15%
Total	26 M	0.02%	-11.91%	137 M	28 M	-1.20%

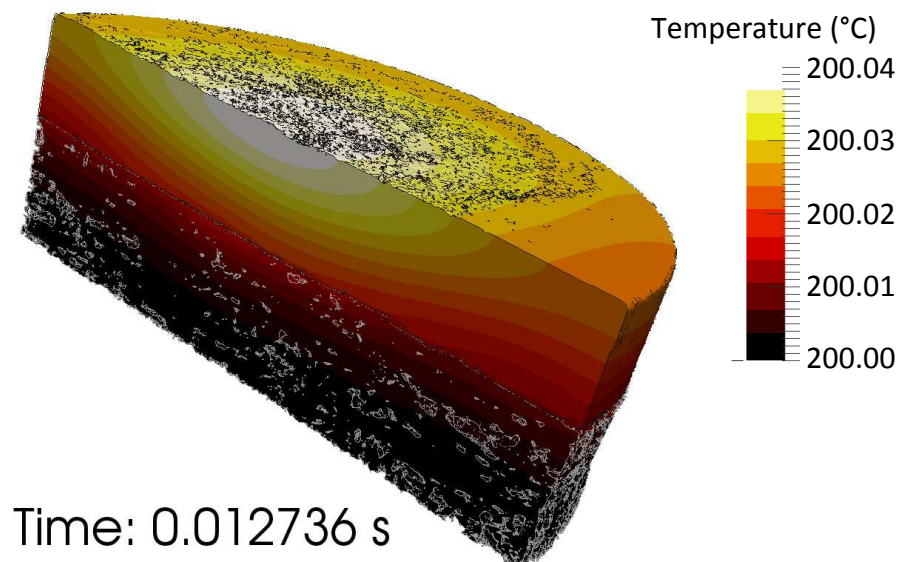
#### 5.4.4 FEA

##### 5.4.4.1 Case Study 1: CFC-Cu disc

Figure 5.18 shows a temperature cross-section of the CFC-Cu disc during a simulation of the LFA. A very low thermal gradient in the x-y plane demonstrates that the LFA can indeed be approximated to a one dimensional problem. Additionally, the temperature rise caused by the laser is low in comparison to the initial temperature, therefore variations in temperature dependent material properties are negligible. Material properties used are given in Table 5.7.

**Table 5.7**  
Material properties used for FEA.

Material	Conductivity ( $\text{W}\cdot\text{m}^{-1}\cdot\text{K}^{-1}$ )	Density ( $\text{g}\cdot\text{cm}^{-3}$ )	Specific Heat ( $\text{J}\cdot\text{g}^{-1}\cdot\text{K}^{-1}$ )
Cu	405.97	8.6098	0.555
CFC	232.43	1.8148	1.202
Gemco	24.300	8.8000	0.390
Porosity	0.0380	0.7380 E-03	1.030



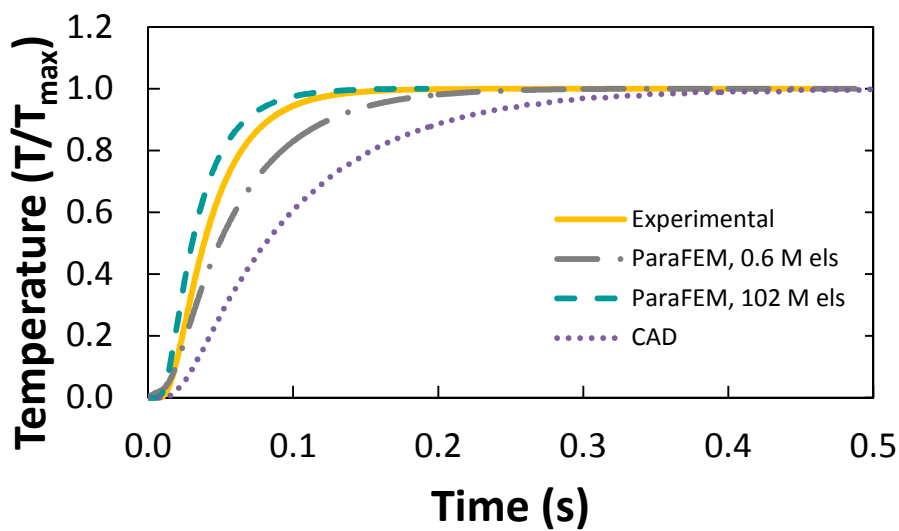
**Figure 5.18.** Cross section of temperature within CFC-Cu sample at  $t = 1.27 \times 10^{-2}$  s calculated by FEA, showing low thermal gradients in the x-y plane and low temperature rise.

Figure 5.19 compares the results obtained for the CAD model, the low and high resolution IBFEM models and the experimental LFA. The results are normalized with respect to the

maximum temperature. This graph can be used to determine thermal diffusivity through the half rise time using the “Cowan + pulse correction” method [86].

The CAD model (Figure 5.19) underestimates the sample’s thermal diffusivity by approximately 110 %. The low resolution IBFEM model which includes the largest pores and some surface detail underestimates the thermal diffusivity by approximately 30 %. The high resolution IBFEM provides the most accurate result, overestimating the thermal diffusivity by approximately 20 %. As predicted, the result shows a correlation between increasing model complexity and closeness to the experimental results.

In the high resolution analysis, the high diffusivity values (compared with the experimental results) may be due to the omission of some underlying thermodynamics. It is expected that model accuracy could be further improved by increasing the complexity of the simulation, achievable by the addition of features such as radiative boundary conditions, heat transfer coefficients, material properties that are temperature dependent or take into consideration anisotropic behaviour.



**Figure 5.19.** Rear surface temperature of CFC-Cu disc during LFA experiment and simulation.

#### 5.4.4.2 Case Study 2: Divertor monoblock

Figure 5.20 shows a plot of the temperature at various time intervals for the divertor monoblock. Figure 5.21 shows temperature versus time in the CFC either side of the Cu pipe, midway between the CFC-Cu interface and the sample edge. Finite element analysis of the divertor monoblock was carried out in two orientations, firstly with the delamination region situated in line with the source (thermal loading) and the sink (Cu pipe) and secondly with the delamination region rotated by  $180^\circ$  with respect to this direction. When the delamination region was in line with the source and sink, temperatures in the delamination region exhibited a more extreme range of maxima and minima in comparison with the other orientation. This observation is supported by Figure 5.22 and Figure 5.23 which compare the temperature profile along a central line between the front and rear surfaces of the divertor monoblock at steady-state operation for both orientations.

In Figure 5.23, the delamination creates a large thermal gradient at the boundary of the CFC and Cu by acting as a thermal barrier. This is more significant than the gradient caused by the relatively low conductivity of the Gemco layer. Zones of high thermal gradient will result in the generation of internal stresses. If aligned unfavourably in service, the delamination region would reduce the component's expected lifetime and increase the chance of failure.

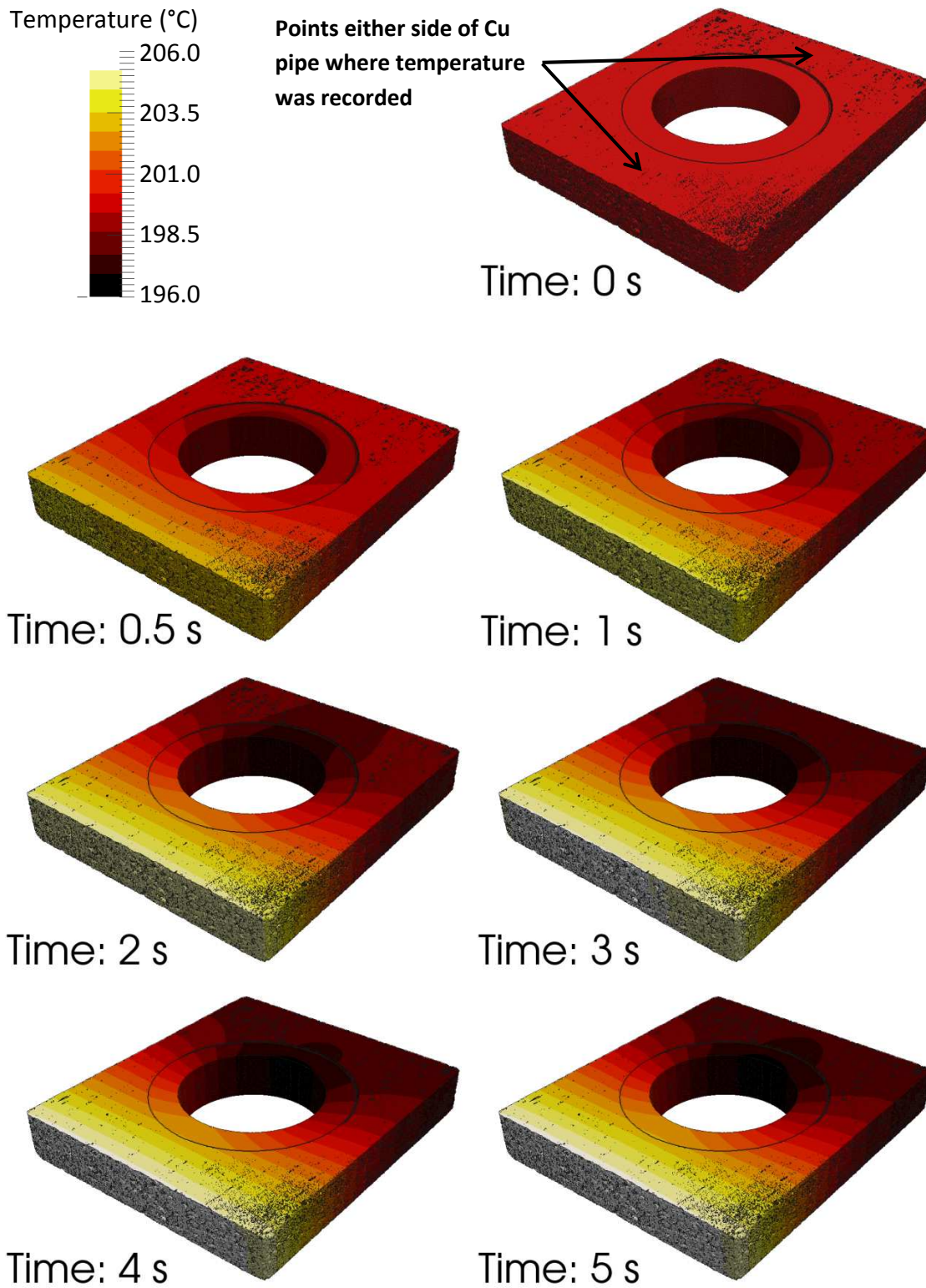


**Figure 5.20.** Time series analysis of the divertor monoblock tile created from an X-ray tomography image.



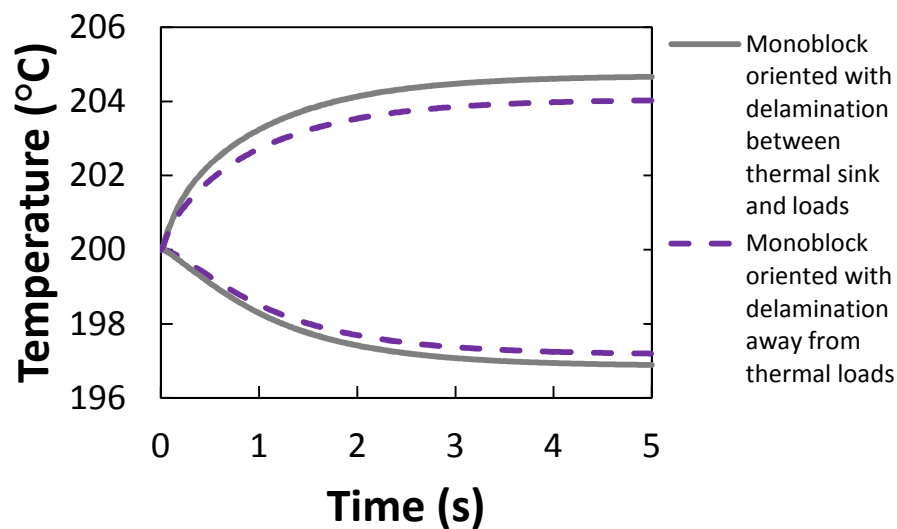


**Figure 5.21.** Temperature of nodes either side of Cu pipe, as shown in Figure 5.20, versus time for both orientations of the monoblock.

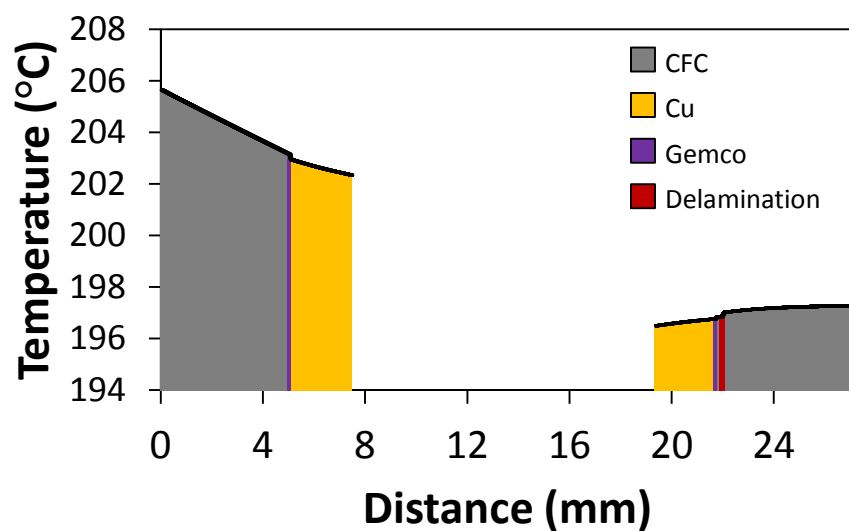


**Figure 5.22.** Temperature profile between the front and rear surfaces of the divertor monoblock with delamination not aligned with the heat source and sink.

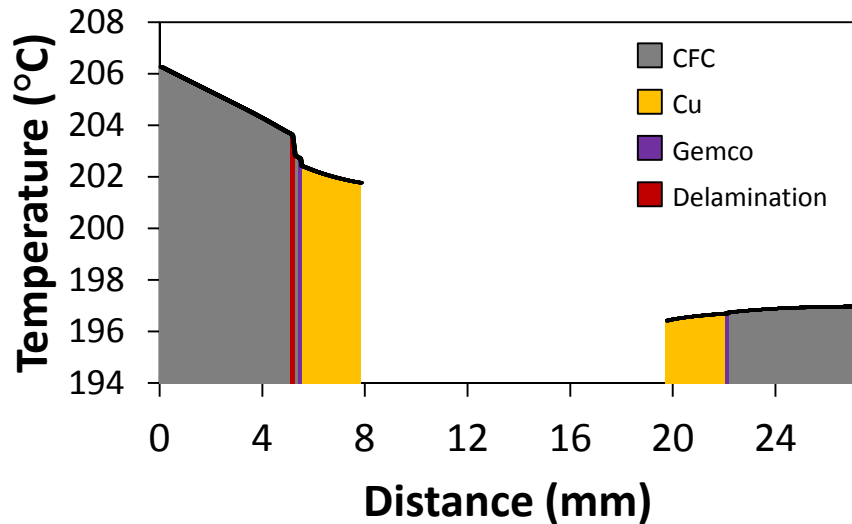


**Figure 5.23.** Temperature profile between the front and rear surfaces of the divertor monoblock with delamination positioned between the Cu pipe and the thermal loads.

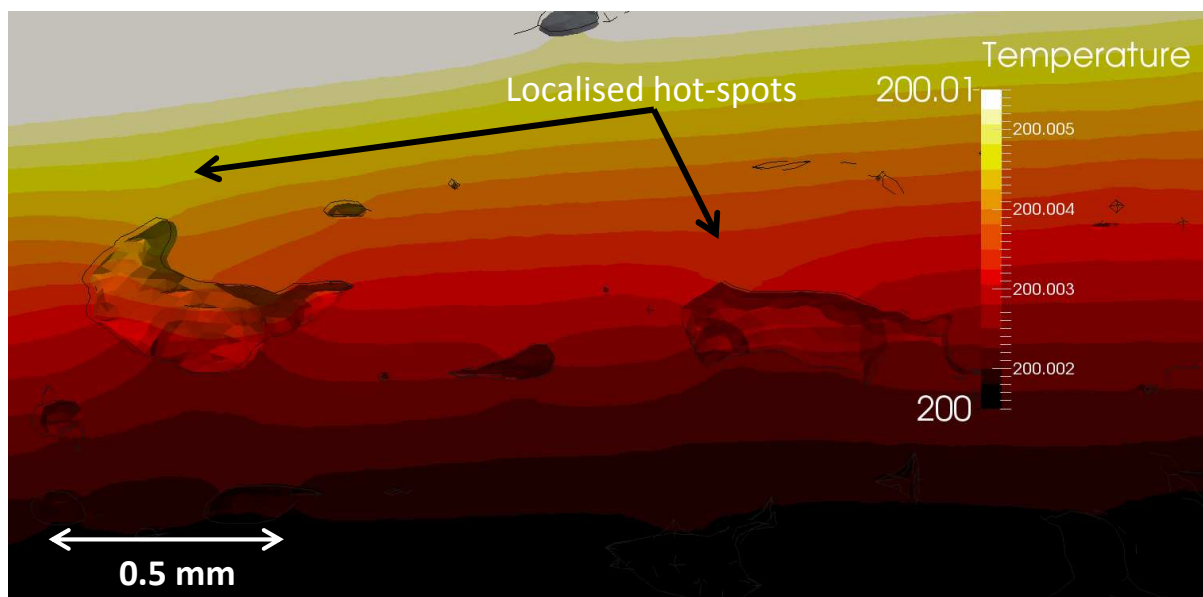


**Figure 5.24.** Example of localised “hot spots” caused by characteristic porosity located internally within the CFC section of the CFC-Cu divertor monoblock.

The porosity within the CFC had a less significant influence on the thermal behaviour. This is largely due to the favourable porosity alignment discussed earlier (shown in Figure 5.15). At the micro-structural level, the finite element results in Figure 5.24 show that the pores behave as thermal barriers causing “hot spots”. When the effect of these hot-spots is summed across the component, their contribution would be non-negligible. Regions

surrounding the small veins of Cu had increased cooling opportunity and were therefore “cool spots”. These results show that reducing porosity and increasing Cu surface area is likely to improve efficiency.

## **5.5 Conclusions**

In the first case study, laser flash analysis was carried out for a CFC-Cu disc where the interface had been joined by a novel brazing process using a Gemco foil pre-coated with chromium. It was shown that the thermal conductivity of the CFC-Cu disc decreased by 35% over a temperature range of 100 °C to 700 °C. This was in line with the average decrease of thermal conductivity for CFC and Cu. The thermal conductivity was little higher than that for CFC, which accounted for 57% of the sample’s thickness, and not quite within the required parameters specified in the ITER MPDB. This demonstrates the influence of the interface on thermal conductivity, and thus the importance of being able to predict the behaviour of the interface.

It was shown that high resolution image-based modelling of the LFA for the CFC-Cu disc provided a closer match with the experimental results than was achieved using traditional CAD based FEA. This verification and validation exercise demonstrated the reliability of the image-based modelling technique, and therefore confirmed its suitability for use in simulating conditions not easily reproduced in the laboratory, such as those expected in the ITER.

In the second case study, the CFC-Cu divertor monoblock, X-ray tomography highlighted difficulties in the manufacturing process by clearly showing the delamination of the CFC from the Cu pipe on one side of the interface. The image-based modelling, which captured this defect, showed that the delamination would result in lower thermal conductivity thus

leading to a shorter life-expectancy and a higher chance of component failure due to increased internal stresses. Suggestions were made regarding improving component cooling efficiency such as: increasing the Cu surface area at the interface; reducing porosity; minimising the braze foil's thickness or selection of an alternative braze with higher thermal conductivity.

In the future, the image-based modelling techniques developed here could be used to simulate other scenarios expected in ITER, such as plasma instabilities or loss of coolant. Due to the nature of the technique it would also be easy to digitally alter the geometry to investigate the effect of varying porosity or interface properties.

The ParaFEM software together with the modifications required to carry out the research in this paper is freely available for download in source code form (see <http://www.parafem.org.uk>).

## **Acknowledgements**

The authors would like to acknowledge support of the Engineering and Physical Sciences Research Council for the Fusion Doctoral Training Network (Grant EP/K504178/1) and Culham Centre for Fusion Energy (CCFE). This work made use of HECToR (Project e254), the UK's national high-performance computing service, which is provided by UoE HPCx Ltd at the University of Edinburgh, Cray Inc and NAG Ltd, and funded by the Office of Science and Technology through EPSRC's High End Computing Programme. This work also made use of the facilities of N8 HPC provided by the N8 consortium under EPSRC Grant No.EP/K000225/1. The Centre is co-ordinated by the Universities of Leeds and Manchester. Additionally, the authors would like to thank the Manchester X-ray Imaging Facility for use of tomography equipment, which was funded in part by the

EPSRC (grants EP/F007906/1, EP/F001452/1 and EP/I02249X/1) and the staff at the University of Manchester for guidance in preparing this work.

## References

- [73] A. Kukushkin, H. Pacher, V. Kotov, G. Pacher and D. Reiter, “Finalizing the ITER divertor design: The key role of SOLPS modeling,” *Fusion Engineering and Design*, vol. 86, no. 12, pp. 2865-2873, 2011.
- [74] R. Pitts, A. Kukushkin, A. Loarte, A. Martin, M. Merola and C. Kessel, “Status and physics basis of the ITER divertor,” *Physica Scripta*, vol. T138, p. 014001, 2009.
- [75] M. Merola and G. Vieider, “On the use of flat tile armour in high heat flux components,” *Journal of Nuclear Materials*, vol. 258–263, no. Part 1, pp. 672-676, 1998.
- [107] “A blast of heat for ITER's plasma-facing components,” [Online]. Available: <http://www.iter.org/newsline/251/1436>. [Accessed 31 July 2013].
- [108] L. M. Evans, “Thermal Characterisation of Ceramic/Metal Joining Techniques for Fusion Applications Using X-ray Tomography,” *Journal of Nuclear Materials*, vol. v, p. pp, 2013. (PhD Thesis, Chapter 4)
- [84] V. Casalegno, T. Koppitz, G. Pintsuk, M. Salvo, S. Rizzo, S. Perero and M. Ferraris, “Proposal for a new brazing alloy for joining CFC composites to copper,” *Composites Part B: Engineering*, 2013.
- [109] P. Appendino, V. Casalegno, M. Ferraris, M. Grattarola, M. Merola and M. Salvo, “Direct joining of CFC to copper,” *Journal of Nuclear Materials*, Vols. 329-333, Part B, p. 1563–1566, 2004.
- [78] P. Appendino, M. Ferraris, V. Casalegno, M. Salvo and M. Merola, “Proposal for a new technique to join CFC composites to copper,” *Journal of Nuclear Materials*, vol. 348, pp. 102-107, 2006.
- [48] J. Ali, C. Berre and P. M. Mummery, “Image based modelling of stress-strain behaviour in carbon/carbon composites,” *Energy Materials: Materials Science and Engineering for Energy Systems*, vol. 1, no. 3, pp. 179-186, 2006.
- [94] P. Young, T. Beresford-West, S. Coward, B. Notarberardino, B. Walker and A. Abdul-Aziz, “An efficient approach to converting three-dimensional image data into highly accurate computational models,” *Philosophical Transactions of The Royal Society A*, vol. 366, no. 1878, pp. 3155-3173, 2008.
- [50] S. Min, J. Blumm and A. Lindemann, “A new laser flash system for measurement of the thermophysical properties,” *Thermochimica Acta*, vol. 455, no. 1-2, pp. 46-49,

2007.

- [88] “MXIF,” [Online]. Available: <http://www.mxif.manchester.ac.uk/>. [Accessed 25 July 2013].
- [110] “3D images to RP, CAD, FE and CFD models with Simpleware software,” [Online]. Available: <http://www.simpleware.com>. [Accessed 31 July 2013].
- [99] “ParaFEM,” [Online]. Available: <http://www.parafem.org.uk>. [Accessed 15 July 2013].
- [111] Ll. M. Evans, “Thermal finite element analysis on massively parallel computing platforms,” *Finite Elements in Analysis and Design*, 2013. (PhD Thesis, Chapter 5)
- [112] I. M. Smith and L. Margetts, “The Convergence Variability of Parallel Iterative Solvers,” *Engineering Computations*, vol. 23, no. 2, pp. 154-165, 2006.
- [66] I. M. Smith, D. V. Griffiths and L. Margetts, *Programming the Finite Element Method* 5th Ed., Chichester: Wiley, 2013.
- [105] “xx12.f90 - parafem,” [Online]. Available: <http://code.google.com/p/parafem/source/browse/trunk/parafem/src/programs/dev/xx12/xx12.f90?r=1445>. [Accessed 15 July 2013].
- [113] “Mechanical & Physical Properties,” [Online]. Available: <http://www.wesgomaterials.com/resources/mechanical-physical-properties/>. [Accessed 31 July 2013].
- [114] W. M. Haynes, T. J. Bruno and D. R. Lide, “Thermophysical Properties of Air,” in *94th Edition of the Handbook of Chemistry and Physics*, Boca Raton, FL, CRC Press/Taylor and Francis Group, 2013, pp. 6-18.
- [69] “ParaView - Open Source Scientific Visualization,” [Online]. Available: <http://www.paraview.org/>. [Accessed 15 July 2013].
- [115] J. Linke, M. Akiba, H. Bolt, G. Breitbach, R. Duwe, A. Makhankov, I. Ovchinnikov, M. Rödig and E. Wallura, “Performance of Beryllium, Carbon and Tungsten under intensive thermal fluxes,” *Journal of Nuclear Materials*, Vols. 241-243, pp. 1210-1216, 1997.
- [86] R. D. Cowan, “Pulse Method of Measuring Thermal Diffusivity at High Temperatures,” *J. Appl. Phys.*, vol. 34, no. 4, pp. 926-927, 1963.

## CHAPTER SIX: Conclusions

### 6.1 Discussion

This work investigated the use of 3D imaging to create microstructurally-faithful FE models, developed open source parallel FE code capable of utilising this data to solve transient thermal problems and used this technique to investigate the thermal performance of a ceramic/metal join in a component designed for fusion energy.

The experimental aspect of the work entailed collecting thermal property data by means of LFA and 3D imaging through X-ray tomography, chosen for its non-destructive testing quality. The LFA was used to measure the thermal diffusivity across the interface of four CFC-Cu samples joined by direct casting, one step brazing and two by brazing with a foil pre-coated with chromium by galvanisation and radio frequency magnetron sputtering to improve the wettability on the CFC. In addition, samples of the constituent materials were also measured. Specific heat capacity and thermal conductivity were calculated from these results by calibration with a reference sample. The X-ray tomography was performed on the exact same samples to determine variations in microstructures at the interface that could cause differences in results between the samples. It was found by LFA that the sample joined by a braze pre-coated with chromium by magnetic radio frequency sputtering provided the best conductivity across the interface, which was also the sample shown by X-ray tomography to have the least amount of voids at the interface. From this investigation it was shown that the dominant mechanism in influencing the conductivity across the interface was the lateral area of voids acting as a thermal barrier rather than a large Cu-CFC contact area enhancing conductivity.

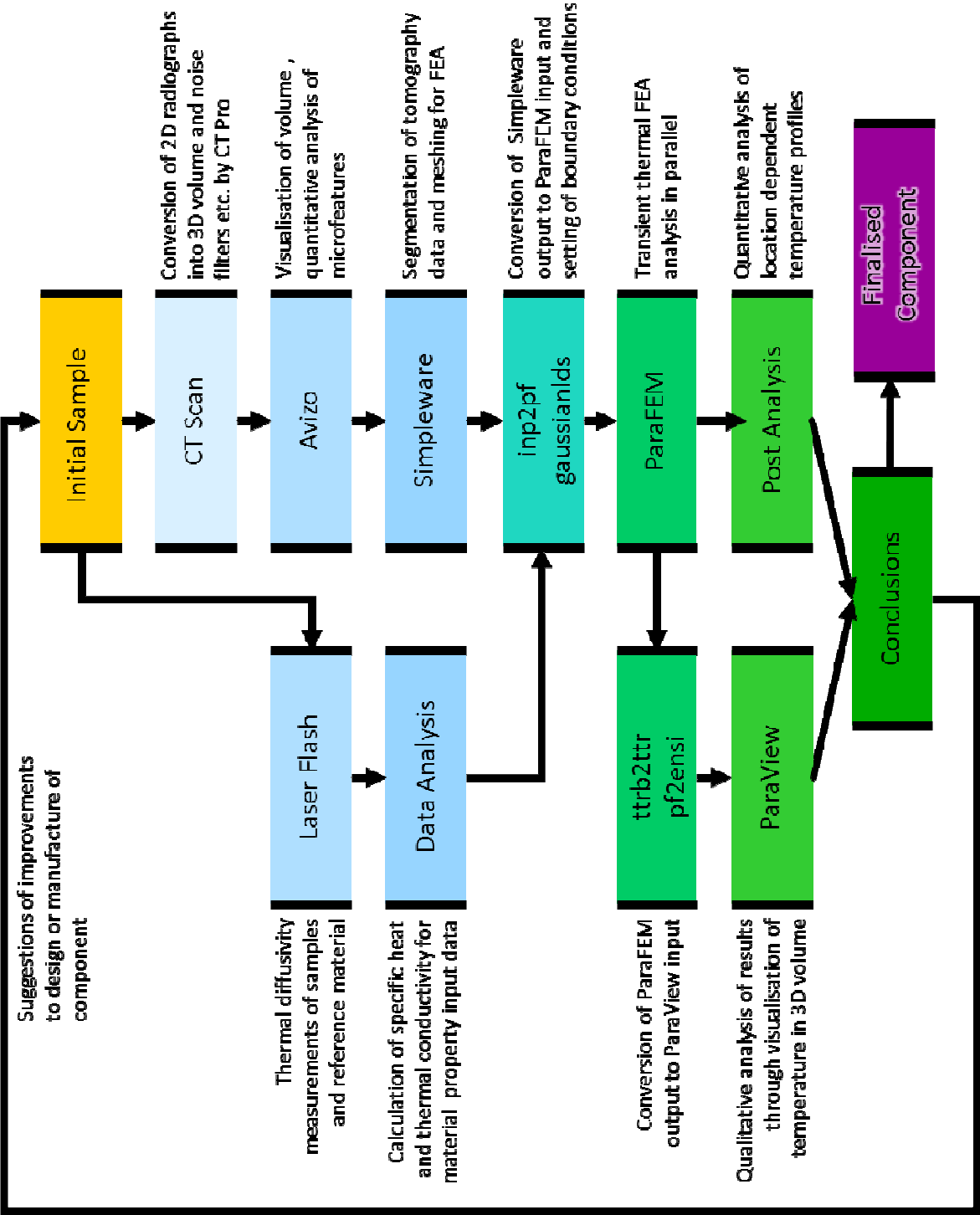


Figure 6.1. Workflow overview of image-based modelling technique.



To further investigate the influence of the microstructures on the thermal performance it was desired to use the already collected data to perform image-based modelling, a technique which constructs FE models from 3D image data. It was found that currently available commercial FE software was not well adapted to deal with such large datasets and downsampling to a resolution that only retained the largest features was required to successfully run the model.

This acted as motivation to develop FE code capable of handling the requirements of such a large model. In order to achieve this, open source parallel code from the ParaFEM project was adapted to solve transient thermal problems. The resultant code was found to be sufficiently accurate when compared to analytical results and the speed-up observed when increasing computing cores scaled well initially to 4096 cores on the size of problem attempted but it was shown that scaling improved with problem size. As a case study, the program was used to model thermal loads on a SiC composite demonstrating its feasibility of use with IBFEM.

To conclude the work, it was desired to use the developed technique to model a CFC-Cu divertor monoblock under reactor conditions. Further X-ray tomography was performed and the 3D image of the component was converted into an FE model. The technique was validated by simulating the LFA performed on one of the previous samples which used the same bonding technique as the monoblock using material properties for CFC and Cu collected by LFA. It was shown that results agreed moderately well and were an improvement on CAD and the low resolution IBFEM. It was proposed that further accuracy might be achieved by inclusion of additional underlying physics rather than increased resolution.

Once validated, the technique was used on the monoblock. The X-ray tomography exposed an area of delamination between the CFC and Cu caused by the manufacturing process. The delamination area was on one side of the Cu pipe and, depending on the orientation of the monoblock, would be between the pipe and front face where the thermal loads were applied or between the pipe and rear face. The monoblock was modelled as in-service in both orientations. It was seen that when the delamination was between the pipe and loads, more extreme maximum and minimum temperatures were reached causing larger thermal gradients, which in turn would cause larger thermal stresses. Additionally, the maximum temperature was reached more rapidly in this orientation. It was inferred from these observations that using the monoblock in this orientation would likely reduce its life expectancy and increase the likelihood of failure. Suggestions on changes to the microstructures at the interface were made to improve the monoblock's performance. A graphical overview of the workflow basics are shown in Figure 6.1.

## **6.2 Further work**

Hindsight allows the opportunity to consider the successes and deficiencies of the work. Due to the nature of computational simulations, it can be relatively straightforward to return to a set of analyses where improvements are identified and apply these. This is often not the case for the experimental side of the work due to lengthy timescales inherent with sample manufacturing, preparation and experimentation. It is, therefore, felt that should the work be conducted again, improvements could be made by applying the following changes to the experimental investigations.

Even though comparison between samples was possible, this would have been facilitated if the CFC-Cu samples all had equal thicknesses of each layer. Further grinding of samples in the preparation stage would have provided this. Experimental results for individual

samples were highly repeatable, however, due to the nature of CFC having large variations within its bulk, a larger number of samples would have given statistical confidence that observed behaviours were not specific to an individual sample. The sample joined by direct casting was machined into a cylinder by boring out a tile. It was found that this was inferior to lathing the samples into the same shape. Due to the availability of material, it was not possible to return and produce a further sample using the same machining process. It was felt that not enough was known about the Gemco braze layer, because of its form as a thin foil and the material changes it underwent during the brazing process it would have been technically difficult to gather material properties. These were therefore obtained from the manufacturer but the level of detail was low, it would have been desirable to acquire this data experimentally.

In retrospect of the programme of work followed, several areas of further work have been identified. Relating to the development of the code there are two areas; addition of features and efficiency improvement. The number of features that could be added is open ended but priority should be given to the inclusion of the effects caused by surface radiation and heat transfer coefficient which would allow direct calculation of internal thermal stresses. This would also involve further experimental work to collect the relevant material properties. The primary areas that could provide improvements in efficiency are the use of adaptive time stepping and iterative stopping criterion, which reduce the number of time steps and iterations respectively, and parallelising the I/O to reduce overheads.

With regards to development of the divertor monoblock, by collecting direction specific material properties for the CFC anisotropic modelling would be possible, thus allowing improved accuracy. Investigating the transient events such as plasma disruptions or loss of coolant would provide further interesting insight into the component's performance.

Ultimately, these results would be used to suggest further improvements to the component's design or manufacture e.g. vary joining conditions to minimise voids and increase CFC-Cu contact area. Once developed, these could be investigated again to see whether proposed changes translate into improved performance.

### **6.3 Research impact**

Although this technique was developed for the purpose of fusion applications, it could be used much further afield. By studying a component, originally designed by CAD, it was successfully demonstrated that it exhibited behaviour not intended by original design specifications. Through a better understanding of its operation under thermal loading, the reason for this behaviour was found to be caused by imperfections introduced in the manufacturing process.

The use of non-medical tomography scanners has shown growth of 10 % year on year and the number of research papers in the field doubling roughly every three years. Coupled with the introduction of multi-core computing into standard desktop PCs, this will allow the technique to become increasingly more prevalent.

Within academic circles the method is likely to be used in a similar fashion, to predict behaviour in extreme environments not easily replicated. The choice of an open-source route for development within an on-going project that had an online community has allowed both peer review and immediate impact because of the pre-installed user base. Further to that, inclusion of the final version of the code within the most recent edition of the 'Programming the Finite Element' text book [66], the previous edition of which included the subroutines on which the work was based, will facilitate further development.

In the long term, it is conceivable that such a tool could be used by any manufacturing industry wishing to verify that constructed components meet design requirements either in a later stage of R&D or, if streamlined, as an automated quality assurance control in the production line. Similarly large scale consumers could verify the claims of manufacturers about their products. This is attractive to industry because it often holds true that increased knowledge about performance can be used to increase reliability, reduce safety margins or operate under previously unattainable regimes, thus maximising profits.



## Bibliography

- [1] R. W. Clough, "The finite element method after twenty-five years: A personal view," *Computers & Structures*, vol. 12, no. 4, pp. 361-370, 1980.
- [2] J. MacKay and F. van Keulen, "Partial safety factor approach to the design of submarine pressure hulls using nonlinear finite element analysis," *Finite Elements in Analysis and Design*, vol. 65, pp. 1-16, 2013.
- [3] F. Andritsos and M. Zucchetti, "Afterheat transient in ITER after a total loss of coolant accident," *Fusion Engineering and Design*, vol. 15, no. 2, p. 113–119, 1991.
- [4] M. S. Shaikh, H. Pathak, T. Oliver and X. Wang, "Structural finite element analysis of ITER In-wall shield," *Fusion Engineering and Design*, vol. 88, no. 9-10, pp. 2105-2109, 2013.
- [5] N. Chawla, B. V. Patel, M. Koopman, K. K. Chawla, R. Saha, B. R. Patterson, E. R. Fuller and S. A. Langer, "Microstructure-based simulation of thermomechanical behavior of composite materials by object-oriented finite element analysis," *Materials Characterization*, vol. 49, no. 5, p. 395–407, 2002.
- [6] I. M. Smith and D. V. Griffiths, *Steady State Flow*, Chichester: Wiley, 2004, pp. 344-346.
- [7] IEA, "World Energy Outlook 2006," Paris, International Energy Agency, 2006, pp. 65-84.
- [8] "Biofuels 2008 and the Impact on Chemicals | IHS Chemical," [Online]. Available: <http://www.ihs.com/products/chemical/planning/special-reports/safe-sustainable/biofuels-2008.aspx>. [Accessed 29 August 2013].
- [9] S. Solomon, D. Qin, M. Manning, Z. Chen, M. Marquis, K. B. Averyt, M. Tignor and H. L. Miller (eds.), "Contribution of Working Group I to the Fourth Assessment Report of the Intergovernmental Panel on Climate Change," Cambridge University Press, Cambridge, United Kingdom, 2007.
- [10] V. Ramanathan and Y. Fenga, "Air pollution, greenhouse gases and climate change: Global and regional perspectives," *Atmospheric Environment*, vol. 43, no. 1, pp. 37-50, 2009.
- [11] W. C. Wang, Y. L. Yung, A. A. Lacis, T. Mo and J. E. Hansen, "Greenhouse

effects due to man made perturbations of trace gases. Anthropogenic gases may alter our climate by plugging an atmospheric window for escaping thermal radiation,” *Science*, vol. 194, no. 4266, pp. 685-690, 1976.

- [12] J. E. Bistline and V. Rai, “The role of carbon capture technologies in greenhouse gas emissions-reduction models: A parametric study for the U.S. power sector,” *Energy Policy*, vol. 38, no. 2, pp. 1177-1191, 2010.
- [13] UKERC (UK Energy Research Centre), “Decarbonising the UK Energy System: Accelerated Development of Low Carbon Energy Supply Technologies,” UKERC Energy 2050 Research Report Number 2, Version 2, March 2009.
- [14] S. Shafieea and E. Topal, “When will fossil fuel reserves be diminished?,” *Energy Policy*, vol. 37, no. 1, pp. 181-189, 2009.
- [15] D. J. C. MacKay, in *Sustainable Energy — without the hot air*, UIT Cambridge Ltd., 2008, pp. 103-112.
- [16] “World CO2 emissions - total,” [Online]. Available: <http://www.climatechangeconnection.org/emissions/WorldCO2emissions-total.htm>. [Accessed 29 August 2013].
- [17] WHO/IAEA/UNDP, “Chernobyl: the true scale of the accident: 20th anniversary statement,” WHO, Geneva, 2005.
- [18] IAEA, “Nuclear Power Reactors in the World, 2010 Edition,” International Atomic Energy Agency, Vienna, July 2010.
- [19] N. F. Pidgeona, I. Lorenzonib and W. Poortingac, “Climate change or nuclear power—No thanks! A quantitative study of public perceptions and risk framing in Britain,,” *Global Environmental Change*, vol. 18, no. 1, pp. 69-85, 2008.
- [20] “ITER - the way to new energy,” [Online]. Available: <http://www.iter.org/sci/whatisfusion>. [Accessed 29 August 2013].
- [21] G. McCracken and P. Stott, “Chapter 6 - The Hydrogen Bomb,” in *Fusion*, Burlington, Academic Press, 2005, pp. 61-67.
- [22] J. A. Wesson, “Fusion,” in *J. A. Wesson (ed.), Tokamaks*, Oxford, Oxford University Press, 2004, pp. 1-31.
- [23] “Fusion Reactors,” [Online]. Available: <http://www.polywellnuclearfusion.com/NuclearFusion/FusionReactors.html>. [Accessed 29 August 2013].
- [24] J. A. Wesson and J. Hugill, “Tokamak Experiments,” in *J. A. Wesson (ed.) Tokamaks*, Oxford, Oxford University Press, 2004, pp. 562-592.
- [25] C. M. Braams and P. E. Stott, in *Nuclear Fusion: half a century of magnetic*



*confinement research*, IoP Publishing Ltd., 2002, pp. 124-151.

- [26] UKERC, "Research Atlas: Overview of Energy Research and Development in the UK, The Conduct of Energy RD&D," UK Energy Research Centre, 2006.
- [27] [Online]. Available: <http://www.jet.efda.org/wp-content/gallery/graphics/jg05-537-1c.jpg>. [Accessed 29 August 2013].
- [28] I. Cook, N. Taylor, D. Ward, L. Baker and T. Hender, "Accelerated development of Fusion Power, UKAEA FUS 521," UK Atomic Energy Authority, 2005.
- [29] S. Şahin, H. Yapici and E. Baltacıoğlu, "Fusion breeder with enhanced safeguarding capabilities against nuclear weapon proliferation," *Energy Conversion and Management*, vol. 39, no. 9, pp. 899-909, 1998.
- [30] Panel on the Assessment of Inertial Confinement Fusion Targets; Board on Physics and Astronomy (BPA); Board on Energy and Environmental Systems (BEES); Division on Engineering and Physical Sciences (DEPS); National Research Council, Assessment of Inertial Confinement Fusion Targets, Washington, D.C.: The National Academies Press, 2013.
- [31] S. Konishi, S. Nishio and K. Tobita, "The DEMO design team, DEMO plant design beyond ITER," *Fusion Engineering and Design*, Vols. 63-64, pp. 11-17, 2002.
- [32] "Specific manufacturing : heat removal system with cooling water system," [Online]. Available: <http://www.atmostat-alcen.com/en/activities/specific-manufacturing>. [Accessed 29 August 2013].
- [33] G. S. Was, Fundamentals of Radiation Materials Science: Metals and Alloys, Springer Berlin Heidelberg, 2007, pp. 73-124.
- [34] "Defects in crystals," [Online]. Available: [http://www.tf.uni-kiel.de/matwis/amat/def\\_en/overview\\_main.html](http://www.tf.uni-kiel.de/matwis/amat/def_en/overview_main.html). [Accessed 29 August 2013].
- [35] "DoITPoMS - TLP Library - Materials for Nuclear Power Generation - Effects of Radiation Damage," [Online]. Available: [www.doitpoms.ac.uk/tlplib/nuclear\\_materials/damage\\_effects.php](http://www.doitpoms.ac.uk/tlplib/nuclear_materials/damage_effects.php). [Accessed 29 August 2013].
- [36] J. A. DiCarlo and S. Dutta, in *Handbook on continuous fiber-reinforced ceramic matrix composites (A97-14363 02-24)*, West Lafayette, IN/Westerville, OH, Ceramics Information Analysis Center and Purdue Univ./American Ceramic Society, 1995, pp. 137-183.
- [37] P. Boch and J. Nièpce, Ceramic Materials, London: Iste, 2007.
- [38] Committee on Advanced Fibers for High-Temperature Ceramic Composites, National Materials Advisory Board, Commission on Engineering and Technical Systems, National Research Council, D.W. Johnson (chair), in *Ceramic Fibers and*

*Coatings: Advanced Materials for the Twenty-First Century*, Publication NMAB-494, Washington, D.C., National Academy Press, 1998, pp. 6-11.

- [39] G. B. Engle and B. Kelly, "Radiation damage of graphite in fission and fusion reactor systems," *Journal of Nuclear Materials*, vol. 122, no. 1-3, pp. 122-129, 1984.
- [40] J. P. Coad, P. Andrew, D. E. Hole, S. Lehto, J. Likonen, G. F. Matthews and M. Rubel, "Contributors to the EFDA-JET work-programme, Erosion/deposition in JET during the period 1999–2001," *Journal of Nuclear Materials*, Vols. 313-316, p. 419–423, 2003.
- [41] M. Rubel, J. P. Coad, N. Bekris, S. K. Erents, D. Hole, G. F. Matthews and R. D. Penzhorn, "Contributors to EFDA-JET work programme, Beryllium and carbon films in JET following D–T operation," *Journal of Nuclear Materials*, vol. 313–316, p. 321–326, 2003.
- [42] N. Bekris, J. P. Coad, R. D. Penzhorn, S. Knipe, L. Doerr, R. Rolli and W. Nägele, "Characterisation of flakes generated in JET after DD and DT plasma operations," *Journal of Nuclear Materials*, Vols. 337-339, p. 659–663, 2005.
- [43] J. P. Sharpe, D. A. Petti and H. W. Bartels, "A review of dust in fusion devices: Implications for safety and operational performance," *Fusion Engineering and Design*, Vols. 63-64, pp. 153-163, 2002.
- [44] D. R. Quisenberry, "Environmental aspects of tritium," *Environmental Pollution (1970)*, vol. 20, no. 1, pp. 33-42, 1979.
- [45] G. Federici, R. A. Anderl, P. Andrew, J. N. Brooks, R. A. Causey, J. P. Coad, D. D. R. Cowgill, A. Haasz, G. Janeschitz, W. Jacob, G. Longhurst, R. Nygren, A. Peacock, M. P. V. Pick, J. Roth, C. Skinner and W. W.R., "In-vessel tritium retention and removal in ITER," *Journal of Nuclear Materials*, Vols. 266-269, pp. 14-29, 1999.
- [46] V. Philipps, P. Mertens, G. F. Matthews, H. Maier and JET-EFDA contributors, "Overview of the JET ITER-like Wall Project," *Fusion Engineering and Design*, vol. 85, p. 1581–1586, 2010.
- [47] "TCV surface and edge diagnostics," [Online]. Available: <http://crppwww.epfl.ch/tcv/diag/edgeb.htm>. [Accessed 2013 August 29].
- [48] J. Ali, C. Berre and P. M. Mummery, "Image based modelling of stress-strain behaviour in carbon/carbon composites," *Energy Materials: Materials Science and Engineering for Energy Systems*, vol. 1, no. 3, pp. 179-186, 2006.
- [49] P. M. Mummery, "Composites," [Online]. Available: <http://wiki.rac.manchester.ac.uk/community/ImageBasedModelling/Presentations?action=AttachFile&do=get&target=composites.pdf>. [Accessed 27 November

- 2013].
- [50] S. Min, J. Blumm and A. Lindemann, "A new laser flash system for measurement of the thermophysical properties," *Thermochimica Acta*, vol. 455, no. 1-2, pp. 46-49, 2007.
- [51] W. J. Parker, R. J. Jenkins, C. P. Butler and G. L. Abbott, "Flash Method of Determining Thermal Diffusivity, Heat Capacity, and Thermal Conductivity," *J. Appl. Phys.*, vol. 32, no. 9, pp. 1679-1684, 1961.
- [52] H. S. Carslaw and J. C. Jaeger, in *Conduction of Heat in Solids*, Oxford, Clarendon Press, 1959, p. 101.
- [53] "3D Computed Tomography (Cone beam)," [Online]. Available: [http://www.phoenix-xray.com/en/company/technology/principles\\_of\\_operation/principle\\_060.html](http://www.phoenix-xray.com/en/company/technology/principles_of_operation/principle_060.html) . [Accessed 29 August 2013].
- [54] C. Berre, S. L. Fok, B. J. Marsden, L. Babout, A. Hodgkins, T. J. Marrow and M. P. M., "Numerical modelling of the effects of porosity changes on the mechanical properties of nuclear graphite," *Journal of Nuclear Materials*, vol. 352, no. 1-3, pp. 1-5, 2006.
- [55] G. T. Herman, *Fundamentals of Computerized Tomography: Image Reconstruction from Projections* 2nd Ed., London: Springer, 2009.
- [56] W. Kalender, *Computed Tomography* 3rd Ed., Erlangen: Publicis Publishing, 2011.
- [57] T. M. Buzug, *Computed Tomography: From Photon Statistics to Modern Cone-Beam CT*, Verlag Berlin Heidelberg: Springer, 2008.
- [58] "Beam hardening: calibration correction," [Online]. Available: <http://www.impactscan.org/slides/impactcourse/artefacts/img9.html>. [Accessed 30 November 2013].
- [59] Z. Fouriea, J. Damstraa, R. H. Schepersb, P. O. Gerritsc and Y. Rena, "Segmentation process significantly influences the accuracy of 3D surface models derived from cone beam computed tomography," *European Journal of Radiology*, vol. 81, no. 4, pp. e524-e530, 2012.
- [60] "EyeWire," [Online]. Available: <http://eyewire.org/>. [Accessed 01 December 2013].
- [61] R. J. Giuly, K. Kim and M. H. Ellisman, "DP2: Distributed 3D image segmentation using micro-labor workforce," *Bioinformatics*, vol. 29, no. 10, pp. 1359-1360, 2013.
- [62] S. E. Benzley, E. Perry, K. Merkley, B. Clark and G. Sjaardema, "A Comparison of All-Hexahedral and All-Tetrahedral Finite Element Meshes for Elastic and Elasto-

- Plastic Analysis,” in *Proceedings of 4th international meshing roundtable*, Sandia National Laboratories, 1995, p. 179–191.
- [63] Simpleware, “ScanIP - meshing and exporting,” in *ScanIP, ScanFE and ScanCAD Reference Guide, Version 4.0*, Simpleware Ltd., UK, 2010, pp. 161–186.
- [64] “Gridgen Application - Helical Intake Port,” [Online]. Available: [www.pointwise.com/apps/helical.shtml](http://www.pointwise.com/apps/helical.shtml). [Accessed 29 August 2013].
- [65] G. R. Liu and S. S. Quek, in *The Finite Element Method, A practical course*, Butterworth-Heinemann, 2003, pp. 1–11.
- [66] I. M. Smith, D. V. Griffiths and L. Margetts, *Programming the Finite Element Method* 5th Ed., Chichester: Wiley, 2013.
- [67] R. W. Lewis, P. Nithiarasu and K. N. Seetharamu, *Fundamentals of the Finite Element Method for Heat and Fluid Flow*, Chichester: Wiley, 2004.
- [68] “Input - ParaFEM ASCII input decks explained,” [Online]. Available: <https://code.google.com/p/parafem/wiki/Input>. [Accessed 29 August 2013].
- [69] “ParaView - Open Source Scientific Visualization,” [Online]. Available: <http://www.paraview.org/>. [Accessed 15 July 2013].
- [70] “ITER - the way to new energy,” [Online]. Available: <http://www.iter.org/proj/itermission>. [Accessed 25 July 2013].
- [71] R. Tivey, T. Ando, A. Antipenkov, V. Barabash, S. Chiocchio, G. Federici, C. Ibbott, R. Jakeman, G. Janeschitz, R. Raffray, M. Akiba, I. Mazul, H. Pacher, M. Ulrickson and G. Vieider, “ITER divertor, design issues and research and development,” *Fusion Engineering and Design*, vol. 46, no. 2–4, pp. 207–220, 1999.
- [72] E. Rigal, P. Bucci and G. Le Marois, “Fabrication of monoblock high heat flux components for ITER divertor upper vertical target using hot isostatic pressing diffusion welding,” *Fusion Engineering and Design*, Vols. 49–50, pp. 317–322, 2000.
- [73] A. Kukushkin, H. Pacher, V. Kotov, G. Pacher and D. Reiter, “Finalizing the ITER divertor design: The key role of SOLPS modeling,” *Fusion Engineering and Design*, vol. 86, no. 12, pp. 2865–2873, 2011.
- [74] R. Pitts, A. Kukushkin, A. Loarte, A. Martin, M. Merola and C. Kessel, “Status and physics basis of the ITER divertor,” *Physica Scripta*, vol. T138, p. 014001, 2009.
- [75] M. Merola and G. Vieider, “On the use of flat tile armour in high heat flux components,” *Journal of Nuclear Materials*, vol. 258–263, no. Part 1, pp. 672–676, 1998.

- [76] V. Casalegno, M. Salvo, S. Murdaca and M. Ferraris, "One-step brazing process for CFC monoblock joints and mechanical testing," *Journal of Nuclear Materials*, vol. 393, no. 2, pp. 300-305, 2009.
- [77] B. Schedler, T. Huber, T. Friedrich, E. Eidenberger, M. Kapp, C. Scheu, R. Pippan and H. Clemens, "Characteristics of an optimized active metal cast joint between copper and C/C," *Physica Scripta*, vol. T128, pp. 200-203, 2007.
- [78] P. Appendino, M. Ferraris, V. Casalegno, M. Salvo and M. Merola, "Proposal for a new technique to join CFC composites to copper," *Journal of Nuclear Materials*, vol. 348, pp. 102-107, 2006.
- [79] E. Visca, S. Libera, A. Mancini, G. Mazzone, A. Pizzuto and C. Testani, "Hot radial pressing: an alternative technique for the manufacturing of plasma-facing components," *Fusion Engineering and Design*, Vols. 75-79, pp. 485-489, 2005.
- [80] M. Bisio, V. Branca, M. Di Marco, A. Federici, M. Grattarola, C. Gualco, P. Guarnone, U. Luconi, M. Merola, C. Ozzano, G. Pasquale, P. Poggi, S. Rizzo and F. Varone, "Manufacturing and testing in reactor relevant conditions of brazed plasma facing components of the ITER divertor," *Fusion Engineering and Design*, Vols. 75-79, pp. 277-283, 2005.
- [81] M. Salvo, V. Casalegno, S. Rizzo, F. Smeacetto, F. Ferraris and M. Merola, "One-step brazing process to join CFC composites to copper and copper alloy," *Journal of Nuclear Materials*, vol. 374, pp. 69-74, 2008.
- [82] K. Ezato, M. Dairaku, M. Taniguchi, K. Sato, S. Suzuki, M. Akiba, C. Ibbott and R. Tivey, "Development of ITER divertor vertical target with annular flow concept - II: development of brazing technique for CFC/CuCrZr joint and heating test of large-scale mock-up," *Fusion Science and Technology*, vol. 46, no. 4, pp. 530-540, 2004.
- [83] P. Appendino, M. Ferraris, V. Casalegno, M. Salvo, M. Merola and M. Grattarola, "Direct joining of CFC to copper," *Journal of Nuclear Materials*, Vols. 329-333, no. Part B, pp. 1563-1566, 2004.
- [84] V. Casalegno, T. Koppitz, G. Pintsuk, M. Salvo, S. Rizzo, S. Perero and M. Ferraris, "Proposal for a new brazing alloy for joining CFC composites to copper," *Composites Part B: Engineering*, vol. 56, pp. 882-888, 2014.
- [85] O. Abdel Gawad, M. H. Abou Tabl, Z. Abdel Hamid and S. F. Mostafa, "Electroplating of chromium and Cr-carbide coating for carbon fiber," *Surface and Coatings Technology*, vol. 201, no. 3-4, pp. 1357-1362, 2006.
- [86] R. D. Cowan, "Pulse Method of Measuring Thermal Diffusivity at High Temperatures," *J. Appl. Phys.*, vol. 34, no. 4, pp. 926-927, 1963.
- [87] R. Taylor, J. Jortner and H. Groot, "Thermal diffusivity of fiber-reinforced

- composites using the laser flash technique,” *Carbon*, vol. 23, no. 2, pp. 215-222, 1985.
- [88] “MXIF,” [Online]. Available: <http://www.mxif.manchester.ac.uk/>. [Accessed 25 July 2013].
- [89] V. Casalegno, M. Salvo, M. Ferraris, F. Smeacetto, M. Merola and M. Bettuzzi, “Non-destructive characterization of carbon fiber composite/Cu joints for nuclear fusion applications,” *Fusion Engineering and Design*, vol. 83, no. 5-6, pp. 792-712, 2008.
- [90] R. W. Clough, “The Finite Element Analysis in Plane Stress Analysis,” in *Proc 2nd ASCE Conf. on Electronic Computation*, Pittsburgh, PA, 1960.
- [91] O. C. Zienkiewicz and K. Cheung, “Finite elements in the solution of field problems,” *Engineer*, vol. 200, pp. 507-510, 1965.
- [92] H. J. Kim, I. E. Vignon-Clementel, C. A. Figueroa, K. E. Jansen and C. A. Taylor, “Developing computational methods for three-dimensional finite element simulations of coronary blood flow,” *Finite Elements in Analysis and Design*, vol. 46, pp. 514-525, 2010.
- [93] R. Hambli, “Numerical procedure for multiscale bone adaptation prediction based on neural networks and finite element simulation,” *Finite Elements in Analysis and Design*, vol. 47, pp. 835-842, 2011.
- [94] P. Young, T. Beresford-West, S. Coward, B. Notarberardino, B. Walker and A. Abdul-Aziz, “An efficient approach to converting three-dimensional image data into highly accurate computational models,” *Philosophical Transactions of The Royal Society A*, vol. 366, no. 1878, pp. 3155-3173, 2008.
- [95] S. Shaw and M. Dunbar, “Abaqus FEA Software on Multi-Core HP Servers,” Hewlett-Packard Development Company, Richardson, TX, USA, 2007.
- [96] J. H. Kim, C. S. Lee and S. J. Kim, “Development of a high-performance domain-wise parallel direct solver for large-scale structural analysis,” in *Proceedings of the Seventh International Conference on High Performance Computing and Grid*, Asia Pacific Region, 2004.
- [97] O. Goury, “Analysis and Optimisation of a parallel finite element code,” MSc Dissertation, The University of Edinburgh, UK, 2010.
- [98] “Code\_aster - Software - EDF R&D,” [Online]. Available: <http://research.edf.com/research-and-the-scientific-community/software/code-aster-44332.html>. [Accessed 15 July 2013].
- [99] “ParaFEM,” [Online]. Available: <http://www.parafem.org.uk>. [Accessed 15 July 2013].

- [100] L. Margetts, Parallel Finite Element Analysis, PhD Thesis, University of Manchester, UK, 2002.
- [101] W. Gropp, E. Lusk and A. Skjellum, Using MPI, 2nd Edition: Portable Parallel Programming with the Message Passing Interface, Cambridge, MA, USA: MIT Press Scientific And Engineering Computation Series, 1999.
- [102] M. Snir, S. Otto, S. Huss-Lederman, D. Walker and J. Dongarra, MPI: The Complete Reference, Cambridge, MA, USA: MIT Press, 1995.
- [103] P. Kerfriden, O. Goury, T. Rabczuk and S. P. A. Bordas, "A partitioned model order reduction approach to rationalise computational expenses in nonlinear fracture mechanics," *Computer Methods in Applied Mechanics and Engineering*, vol. 256, no. 1, pp. 169-188, 2013.
- [104] H. S. Carslaw and J. C. Jaeger, "VI. The flow of heat in a rectangular parallelepiped," in *Conduction of Heat in Solids*, Oxford, Clarendon Press, 1959, pp. 184-185.
- [105] "xx12.f90 - parafem," [Online]. Available: <http://code.google.com/p/parafem/source/browse/trunk/parafem/src/programs/dev/xx12/xx12.f90?r=1445>. [Accessed 15 July 2013].
- [106] G. Söderlind and L. Wang, "Adaptive Time-Stepping and Computational Stability," *Journal of Computational Methods in Sciences and Engineering*, vol. 2, no. 3, pp. 1-3, 2003.
- [107] "A blast of heat for ITER's plasma-facing components," [Online]. Available: <http://www.iter.org/newsline/251/1436>. [Accessed 31 July 2013].
- [108] Ll. M. Evans, "Thermal Characterisation of Ceramic/Metal Joining Techniques for Fusion Applications Using X-ray Tomography," *Journal of Nuclear Materials*, vol. v, p. pp, 2013. (PhD Thesis, Chapter 4)
- [109] P. Appendino, V. Casalegno, M. Ferraris, M. Grattarola, M. Merola and M. Salvo, "Direct joining of CFC to copper," *Journal of Nuclear Materials*, Vols. 329-333, Part B, p. 1563–1566, 2004.
- [110] "3D images to RP, CAD, FE and CFD models with Simpleware software," [Online]. Available: <http://www.simpleware.com>. [Accessed 31 July 2013].
- [111] Ll. M. Evans, "Thermal finite element analysis on massively parallel computing platforms," *Finite Elements in Analysis and Design*, 2013. (PhD Thesis, Chapter 5)
- [112] I. M. Smith and L. Margetts, "The Convergence Variability of Parallel Iterative Solvers," *Engineering Computations*, vol. 23, no. 2, pp. 154-165, 2006.
- [113] "Mechanical & Physical Properties," [Online]. Available: <http://www.wesgometals.com/resources/mechanical-physical-properties/>.

[Accessed 31 July 2013].

- [114] W. M. Haynes, T. J. Bruno and D. R. Lide, “Thermophysical Properties of Air,” in *94th Edition of the Handbook of Chemistry and Physics*, Boca Raton, FL, CRC Press/Taylor and Francis Group, 2013, pp. 6-18.
- [115] J. Linke, M. Akiba, H. Bolt, G. Breitbach, R. Duwe, A. Makhankov, I. Ovchinnikov, M. Rödiger and E. Wallura, “Performance of Beryllium, Carbon and Tungsten under intensive thermal fluxes,” *Journal of Nuclear Materials*, Vols. 241-243, pp. 1210-1216, 1997.



## Appendix

### A: Nikon Metrology 225/320 kV system at Manchester X-ray Imaging Facility



**Figure A.1.** Nikon Metrology 225/320 kV system.

- Housed in a walk-in radiation bay.
- Heavy-duty 5-axis sample manipulator stage with a 100kg load capacity. Provided with an extendible jib crane for heavy sample and/or sample rig handling.
- Provided with a labyrinth for the external control and monitoring of User-installed equipment.
- Optional X-ray sources available:
  - 225kV (225W) high-energy microfocus X-ray source with a  $3\mu\text{m}$  spot size.
  - 100kV positive module for attachment to the 225kV source for up to 320kV X-ray energies.
  - 225kV rotating anode source with a tungsten target.
- $2\text{k} \times 2\text{k}$  Perkin Elmer 1621 XRD 16-bit amorphous silicon flat-panel detector with  $\sim 200\mu\text{m}$  pixel pitch.
- Maximum field of view is  $\sim 410\text{mm} \times 410\text{mm}$ .



**B: Netzsch 457 MicroFlash®**

**Figure B.2.** Netzsch 457 MicroFlash®.

- Temperature range: -125 °C to 500 °C, RT to 1100 °C, (2 exchangeable furnaces)
- Heating- and cooling rates: 0.01 K·min<sup>-1</sup> to 50 K·min<sup>-1</sup>
- Laser pulse energy: up to 18 J·pulse<sup>-1</sup>, (adjustable power)
- Contactless measurement of temperature rise with IR detector
- Measuring range: 0.01 mm<sup>2</sup>·s<sup>-1</sup> to 1000 mm<sup>2</sup>·s<sup>-1</sup> (thermal diffusivity)
- Measuring range: 0.1 W·mK<sup>-1</sup> to 2000 W·mK<sup>-1</sup> (thermal conductivity)
- Sample dimensions: 10 mm to 25.4 mm diameter (also 8x8 mm and 10x10 mm, square) 0.1 mm to 6 mm thickness
- Sample holder: SiC, graphite
- Liquid metal holder : sapphire
- Sample holder for liquids: platinum
- Atmosphere: inert, oxidizing, reducing, static, dynamic
- Vacuum-tight assembly up to 10<sup>-2</sup> mbar (1 Pa)



**C: FORTRAN code for pre-processing of load distribution for LFA simulation**

```

PROGRAM gaussianlds
!-----
!       Program gaussianlds Pre-processing tool to produce .lds input file
!                               which simulates the thermal flux from a laser
!                               flash analysis pulse
!-----

USE precision ; USE global_variables ; USE mp_interface
USE input     ; USE output           ; USE loading
USE timing    ; USE maths            ; USE gather_scatter
USE partition ; USE elements          ; USE steering
USE geometry  ; USE pcg               ; USE new_library

IMPLICIT NONE

!-----
! 1. Declare variables used in the main program
!-----

! neq,ntot are now global variables - not declared

INTEGER, PARAMETER :: ndim=3,nodof=1,nprops=5
INTEGER              :: nod,nn,nr,nip
INTEGER              :: i,j,k,l,itors,limit,iel
INTEGER              :: nxe,nye,nze,neq_temp,nn_temp
INTEGER              :: nstep,npri,nres,it,is,nlen
INTEGER              :: node_end,node_start,nodes_pp
INTEGER              :: loaded_freedoms,fixed_freedoms,loaded_nodes
INTEGER              :: fixed_freedoms_pp,fixed_freedoms_start
INTEGER              :: loaded_freedoms_pp,loaded_freedoms_start
INTEGER              :: nels,ndof,ielpe,npes_pp
INTEGER              :: argc,iargc,meshgen,partitioner
INTEGER              :: np_types,nsurf
INTEGER              :: prog,tz
REAL(iwp)            :: aa,bb,cc,kx,ky,kz,det,theta,dtim,real_time
REAL(iwp)            :: tol,alpha,beta,up,big,q
REAL(iwp)            :: rho,cp,val0
REAL(iwp)            :: sigma,Rad,PI,area_face,area_fraction,area_total
REAL(iwp)            :: Fn,xmax,xmin,xc,ymax,ymin,yc,r
REAL(iwp),PARAMETER :: zero = 0.0_iwp,penalty=1.e20_iwp
REAL(iwp),PARAMETER :: t0 = 0.0_iwp
CHARACTER(LEN=15)    :: element
CHARACTER(LEN=50)    :: fname,job_name,label
CHARACTER(LEN=50)    :: program_name='xx12'
LOGICAL              :: converged = .false.

!-----
! Sections 2 - 9 are essentially identical to that found in program xx12
!-----

!-----
! 10. Allocate disp_pp array and open file to write temperature output
!-----

CALL calc_nodes_pp(nn,npes,numpe,node_end,node_start,nodes_pp)
ALLOCATE(disp_pp(nodes_pp))
ALLOCATE(eld_pp(ntot,nels_pp))
ALLOCATE(lds(nodes_pp*ndim))

```

```

!---Open file for loads outputs in ParaFEM format
IF(numpe==1) THEN
  fname = job_name(1:INDEX(job_name, " ")-1)//".lds2"
  OPEN(24, file=fname, status='replace', action='write')
  label = "*LOADS"
END IF

IF(numpe==1) PRINT *, "End of 10"

!-----
! 11. Calculate loads
!-----

lds=zero
Fn      = 4.738
sigma   = 10.892
Rad      = 7.5
PI       = 4.0*ATAN(1.0)
area_total = PI*(Rad**2)

ALLOCATE(surf(nels_pp,2))
CALL read_surface(job_name,numpe,surf,nsurf)

!Tet numbering S&G (1,2,3,4) = Abaqus (1,3,2,4)
ALLOCATE(surf2nd(4,3))
surf2nd(1,:)=(/1,2,3/)
surf2nd(2,:)=(/1,2,4/)
surf2nd(3,:)=(/2,3,4/)
surf2nd(4,:)=(/1,3,4/)

ALLOCATE(x(4),y(4))
xmax=-1E34
xmin=1E34
ymax=-1E34
ymin=1E34

! Loop through all nodes to find min/max of x,y coord
DO i=1,nels_pp
  num=g_num_pp(:,i)
  DO j = 1,nod
    x(j)=g_coord_pp(j,1,i)
    y(j)=g_coord_pp(j,2,i)
  END DO
  IF (MAXVAL(x)>xmax) xmax=MAXVAL(x)
  IF (MINVAL(x)<xmin) xmin=MINVAL(x)
  IF (MAXVAL(y)>ymax) ymax=MAXVAL(y)
  IF (MINVAL(y)<ymin) ymin=MINVAL(y)
END DO

WRITE(*,'(A,2E12.4)') "xrange = ",xmin,xmax
WRITE(*,'(A,2E12.4)') "yrange = ",ymin,ymax

xc = (xmax-xmin)/2
yc = (ymax-ymin)/2
WRITE(*,'(A,2E12.4)') "Centre coords (x,y) = ",xc,yc

DEALLOCATE(x,y)
ALLOCATE(x(3),y(3),MGD(3))

! Loop through surface elements to calculate area fraction of faces
IF(numpe==1)WRITE(*,'(A,I5,A)') "This job ran on ",npes," processors"

```

```

DO i=1,nsurf
  j = surf(i,1)
  num=g_num_pp(:,j)

  DO k = 1,3
    l = surf2nd(surf(i,2),k)
    x(k)=g_coord_pp(1,1,j)
    y(k)=g_coord_pp(1,2,j)
    r = sqrt((x(k)-xc)**2 +(y(k)-yc)**2)
    MGD(k) = (1/(2*PI*(sigma**2)))*EXP((-1/2)*((r/sigma)**2))
  END DO

  area_face=(abs(x(1)*(y(2)-y(3))+x(2)*(y(3)-y(1))+x(3)*(y(1)-y(2))))/2
  area_fraction=area_face/area_total

  DO k = 1,3
    l = surf2nd(surf(i,2),k)
    lds(num(l)*3-2) = lds(num(l)*3-2)+MGD(k)*(area_fraction/3)
  END DO

END DO

!-----
! 12. Write loads to file
!-----

j=1
!---Write loads outputs in ParaFEM format
CALL write_nodal_variable(label,24,j,nodes_pp,npes,numpe,ndim,lds)

IF(numpe==1) PRINT *, "End of 12"

IF(numpe==1)THEN
  CLOSE(24)
END IF

CALL shutdown()

END PROGRAM gaussianlds

```





## **D: FORTRAN code for transient thermal FEA in parallel**

The following section is a comparison of the developed transient thermal parallel FE code (xx12) with a version of program p124 from Smith, Griffiths & Margetts [66] adapted to comply within the ParaFEM framework. The p124 code is shown on the even numbered pages with xx12 on the opposite odd numbered pages. Where possible it has been attempted to align complementary sections of the code to facilitate comparison.

```

PROGRAM p124
!-----
!       Program 12.4 conduction equation using 8-node hexahedral elements;
!       pcg version implicit; integration in time using 'theta' method
!       parallel version
!-----

USE precision ; USE global_variables ; USE mp_interface
USE input     ; USE output           ; USE loading
USE timing    ; USE maths            ; USE gather_scatter
USE geometry  ; USE new_library

IMPLICIT NONE

!-----
! 1. Declare variables used in the main program
!-----

! neq,ntot are now global variables - not declared

INTEGER, PARAMETER :: nodof=1,ndim=3
INTEGER              :: nod
INTEGER              :: nxe,nye,nze,nn,nr,nip,neq_temp,nn_temp,i,j
INTEGER              :: k,iel,nstep,npri,nres,itors,limit,it,is,nlen
INTEGER              :: loaded_nodes,fixed_freedoms
INTEGER              :: argc,iargc,meshgen,partitioner
INTEGER              :: nels,ndof,ielpe,npes_pp
REAL(iwp)            :: aa,bb,cc,kx,ky,kz,det,theta,dtim,real_time
REAL(iwp)            :: val0 = 100.0_iwp
REAL(iwp)            :: tol,alpha,beta,up,big
REAL(iwp),PARAMETER :: zero = 0.0_iwp
CHARACTER(LEN=15)    :: element
CHARACTER(LEN=50)    :: fname,job_name,label
CHARACTER(LEN=50)    :: program_name='p124'
LOGICAL              :: converged = .false.

!-----
! 2. Declare dynamic arrays
!-----

REAL(iwp),ALLOCATABLE :: loads_pp(:),u_pp(:),p_pp(:),points(:,:)
REAL(iwp),ALLOCATABLE :: coord(:,:),fun(:),jac(:,:),der(:,:),deriv(:,:)
REAL(iwp),ALLOCATABLE :: weights(:),d_pp(:),kc(:,:),pm(:,:),funny(:,:)
REAL(iwp),ALLOCATABLE :: p_g_co_pp(:,:,:),storka_pp(:,:,:),kay(:,:)
REAL(iwp),ALLOCATABLE :: storkb_pp(:,:,:),x_pp(:),xnew_pp(:)
REAL(iwp),ALLOCATABLE :: diag_precon_pp(:),diag_precon_tmp(:,:)
REAL(iwp),ALLOCATABLE :: g_coord_pp(:,:,:),timest(:)
REAL(iwp),ALLOCATABLE :: pmul_pp(:,:),utemp_pp(:,:)
INTEGER,ALLOCATABLE    :: rest(:,:),g(:),num(:),g_num_pp(:,:),g_g_pp(:,:)

```

```

PROGRAM xx12
!-----
!       Program XX.12 Three dimensional anallysis of conduction equation
!       using 8-node hexahedral elements; pcg version implicit;
!       integration in time using 'theta' method parallel version
!-----

USE precision ; USE global_variables ; USE mp_interface
USE input      ; USE output            ; USE loading
USE timing     ; USE maths             ; USE gather_scatter
USE partition  ; USE elements          ; USE steering
USE geometry   ; USE pcg               ; USE new_library

IMPLICIT NONE

!-----
! 1. Declare variables used in the main program
!-----

! neq,ntot are now global variables - not declared

INTEGER, PARAMETER :: ndim=3,nodof=1,nprops=5
INTEGER             :: nod,nn,nr,nip
INTEGER             :: i,j,k,l,itors,itorsT,limit,iel
INTEGER             :: nxe,nye,nze,neq_temp,nn_temp
INTEGER             :: nstep,npri,nres,it,is,nlen
INTEGER             :: node_end,node_start,nodes_pp
INTEGER             :: loaded_freedoms,fixed_freedoms,loaded_nodes
INTEGER             :: fixed_freedoms_pp,fixed_freedoms_start
INTEGER             :: loaded_freedoms_pp,loaded_freedoms_start
INTEGER             :: nels,ndof,ielp,npes_pp
INTEGER             :: argc,iargc,meshgen,partitioner
INTEGER             :: np_types
INTEGER             :: prog,tz
REAL(iwp)           :: aa,bb,cc,kx,ky,kz,det,theta,dtim,real_time
REAL(iwp)           :: tol,alpha,beta,up,big,q
REAL(iwp)           :: rho,cp,val0
REAL(iwp),PARAMETER :: zero = 0.0_iwp,penalty=1.e20_iwp
REAL(iwp),PARAMETER :: t0 = 0.0_iwp
CHARACTER(LEN=15)   :: element
CHARACTER(LEN=50)   :: fname,job_name,label
CHARACTER(LEN=50)   :: program_name='xx12'
LOGICAL             :: converged = .false.

!-----
! 2. Declare dynamic arrays
!-----

REAL(iwp),ALLOCATABLE :: loads_pp(:),u_pp(:),p_pp(:),points(:, :)
REAL(iwp),ALLOCATABLE :: coord(:, :),fun(:),jac(:, :),der(:, :),deriv(:, :)
REAL(iwp),ALLOCATABLE :: weights(:),d_pp(:),kc(:, :),pm(:, :),funny(:, :)
REAL(iwp),ALLOCATABLE :: p_g_co_pp(:, :, :),storka_pp(:, :, :),kay(:, :)
REAL(iwp),ALLOCATABLE :: storkb_pp(:, :, :),x_pp(:),xnew_pp(:)
REAL(iwp),ALLOCATABLE :: diag_precon_pp(:),diag_precon_tmp(:, :)
REAL(iwp),ALLOCATABLE :: g_coord_pp(:, :, :),timest(:)
REAL(iwp),ALLOCATABLE :: disp_pp(:),eld_pp(:, :)
REAL(iwp),ALLOCATABLE :: val(:, :),val_f(:),store_pp(:),r_pp(:)
REAL(iwp),ALLOCATABLE :: kcx(:, :),kcy(:, :),kcz(:, :)
REAL(iwp),ALLOCATABLE :: eld(:),col(:, :),row(:, :),storkc_pp(:, :, :)
REAL(iwp),ALLOCATABLE :: prop(:, :),amp(:),pmul_pp(:, :),utemp_pp(:, :)
INTEGER,ALLOCATABLE :: g(:),num(:),g_num_pp(:, :),g_g_pp(:, :),no(:)

```

```

!-----
! 3. Read job_name from the command line.
!   Read control data, mesh data, boundary and loading conditions
!-----

ALLOCATE(timest(25))
timest   = zero
timest(1) = elap_time()

CALL find_pe_procs(numpe,npes)
PRINT *, "FIND_PE_PROCS on processor ", numpe, " of ", npes

argc = iargc()
IF(argc /= 1) CALL job_name_error(numpe,program_name)
CALL GETARG(1,job_name)

CALL read_p124_4(job_name,numpe,dtim,element,fixed_freedoms,kx,ky,kz, &
                limit,loaded_nodes,meshgen,nels,nip,nn,nod,npri,nr, &
                nstep,partitioner,theta,tol)

CALL calc_nels_pp(job_name,nels,npes,numpe,partitioner,nels_pp)

ndof = nod*nodof
ntot = ndof

ALLOCATE(g_num_pp(nod,nels_pp))
ALLOCATE(g_coord_pp(nod,ndim,nels_pp))
ALLOCATE(rest(nr,nodof+1))

g_num_pp   = 0
g_coord_pp = zero
rest       = 0

timest(2) = elap_time()

CALL read_g_num_pp2(job_name,iel_start,nn,npes,numpe,g_num_pp)
timest(3) = elap_time()

IF(meshgen == 2) CALL abaqus2sg(element,g_num_pp)
timest(4) = elap_time()

CALL read_g_coord_pp(job_name,g_num_pp,nn,npes,numpe,g_coord_pp)
timest(5) = elap_time()

CALL read_rest(job_name,numpe,rest)
timest(6) = elap_time()

```

```

INTEGER,ALLOCATABLE    :: no_pp(:),no_f_pp(:),no_pp_temp(:)
INTEGER,ALLOCATABLE    :: sense(:),node(:),rest(:,:)
INTEGER,ALLOCATABLE    :: etype_pp(:)

!-----
! 3. Read job_name from the command line.
!   Read control data, mesh data, boundary and loading conditions
!-----

ALLOCATE(timest(25))
timest   = zero
timest(1) = elap_time()

CALL find_pe_procs(numpe,npes)
PRINT *, "FIND_PE_PROCS on processor ", numpe, " of ", npes

argc = iargc()
IF(argc /= 1) CALL job_name_error(numpe,program_name)
CALL GETARG(1,job_name)

CALL read_xx12(job_name,numpe,dtim,element,fixed_freedoms,limit,      &
               loaded_nodes,meshgen,nels,nip,nn,nod,npri,nr,nstep,    &
               partitioner,theta,tol,np_types,val0,nres)

CALL calc_nels_pp(job_name,nels,npes,numpe,partitioner,nels_pp)

ndof = nod*nodof
ntot = ndof

ALLOCATE(g_num_pp(nod,nels_pp))
ALLOCATE(g_coord_pp(nod,ndim,nels_pp))
IF (nr>0) ALLOCATE(rest(nr,nodof+1))
ALLOCATE(etype_pp(nels_pp))
ALLOCATE(prop(nprops,np_types))

g_num_pp      = 0
g_coord_pp    = zero
IF (nr>0) rest = 0
etype_pp      = 0
prop          = zero
q             = zero

timest(2) = elap_time()

CALL read_elements(job_name,iel_start,nn,npes,numpe,etype_pp,g_num_pp)
timest(3) = elap_time()

IF(meshgen == 2)THEN
  PRINT *, "Calling abaqus2sg, meshgen = ", meshgen
  CALL abaqus2sg(element,g_num_pp)
END IF
timest(4) = elap_time()

CALL read_g_coord_pp(job_name,g_num_pp,nn,npes,numpe,g_coord_pp)
timest(5) = elap_time()

IF (nr>0) CALL read_rest(job_name,numpe,rest)
timest(6) = elap_time()

PRINT *, "np_types = ", np_types

```

```

IF(numpe==1) PRINT *, " *** Read input data in: ",           &
                    timest(6)-timest(1)," s"

!-----
! 4. Allocate dynamic arrays used in main program
!-----

ALLOCATE (points(nip,ndim),weights(nip),kay(ndim,ndim),      &
          coord(nod,ndim),fun(nod),jac(ndim,ndim),der(ndim,nod), &
          g(ntot),deriv(ndim,nod),pm(ntot,ntot),           &
          kc(ntot,ntot),funny(1,nod),num(nod),             &
          g_g_pp(ntot,nels_pp),storka_pp(ntot,ntot,nels_pp), &
          utemp_pp(ntot,nels_pp),storkb_pp(ntot,ntot,nels_pp), &
          pmul_pp(ntot,nels_pp))

IF(numpe==1) PRINT *, " *** Allocated dynamic arrays in: ",   &
                    elap_time()-timest(6)," s"

!-----
! 5. Loop the elements to find the steering array and the number of
!    equations to solve.
!-----

CALL rearrange_2(rest)

g_g_pp = 0

elements_1: DO iel = 1, nels_pp
  CALL find_g4(g_num_pp(:,iel),g_g_pp(:,iel),rest)
END DO elements_1

neq = 0

elements_2: DO iel = 1, nels_pp
  i = MAXVAL(g_g_pp(:,iel))
  IF(i > neq) neq = i
END DO elements_2

neq = MAX_INTEGER_P(neq)

timest(7) = elap_time()

```

```

fname = job_name(1:INDEX(job_name, " ")-1) // ".mat"
CALL read_materialValue(prop,fname,numpe,npes)

IF(numpe==1) PRINT *, " *** Read input data in: ",           &
                    timest(6)-timest(1)," s"

!-----
! 4. Allocate dynamic arrays used in main program
!-----

ALLOCATE (points(nip,ndim),weights(nip),kay(ndim,ndim),      &
          coord(nod,ndim),fun(nod),jac(ndim,ndim),der(ndim,nod), &
          g(ntot),deriv(ndim,nod),pm(ntot,ntot),           &
          kc(ntot,ntot),funny(1,nod),num(nod),             &
          g_g_pp(ntot,nels_pp),storka_pp(ntot,ntot,nels_pp), &
          utemp_pp(ntot,nels_pp),storkb_pp(ntot,ntot,nels_pp), &
          pmul_pp(ntot,nels_pp))
ALLOCATE (kcx(ntot,ntot),kcy(ntot,ntot),kcz(ntot,ntot), eld(ntot), &
          col(ntot,1),row(1,ntot),storkc_pp(ntot,ntot,nels_pp))
ALLOCATE (amp(nstep))

IF(numpe==1) PRINT *, " *** Allocated dynamic arrays in: ",   &
                    elap_time()-timest(6)," s"

!-----
! 5. Loop the elements to find the steering array and the number of
!    equations to solve.
!-----

IF (nr>0) CALL rearrange_2(rest)

g_g_pp = 0

! When nr = 0, g_num_pp and g_g_pp are identical
IF(nr>0) THEN
  elements_1: DO iel = 1, nels_pp
    CALL find_g4(g_num_pp(:,iel),g_g_pp(:,iel),rest)
  END DO elements_1
  DEALLOCATE(rest)
ELSE
  g_g_pp = g_num_pp
END IF

neq = 0

elements_2: DO iel = 1, nels_pp
  i = MAXVAL(g_g_pp(:,iel))
  IF(i > neq) neq = i
END DO elements_2

neq = MAX_INTEGER_P(neq)

timest(7) = elap_time()
IF(numpe==1) PRINT *, "End of 5"

```

```

!-----
! 6. Create interprocessor communication tables
!-----

CALL calc_neq_pp
CALL calc_npes_pp(npes,npes_pp)
CALL make_ggl2(npes_pp,npes,g_g_pp)

nres = nxe*(nze-1) + 1

DO i = 1,neq_pp
  IF(nres==ieq_start+i-1) THEN
    it = numpe; is = i
  END IF
END DO

timest(8) = elap_time()

IF(numpe==1) PRINT *, " *** Created ggl in: ",           &
                    timest(8)-timest(7), " s"

!-----
! 7. Allocate arrays dimensioned by neq_pp
!-----

ALLOCATE(loads_pp(neq_pp),diag_precon_pp(neq_pp),u_pp(neq_pp),           &
          d_pp(neq_pp),p_pp(neq_pp),x_pp(neq_pp),xnew_pp(neq_pp))

loads_pp = zero ; diag_precon_pp = zero ; u_pp = zero
d_pp      = zero ; p_pp              = zero ; x_pp = zero ; xnew_pp = zero

timest(9) = elap_time()

IF(numpe==1) PRINT *, " *** Allocated arrays dimensioned by neq_pp      &
                    in: ", timest(9)-timest(8), " s"

!-----
! 8. Element stiffness integration and storage
!-----

CALL sample(element,points,weights)

storka_pp = zero
storkb_pp = zero

kay       = zero
kay(1,1)  = kx
kay(2,2)  = ky
kay(3,3)  = kz

elements_3: DO iel=1,nels_pp

  kc = zero ; pm = zero

```



```

!-----
! 6. Create interprocessor communication tables
!-----

CALL calc_neq_pp
CALL calc_npes_pp2(npes,npes_pp)
CALL make_ggl(npes_pp,npes,g_g_pp)

DO i = 1,neq_pp
  IF(nres==ieq_start+i-1) THEN
    it = numpe; is = i
    IF(numpe==it) PRINT *, " *** it = ", it, " is = ", i
  END IF
END DO

timest(8) = elap_time()
IF(numpe==1) PRINT *, "End of 6"

!-----
! 7. Allocate arrays dimensioned by neq_pp
!-----

ALLOCATE(loads_pp(neq_pp),diag_precon_pp(neq_pp),u_pp(neq_pp),      &
          d_pp(neq_pp),p_pp(neq_pp),x_pp(neq_pp),                  &
          xnew_pp(neq_pp),r_pp(neq_pp))

loads_pp = zero ; diag_precon_pp = zero ; u_pp = zero ; r_pp      = zero
d_pp      = zero ; p_pp              = zero ; x_pp = zero ; xnew_pp = zero

timest(9) = elap_time()
IF(numpe==1) PRINT *, "End of 7"

!-----
! 8. Element stiffness integration and storage
!-----

CALL sample(element,points,weights)

storka_pp = zero
storkb_pp = zero

elements_3: DO iel=1,nels_pp

  kay      = zero
  kay(1,1) = prop(1,etype_pp(iel)) ! kx
  kay(2,2) = prop(2,etype_pp(iel)) ! ky
  kay(3,3) = prop(3,etype_pp(iel)) ! kz
  rho      = prop(4,etype_pp(iel)) ! rho
  cp       = prop(5,etype_pp(iel)) ! cp

  kc = zero ; pm = zero

```

```

gauss_pts: DO i=1,nip
  CALL shape_der(der,points,i)
  CALL shape_fun(fun,points,i)
  funny(1,:) = fun(:)
  jac      = MATMUL(der,g_coord_pp(:, :, iel))
  det      = determinant(jac)
  CALL invert(jac)
  deriv    = MATMUL(jac,der)
  kc       = kc +
            MATMUL(MATMUL(TRANSPPOSE(deriv),kay),deriv)*det*weights(i) &
  pm       = pm + MATMUL(TRANSPPOSE(funny),funny)*det*weights(i)
END DO gauss_pts

storka_pp(:, :, iel)=pm+kc*theta*dtim
storkb_pp(:, :, iel)=pm-kc*(1._iwp-theta)*dtim

END DO elements_3

timest(10) = elap_time()

!-----
! 9. Build the diagonal preconditioner
!-----

ALLOCATE(diag_precon_tmp(ntot,nels_pp))
diag_precon_tmp = zero

elements_4: DO iel = 1,nels_pp
  DO k=1,ntot
    diag_precon_tmp(k,iel)=diag_precon_tmp(k,iel)+storka_pp(k,k,iel)
  END DO
END DO elements_4

CALL scatter(diag_precon_pp,diag_precon_tmp)

DEALLOCATE(diag_precon_tmp)

diag_precon_pp=1._iwp/diag_precon_pp ! needs moving

!-----
! 10. Read in the initial conditions and assign to equations
!-----

loads_pp = val0      ! needs to be read in from file
pmul_pp  = .0_iwp

IF(numpe==it)THEN
  fname = job_name(1:INDEX(job_name, " ")-1) // ".res"
  OPEN(11,FILE=fname,STATUS='REPLACE',ACTION='WRITE')
  WRITE(11,'(A)') "      Time      Pressure  Iterations"
END IF

```

```

gauss_pts: DO i=1,nip
  CALL shape_der(der,points,i)
  CALL shape_fun(fun,points,i)
  funny(1,:) = fun(:)
  jac      = MATMUL(der,g_coord_pp(:, :, iel))
  det      = determinant(jac)
  CALL invert(jac)
  deriv    = MATMUL(jac,der)
  kc       = kc +
            MATMUL(MATMUL(TRANPOSE(deriv),kay),deriv)*det*weights(i) &
  pm       = pm +
            MATMUL(TRANPOSE(funny),funny)*det*weights(i)*rho*cp &
END DO gauss_pts

storka_pp(:, :, iel)=pm+kc*theta*dtim
storkb_pp(:, :, iel)=pm-kc*(1._iwp-theta)*dtim

END DO elements_3

timest(10) = elap_time()
IF(numpe==1) PRINT *, "End of 8"

!-----
! 9. Build the diagonal preconditioner
!-----

ALLOCATE(diag_precon_tmp(ntot,nels_pp))
diag_precon_tmp = zero

elements_4: DO iel = 1,nels_pp
  DO k=1,ntot
    diag_precon_tmp(k,iel)=diag_precon_tmp(k,iel)+storka_pp(k,k,iel)
  END DO
END DO elements_4

CALL scatter(diag_precon_pp,diag_precon_tmp)

DEALLOCATE(diag_precon_tmp)

timest(11) = elap_time()
IF(numpe==1) PRINT *, "End of 9"

!-----
! 10. Allocate disp_pp array and open file to write temperature output
!-----

!---Open file for temperature outputs in Excel format
IF(numpe==it) THEN
  fname = job_name(1:INDEX(job_name, " ") -1) // ".ttr2"
  OPEN(11, FILE=fname, STATUS='REPLACE', ACTION='WRITE')
END IF

CALL calc_nodes_pp(nn,npes,numpe,node_end,node_start,nodes_pp)
ALLOCATE(disp_pp(nodes_pp))
ALLOCATE(eld_pp(ntot,nels_pp))

!---Open file for temperature outputs in ParaFEM format
IF(numpe==1) THEN
  fname = job_name(1:INDEX(job_name, " ") -1) // ".ttr"
  OPEN(24, file=fname, status='replace', action='write')
  fname = job_name(1:INDEX(job_name, " ") -1) // ".ttrb"

```



```

OPEN(25, file=fname, status='replace', action='write',
      access='sequential', form='unformatted')
fname = job_name(1:INDEX(job_name, " ") - 1) // ".npp"
OPEN(26, file=fname, status='replace', action='write')
label = "*TEMPERATURE"
WRITE(26,*) nn
WRITE(26,*) nstep/npri
WRITE(26,*) npes
END IF

IF(numpe==1) PRINT *, "End of 10"

!-----
! **. Moved steps 11 & 12 into time stepping loop,
!    Need to leave certain items outside
!-----

IF(fixed_freedoms > 0) THEN
  ALLOCATE(val_f(fixed_freedoms))
END IF

IF(numpe==1) PRINT *, "End of **"

!-----
! 11. Read in fixed nodal temperatures and assign to equations
!-----

IF(fixed_freedoms > 0) THEN

  ALLOCATE(node(fixed_freedoms),no(fixed_freedoms),
            no_pp_temp(fixed_freedoms),sense(fixed_freedoms))

  node = 0 ; no = 0 ; no_pp_temp = 0 ; sense = 0
  val_f = zero

  CALL read_fixed(job_name,numpe,node,sense,val_f)
  CALL find_no2(g_g_pp,g_num_pp,node,sense,no)

  CALL reindex(ieq_start,no,no_pp_temp,
               fixed_freedoms_pp,fixed_freedoms_start,neq_pp)

  ALLOCATE(no_f_pp(fixed_freedoms_pp),store_pp(fixed_freedoms_pp))

  no_f_pp = 0
  store_pp = zero
  no_f_pp = no_pp_temp(1:fixed_freedoms_pp)

  DEALLOCATE(node,no,sense,no_pp_temp)

END IF

IF(fixed_freedoms == 0) fixed_freedoms_pp = 0

timest(12) = elap_time()
IF(numpe==1) PRINT *, "End of 11"

```

```
!-----  
! 11. Time-stepping loop  
!-----  
  
timesteps: DO j=1,nstep  
  
    real_time = j*dtim  
    u_pp      = zero  
  
    CALL gather(loads_pp,pmul_pp)  
    elements_5: DO iel=1,nels_pp  
        utemp_pp(:,iel)=MATMUL(storkb_pp(:, :, iel),pmul_pp(:, iel))  
    END DO elements_5  
    CALL scatter(u_pp,utemp_pp)  
  
    loads_pp=u_pp
```

```

!-----
! 12. Invert the preconditioner.
!     If there are fixed freedoms, first apply a penalty
!-----

  IF(fixed_freedoms_pp > 0) THEN
    DO i = 1,fixed_freedoms_pp
      l = no_f_pp(i) - ieq_start + 1
      diag_precon_pp(l) = diag_precon_pp(l) + penalty
      store_pp(i)       = diag_precon_pp(l)
    END DO
  END IF

  diag_precon_pp = 1._iwp/diag_precon_pp

  IF(numpe==1) PRINT *, "End of 12"

!-----
! 13. Read in loaded nodes and get starting r_pp
!-----

  loaded_freedoms = loaded_nodes

  IF(loaded_freedoms > 0) THEN

    ALLOCATE(node(loaded_freedoms),val(nodof,loaded_freedoms))
    ALLOCATE(no_pp_temp(loaded_freedoms))

    val = zero ; node = 0

    CALL read_amplitude(job_name,numpe,nstep,amp)
    CALL read_loads(job_name,numpe,node,val)
    CALL reindex(ieq_start,node,no_pp_temp,loaded_freedoms_pp,      &
                loaded_freedoms_start,neq_pp)

    ALLOCATE(no_pp(loaded_freedoms_pp))

    no_pp      = no_pp_temp(1:loaded_freedoms_pp)

    DEALLOCATE(no_pp_temp)
    DEALLOCATE(node)

  END IF

  IF(numpe==1) PRINT *, "End of 13"

  timest(12) = elap_time()

!-----
! 14. Start time stepping loop
!-----

  itersT = 0
  timesteps: DO j=1,nstep

    timest(15) = elap_time()

    real_time = j*dtim

```





```

!-----
! 15. Apply loads (sources and/or sinks) supplied as a boundary value
!-----

      loads_pp = zero

      DO i = 1, loaded_freedoms_pp
        IF(amp(j)==0.0) THEN
          loads_pp(no_pp(i)-ieq_start+1) = val(loaded_freedoms_start+      &
                                                    i-1,1)*dtim*(1.0E-34)
        ELSE
          loads_pp(no_pp(i)-ieq_start+1) = val(loaded_freedoms_start+      &
                                                    i-1,1)*dtim*amp(j)
        END IF
      END DO

      q = q + SUM_P(loads_pp)

!-----
! 16. Compute RHS of time stepping equation, using storkb_pp, then add
!      result to loads
!-----

      u_pp          = zero
      pmul_pp       = zero
      utemp_pp      = zero

      IF(j/=1) THEN

        CALL gather(xnew_pp,pmul_pp)
        elements_2a: DO iel=1,nels_pp
          utemp_pp(:,iel)=MATMUL(storkb_pp(:, :, iel),pmul_pp(:, iel))
        END DO elements_2a
        CALL scatter(u_pp,utemp_pp)

        IF(fixed_freedoms_pp > 0) THEN
          DO i = 1, fixed_freedoms_pp
            l      = no_f_pp(i) - ieq_start + 1
            k      = fixed_freedoms_start + i - 1
            u_pp(l) = store_pp(i)*val_f(k)
          END DO
        END IF

        loads_pp = loads_pp+u_pp

      ELSE

!-----
! 17. Set initial temperature
!-----

      x_pp = val0

      IF(fixed_freedoms_pp > 0) THEN
        DO i = 1, fixed_freedoms_pp
          l      = no_f_pp(i) - ieq_start + 1
          k      = fixed_freedoms_start + i - 1
          x_pp(l) = val_f(k)
        END DO
      END IF

```



```

CALL gather(x_pp,pmul_pp)
elements_2c: DO iel=1,nels_pp
  utemp_pp(:,iel)=MATMUL(storka_pp(:, :, iel),pmul_pp(:, iel))
END DO elements_2c
CALL scatter(u_pp,utemp_pp)

loads_pp = loads_pp + u_pp
!-----
! 18. Output "results" at t=0
!-----

eld_pp    = zero
disp_pp   = zero
tz        = 0
CALL gather(x_pp(1:),eld_pp)

CALL scatter_nodes(npes,nn,nels_pp,g_num_pp,nod,nodof,nodes_pp,    &
  node_start,node_end,eld_pp,disp_pp,1)

IF(numpe==it)THEN
  !---Write temperature outputs in Excel format
  WRITE(11, '(E12.4,8E19.8)')t0,disp_pp(is)
END IF

!---Write temperature outputs in ParaFEM format
CALL write_nodal_variable_binary(label,25,tz,nodes_pp,npes,      &
  numpe,nodof,disp_pp)

END IF ! From section 16

!-----
! 19. Initialize PCG process
!
!   When  $x = 0$ ,  $iwp$  p and r are just loads but in general
!    $p=r=loads-A*x$ , so form  $r = A*x$ . Here, use LHS part of the transient
!   equation storka_pp
!-----

r_pp          = zero
pmul_pp       = zero
utemp_pp      = zero
x_pp          = zero

CALL gather(x_pp,pmul_pp)
elements_2b: DO iel=1,nels_pp
  utemp_pp(:,iel)=MATMUL(storka_pp(:, :, iel),pmul_pp(:, iel))
END DO elements_2b
CALL scatter(r_pp,utemp_pp)

IF(fixed_freedoms_pp > 0) THEN
  DO i = 1, fixed_freedoms_pp
    l      = no_f_pp(i) - ieq_start + 1
    k      = fixed_freedoms_start + i - 1
    r_pp(l) = store_pp(i)*val_f(k)
  END DO
END IF

r_pp = loads_pp - r_pp
d_pp = diag_precon_pp*r_pp
p_pp = d_pp

```

```

!-----
! 12. Solve simultaneous equations by pcg
!-----

d_pp = diag_precon_pp*loads_pp
p_pp = d_pp
x_pp = zero

iters = 0

iterations: DO

    iters    = iters+1
    u_pp     = zero
    pmul_pp  = zero

    CALL gather(p_pp,pmul_pp)
    elements_6: DO iel=1,nels_pp
        utemp_pp(:,iel)=MATMUL(storka_pp(:, :, iel),pmul_pp(:,iel))
    END DO elements_6
    CALL scatter(u_pp,utemp_pp)

!-----
! 13. PCG equation solution
!-----

up      = DOT_PRODUCT_P(loads_pp,d_pp)
alpha   = up/DOT_PRODUCT_P(p_pp,u_pp)
xnew_pp = x_pp+p_pp*alpha
loads_pp = loads_pp-u_pp*alpha
d_pp     = diag_precon_pp*loads_pp
beta    = DOT_PRODUCT_P(loads_pp,d_pp)/up
p_pp     = d_pp+p_pp*beta
u_pp     = xnew_pp

CALL checon_par(xnew_pp,tol,converged,x_pp)
IF(converged.OR.iters==limit)EXIT

END DO iterations

loads_pp=xnew_pp

```

```

!-----
! 20. Solve simultaneous equations by pcg
!-----

      iters = 0

      iterations: DO

          iters      = iters+1
          itersT     = itersT+1

          u_pp       = zero
          pmul_pp    = zero
          utemp_pp   = zero

          CALL gather(p_pp,pmul_pp)
          elements_6: DO iel=1,nels_pp
              utemp_pp(:,iel)=MATMUL(storka_pp(:, :, iel),pmul_pp(:, iel))
          END DO elements_6
          CALL scatter(u_pp,utemp_pp)

!-----
! 21. PCG equation solution
!-----

      IF(fixed_freedoms_pp > 0) THEN
          DO i = 1, fixed_freedoms_pp
              l      = no_f_pp(i) - ieq_start + 1
              u_pp(l) = p_pp(l) * store_pp(i)
          END DO
      END IF

      up      = DOT_PRODUCT_P(r_pp,d_pp)
      alpha   = up/DOT_PRODUCT_P(p_pp,u_pp)
      xnew_pp = x_pp+p_pp*alpha
      r_pp    = r_pp-u_pp*alpha
      d_pp    = diag_precon_pp*r_pp
      beta    = DOT_PRODUCT_P(r_pp,d_pp)/up
      p_pp    = d_pp+p_pp*beta

      CALL checon_par(xnew_pp,tol,converged,x_pp)
      IF(converged.OR.iters==limit)EXIT

      END DO iterations

```

```

IF(j/npri*npri==j.AND.numpe==1)WRITE(11,'(2E12.4,I5)')real_time,      &
loads_pp(is),iters

END DO timesteps
IF(numpe==it)THEN
WRITE(11,'(A,I5,A)') "This job ran on ",npes," processors"
WRITE(11,'(A)') "Global coordinates and node numbers"
DO i=1,nels_pp,nels_pp - 1
WRITE(11,'(A,I8)') "Element ",i
num=g_num_pp(:,i)
DO k=1,nod
WRITE(11,'(A,I8,3E12.4)') " Node",num(k),p_g_co_pp(k,:,i)
END DO
END DO
WRITE(11,'(A,3(I8,A))') "There are ",nn," nodes",nr," restrained and",&
neq," equations"
WRITE(11,*)"Time after setup is :",elap_time()-timest(1)
END IF

IF(numpe==it) WRITE(11,*)"This analysis took :",elap_time()-timest(1)

CALL shutdown()

END PROGRAM p124

```

```

timest(13) = timest(13) + (elap_time() - timest(15))
timest(16) = elap_time()

IF(j/npri*npri==j)THEN

    eld_pp    = zero
    disp_pp   = zero
    CALL gather(xnew_pp(1:),eld_pp)

    CALL scatter_nodes(npes,nn,nels_pp,g_num_pp,nod,nodof,nodes_pp,    &
        node_start,node_end,eld_pp,disp_pp,1)

    IF(numpe==it)THEN
        !---Write temperature outputs in Excel format
        WRITE(11,'(8E19.8,8E19.8)')real_time,disp_pp(is)
    END IF

    !---Write temperature outputs in ParaFEM format
    CALL write_nodal_variable_binary(label,25,j,nodes_pp,npes,numpe,    &
        nodof,disp_pp)

    IF(numpe==1) PRINT *, "Time ", real_time, "Iters ", iters
END IF

timest(14) = timest(14) + (elap_time() - timest(16))

END DO timesteps

timest(13) = timest(12) + timest(13)
timest(14) = timest(13) + timest(14)

IF(numpe==1)THEN
    CLOSE(11)
    CLOSE(24)
END IF

IF(numpe==1) PRINT *, "Total number of iterations = ", itersT
IF(numpe==1) PRINT *, "Timest ", timest

CALL WRITE_P123(fixed_freedoms,iters,job_name,loaded_freedoms,neq,    &
    nn,npes,nr,numpe,timest,q)

CALL shutdown()

END PROGRAM xx12

```





## E: FORTRAN code for post-processing of nodal temperatures

```
PROGRAM ndttrget
IMPLICIT NONE

INTEGER                :: nstep,nres,i,j,k
REAL                  :: ttr
CHARACTER(LEN=50)      :: job_name,arg1,arg2,fname

!-----
! 1. Read arguments
!-----

CALL GETARG(1,job_name)
CALL GETARG(2,arg1)
CALL GETARG(3,arg2)

read(arg1,*) nstep !Convert string to integer
read(arg2,*) nres

PRINT *, "job_name = ", job_name
PRINT *, "nstep = ", nstep
PRINT *, "nres = ", nres

!-----
! 2. Open files, read and write ttr
!-----

fname=job_name(1:INDEX(job_name, " ") -1)//".ndttr"
PRINT *, "open: ", fname
OPEN(10,file=fname,status='replace',action='write')

DO i=1,nstep
  WRITE(arg1,'(i10)')i !Convert integer to string
  arg1=ADJUSTL(arg1)   !Remove trailing spaces
  IF (i<10) THEN
    fname=job_name(1:INDEX(job_name, " ") -1)//".ensi.NDTTR-00000"//arg1
  ELSE IF (i<100 .AND. i>9) THEN
    fname=job_name(1:INDEX(job_name, " ") -1)//".ensi.NDTTR-0000"//arg1
  ELSE IF (i<1000 .AND. i>99) THEN
    fname=job_name(1:INDEX(job_name, " ") -1)//".ensi.NDTTR-000"//arg1
  ELSE IF (i<10000 .AND. i>999) THEN
    fname=job_name(1:INDEX(job_name, " ") -1)//".ensi.NDTTR-00"//arg1
  ELSE IF (i<100000 .AND. i>9999) THEN
    fname=job_name(1:INDEX(job_name, " ") -1)//".ensi.NDTTR-0"//arg1
  ELSE IF (i<1000000 .AND. i>99999) THEN
    fname=job_name(1:INDEX(job_name, " ") -1)//".ensi.NDTTR-"//arg1
  END IF
  PRINT *, "read: ", fname
  OPEN(11,file=fname,status='old',action='read')

  DO j=1,4+nres-1      !Skip header and ttr values before nres
    READ (11,*)
  END DO
  READ (11,*)ttr
  WRITE(10,'(E16.8)')ttr
  CLOSE(11)
END DO
CLOSE(10)

END PROGRAM ndttrget
```



## **F: xx12 input file details [68]**

This section describes the format of the ParaFEM ASCII input decks. The input decks comprise a number of separate files:

**Table F.1**

Input files required by program xx12

File extension	Content
.dat	Basic control data
.d	The geometry of the problem
.fix	The boundary conditions for fixed temperatures
.lds	The loads to be applied
.mat	The material properties
.amp	Temporal amplitude of loads

The xx12.dat file has the following format:

```

element
mesh
partitioner
np_types
nels nn nr nip nod loaded_nodes fixed_freedoms
val0
dtim nsteps npri theta
tol limit
nres

```

**Table F.2**  
Required variables for the .dat input file

Variable Name	Type	Meaning
element	Character	The element type. Permitted values are hexahedron and tetrahedron.
mesh	Integer	Element node ordering scheme. Permitted values are 1 (Smith and Griffiths scheme) or 2 (Abaqus scheme).
partitioner	Integer	Partitioning strategy. Permitted values are 1 (Smith and Griffiths partitioning) or 2 (use external partitioner).
np_types	Integer	Number of property types.
nels	Integer	Number of elements in the mesh.
nn	Integer	Number of nodes in the mesh.
nr	Integer	Number of restrained nodes in the mesh.
nip	Integer	Number of integration points.
nod	Integer	Number of nodes per element.
loaded_nodes	Integer	Number of nodes with externally applied loads.
fixed_freedoms	Integer	Number of freedoms with fixed displacements.
val0	Real	Initial temperature of whole model.
dtim	Real	Timestep.
nsteps	Integer	Number of timesteps in analysis.
npri	Integer	Print interval.
theta	Real	Parameter in theta integrator (0.5 recommended).
tol	Real	Convergence tolerance for PCG.
limit	Integer	Iteration ceiling for PCG.
nres	Integer	Element number to print its values to .ttr2.

A real example follows;

```

hexahedron
2
1
1
64 125 0 8 8 25 25
10.0
0.01 150 10 0.5
0.1000E-04 500
43

```

The xx12.d file has the following format:

```
*THREE_DIMENSIONAL
*NODES
nodeID x-coordinate y-coordinate z-coordinate
*ELEMENTS"
elementID ndim nod type num materialID
```

**Table F.3**

Required variables for the xx12.d input file

Variable Name	Type	Purpose
*THREE_DIMENSIONAL	Character	A keyword describing the model as three dimensional.
*NODES	Character	A keyword marking the start of a list of nodes and their coordinates.
*ELEMENTS	Character	A keyword marking the start of a list of element data.
nodeID	Integer	A unique number that identifies the node. ParaFEM assumes sequential numbering from 1 to nn.
x-coordinate	Real	The x-coordinate of the node.
y-coordinate	Real	The y-coordinate of the node.
z-coordinate	Real	The z-coordinate of the node.
elementID	Integer	A unique number that identifies the element. ParaFEM assumes sequential numbering from 1 to nels.
ndim	Integer	The number of dimensions. ParaFEM only supports 3D elements.
nod	Integer	The number of nodes in the element. ParaFEM only supports the values 4, 8, 10, 20: 4-node tetrahedra, 8-node hexahedra, 10-node tetrahedra and 20-node hexahedra.
type	Integer	Code for element type. Default is 1.
num	Integer List	A list of nodes that belong to the element. 4 nodes are expected for 4-node tetrahedra, 8 nodes for 8-node hexahedra and so on. Refer to Smith and Griffiths for the correct node ordering.

A real example follows;

```
*THREE_DIMENSIONAL
*NODES
1 15.0989017 2.49846721 0.940066218
2 15.0960474 2.40614152 0.983345568
3 15.0937481 2.51739144 0.975006104
4 15.0070047 2.48403239 0.964258492
5 15.1986771 2.4753387 0.957266092
*ELEMENTS
1 3 4 1 1 2 3 4 1
2 3 4 1 5 2 3 1 1
```

The xx12.fix file has the following format:

```
nodeID-1 direction value
nodeID-2 direction value
nodeID-3 direction value
...
nodeID-fixed_nodes direction value
```

**Table F.4**

Required variables for the xx12.fix input file

Variable Name	Type	Purpose
nodeID	Integer	A unique number that identifies the fixed node. ParaFEM assumes sequential numbering from 1 to fixed_nodes, shown here as nodeID-1, nodeID-2, nodeID-3, ... , nodeID-fixed_nodes. Nodes which are not fixed need not be included.
direction	Integer	Direction in which value is fixed. For scalar use 1.
value	Real	Value of fixed temperature applied.
fixed_nodes	Integer	The number of fixed nodes in the model.

A real example follows;

```
42    1 0.0
44    1 0.0
45    1 0.0
```

The xx12.lds file has the following format:

```
nodeID-1 value_x value_y value_z
nodeID-2 value_x value_y value_z
nodeID-3 value_x value_y value_z
...
nodeID-loaded_nodes value_x value_y value_z
```

**Table F.5**

Required variables for the xx12.lds input file

Variable Name	Type	Purpose
nodeID	Integer	A unique number that identifies the loaded node. ParaFEM assumes sequential numbering from 1 to loaded_nodes, shown here as nodeID-1, nodeID-2, nodeID-3, ... , nodeID-loaded_nodes. Nodes which do not have applied loads need not be included.
value_x	Real	Value of load applied in X direction.
value_y	Real	Value of load applied in Y direction.
value_z	Real	Value of load applied in Z direction.
loaded_nodes	Integer	The number of loaded nodes in the model.

A real example follows:

```
11935 0. 0. 2.08333333
11936 0. 0. 8.33333333
27347 0. 0. 4.16666666
27349 0. 0. 8.33333333
```

The xx12.mat file has the following format:

```
*MATERIAL nmats nvals
```

```
Keywords
```

```
matID-1 kx ky kz rho cp
```

```
matID-2 kx ky kz rho cp
```

```
matID-3 kx ky kz rho cp
```

```
...
```

```
matID-nmats e v
```

**Table F.6**

Required variables for the xx12.mat input file

Variable Name	Type	Purpose
nmats	Integer	Number of different materials.
nvals	Integer	Number of different property types.
Keywords	String	Titles for each material property
matID	Integer	A unique number that identifies the material type.
kx	Real	Thermal conductivity in X direction.
ky	Real	Thermal conductivity in Y direction.
kz	Real	Thermal conductivity in Z direction.
rho	Real	Mass density.
cp	Real	Specific heat capacity.

A real example follows:

```
*MATERIAL 4 5
```

```
kx ky kz rho cp
```

```
1 3.4745E+02 3.4745E+02 3.4745E+02 8.6098E-09 4.8000E+08
```

```
2 2.1489E+02 2.1489E+02 2.1489E+02 1.8148E-09 1.0290E+09
```

```
3 2.4300E+01 2.4300E+01 2.4300E+01 8.8000E-09 3.9000E+08
```

```
4 3.8000E-02 3.8000E-02 3.8000E-02 0.7380E-12 1.0300E+09
```



The xx12.amp file has the following format:

Amplitude

...

Amplitude-nstep

**Table F.7**

Required variables for the xx12.amp input file

Variable Name	Type	Purpose
Amplitude	Real	A value whose product with .lds gives the load amplitude for a given time step.
nstep	Integer	The number of time steps in the model.

A real example follows:

0.0

0.1

0.5

0.0